Meinhard Kuna
Andreas Ricoeur
Editors

IUTAM Bookseries

IUTAM Symposium on Multiscale Modelling of Fatigue, Damage and Fracture in Smart Materials

Proceedings of the IUTAM Symposium on Multiscale Modelling of Fatigue, Damage and Fracture in Smart Materials, held in Freiberg, Germany, September 1-4, 2009

Springer

IUTAM Symposium on Multiscale Modelling of Fatigue, Damage and Fracture in Smart Materials

IUTAM BOOKSERIES
Volume 24

Aims and Scope of the Series

The IUTAM Bookseries publishes the proceedings of IUTAM symposia under the auspices of the IUTAM Board.

For other titles published in this series, go to
http:www.springer.com/series/7695

Meinhard Kuna · Andreas Ricoeur
Editors

IUTAM Symposium on Multiscale Modelling of Fatigue, Damage and Fracture in Smart Materials

Proceedings of the IUTAM Symposium on Multiscale Modelling of Fatigue, Damage and Fracture in Smart Materials, held in Freiberg, Germany, September 1–4, 2009

Springer

Editors
Meinhard Kuna
TU Bergakademie Freiberg
Inst. Mechanik und Fluiddynamik
Lampadiusstr. 4
09596 Freiberg
Germany
Meinhard.Kuna@imfd.tu-freiberg.de

Andreas Ricoeur
Universität Kassel
Inst. Mechanik
Mönchebergstr. 7
34109 Kassel
Germany
ricoeur@uni-kassel.de

ISSN 1875-3507 e-ISSN 1875-3493
ISBN 978-90-481-9886-3 e-ISBN 978-90-481-9887-0
DOI 10.1007/978-90-481-9887-0
Springer Dordrecht Heidelberg London New York

Library of Congress Control Number: 2010938713

Cover design: SPi Publisher Services

Printed on acid-free paper

Springer is part of Springer Science+Business Media (www.springer.com)

Preface

Multi-functional materials as piezoelectric/ferroelectric ceramics, magnetostrictive and shape memory alloys are gaining increasing applications as sensors, actuators or smart composite materials systems for promising high tech areas. One primary problem is, however, that these functional materials suffer from various mechanical and/or electromagnetical degradation mechanisms as fatigue, damage and fracture. As a consequence of field coupling effects, fabrication processes and service loads, smart materials systems are exposed to high mechanical and/or electromagnetical field concentrations under internal and external loading of static, cyclic and dynamic type. For this reason, the investigation of fatigue, damage and fracture plays a decisive role for the optimum design, reliability and durability of smart materials systems. Thus, the topic of the symposium represents an active international research area in mechanics of materials. From the experience and investigations during the last decade it has become evident that progress in this scientific discipline is only possible, if material models are based on the true physical nature of the phenomena and if theoretical predictions are verified by skilful experiments. Therefore, the scientific challenges can only be solved by

- A multi-scale modelling at several length scales from atomistic to macroscopic level
- An interdisciplinary cooperation between solid mechanics, materials science and physics

To promote the international scientific exchange in this important field, in 2006 the General Assembly of IUTAM approved the proposal to host this symposium in Freiberg, Germany and appointed the International Scientific Committee. The IUTAM Symposium (GA. 06-16) "Multiscale Modelling of Fatigue, Damage and Fracture in Smart Materials Systems" was held on September 1–4, 2009 at Technische Universität Bergakademie Freiberg, Germany, organized by the Institute of Mechanics and Fluid Dynamics.

This symposium stands in a line with former symposia on related topics held under the auspices of IUTAM in 2000 at Magdeburg and in 2004 at Beijing. The helpful assistance of the International Scientific Committee to communicate the symposium and to recommend invited speakers is thankfully appreciated.

According to the rules and tradition of IUTAM, the aim of the Symposium is to bring together internationally leading researchers working in the area of smart materials. The goal is to exchange recent scientific results, to discuss new achievement and actual problems in an open and frank atmosphere. The organizers were happy to welcome a lot of outstanding scientists in this field from all parts of the globe as well as many young researchers. In total there were 44 participants coming from 14 countries: Australia (1), Austria (3), Belgium (1), Canada (1), China (8), Great Britain (1), France (2), Germany (19), Israel (1), Italy (1), Japan (2), Slovakia (1), Ukraine (1) and USA (2). The scientific program covered 35 invited oral contributions presented in 10 sessions.

The following main topics have been addressed during the symposium:

- Development of computational methods for coupled electromechanical field analysis, especially extended, adaptive and multi-level finite element techniques in combination with boundary elements.
- Constitutive modeling of smart materials with coupled electric, magnetic, thermal and mechanical fields, especially of nonlinear dissipative hysteresis behavior. Major trend is the development of micromechanical models. Especially for ferroelectric materials and shape memory alloys the simulation of microstructure (domain switching, martensitic transformation etc.) are of paramount concern.
- Further understanding and modeling of fracture and fatigue in piezoelectric and ferroelectric ceramics, especially the modeling of fracture process zone and of electric boundary conditions at crack faces. Applications of phase field simulation and configurational mechanics.
- Reliability and durability of sensors and actuators under in service loading by alternating mechanical, electrical and thermal fields. The role of interface cracks between layers and in thin films is addressed.
- Experimental methods to measure fracture strength and to investigate fatigue crack growth in ferroelectric materials under electromechanical loading. It has been pointed out that complicated theoretical predictions have to be contrasted and verified by skilful experiments.
- New ferroelectric materials, compounds and composites with enhanced strain capabilities.

The chairman and its organizing team tried to make this IUTAM symposium not only a successful scientific meeting but an outstanding social event, too. Many thanks are due to Prof. Dr. A. Ricoeur, who carried the main workload in organizing all details of this symposium.

The Technische Universität Bergakademie Freiberg is located in the East German Federal State Saxony. Besides Dresden and Chemnitz, TU Bergakademie Freiberg is considered as the “smallest” but “smartest” among these Technical Universities. Its history started with the discovery of silver in the middle ages. The “Mining Academy” Freiberg was founded by the Saxon King in 1765 in order to promote the technologies in surveying, mining and metallurgy. Thus, TU Bergakademie Freiberg possesses a long and famous tradition as one of the oldest montanistic universities in the world. Nowadays, TU Bergakademie Freiberg is established as modern

Technical University focusing mainly on Geoscience, Resources, Materials Science, Energy and Environmental Technologies.

Freiberg has one of the largest and most splendid mineralogical exhibitions "Terra Mineralia" in the world hosted in the old castle "Freudenstein". The participants of the symposium enjoyed the visit very much.

Freiberg, 2009

Meinhard Kuna
Chairman of the Symposium

International Scientific Committee

Kuna, M. (Freiberg, chair, Germany)
Gabbert, U. (Magdeburg, Germany)
Huber, J.E. (Oxford, Great Britain)
Mai, Y.W. (Sydney, Australia)
McMeeking, R.M. (Santa Barbara, USA)
Rajapakse, N. (Burnaby, Canada)
Shindo, Y. (Sendai, Japan),
Yang, W. (Hangzhou, IUTAM representative, China)

Local Organizing Committee at TU Bergakademie Freiberg

Meinhard Kuna (Chair, Germany)
Andreas Ricoeur (Germany)

Sponsors

International Union of Theoretical and Applied Mechanics
Technische Universität Bergakademie Freiberg
Springer Verlag

This page intentionally left blank

Contents

This page intentionally left blank

List of Participants

K. Albe	TU Darmstadt, Institut für Materialwissenschaft, FG Materialmodellierung, Petersenstraße 23, 64287 Darmstadt albe@mm.tu-darmstadt.de
T. Antretter	Institut für Mechanik, Montanuniversität Leoben Peter-Tunner-Straße 5, 8700 Leoben, Austria thomas.antretter@unileoben.ac.at
H. Balke	Technische Universität Dresden, Institut für Festkörpermechanik, 01062 Dresden, Germany Herbert.Balke@tu-dresden.de
F. Auricchio	Dipartimento di Meccanica Strutturale, Universita' di Pavia, Via Ferrata 1, 27100 Pavia, Italy auricchio@unipv.it
L. Banks-Sills	Dreszer Fracture Mechanics Laboratory, School of Mechanical Engineering, Tel Aviv University, Ramat Aviv 69978, Israel banks@eng.tau.ac.il
É. Béchet	Department of Aerospace and Mechanical Engineering, Université de Liège, Chemin des Chevreuils 1, 4000 Liège, Belgium eric.bechet@ulg.ac.be
A. Benjeddou	Supméca, Structures, 3 rue Fernand Hainault, 93407 Saint Ouen CEDEX, France benjeddou@supmeca.fr
R. Danzer	Institut für Struktur- und Funktionskeramik, Montanuniversität Leoben Peter-Tunner-Straße 5, 8700 Leoben, Austria isfk@unileoben.ac.at
K. Dayal	Civil and Environmental Engineering, Carnegie Mellon University 118J Porter Hall, Pittsburgh, PA 15213-3890, USA kaushik@cmu.edu

F. Fang	Tsinghua University, School of Mechanical Engineering, Beijing 100084, China fangf@mail.tsinghua.edu.cn
C.F. Gao	Nanjing University of Aeronautics and Astronautics, Nanjing 210016, China cfgao@nuaa.edu.cn
L. Gao	Chair of Structural Mechanics, Department of Civil Engineering, University of Siegen, Paul-Bonatz-Street 9-11, 57076 Siegen, Germany c.zhang@uni-siegen.de
D. Gross	Institute of Mechanics, TU Darmstadt, D-64289 Darmstadt, Germany gross@mechanics.tu-darmstadt.de
H. Grünbichler	Institut für Struktur- und Funktionskeramik, Montanuniversität Leoben Peter-Tunner-Straße 5, 8700 Leoben, Austria hannes.gruenbichler@mcl.at
C. Häusler	TU Bergakademie Freiberg, IMFD, Lampadiusstr. 4, 09596 Freiberg Christoph.Haeusler@imfd.tu-freiberg.de
J.E. Huber	Department of Engineering Science, University of Oxford, Parks Road, Oxford, OX1 3PJ, UK john.huber@eng.ox.ac.uk
Ł. Janski	Technische Universität Bergakademie Freiberg, Institut für Mechanik und Fluiddynamik, Lampadiusstr. 4, 09599 Freiberg, Germany Lukasz.Janski@imfd.tu-freiberg.de
S. Klinkel	Statik und Dynamik der Tragwerke, Technische Universität Kaiserslautern, Paul-Ehrlich-Str. 14, 67663 Kaiserslautern, Germany klinkel@rhrk.uni-kl.de
B. Kranz	Fraunhofer-Institut für Werkzeugmaschinen und Umformtechnik IWU, Nöthnitzer Straße 44, 81187 Dresden Burkhard.kranz@iwu.fraunhofer.de
M. Kuna	Technische Universität Bergakademie Freiberg, Institut für Mechanik und Fluiddynamik, Lampadiusstr. 4, 09599 Freiberg, Germany Meinhard.Kuna@imfd.tu-freiberg.de
C. Lexcellent	Université de Franche Comté, Dept. de Mécanique Appliquée, 24 Chemin de l'Epitaphe, 25030 Besancon Cedex, France Christian.lexcellent@univ.-fcomte.fr
F. Li	State Key Lab for Turbulence and Complex Systems, College of Engineering, Peking University, Beijing, 100871, China lifaxin@pku.edu.cn
Q. Li	Technische Universität Bergakademie Freiberg, Institut für Mechanik und Fluiddynamik, Lampadiusstr. 4, 09599 Freiberg, Germany qunli@imfd.tu-freiberg.de

C. Linder	Universität Stuttgart, Institute of Applied Mechanics, Pfaffenwaldring 7, 70550 Stuttgart linder@mechbau.uni-stuttgart.de
A. Liskowsky	Technische Universität Dresden, Institut für Festkörpermechanik, 01062 Dresden, Germany Albrecht.Liskowsky@tu-dresden.de
V.V. Loboda	Department of Theoretical and Applied Mechanics, Dniepropetrovsk National University, St. Kosakova 18, Building No. 14, 49050 Dnipropetrovsk, Ukraine loboda@mail.dsu.dp.ua
R. McMeeking	Department of Mechanical and Enviromental Engineering, University of California, Santa Barbara, CA 93106, USA rmcm@engineering.ucsb.edu
R. Müller	Technische Universität Kaiserslautern, Lehrstuhl für Technische Mechanik Postfach 3049, 67653 Kaiserslautern ram@rhrk.uni-kl.de
A. Ricoeur	Universität Kassel, Institut für Mechanik, Mönchebergstraße 7, 34109 Kassel andreas.ricoeur@uni-kassel.de
J. Rödel	TU Darmstadt, MatGeo, FG Nichtmetallisch-Anorganische Werkstoffe, Petersenstraße 23, 64287 Darmstadt roedel@ceramics.tu-darmstadt.de
S. Roth	Technische Universität Bergakademie Freiberg, Institut für Mechanik und Fluiddynamik, Lampadiusstr. 4, 09599 Freiberg, Germany Stephan.Roth@imfd.tu-freiberg.de
G.A. Schneider	Technische Universität Hamburg-Harburg, Institut für Keramische Hochleistungswerkstoffe, Denickestraße 15 (K), 21073 Hamburg g.schneider@tu-harburg.de
J. Schröder	Universität Duisburg-Essen, Institut für Mechanik, Universitätsstraße 15, 45117 Essen j.schroeder@uni-due.de
A.S. Semenov	Technische Universität Dresden, Institut für Festkörpermechanik, 01062 Dresden, Germany artem.semenov@tu-dresden.de
M.S. Senousy	The University of British Columbia, Department of Mechanical Engineering, 2054-6250 Applied Science Lane, Vancouver, B.C., V6T 1Z4, Canada msenousy@interchange.ubc.ca

F. Shang — Department of Engineering Mechanics, School of Aerospace, Xi'an Jiaotong University, 28 West Xian-Ning Road, Xi'an 710049, China, shangfl@mail.xjtu.edu.cn

Y. Shindo — Tohoku Universtiy, Graduate School of Engineering, Department of Materials Processing, Sendai 980-8579, Japan, shindo@material.tohoku.ac.jp

D.K. Vu — LTM, University of Erlangen, Egerlandstr. 5, 91058 Erlangen, Germany, vu@ltm.uni-erlangen.de

M. Wagner — Ruhr-Universität Bochum, Institut für Werkstoffe (WW), Fakultät für Maschinenbau, Universitätsstraße 150, 44801 Bochum, martin.wagner@ruhr-uni-bochumg.de

J.S. Wang — Department of Mechanics, Tianjin University, Weijin Road, No. 92, Nankai district, Tianjin 300072, China, wjs_tju@163.com

S. Wang — Institute of Applied Mechanics, Zhejiang University, Hangzhon, Zhejiang 310027, China, jw@zju.edu.cn

K. Webber — TU Darmstadt, MatGeo, FG Nichtmetallisch-Anorganische Werkstoffe, Petersenstraße 23, 63287 Darmstadt, webber@ceramics.tu-darmstadt.de

S. Yu — Tsingua University, Department of Mechanics, School of Aerospace, Beijing, 100084, China, yusw@mail.tsinghua.edu.cn

Scientific Program

Tuesday, September 01

Opening and Welcome Address by the Chairman of the Symposium M. Kuna

Fracture Mechanics I (session leader: T. Kitamura)

Leslie Banks-Sills, Yael Motola: "*Failure of piezoelectric ceramics*"

Gerold Schneider, A. Engert, H. Jelitto: "*What do we know about crack surface charges and the difference between intrinsic and extrinsic process during fracture in ferroelectric ceramics?*"

Yasuhide Shindo**,** Fumio Narita: "*Effects of electric field and poling on fatigue behavior of PZT ceramics with single-edge crack by three-point bending*"

Daining Fang**,** Yihui Zhang, Guanzhong Mao, Bin Liu: "*Electric field induced fatigue crack growth in ferroelectric ceramics*"

Shape Memory Alloys I (session leader: C. Lexcellent)

Martin F.-X. Wagner, Christian Grossmann, Marcus Young, Gunther Eggeler: "*Localized deformation, mesoscopic phase interfaces and functional fatigue in pseudoelastic NiTi shape memory alloys*"

F. Auricchio, M. Conti, S. Morganti, A. Reali, U. Stefanelli: "*Shape-memory alloys: effective 3D modelling, computational aspects and biomedical device analysis*"

Ferroelectrics I (session leader: R. McMeeking)

Artem S. Semenov, Albrecht C. Liskowsky, Herbert Balke: "*Effective computational methods for the modeling of ferroelectroelastic hysteresis behavior*"

Stephan Roth, Peter Neumeister, Artem Semenov, Herbert Balke: "*Finite element simulation of the non-remanent straining ferroelectric material behaviour based on the electric scalar potential – convergence and stability*"

Li Yu, Shouwen Yu, Dietmar Gross: "*Constitutive behaviour of nano-particle ferroelectric ceramics*"

Wednesday, September 02

Ferroelectrics II (session leader: J. Huber)

Faxin Li: "*An optimization-based computational model for polycrystalline ferroelastics*"

Ralf Müller, David Schrade, Baixiang Xu, Dietmar Gross: "*Modelling of domain structure evolution in ferroelectric materials*"

Qun Li, Marco Enderlein, Meinhard Kuna: "*Microstructural FEM modeling of domain switching in tetragonal/rhombohedral ferroelectrics*"

Sven Klinkel, K. Linnemann: "*A phenomenological constitutive model for piezoelectric ceramics and magnetostrictive materials*"

Shape Memory Alloys II (session leader: F. Auricchio)

Christian Lexcellent, R. Laydi, V. Taillebot, P. Malecot: "*Prediction of the phase transformation zone around the crack tip of a shape memory alloy exhibiting an asymmetry between tension and compression*"

Thomas Antretter, Wolfgang Pranger, Thomas Waitz, Franz D. Fischer: "*Martensite morphologies in nanostructured NiTi shape memory alloys – energetic considerations*"

Fracture Mechanics II (session leader: L. Banks-Sills)

Duc Khoi Vu, Paul Steinmann: "*The concept of material forces and the coupled boundary-finite element method in electroelastostatics*"

Cun-Fa Gao, Yiu-Wing Mai: "*Stresses in an electrostrictive solid containing an elliptic cavity*"

Eric Béchet, Meinhard Kuna: "*Some numerical experiments about cracked piezoelectric media*"

Qing-Hua Qin, X.Q. He, J.S. Wang: "*Singularity analysis of electro-mechanical fields in angularly inhomogeneous piezoelectric composites wedges*"

Thursday, September 03

Fracture Mechanics III (session leader: Y. Shindo)

Jie Wang, Marc Kamlah: "*Three dimensional finite element modeling of nonlinear fracture of ferroelectric materials*"

Ł. Janski, P. Steinhorst, M. Kuna: "*Crack propagation simulations in piezoelectric structures with an efficient adaptive finite element tool*"

Volodymyr Loboda, S.V. Kozinov: "*Periodic set of interface cracks with limited electric permeability*"

Fulin Shang, Yabin Yan, Takayuki Kitamura: "*Interfacial delamination of PZT thin films*"

Nano (session leader: J. Schröder)

Karsten Albe, Paul Erhart: "*Modelling of point defects in ferroelectric materials*"

Takayuki Kitamura, Takashi Sumigawa, Taisuke Sueta: "*Mechanical behaviour of thin film comprised of sculptured nano-elements*"

Actuators (session leader: J. Rödel)

L.M. Gao, Ch. Zhang, Z. Zhong, C.-P. Fritzen, X. Jiang, H.-J. Christ, U. Pietsch: "*Propagation of SAW and PSAW in a Smart AlN/Diamond/γ-TiAl Structure*"

M.S. Senousy, R.K.N.D. Rajapakse, M. Gadala: "*Modeling of thermo-electromechanical response of PZT stack actuators used in fuel injectors*"

Ayech Benjeddou, Mohammad Al-Ajmi: "*Analytical homogenization of piezoceramic shear macro-fibre composites*"

Hannes Grünbichler, Raúl Bermejo, Peter Supancic, Robert Danzer: "*Influence of the load dependent material properties on the performance of multilayer piezoelectric actuators*"

Technical Visit: Laboratories of the host Institute of Mechanics and Fluid Dynamics

Friday, September 04

Ferroelectrics III (session leader: S. Yu)

Robert McMeeking, S.M.A. Jimenez: "*Models for actuation, failure and tearing of electroactive materials*"

Fei Fang, W. Yang, X. Luo: "*In-situ observations of multi-phase coexistence and polarization rotation under electric loadings for* $Pb(Mg_{1/3}Nb_{2/3})O_3$-$PbTiO_3$ *single crystals at the morphotropic phase boundary*"

Jörg Schröder, Marc-André Keip: "*Multiscale modeling of electromechanically coupled materials: homogenization procedure and computation of overall moduli*"

Kaushik Dayal, Kaushik Bhattacharya: "*A boundary element method coupled to phase field to compute ferroelectric domains in complex geometries*"

Jürgen Rödel, Kyle Webber, Emil Aulbach, Wook Jo, Thorsten Leist: "*Temperature-dependent ferroelasticity of ferroelectrics*"

Nien-Ti Tsou, Ingo Münch, John Huber: "*Low energy periodic microstructure in ferroelectric single crystals*"

Closing Address: M. Kuna

A Fracture Criterion for Piezoelectric Material

Leslie Banks-Sills and Yael Motola

Abstract A fracture criterion for piezoelectric ceramics is proposed which is based upon the energy release rate and two phase angles determined from the ratio between the intensity factors. It is assumed that the crack plane is at an angle to the poling direction within a symmetry plane of the body. The special cases of a crack perpendicular and parallel to the poling direction are presented. This criterion was implemented with experimental results from the literature in which the crack faces were perpendicular to the poling direction and the applied electric field. Excellent agreement was found between the fracture curve and the experimental results.

1 Introduction

Piezoelectric ceramics are in widespread use as sensors and actuators in smart structures, despite the absence of a fundamental understanding of their fracture behavior. Piezoceramics are brittle and susceptible to cracking. As a result of the importance of the reliability of these devices, there has been tremendous interest in studying the fracture and failure behavior of such materials. To understand failure mechanisms of piezoelectric materials and maintain the stability of cracked piezoelectric structures operating in an environment of combined electro-mechanical loading, analysis of its mechanical and electrical behavior is a prerequisite.

For cracks in piezoelectric material, there are three stress intensity factors K_I, K_{II} and K_{III}, representing the usual three deformation modes, and an electric flux density intensity factor K_{IV}. Depending on the applied load and electric field, as well as the poling direction relative to the crack faces, various modes are excited. In this paper, a fracture criterion, presented in Section 2, is proposed based upon the energy release rate and two phase angles determined from the ratio between the

L. Banks-Sills (✉) and Y. Motola
Dreszer Fracture Mechanics Laboratory, School of Mechanical Engineering,
Tel Aviv University, Ramat Aviv 69978, Israel
e-mail: banks@eng.tau.ac.il; sphera4u@gmail.com

M. Kuna and A. Ricoeur (eds.), *IUTAM Symposium on Multiscale Modelling of Fatigue, Damage and Fracture in Smart Materials*, IUTAM Bookseries 24,
DOI 10.1007/978-90-481-9887-0_1,

intensity factors. It is assumed that the crack plane is at an angle to the poling direction within a symmetry plane of the body. Four point bend fracture tests carried out in [1] were analyzed in [2] to obtain the non-zero intensity factors K_I and K_{IV}. These values are used to obtain a fracture criterion for this material (PIC-151) when the crack faces are perpendicular to the poling direction and the electric field. These results are presented in Section 3.

2 Fracture Criterion

A mixed mode fracture criterion is developed for piezoelectric ceramics. This criterion is based upon the energy release rate and one or two phase angles, determined from the ratio between the intensity factors. It is assumed that the crack plane is at an angle to the poling direction with poling within a symmetry plane of the body. The special cases of a crack perpendicular and parallel to the poling direction are presented, as well.

A general expression for the energy release rate for piezoelectric ceramics was derived in [3] as

$$\mathscr{G} = \frac{1}{2}\,\mathbf{k}^T\,\mathbf{L}^{-1}\,\mathbf{k} \tag{1}$$

where $\mathbf{k}$ is the intensity factor vector defined as

$$\mathbf{k}^T = [K_{II}, K_I, K_{III}, K_{IV}] \tag{2}$$

where the superscript T represents transpose. The matrix $\mathbf{L}$ is one of the Barnett–Lothe tensors [4] whose components are related to material properties. Based on Eq. 1, the energy release rate for a crack at an angle to the poling direction with poling within a symmetry plane is obtained as

$$\begin{aligned}\mathscr{G} = \frac{1}{2}\Big(&\hat{L}_{22}^{-1}\hat{K}_I^2 + \hat{L}_{11}^{-1}\hat{K}_{II}^2 + \hat{L}_{44}^{-1}\hat{K}_{IV}^2 + 2\hat{L}_{12}^{-1}\hat{K}_I\hat{K}_{II}\\ &+2\hat{L}_{14}^{-1}\hat{K}_{II}\hat{K}_{IV} + 2\hat{L}_{24}^{-1}\hat{K}_I\hat{K}_{IV}\Big).\end{aligned} \tag{3}$$

Out-of-plane loading is omitted here. The parameters $\hat{L}_{11}^{-1}$, $\hat{L}_{12}^{-1}$, $\hat{L}_{14}^{-1}$, $\hat{L}_{22}^{-1}$, $\hat{L}_{24}^{-1}$ and $\hat{L}_{44}^{-1}$ in Eq. 3 are given by

$$\begin{aligned}&\hat{L}_{11}^{-1} = {E_A}^2 L_{11}^{-1} L, \quad \hat{L}_{12}^{-1} = {E_A}^2 L_{12}^{-1} L, \quad \hat{L}_{14}^{-1} = E_A e_{26} L_{14}^{-1} L,\\ &\hat{L}_{22}^{-1} = {E_A}^2 L_{22}^{-1} L, \quad \hat{L}_{24}^{-1} = E_A e_{26} L_{24}^{-1} L, \; \hat{L}_{44}^{-1} = e_{26}^2 L_{44}^{-1} L\end{aligned} \tag{4}$$

where L_{ij}^{-1} are elements of the matrix $\mathbf{L}^{-1}$, E_A and e_{26} are the Young's modulus in the poling direction and a piezoelectric coupling coefficient, respectively, and L is a characteristic length of the problem. The Barnett–Lothe tensor $\mathbf{L}^{-1}$ is ill-conditioned. Hence, it was normalized as

$$\hat{\mathbf{L}}^{-1} = \mathbf{V}\mathbf{L}^{-1}\mathbf{V} \tag{5}$$

where

$$\mathbf{V} = \begin{bmatrix} E_A\sqrt{L} & 0 & 0 & 0 \\ 0 & E_A\sqrt{L} & 0 & 0 \\ 0 & 0 & G_T\sqrt{L} & 0 \\ 0 & 0 & 0 & e_{26}\sqrt{L} \end{bmatrix} \tag{6}$$

and G_T is the shear modulus perpendicular to the poling direction. In this way, the diagonal and off-diagonal elements are the same order of magnitude [5]. It is worth mentioning that the units of $\hat{L}_{ij}^{-1}$ are N/m. Finally, the intensity factors in Eq. 3 are normalized according to

$$\hat{K}_I = \frac{K_I}{E_A\sqrt{L}} \qquad \hat{K}_{II} = \frac{K_{II}}{E_A\sqrt{L}} \qquad \hat{K}_{IV} = \frac{K_{IV}}{e_{26}\sqrt{L}}. \tag{7}$$

The energy release rate $\mathscr{G}$ may be rewritten as

$$\mathscr{G} = \frac{1}{2}\hat{L}_{22}^{-1}\hat{K}_I^2\left(1 + 2\frac{\hat{L}_{24}^{-1}}{\hat{L}_{22}^{-1}}\frac{\hat{K}_{IV}}{\hat{K}_I} + 2\frac{\hat{L}_{12}^{-1}}{\hat{L}_{22}^{-1}}\frac{\hat{K}_{II}}{\hat{K}_I} + 2\frac{\hat{L}_{14}^{-1}}{\hat{L}_{22}^{-1}}\frac{\hat{K}_{II}\hat{K}_{IV}}{\hat{K}_I^2} + \frac{\hat{L}_{44}^{-1}}{\hat{L}_{22}^{-1}}\frac{\hat{K}_{IV}^2}{\hat{K}_I^2} + \frac{\hat{L}_{11}^{-1}}{\hat{L}_{22}^{-1}}\frac{\hat{K}_{II}^2}{\hat{K}_I^2}\right). \tag{8}$$

Thus, it is possible to define

$$\mathscr{G}_I \equiv \frac{1}{2}\hat{L}_{22}^{-1}\hat{K}_I^2. \tag{9}$$

When the crack propagates $\mathscr{G} = \mathscr{G}_c$, so that

$$\mathscr{G}_c = \mathscr{G}_{Ic}\left(1 + 2\frac{\hat{L}_{24}^{-1}}{\hat{L}_{22}^{-1}}\frac{\hat{K}_{IV}}{\hat{K}_I} + 2\frac{\hat{L}_{12}^{-1}}{\hat{L}_{22}^{-1}}\frac{\hat{K}_{II}}{\hat{K}_I} + 2\frac{\hat{L}_{14}^{-1}}{\hat{L}_{22}^{-1}}\frac{\hat{K}_{II}\hat{K}_{IV}}{\hat{K}_I^2} + \frac{\hat{L}_{44}^{-1}}{\hat{L}_{22}^{-1}}\frac{\hat{K}_{IV}^2}{\hat{K}_I^2} + \frac{\hat{L}_{11}^{-1}}{\hat{L}_{22}^{-1}}\frac{\hat{K}_{II}^2}{\hat{K}_I^2}\right) \tag{10}$$

where

$$\mathscr{G}_{Ic} = \frac{1}{2}\hat{L}_{22}^{-1}\hat{K}_{Ic}^2\,. \tag{11}$$

To obtain $\mathscr{G}_{Ic}$, values of $\mathscr{G}_I$ from Eq. 9 are obtained at failure for each test and averaged, as will be discussed in Section 3. Introducing two phase angles

$$\psi = \tan^{-1}\frac{\hat{K}_{IV}}{\hat{K}_I}, \quad \phi = \tan^{-1}\frac{\hat{K}_{II}}{\hat{K}_I}, \tag{12}$$

Equation 10 becomes

$$\mathcal{G}_c = \mathcal{G}_{Ic}\left(1 + 2\frac{\hat{L}_{24}^{-1}}{\hat{L}_{22}^{-1}}\tan\psi + 2\frac{\hat{L}_{12}^{-1}}{\hat{L}_{22}^{-1}}\tan\phi + 2\frac{\hat{L}_{14}^{-1}}{\hat{L}_{22}^{-1}}\tan\psi\tan\phi + \frac{\hat{L}_{44}^{-1}}{\hat{L}_{22}^{-1}}\tan^2\psi + \frac{\hat{L}_{11}^{-1}}{\hat{L}_{22}^{-1}}\tan^2\phi\right). \tag{13}$$

This is a three-dimensional failure surface for the case in which the crack faces are at an angle to the poling direction and in which the critical energy release rate $\mathcal{G}_c$ is a function of the phase angles ψ and ϕ.

For a crack perpendicular to the poling direction, the component $\hat{L}_{14}^{-1}$ is zero. In addition, for symmetric applied loading and electric field, $\hat{K}_{II}$ was found to be negligible [2]. Therefore, for this case, there is only one non-zero phase angle ψ given in Eq. 12_1 leading to the failure curve

$$\mathcal{G}_c = \mathcal{G}_{Ic}\left(1 + 2\frac{\hat{L}_{24}^{-1}}{\hat{L}_{22}^{-1}}\tan\psi + \frac{\hat{L}_{44}^{-1}}{\hat{L}_{22}^{-1}}\tan^2\psi\right). \tag{14}$$

For a crack perpendicular to the poling direction, there is coupling between the first and fourth modes of fracture. This coupling is expressed by the second term in the parentheses of the right hand side of Eq. 14.

For a crack parallel to the poling direction, $\hat{L}_{24}^{-1}$ is zero. In addition, if both the applied loading and electric field are symmetric, then $\hat{K}_{II}$ is negligible (implying $\phi = 0$) and there is nearly no coupling between modes I and IV (see [2]). Thus, the failure curve for a crack parallel to the poling direction with symmetric applied loading and electric field may be found based on Eq. 13 as

$$\mathcal{G}_c = \mathcal{G}_{Ic}\left(1 + \frac{\hat{L}_{44}^{-1}}{\hat{L}_{22}^{-1}}\tan^2\psi\right). \tag{15}$$

3 Fracture Tests

Test were reported in [1] on four-point bend specimens (see Fig. 1) fabricated from the piezoelectric ceramic PIC-151. In these experiments the crack faces were perpendicular to the poling direction and both mechanical loads and electric fields were applied. The dimensions of the specimens are $L = 24$, $S_1 = 20$, $S_2 = 10$ mm, the width $W = 4$ mm and the thickness $B = 3$ mm (see Fig. 1). The samples were placed in a Fluorinert-liquid to prevent electric sparks; this material is dielectrically isotropic with the permittivity $\kappa_a = 1.75\kappa_0$.

Using the same boundary conditions applied in the tests [1], numerical analyses were carried in [2]. These included the finite element method and the interaction

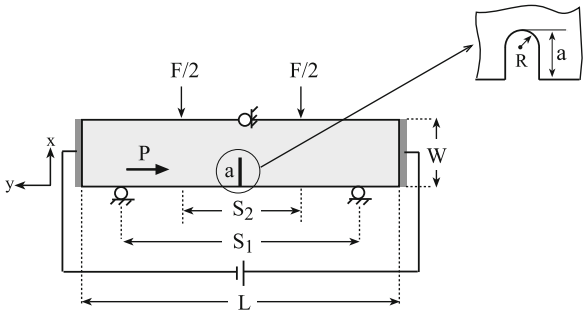

Fig. 1 Four-point bend specimen and an enlargement of the notch [1]

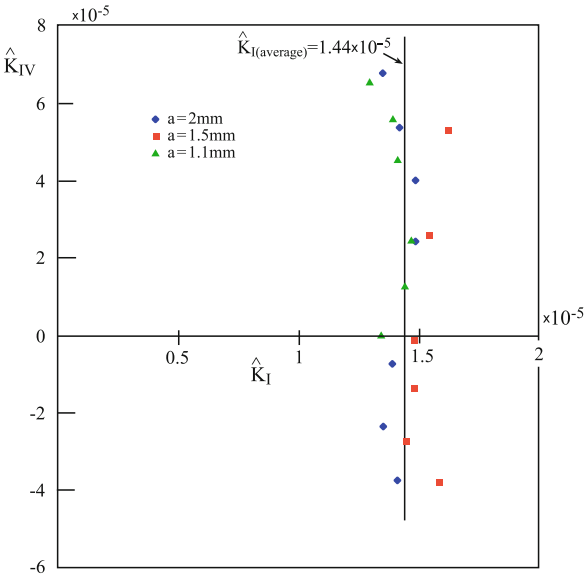

Fig. 2 The intensity factor $\hat{K}_{IV}$ versus $\hat{K}_I$ from analyses of experimental results from [1]

energy or M-integral for obtaining the intensity factors. The Fluorinert-liquid within the notch was modeled as a dielectric isotropic material. Average values of $\hat{K}_I$ and $\hat{K}_{IV}$, given in Eqs. 7_1 and 7_3, respectively, with application of different loads and electric fields for all notch lengths were determined. In Eqs. 7, $E_A = 60.2$ GPa, as calculated according to material properties given in [1] and $e_{26} = 12.0$ C/m^2. Results for $\hat{K}_{II}$ were negligible in comparison to the other intensity factors.

Values of $\hat{K}_{IV}$ are plotted versus those of $\hat{K}_I$ and presented in Fig. 2. It is observed that values of $\hat{K}_I$ are relatively constant with respect to $\hat{K}_{IV}$. The average value of $\hat{K}_I$, obtained for all points, is 1.44×10^{-5}. This leads to an average value

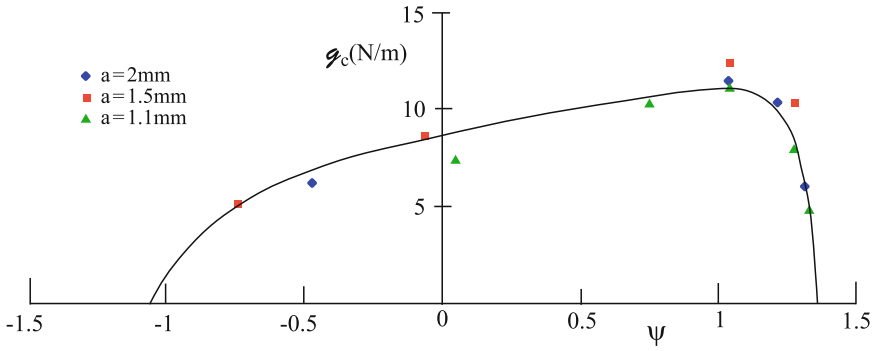

Fig. 3 Fracture curve and experimental results of [1]

of the mode I stress intensity factor $K_I = 0.86$ MPa$\sqrt{\text{m}}$ and K_{IV} ranges between -0.46×10^{-3} and 0.82×10^{-3} C/m$^{3/2}$.

The fracture criterion in Eq. 14 is applied using the intensity factors in Table 6 of [2] and presented in Fig. 2. From those values and with $\hat{K}_{II} = 0$, the critical energy release rate $\mathcal{G}_c$ and the phase angle ψ were calculated using Eqs. 3 and 12_1 for each test. It was found that some of the values of the critical energy release rate are negative or close to zero; hence, these values are not physically plausible. It is possible that this phenomenon occurs because of a large domain switching zone in the vicinity of the notch tip. This aspect of the problem will be examined in the future. The calculated points are plotted as the colored symbols in Fig. 3 omitting those points in which $\mathcal{G}_c \leq 0$. In addition, Eq. 14 is plotted as the solid curve in Fig. 3. Values below this curve are safe; for those above it, failure is expected. The value of $\mathcal{G}_{Ic}$ used for this curve is given in Eq. 11. The value of $\hat{K}_{Ic}$ is found as the average of the values of $\hat{K}_I$ at failure in Fig. 2 excluding those for which $\mathcal{G}_c$ is negative or close to zero. Its value is 1.46×10^{-5} which is slightly different from the value shown in Fig. 2 which includes all of the tests. With $\hat{L}_{22}^{-1} = 8.151 \times 10^{10}$ N/m a value of $\mathcal{G}_{Ic} = 8.6$ N/m is found. Excellent agreement is observed between the experimental results and the curve. As a result of the coupling between the first and fourth modes of fracture, which is expressed by the second term in parentheses of the right hand side of Eq. 14, the fracture curve in Fig. 3 is not symmetric with respect to ψ. Recall that the crack faces are perpendicular to the poling direction. Furthermore, it should be emphasized that the apparent fracture toughness $\mathcal{G}_{Ic}$ should not be used to predict catastrophic failure. Only the mixed mode fracture curve presented in Eq. 14 and Fig. 3 should be used to predict failure.

4 Conclusions

A fracture criterion has been presented for piezoelectric material for poling at an angle to the crack plane and within a material symmetry plane. It is based upon the energy release rate and one or two phase angles. If mode III deformation was added and/or poling would be in a more general direction, the criterion could easily be generalized with the addition of third phase angle. Experimental results [1] were used in a special case of the criterion for which the crack is perpendicular to the poling direction. Excellent agreement was observed between the fracture curve and the experimental results. Nevertheless, some values of the critical energy release rate were negative or close to zero. These points were neglected as being physically unreasonable. Future study is required to understand this behavior. The criterion presented may be used for other poling directions.

References

1. Jelitto H, Kessler H, Schneider GA, Balke H (2005) Fracture behavior of poled piezoelectric PZT under mechanical and electrical loads. J Euro Cer Soc 25:749–757
2. Motola Y, Banks-Sills L, Fourman V (2009) On fracture testing of piezoelectric ceramics. Int J Fract 159:167–190, DOI 10.1007/s10704-009-9392-x
3. Suo Z, Kuo CM, Barnett DM, Willis JR (1992) Fracture mechanics for piezoelectric ceramics. J Mech Phys Solids 40:739–765
4. Barnett DM, Lothe J (1975) Dislocations and line charges in anisotropic piezoelectryc insulators. Physica Status Solidi (b) 67:105–111
5. Banks-Sills L, Motola Y, Shemesh L (2008) The M-integral for calculating intensity factors of an impermeable crack in a piezoelectric material. Engng Fract Mech 75:901–925

This page intentionally left blank

What Do We Know About Surface Charges on Cracks in Ferroelectric Ceramics?

Andrea R. Engert, Frank Felten, Hans Jelitto, and Gerold A. Schneider

Abstract The present work investigates the static and time dependent electric potential distribution around cracks in a poled ferroelectric ceramic by Kelvin Probe Force Microscopy (KFM). In a first step a Vickers indentation crack in poled lead zirconate titanate (PZT) was subjected to static electric fields of up to 500 V/mm in poling direction, and the potential distribution around the crack was measured. In a second step, the polarity of the applied voltage was reversed against the poling direction during the measurement of the potential. Using a simple model, an effective dielectric constant of the crack, as well as the surface charge density on the crack face were calculated as a function of the distance from the crack tip, the applied field and the time. The results are discussed with reference to free charges on the crack surface, electrically induced domain switching at the crack tip and crack bridging.

1 Introduction

Ferroelectric materials are used, amongst other applications, in electro-mechanical transducer applications, converting mechanical forces into an electrical potential (direct piezoelectric effect) or vice versa (inverse piezoelectric effect). During their lifetime, ferroelectric ceramics must be capable to operate under long-term electro-mechanical loading. While they continue to find increasing use, their fracture mechanics are still investigated due to their low fracture toughness and complex material behavior. This work contributes to the understanding of the effect of electrical loading on fracture in ferroelectric ceramics.

A.R. Engert, H. Jelitto, and G.A. Schneider (✉)
Technische Universität Hamburg-Harburg, Institut für keramische Hochleistungswerkstoffe, Hamburg, Germany
e-mail: g.schneider@tu-harburg.de, www.tu-harburg.de/gk

F. Felten
Robert Bosch GmbH, Corporate Sector Research and Advance Engineering, Applied Research 1 – Materials, 70049 Stuttgart Germany

M. Kuna and A. Ricoeur (eds.), *IUTAM Symposium on Multiscale Modelling of Fatigue, Damage and Fracture in Smart Materials*, IUTAM Bookseries 24,
DOI 10.1007/978-90-481-9887-0_2,

A crack filled with air in a dielectric material with a high permittivity, is a void with a relative dielectric constant of one in a matrix with a dielectric constant that can be up to three orders of magnitude higher. If an electrical field is applied normal to the crack surface, it will penetrate the crack. The crack shape, the crack opening displacement and the ratio of the permittivities of the crack interior and the ceramic, will determine to what extent the electric flux through the crack will be diluted, and increased ahead of the tip. For cracks in a ferroelectric ceramic, i.e. in an electromechanically coupled material, this leads to a non-linear boundary value problem. In the literature three approaches are used to describe cracks in ferroelectric materials assuming impermeable boundaries (impermeable crack), permeable boundaries with an infinite dielectric constant of the crack (permeable crack), and permeable boundaries with a dielectric constant of the crack higher than one (semi-permeable crack). Theoretical works, e.g. from Balke et al [1] using the capacitor model of Hao and Shen [2] have shown that the latter results in the most realistic representation of the electric field around the crack. However, the capacitor model proved to be energetically not consistent [3]. In consequence, Landis [4,5] derived the so called "energetically consistent" boundary conditions along the crack faces that include electrostatic tractions, which are caused by an electric field perpendicular to the crack faces closing the crack. His improved model, that also includes surface charges on the crack faces, and an electrical discharge model within the crack, predicts that an electrical load increases the critical mechanical load for fracture. Except of the permeable crack model, all other theoretical approaches predict that the electric field applied perpendicular to the crack plane increases the critical mechanical load for crack growth [6]. These theoretical predictions could not be observed experimentally. E.g. Jelitto et al. [7–9] and Häusler [10] show that DC electric fields of 1/3 of the coercive field only influence the critical loads for crack growth to a very small extent.

Haug and McMeeking [11] showed, that screening charges on the crack surface would change the fracture behavior of the crack dramatically. Schneider et al. [12] already successfully used Kelvin Probe Force Microscopy (KFM) to study the potential distribution around an electrically loaded Vickers crack in PZT. From the results an effective dielectric constant was calculated for the crack tip. On the basis of a Griffith crack it was further shown, that a higher dielectric constant of the crack reduces the dependency of the crack tip energy release rate on an applied electric field. The present work is a continuation of the work presented by Schneider et al. [12]. It takes into account not only a single applied electric field, but different field strengths up to 500 V/mm. Besides, the potential distribution is not only analyzed at the crack tip, but to a crack length of around 60 μm. The objective was to analyze whether or not the crack could also be described by a single effective dielectric constant farther away from the tip and at different applied electric fields. This part of the work is described in more detail in the Ph.D. thesis from Felten [13]. In addition, the time response of the electric potential distribution upon a reversal of the electric field against the polarization direction was studied. The motivation for this experiment was the assumption that free charges on the crack surface would

not immediately change after the reversal of the applied voltage. The objective of all experiments was to verify the theoretical assumption of screening charges on the crack surface, trying to quantify and characterize them.

2 Samples, Experimental Setup and Methods

KFM is a scanning probe technique, which allows mapping the surface potential of a sample versus the in-plane coordinates x and y in a two-pass technique. During the first pass the topography is recorded in tapping-mode. In the second pass, the so-called interleave scan, the topography is retraced in a set lift height and the contact potential difference is measured. As the tip travels over the sample surface in lift-mode, the tip and the cantilever experience a force wherever the potential on the surface is different from the potential of the tip. The force is nullified by varying the voltage of the tip so that the tip is at the same potential as the region of the sample surface underneath it. This voltage is plotted versus the in-plane x-y-coordinates, creating the surface potential image. The principle of the KFM-mode is described e.g. by Kalinin and Bonnell [14], the resolution of KFM is discussed e.g. by Jacobs et al. [15].

The experiments were performed in a similar way as described by Schneider et al. [12]. 270 µm thin plates of a commercial soft PZT (Vibrit1100, Johnson Matthey) covered with thin gold electrodes on both sides were cut into samples of $1 \times 2\,\text{cm}^2$. The plates were poled at room temperature with an electric field of 2 kV/mm. The coercive field extracted from a hysteresis measurement (room temperature, 2 kV/mm maximum field, 8.3 mHz) is around 700 V/mm. According to the data sheet the dielectric constant ε_{33} of the poled material is 4,500 [16]. One thin 4 cm × 260 µm face was polished on a semi-automatic polishing machine (Saphir550, ATM GmbH) using diamond suspension down to a grain size of 0.25 µm (DP-Suspension P on MD-NAP, Struers GmbH). The material's grain size measured with an optical microscope is around 3 µm. After polishing a Vickers indent (0.5 kg, 10 s, Vickers hardness tester 3212 preceding model of ZVH10, Zwick) was induced in the middle of the surface, producing cracks parallel to the surface edges (Fig. 1). The advantage of the indentation methodology was its easy control and simplicity concerning the experimental performance. Vickers indenters produce two basic types of crack systems: radial-median and lateral. After the diamond is removed, local residual stress states hold the cracks open [17, p. 249ff.].

The sample was fixed in a custom made holder and aligned under a Scanning Probe Microscope (SPM) in a way that the cantilever was perpendicular to the applied field, and would not electrostatically interact with the indent. The voltage was externally applied to the sample. For the measurements with constant fields two separate power supplies were used (HCN-35-12500, MCN-35-1250, FuG). For the measurements where the field was reversed, a bipolar power supply with two ports and a fast response (PZD700, large signal bandwidth up to 15 kHz, TREK INC.) was chosen. The power supplies were controlled using a computer program (LabView®, National Instruments). Therewith the voltage was applied in a way that

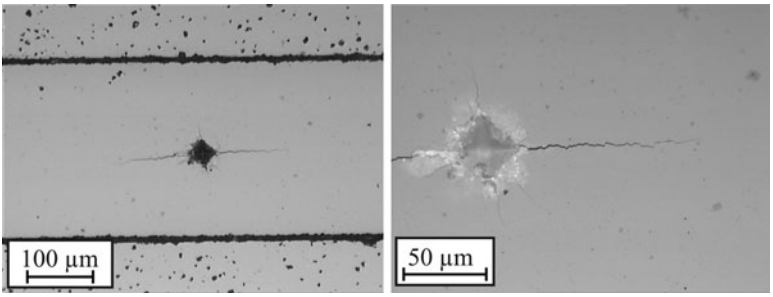

Fig. 1 Images of the Vickers indent taken with an optical microscope showing the two perpendicular crack paths

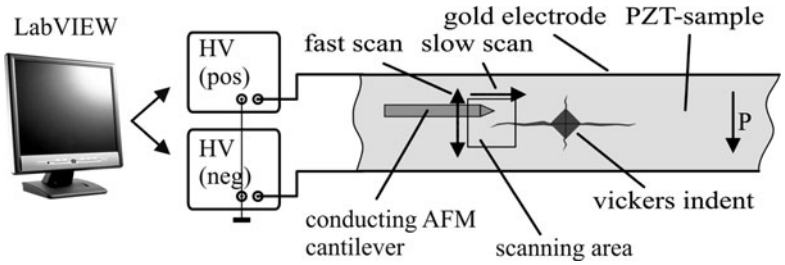

Fig. 2 Schematic of the experimental KFM setup

the line of zero potential laid along the crack. This was necessary for two reasons: the limited measuring range of the KFM-mode of $+/-10$ V, and due to the fact, that the topography of the surface is only recorded well, when the contact potential difference between the tip and the sample is close to zero. The measuring setup is shown in Fig. 2. The KFM-experiments were performed with a commercial SPM (Dimension3000, Nanoscope IV Controller, Veeco) using conducting, PtIr-coated, doped silicon tips with a resonant frequency around 75 Hz (PointProbe plus-tip for Electrostatic Force Microscopy PPP-EFM, Nanosensors). For the interleave scan, the lift height was set to 10–20 nm. 6 V were taken for the driving voltage. The scan rate varied from 0.2 Hz for large scans (60 µm) and 2 Hz for small scans (5 µm), i.e. the scan speed was slightly higher for the larger scans.

Two data sets are received from every KFM measurement: the height (h) and the corresponding surface potential profile (Φ). Topographical images were processed using the microscope's software (NanoScope® 7.2, Veeco) with a flattening function, which means that a polynomial is fitted to each data line and then subtracted to remove tilt and bow. KFM images were not post-processed. The images shown in Fig. 3 are exemplary and were taken with an applied field of 400 V/mm. The voltage steps in the KFM-images mark the location of the crack and reveal the lower dielectric constant of the crack compared to the ferroelectric material. The crack opening displacement COD, the electric field in the PZT E_{PZT} and the

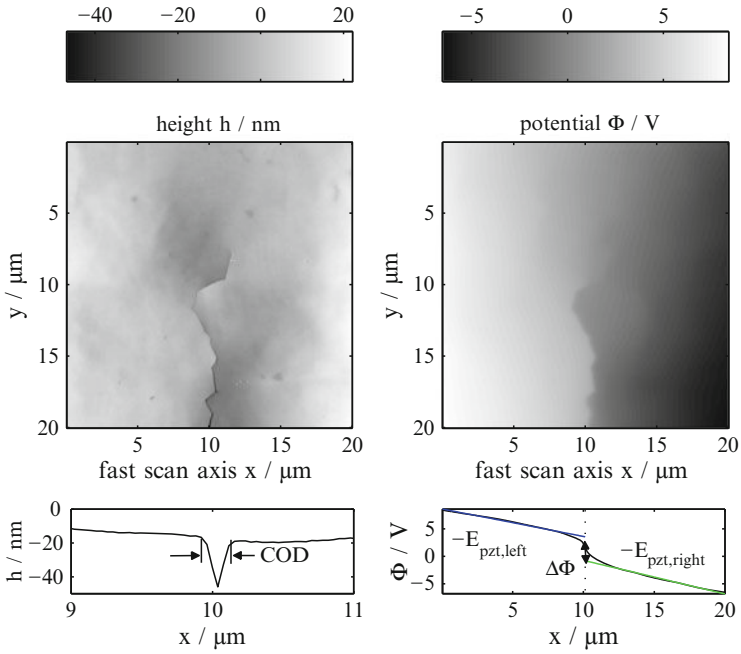

Fig. 3 Images of the topography (*top-left*) and the surface potential (*top-right*) of the scanned surface with an electric field of 400 V/mm applied perpendicular to the crack (electric field and polarization vector from *right* to *left*). The lower graphs show the determination of the COD (*bottom-left*) and the electric field in the PZT and the potential drop across the crack

potential drop across the crack $\Delta\Phi$ were determined as shown in the graphs in Fig. 3. The COD was determined using the microscope's image analysis software (NanoScope® 7.2, Veeco) at positions where neither crack bridges nor kinks were present, i.e. where the crack faces were rather parallel to the crack direction. The distance from the crack tip r was determined graphically (CorelDRAW, Corel). To calculate the potential drop across the crack, the potential distribution was linearly extrapolated on both sides of the crack, and the distance of both lines was calculated at the inflection point of the potential curve (MATLAB®, Mathworks).

3 Results

Since the measurement of the COD requires a high resolution, several overlapping scans were performed along the crack. The main graph of Fig. 4 shows the COD as a function of the distance from the crack tip r at an applied electric field $E_{appl} = 0\,V/mm$. In the inserted graph it is shown that, at a distance of $r = 5\,\mu m$ from the tip, the COD was not influenced by E_{appl}.

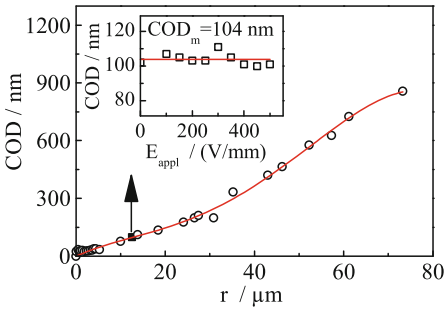

Fig. 4 COD as a function of the distance from the crack tip r at $E_{appl} = 0$ (*main graph*), and COD as a function of the applied electric field E_{appl} at $r = 5\,\mu m$ (*inserted graph*)

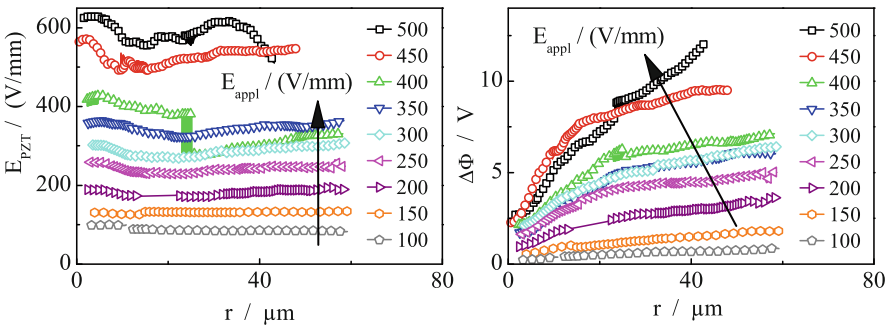

Fig. 5 Plots of the electric field in PZT (*left*) and the potential drop across the crack (*right*) as a function of the distance from the crack tip for different applied electric fields

The electric field in the PZT and the potential drop across the crack as a function of the distance from the crack tip are shown in Fig. 5 for the applied electric fields from 100 to 500 V/mm.

For the measurements with field reversal, the slow scan axis was disabled. Thus, the cantilever was kept at a constant distance from the crack tip during scanning. With the polarity of the applied voltage reversed, the potential distribution was measured as a function of time. The scanning frequency was chosen according to the scan size and the scan velocity. The scan size of 10 µm was selected to be as small as possible, but large enough to allow a linear fitting of the potential on both sides of the crack to determine the electric field in the PZT. In KFM the potential is only measured every second scan in turn with the height. Figure 6 shows the evolution of the potential plotted vs. time of an exemplary measurement, where the applied voltage was changed from −100 V/mm against poling direction to 100 V/mm in poling direction, scanning with a frequency of 0.75 Hz. The measurement was done at a distance of around 15 µm from the rack tip; the COD at this distance was around 0.8 µm.

Using the same procedure as above, the electric field in the PZT and the potential drop across the crack were calculated. As shown in Fig. 7 the electric field in the PZT changes rather step like, while the magnitude of the potential drop first increases before it reduces to the constant value with the opposite sign.

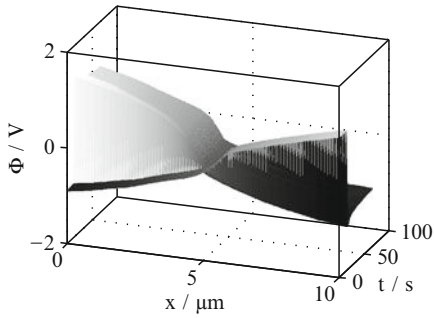

Fig. 6 3D plot showing the evolution of the surface potential with the time after the reversal of the applied field from −100 to 100 V/mm during scanning at a constant distance from the crack tip (r = const.)

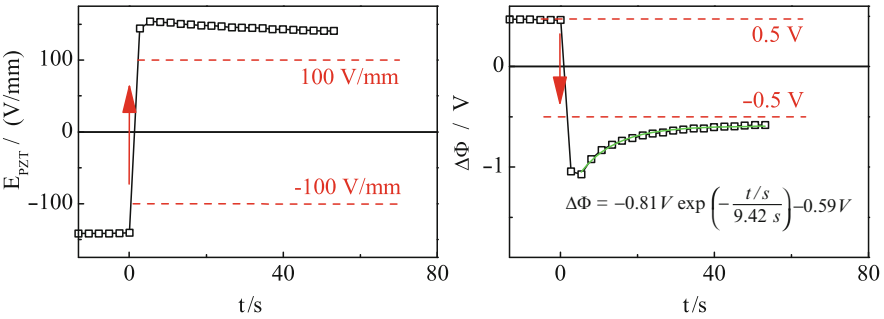

Fig. 7 Graph showing the electric field in the PZT (*left*) and the potential drop across the crack (*right*) as a function of time during the reversal of the applied voltage from −100 to 100 V/mm

4 Discussion

For further analysis a very simple model was used: three capacitors in series connection representing a space filled with air between two layers of material with a dielectric constant of PZT. This model does not take into account the 3D shape of the Vickers crack system, the residual stresses around the indent, and the ferroelectric properties of PZT as well as the remnant polarization of the poled PZT. Using the condenser analogy the problem reduces to a 1D problem, which is fully described by the components of the electric field E, dielectric displacement D, and polarization P that are perpendicular to the crack plane. According to this model the electric field inside the crack E_{crack} was calculated by

$$E_{\text{crack}} = \frac{\Delta\Phi}{\text{COD}}. \tag{1}$$

The results for the electric field in the crack as a function of the distance from the crack tip and the applied electric field are shown in the left graph of Fig. 8. The electric fields inside the crack are four orders of magnitude higher than in the PZT. Knowing the dielectric constant of the PZT ε_{PZT}, either an effective dielectric

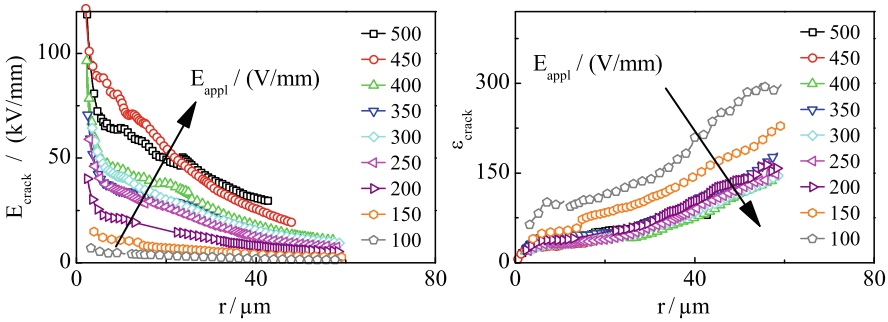

Fig. 8 Plots of the electric field across the crack (*left*) and the effective dielectric constant of the crack (*right*) as a function of the distance from the crack tip for different applied electric fields

constant of the crack ε_{crack}, or an additional surface charge density on the crack surfaces ω_s can be calculated using constitutive equations for the dielectric displacement D. Since the dielectric displacement is continuous across an interface between two different dielectric materials, at the crack surface it is

$$D_{PZT} = \varepsilon_0 \varepsilon_{PZT} E_{PZT} = \varepsilon_0 \varepsilon_{crack} E_{crack} = \varepsilon_0 E_{crack} + \omega_s. \tag{2}$$

The right graph in Fig. 8 shows that the effective dielectric constant rises with the distance from the crack tip and decreases with the applied electric field. For applied fields higher than 200 V/mm a saturation value is reached. The values for ε_{crack} range from around 10 near the tip to over 200 at a distance of 60 µm.

For every applied electric field $\varepsilon_0 E_{crack}$ is small compared to $\varepsilon_0 \varepsilon_{PZT} E_{PZT}$. Hence according to Eq. (2), the free surface charges correspond to the dielectric displacement in the PZT for every applied field strength. Given that a very simple model was chosen to characterize the dielectric constant of the crack, the results of the measurements with a constant applied electric field show that neither a single dielectric constant nor a constant surface charge density on the crack surface can be used to describe the dielectric behavior of the whole crack.

For the time dependent measurement, the decay of the electric potential drop after the field reversal was fitted with an exponential function giving a time constant $\tau_{\Delta\Phi}$ of 9.5 s (Fig. 7, right):

$$\Delta\Phi = -0.81\ \text{V}\ \exp\left(-\frac{t/\text{s}}{9.42\ \text{s}}\right) - 0.59\ \text{V}. \tag{3}$$

Furthermore the electric field inside the crack, the dielectric displacement in the PZT, the effective dielectric constant of the crack and the surface charge density were calculated. It was assumed that the surface charge density is a function of time. According to this assumption the dielectric displacement after the reversal of the voltage is described by:

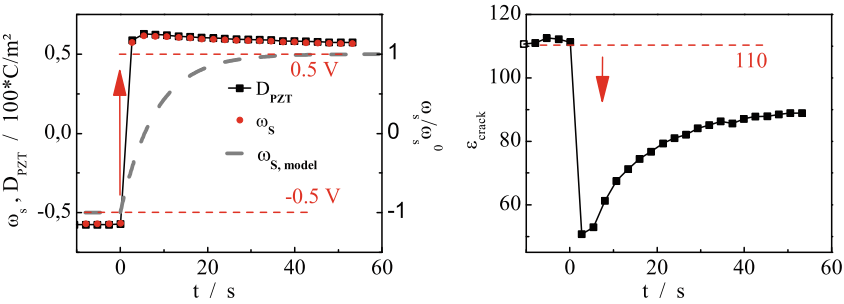

Fig. 9 Graph showing both the dielectric displacement in the PZT and the charge density on the crack surface (*left*) and the dielectric constant of the crack (*right*) as a function of time during the reversal of the applied voltage from −100 to 100 V/mm

$$D_{\mathrm{PZT}}(t) = \varepsilon_0 \mathrm{E}_{\mathrm{crack}} + \omega_{\mathrm{s}}(t). \tag{4}$$

If the charge density on the crack surface and the dielectric displacement in the PZT are plotted vs. time (Fig. 9, right), it turns out that immediately after the reversal $\varepsilon_0 \mathrm{E}_{\mathrm{crack}} << \mathrm{D}_{\mathrm{PZT}}$. If $\varepsilon_0 \mathrm{E}_{\mathrm{crack}}$ can be neglected, $\omega_s \approx \mathrm{D}_{\mathrm{PZT}}$ according to Eq. (4).

It was expected that directly after the field reversal, the surface charge redistribution $\omega_{s,\mathrm{model}}(t)$ could be described by an exponential equation,

$$\varpi_{\mathrm{s,model}}(t) = 2\varpi_{\mathrm{s}}^0 \ \exp\left(-\frac{t}{\tau}\right) - \varpi_{\mathrm{s}}^0, \tag{5}$$

where $\omega_s{}^0$ is the surface charge density before the field reversal. The expected progression of $\omega_{s,\mathrm{model}}$ is added in the plot of ω_s vs. time. It is obvious that if there is an exponential time dependence of ω_s, the time constant $\tau_{\omega s}$ is much smaller than 1 s. The right graph in Fig. 9 shows first a drop in the effective dielectric constant of the crack at the moment of the reversal of the applied voltage and then a slow increase.

In summary this means: the experimental results suggest, that at least two time constants are necessary to describe the time dependent surface charge density on the crack surface. One, much smaller than one second, which can not be measured within the time resolution of the KFM method, and one in the range of 10 s. The first one leads to an instantaneous screening of the bigger part of dielectric displacement in the PZT. The second one leads to slow exponential change of the potential drop.

To explain the charge transport to the crack surface, different approaches are discussed in the following. In time resolved measurements of the conductivity of PZT at 333 and 666 V/mm, a starting value of approximately 10^{-12} C/Vms was measured after 400 ms. Assuming an electric conductivity $\sigma = 10^{-12}$ C/Vms of PZT at an applied electric field of 100 V/mm yields an electric current density of $j = 10^{-7}$ C/m^{2}s. To compensate a dielectric displacement of 0.004 C/m^2 it would take 11 h to carry the charge from the electrode to the crack surface. Therefore the change in the surface charge density can never be due to electrical conductivity

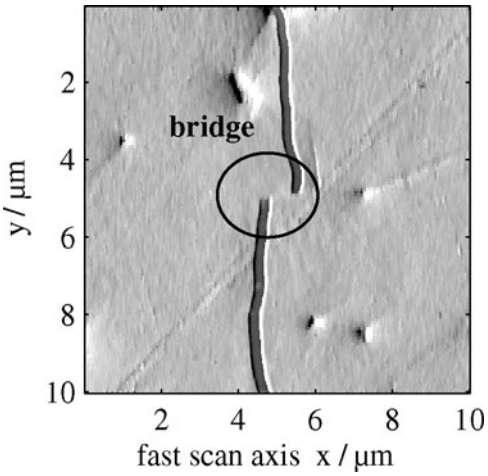

Fig. 10 SPM image of the topography (amplitude signal of the height) showing a frictional bridge

in bulk PZT. Within one second also ferroelectric domain switching could lead to a redistribution of charges on the crack surface. Another approach to explain the behavior of the crack is the assumption of crack bridges. Crack bridges are discontinuous elements along a crack path, like contacting crack faces (frictional bridge) or a discontinuous crack path (elastic bridges). In a linear model an effective dielectric constant of the crack of 40 could be caused by a fraction of $f = 0.9\%$ crack bridges per unit area, which to contacting crack faces:

$$\varepsilon_{\text{crack}} = f\varepsilon_{\text{PZT}} + (1 - \text{f}), \quad \text{f} = \frac{\varepsilon_{\text{crack}} - 1}{\varepsilon_{\text{PZT}} - 1} = \frac{39}{4499} = 0,0087 = 0,9\,\%. \qquad (6)$$

The images of the samples taken with the optical microscope and the scanning probe microscope prove the existence of elastic and frictional crack bridges. The exemplary images in Fig. 1 show a typical crack path. Although the grain boundaries cannot be seen, the crack path suggests intergranular fracture (tortuous path around grains). The crack profile also shows micro cracking and crack bridging (elastic and frictional bridges). Figure 10 shows an exemplary SPM image of a small part of a crack path with a frictional bridge. An argument against the explanation of $\varepsilon_{\text{crack}}$ by crack bridges is the fact that $\varepsilon_{\text{crack}}$ rises with larger distance from the crack tip, although the crack bridges should get less due to the increasing crack opening displacement.

5 Conclusions

Electric field dependent measurements of the crack opening profile and the electrical potential around a Vickers indentation crack in ferroelectric PZT confirm the KFM measurements from Schneider et al. [12] that the potential drop across the crack is

much smaller than expected for a crack filled with air with a dielectric constant of 1. If no surface charges are assumed, the calculated the calculated effective dielectric constant based on a simple model increases from around 10 near the crack tip to 200 at a distance of 60 μm from the crack tip, and decreases slightly and continuously with the applied electric field. If a dielectric constant of 1 inside the crack is assumed, the calculated crack surface charge densities are almost identical with the dielectric displacement in the PZT ceramic.

Time resolved measurements showed that the bigger part of the calculated charge density on the crack surfaces follows the electric field instantaneously. An estimate shows that the electrical conductivity of the PZT is too low to change the surface charges within a few seconds by electrical conduction through the bulk PZT. On the other hand, it could be shown that experimentally observed grain bridges could explain the effective dielectric constant of much bigger than 1 and the fast charge displacement after the reversal of the applied electric field, although they cannot explain the increasing effective dielectric constant of the crack with increasing distance from the crack tip.

Acknowledgements We thank Rodrigo Pacher Fernandez and Claudia Neusel for the measurement of the electrical conductivity of PZT and the DFG (German Science Foundation) for supporting this project under the grant number SCHN 372/12-2.

References

1. Balke H, Kemmer G, Drescher J (1997) Some remarks on the fracture mechanics of piezoelectric solids. MicroMaterials Conference "MicroMat 1997", pp 398–401
2. Hao TH, Shen ZY (1994) A new electric boundary-condition of electric fracture-mechanics and its applications. Eng Fract Mech 47(6):793–802
3. McMeeking RM (2004) The energy release rate for a Griffith crack in a piezoelectric material. Eng Fract Mech 71(7–8):1149–1163
4. Landis CM (2004) Energetically consistent boundary conditions for electromechanical fracture. Int J Solids Struct 41(22–23):6291–6315
5. Landis CM (2005) Energetically consistent boundary conditions for electromechanical fracture (Erratum, vol 41, pg 6291, 2004). Int J Solids Struct 42(8):2461–2463
6. Li WY, McMeeking RM, Landis CM (2008) On the crack face boundary conditions in electromechanical fracture and an experimental protocol for determining energy release rates. Eur J Mech A-Solids 27(3):285–301
7. Jelitto H, Felten F, Swain MV, Balke H, Schneider GA (2007) Measurement of the total energy release rate for cracks in PZT under combined mechanical and electrical loading. J Appl Mech-Trans ASME 74(6):1197–1211
8. Jelitto H, Felten F, Hausler C, Kessler H, Balke H, Schneider GA (2005) Measurement of energy release rates for cracks in PZT under electromechanical loads. J Eur Ceram Soc 25(12):2817–2820
9. Jelitto H, Kessler H, Schneider GA, Balke H (2005) Fracture behavior of poled piezoelectric PZT under mechanical and electrical loads. J Eur Ceram Soc 25(5):749–757
10. Häusler C, Jelitto H, Neumeister P, Balke H, Schneider GA (2009) Interfacial fracture of piezoelectric multilayer actuators under mechanical and electrical loading. Int J Fract 160(1):43–54
11. Haug A, McMeeking RM (2006) Cracks with surface charge in poled ferroelectrics. Eur J Mech A-Solids 25(1):24–41

12. Schneider GA, Felten F, McMeeking RM (2003) The electrical potential difference across cracks in PZT measured by Kelvin Probe Microscopy and the implications for fracture. Acta Mater 51(8):2235–2241
13. Felten F (2006) PhD thesis: Anwendung der Rastersondenmikroskopie zur Bestimmung bruchmechanischer Parameter und lokaler piezoelektrischer Eigenschaften von Ferroelektrika. Book series: Berichte aus der Materialwissenschaft, Shaker Verlag, Aachen
14. Kalinin SV, Bonnell DA (2001) Local potential and polarization screening on ferroelectric surfaces. Phys Rev B 63(12):125411
15. Jacobs HO, Leuchtmann P, Homan OJ, Stemmer A (1998) Resolution and contrast in Kelvin probe force microscopy. J Appl Phys 84(3):1168–1173
16. Johnson Matthey (2009) Piezoceramic Masses. Online available from: http://ect.jmcatalysts.com/ or http://www.piezoproducts.com/de/
17. Lawn BR (1993) Fracture of brittle solids. book series: Cambridge solid state science series, 2 edn. Cambridge University Press, Cambridge

Effects of Electric Field and Poling on Fatigue Behavior of PZT Ceramics with Single-Edge Crack by Three-Point Bending

Yasuhide Shindo and Fumio Narita

Abstract We describe the fatigue behavior in cracked piezoelectric ceramics under electromechanical loading through experimental and finite element characterizations. Static and dynamic fatigue tests were conducted on lead zirconate titanate (PZT) ceramics subjected to electric fields, by three-point bending using single-edge precracked-beam technique. A nonlinear finite element analysis (FEA) was also carried out to calculate the energy release rate for the permeable, impermeable, open and discharging crack models, and the effects of electric field and polarization switching on the energy release rate were examined. The electric field dependence of the lifetime and crack extension versus energy release rate curves was then estimated based on the FEA using measured data.

1 Introduction

The PZT ceramics have been used as sensors and actuators in smart material systems and structures. The high electromechanical fields in the PZT ceramics induce cracking that can lead to premature failure in the piezoelectric devices. The properties of the PZT ceramics are also susceptible to degradation under electromechanical fields. Therefore, an understanding of piezoelectric fracture [1, 2] and fatigue [3–5] is a significant issue for the design of the high performance piezoelectric devices.

In this work, we report a combined experimental and numerical examination of the fatigue behavior in cracked piezoelectric ceramics subjected to electromechanical loading. A crack was created perpendicular to the poling direction. Static and dynamic fatigue tests were carried out in three-point bending under electric fields using single-edge precracked-beam method. A nonlinear FEA was also performed to evaluate the energy release rate for the permeable, impermeable, open and

Y. Shindo (✉) and F. Narita
Department of Materials Processing, Graduate School of Engineering, Tohoku University, Aoba-yama 6-6-02, Sendai 980-8579, Japan
e-mail: shindo@material.tohoku.ac.jp; narita@material.tohoku.ac.jp

M. Kuna and A. Ricoeur (eds.), *IUTAM Symposium on Multiscale Modelling of Fatigue, Damage and Fracture in Smart Materials*, IUTAM Bookseries 24,
DOI 10.1007/978-90-481-9887-0_3,

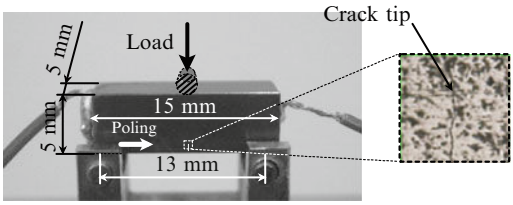

Fig. 1 Schematic representation of the tests

discharging crack models, and the effects of electric field and polarization switching on the energy release rate were discussed. The results were then examined in terms of the lifetime and crack extension versus energy release rate curves.

2 Experimental Procedure

The experimental geometry is shown in Fig. 1. Specimens were commercially supplied hard PZT PCM-80 ceramics (Panasonic Electric Devices Co., Ltd., Japan). The material properties are given in Ref. 3, and the coercive electric field E_c is about 2 MV/m. The size of the specimens was 5 mm thick, 5 mm wide and 15 mm long. Poling was done along the axis of the 15 mm dimension. Through-thickness crack was introduced, and the initial crack length and gap are about 0.5 mm and under 0.2 μm, respectively.

Static fatigue test was carried out (crosshead speed until constant load 135 or 140 N: 0.5 N/s) in three-point flexure fixture with 13 mm span, and the times-to-failure were measured. Dynamic fatigue test was also conducted to apply for load rates from 0.05 to 1 N/s, and the fracture loads were measured. During the tests, crack growth was monitored on the surface of the specimen with the aid of a digital microscope camera at 1,000× magnification.

3 Analysis

3.1 Basic Equations

Consider a piezoelectric material without body force and free charge. The governing equations in the Cartesian coordinate system O-$x_1x_2x_3$ are

$$\sigma_{ji,j} = 0 \tag{1}$$

$$D_{i,i} = 0 \tag{2}$$

where σ_{ij} is the stress tensor, D_i is the electric displacement vector, a comma denotes partial differentiation with respect to the coordinate x_i, and the Einstein summation convention over repeated indices is used. The relation between the strain tensor ε_{ij} and the displacement vector u_i is given by

$$\varepsilon_{ij} = \frac{1}{2}(u_{j,i} + u_{i,j}) \tag{3}$$

and the electric field intensity vector is

$$E_i = -\phi_{,i} \tag{4}$$

where ϕ is the electric potential. In a ferroelectric material, domain switching leads to changes in the remanent strain $\varepsilon^{\mathrm{r}}_{ij}$ and remanent polarization P^{r}_i. The constitutive relation can be written as

$$\sigma_{ij} = c_{ijkl}(\varepsilon_{kl} - \varepsilon^{\mathrm{r}}_{kl}) - e_{kij}E_k \tag{5}$$

$$D_i = e_{ikl}(\varepsilon_{kl} - \varepsilon^{\mathrm{r}}_{kl}) + \varepsilon^{S}_{ik}E_k + P^{\mathrm{r}}_i \tag{6}$$

where c_{ijkl} and e_{ikl} are the elastic and piezoelectric constants, and ε^{S}_{ik} is the dielectric permittivity at constant strain. Valid symmetry conditions for the material constants are

$$c_{ijkl} = c_{jikl} = c_{ijlk} = c_{klij}, \quad e_{kij} = e_{kji}, \quad \varepsilon^{S}_{ik} = \varepsilon^{S}_{ki} \tag{7}$$

The enhanced electromechanical field level results in localized polarization switching. In order to develop a non-linear model incorporating the polarization switching mechanisms with the electromechanical field calculations, two criteria are used. The first criterion [6] states that a polarization switches when the electrical and mechanical work exceeds a critical value

$$\sigma_{ij}\Delta\varepsilon_{ij} + E_i\Delta P_i \geq 2P^{\mathrm{s}}E_{\mathrm{c}} \tag{8}$$

where P^{s} is a spontaneous polarization, and $\Delta\varepsilon_{ij}$ and ΔP_i are the changes in the spontaneous strain and spontaneous polarization during switching, respectively. The values of $\Delta\varepsilon_{ij} = \varepsilon^{\mathrm{r}}_{ij}$ and $\Delta P_i = P^{\mathrm{r}}_i$ for 180° switching can be expressed as

$$\Delta\varepsilon_{11} = 0, \quad \Delta\varepsilon_{22} = 0, \quad \Delta\varepsilon_{33} = 0, \quad \Delta\varepsilon_{12} = 0, \quad \Delta\varepsilon_{23} = 0, \quad \Delta\varepsilon_{31} = 0 \tag{9}$$

$$\Delta P_1 = 0, \quad \Delta P_2 = 0, \quad \Delta P_3 = -2P^{\mathrm{s}} \tag{10}$$

For 90° switching in the x_3x_1 plane, the changes are

$$\Delta\varepsilon_{11} = \gamma^{\mathrm{s}},\ \ \Delta\varepsilon_{22} = 0,\ \ \Delta\varepsilon_{33} = -\gamma^{\mathrm{s}},\ \ \Delta\varepsilon_{12} = 0,\ \ \Delta\varepsilon_{23} = 0, \Delta\varepsilon_{31} = 0 \tag{11}$$

$$\Delta P_1 = \pm P^{\mathrm{s}},\ \ \Delta P_2 = 0,\ \ \Delta P_3 = -P^{\mathrm{s}} \tag{12}$$

where γ^{s} is a spontaneous strain. The polarization switching criterion based on internal energy density (second criterion) [7] is defined as

$$U \geq U_{\mathrm{c}} \tag{13}$$

where U is the internal energy density and U_c is a critical value of internal energy density corresponding to the switching mode. The internal energy density associated with 180° switching can be written as

$$U = \frac{1}{2} D_3 E_3 \tag{14}$$

In the case of 90° switching in the x_3x_1 plane, the internal energy density is

$$U = \frac{1}{2}(\sigma_{11}\varepsilon_{11} + \sigma_{33}\varepsilon_{33} + 2\sigma_{31}\varepsilon_{31} + D_1 E_1) \tag{15}$$

The critical value of internal energy density is assumed in the following form:

$$U_{\mathrm{c}} = \frac{1}{2}\varepsilon_{33}^{\mathrm{T}}(E_{\mathrm{c}})^2 \tag{16}$$

where $\varepsilon_{33}^{\mathrm{T}}$ is the dielectric permittivity at constant stress. The constitutive Eqs. 5 and 6 after polarization switching are given by

$$\sigma_{ij} = c_{ijkl}(\varepsilon_{kl} - \varepsilon_{kl}^{\mathrm{r}}) - e'_{kij}E_k \tag{17}$$

$$D_i = e'_{ikl}(\varepsilon_{kl} - \varepsilon_{kl}^{\mathrm{r}}) + \varepsilon_{ik}^{S}E_k + P_i^{\mathrm{r}} \tag{18}$$

where e'_{ikl} is the new piezoelectric constant [1].

3.2 Model

In order to evaluate the energy release rate G of PZT, plane strain FEA (ANSYS) was carried out for the cracked piezoelectric specimens. The specimen and loading geometries are shown in Fig. 2. Let the coordinate axes $x = x_1$ and $z = x_3$ be chosen such that the $y = x_2$ axis coincides with the thickness direction. The z axis is oriented parallel to the poling direction. The three-point flexure specimen with a

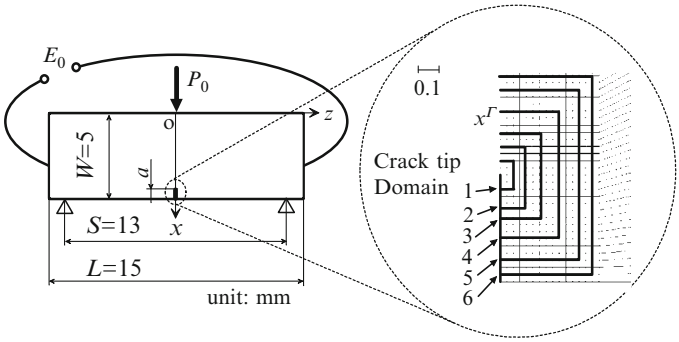

Fig. 2 Schematic representation of the finite element model

span $S = 13$ mm is a beam of width $W = 5$ mm and length $L = 15$ mm containing a crack of length a. Because of symmetry, only the right half of the model was used in the FEA.

The boundary conditions at $z = 0$ can be expressed in the form

$$\sigma_{zx}(x, 0) = 0 \quad (0 \le x \le W) \tag{19}$$

$$\begin{aligned} u_z(x, 0) &= 0 \quad && (0 \le x \le W - a) \\ \sigma_{zz}(x, 0) &= 0 \quad && (W - a < x \le W) \end{aligned} \tag{20}$$

$$\begin{aligned} \phi(x, 0) &= 0 && (0 \le x \le W - a) \\ E_x(x, 0) &= E_x^c(x, 0) && (W - a < x \le W) \\ D_z(x, 0) &= D_z^c(x, 0) && (W - a < x \le W) \end{aligned} \tag{21}$$

where the superscript c stands for the electric quantity in the void inside the crack. The electric potential is all zero on the symmetry planes inside the crack and ahead of the crack, so the boundary conditions of Eqs. 21 reduce to $\phi(x, 0) = 0$ $(0 \le x \le W)$. Equations 21 are the permeable crack boundary conditions [8, 9]. A mechanical load is produced by the application of a prescribed force P_0 at $x = 0, z = 0$ along the x-direction. For electrical loads, a negative or positive electric potential $\phi_0/2$ is applied at the edge $0 \le x \le W$, $z = L/2$, and the electric field E_0 is $-\phi_0/L$. Other boundary conditions are summarized below.
At $z = L/2$ (side surface)

$$\sigma_{zz}(x, L/2) = 0 \quad (0 \le x \le W) \tag{22}$$

$$\sigma_{zx}(x, L/2) = 0 \quad (0 \le x \le W) \tag{23}$$

$$\phi(x, L/2) = \phi_0/2 \quad (0 \le x \le W) \tag{24}$$

At $x = 0$ (top surface)

$$\sigma_{xx}(0,z) = -P_0\delta(z), \quad \sigma_{xx}(0,z) = 0 \quad (0 < z \le L/2) \tag{25}$$
$$\sigma_{xz}(0,z) = 0 \quad (0 < z \le L/2) \tag{26}$$
$$D_x(0,z) = 0 \quad (0 \le z \le L/2) \tag{27}$$

At $x = W$ (bottom surface)

$$\sigma_{xx}(W,z) = 0 \quad (0 \le z < S/2, S/2 < z \le L/2), \quad u_x(W,S/2) = 0 \tag{28}$$
$$\sigma_{xz}(W,z) = 0 \quad (0 \le z \le L/2) \tag{29}$$
$$D_x(W,z) = 0 \quad (0 \le z \le L/2) \tag{30}$$

In Eq. 25, $\delta(z)$ is the Dirac-delta function.

Due to the polarization switching, materials are often non-homogeneous. The piezoelectric properties vary from one location to the other, and the variations are either continuous or discontinuous. The energy release rate G can be obtained from the following J-integral:

$$G = J = \left(\int_{\Gamma_0} - \int_{\Gamma_p}\right)\{Hn_x - (\sigma_{xx}u_{x,x} + \sigma_{zx}u_{z,x})n_x - (\sigma_{zx}u_{x,x} + \sigma_{zz}u_{z,x})n_z + D_xE_xn_x + D_zE_xn_z\}d\Gamma \tag{31}$$

where, Γ_0 is a contour closing a crack tip, Γ_p is a path embracing that part of phase boundary which is enclosed by Γ_0, and n_x, n_z are the components of the outer unit normal vector. The electrical enthalpy density H is expressed as

$$\begin{aligned} H = {} & \frac{1}{2}\{c_{11}(u_{x,x})^2 + c_{33}(u_{z,z})^2 + 2c_{13}u_{x,x}u_{z,z} + c_{44}(u_{x,z} + u_{z,x})^2\} \\ & -\frac{1}{2}\{\varepsilon_{11}^S(E_x)^2 + \varepsilon_{33}^S(E_z)^2\} \\ & -[\{e'_{111}u_{x,x} + e'_{131}(u_{x,z} + u_{z,x}) + e'_{133}u_{z,z}\}E_x \\ & \quad +\{e'_{311}u_{x,x} + e'_{331}(u_{x,z} + u_{z,x}) + e'_{333}u_{z,z}\}E_z] \end{aligned} \tag{32}$$

The energy release rates for the impermeable and open crack face boundary conditions are also discussed. The impermeable boundary condition [10, 11] is

$$\begin{aligned} \phi(x,0) &= 0 \quad (0 \le x \le W - a) \\ D_z(x,0) &= 0 \quad (W - a < x \le W) \end{aligned} \tag{33}$$

The crack face electrical boundary condition for the open crack model [12] becomes

$$\begin{aligned} &\phi(x,0) = 0 && (0 \le x \le W-a) \\ &D_z^+ = D_z^- && (W-a < x \le W) \\ &D_z^+(u_z^+ - u_z^-) = \varepsilon_0(\phi^- - \phi^+) && (W-a < x \le W) \end{aligned} \tag{34}$$

where the superscripts + and − denote, respectively, the right and left sides of the cross-section where the crack is located, as shown in Fig. 2, and $\varepsilon_0 = 8.85 \times 10^{-12}$ C/Vm is the electric permittivity of the vacuum. The energy release rate for the impermeable crack model is obtained, similar to the permeable crack, by Eq. 31. For the open crack model, nonzero contributions to G arise from the contour segments along the crack face, and the value of G can be obtained, by computing contour integrations and then subtracting the electrical enthalpy density of the crack gap H^c times the crack opening displacement evaluated at the intersection x^Γ of the contour with the crack faces [13], as

$$\begin{aligned} G = \left(\int_{\Gamma_0} - \int_{\Gamma_p}\right)\{&H n_x - (\sigma_{xx}u_{x,x} + \sigma_{zx}u_{z,x})n_x - (\sigma_{zx}u_{x,x} + \sigma_{zz}u_{z,x})n_z \\ &+ D_x E_x n_x + D_z E_x n_z\} d\Gamma - 2H^c(x^\Gamma)u_z^+(x^\Gamma) \end{aligned} \tag{35}$$

4 Results and Discussion

We first discuss the dependence of the energy release rate G on the crack face boundary conditions for hard PZT PCM-80, using nonlinear FEA. The spontaneous polarization P^s and strain γ^s are assigned representative values of 0.3 C/m^2 and 0.004, respectively. The J-integrals for the permeable and impermeable crack models are path-independent, and for the calculation of G by the domain integral method [14], six contours were defined in the finite element mesh (see Fig. 2). The G calculation for the open crack model is complicated than for the permeable and impermeable crack models [15]. The Newton–Raphson method is used to find the solution for the open crack model.

Table 1 lists the energy releases rate G for the permeable, impermeable and open crack models under load P_0 = 100 N and electric field E_0 = 0.5 MV/m for crack length a = 0.5 mm. The error is reasonable and not important here from the practical point of view. The fracture load is about 150 N for PZT PCM-80, and the contribution from the gap interior for the open crack model is negligible under practical loading conditions. If we calculate the G for the open crack model under P_0 = 1,000 N, for example, the contribution from the gap interior would become large (it can be computed numerically, but the result is meaningless). We wish to add that the effect of electrical discharge within the crack is not accounted for in calculations of the G for the open crack model. The fifth column in the table shows the solution for the discharging crack model [13] (i.e., the crack gap cannot support electric fields

Table 1 Energy release rate for the piezoelectric specimen under $P_0 = 100$ N and $E_0 = 0.5$ MV/m ($a = 0.5$ mm)

	G (N/m^2)			
	Permeable	Impermeable	Open	Discharging
Domain 1	3.29	1.55	3.10 (-2.57×10^{-2})	3.30 (-5.54×10^{-6})
Domain 2	3.27	1.60	2.97 (-2.57×10^{-2})	3.27 (-1.67×10^{-6})
Domain 3	3.25	1.58	3.07 (-3.50×10^{-2})	3.25 (-1.07×10^{-5})
Domain 4	3.24	1.66	2.96 (-4.23×10^{-2})	3.24 (-1.28×10^{-5})
Domain 5	3.24	1.73	2.89 (-4.67×10^{-2})	3.24 (-1.41×10^{-5})
Domain 6	3.23	1.84	2.83 (-5.12×10^{-2})	3.23 (-1.53×10^{-5})
Average	3.26	1.66	2.96 (-3.63×10^{-2})	3.26 (-1.11×10^{-5})

Values in parentheses are the results of $2H^c(x^\Gamma)u_z^+(x^\Gamma)$ in Eq. 35.

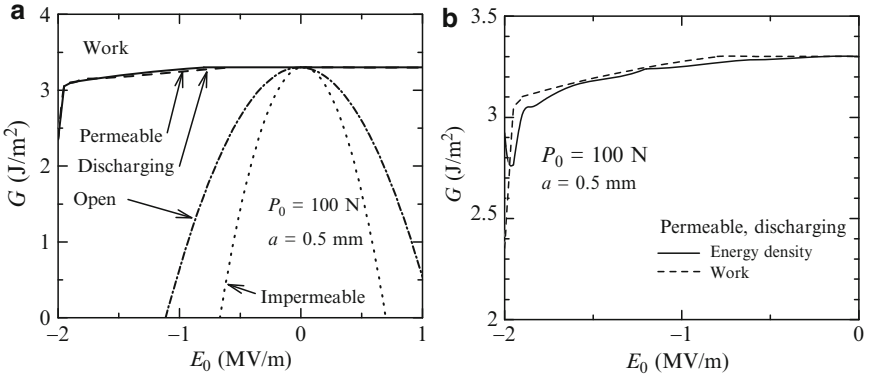

Fig. 3 Energy release rate versus electric field: (**a**) work; (**b**) energy density

larger than a critical discharge level E_d). In the calculations, standard air breakdown field, $E_d = 3$ MV/m, was used [16]. It is interesting to note that the energy release rates predicted by the permeable and discharging crack models are not significantly different.

Figure 3 shows the energy release rate G versus electric filed E_0 for the permeable, impermeable and discharging crack models under $P_0 = 100$ N for $a = 0.5$ mm, predicted by the criteria based on the work (8) and energy density (13). Average values of six domains are presented, and little differences are observed between the values of G for the permeable and discharging crack models. A monotonically increasing negative E_0 causes polarization switching and decreases the values of G for the permeable and discharging crack models. The prediction by the criteria based on the work shows that polarization switching leads to a sudden decrease in G after E_0 reaches about -1.95 MV/m. On the other hand, the prediction according to the energy density shows that when E_0 reaches about -1.8 MV/m, the value of G decreases. However, as E_0 is reduced below -1.95 MV/m, the value of G increases. In the impermeable case, a negative energy release can be induced with

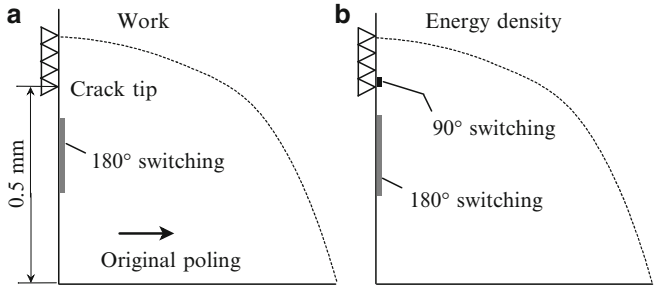

Fig. 4 Polarization switching zone induced by electric field of −1.98 MV/m under load of 100 N and predicted by the criteria based on the work (**a**) as well as energy (**b**) density

large electric fields. The G for the open crack model also becomes negative under high electric fields. So the parameters for the impermeable and open crack models have questionable physical significance. Figure 4 shows the 180° and 90° switching zones near the permeable crack tip ($a = 0.5$ mm) under $E_0 = -1.98$ MV/m, predicted by the criteria based on the (a) work and (b) energy density. The specimen is subjected to $P_0 = 100$ N. The 180° switching occurs behind the crack tip. If the criterion based on the energy density is used, the region ahead of the crack tip is found to undergo 90° switching.

Next, we discuss the experimental and numerical results of the piezoelectric fatigue behavior. Figure 5a shows the experimental results of average time-to-failure t_f (from three or four data) as a function of electric field E_0 for PZT PCM-80 under $P_0 = 135, 140$ N. Times-to-failure under $E_0 = +0.1$ MV/m and $E_0 = -0.1$ MV/m occurs significantly lower and higher than that under zero electric field, respectively. Figure 5b shows the average time-to-failure t_f versus energy release rate G under $E_0 = 0, \pm 0.1$ MV/m. The G is calculated by the FEA for the piezoelectric specimen with a permeable crack. Time-to-failure t_f as a function of G can be expressed by

$$t_f = 6.14 \times 10^{33} G^{-30.5} \tag{36}$$

Fatigue lives are observed to increase with the small decrease in G.

A summary of the results of dynamic fatigue testing for PZT PCM-80 under electric field $E_0 = 0$ and $+0.1$ MV/m is shown in Fig. 6a, where average fracture load P_c (from two or three data) was plotted as a function of load rate. The PZT ceramics show an increase in fracture load as the load rate increases. The fracture load under positive electric field is smaller than that under zero electric field. Figure 6b shows a comparison of measured crack extensions (Δa) under $E_0 = 0$ and $+0.1$ MV/m at load rate of 0.1 N/s, plotted as a function of the calculated energy release rate G for the permeable crack model. The amount of crack extension of the specimen under $E_0 = +0.1$ MV/m is substantially greater than that under $E_0 = 0$ V/m. The decrease in the crack extension amount for $G > 5$ J/m^2 is probably associated with microcrack nucleation and crack bridging.

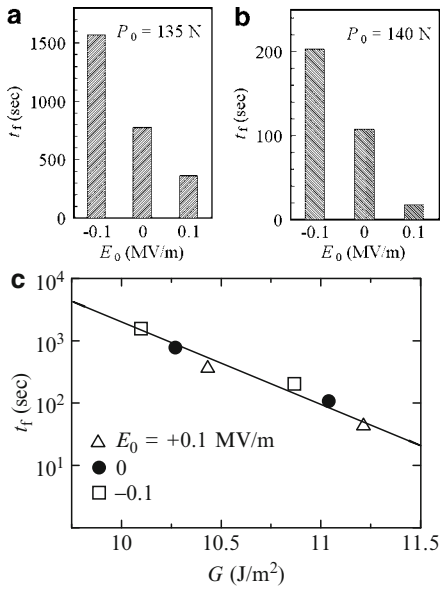

Fig. 5 Static fatigue test results: (**a**) time-to-failure versus electric field; (**b**) time-to-failure versus energy release rate

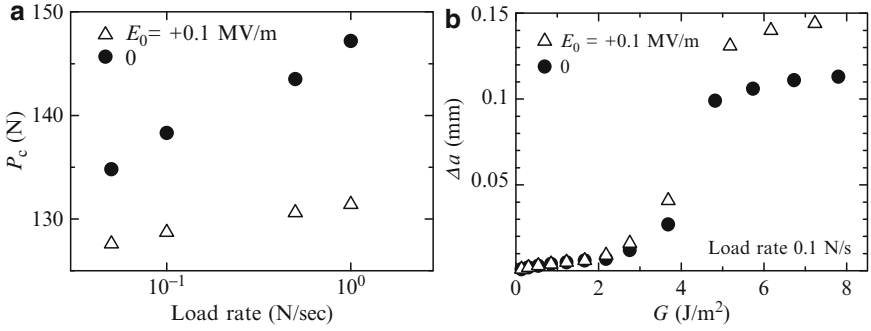

Fig. 6 Dynamic fatigue test results: (**a**) fracture load versus load rate; (**b**) crack extension versus energy release rate

In conclusion, the impermeable and open crack face assumptions can lead to significant errors and the permeable crack face is better assumption, in modeling cracks in piezoelectric materials. The time-to-failure of the PZT ceramics under positive electric field is significantly lower than that under no electric field. Negative electric field increases the time-to-failure, and gives the safety scenario. The PZT ceramics under positive electric field has also low dynamic fatigue resistance, compared to those under no electric field.

References

1. Shindo, Y., Narita, F., Horiguchi, K., Magara, Y., Yoshida M (2003) Electric fracture and polarization switching properties of piezoelectric ceramic PZT studied by the modified small punch test. Acta Mater. 51:4773–4782
2. Shindo Y, Narita F, Mikami M (2005) Double torsion testing and finite element analysis for determining the electric fracture properties of piezoelectric ceramics. J Appl Phys 97:114109
3. Shindo Y, Narita F, Saito F (2007) Static fatigue behavior of cracked piezoelectric ceramics in three-point bending under electric fields. J Euro Ceram Soc 27:3135–3140
4. Narita F, Shindo Y, Saito F (2007) Cyclic fatigue crack growth in three-point bending PZT ceramics under electromechanical loading. J Am Ceram Soc 90:2517–2524
5. Shindo Y, Narita F, Hirama M (2009) Dynamic fatigue of cracked piezoelectric ceramics under electromechanical loading: Three-point bending test and finite element analysis. J. Mech. Mater. Struct 4:719–729
6. Hwang SC, Lynch CS, McMeeking RM (1995) Ferroelectric/ferroelastic interactions and a polarization switching model. Acta Metall Mater 43:2073–2084
7. Sun CT, Achuthan A (2004) Domain-switching criteria for ferroelectric materials subjected to electrical and mechanical loads. J Am Ceram Soc 87:395–400
8. Parton VZ (1976) Fracture mechanics of piezoelectric materials. Acta Astro 3:671–683
9. Shindo Y, Ozawa E, Nowacki JP (1990) Singular stress and electric fields of a cracked piezoelectric strip. Int J Appl Electromagnet Mater 1:77–87
10. Pak YE (1992) Linear electro-elastic fracture mechanics of piezoelectric materials. Int J Fract 54:79–100
11. Sosa HA (1992) On the fracture mechanics of piezoelectric solids. Int J Solids Struct 29:2613–2622
12. Hao T-H, Shen Z-Y (1994) A new electric boundary condition of electric fracture mechanics and its applications. Eng Fract Mech 47:793–802
13. Landis CM (2004) Energetically consistent boundary conditions for electromechanical fracture. Int J Solids Struct 41:6291–6315
14. Li FZ, Shih CF, Needleman A (1985) A comparison of methods for calculating energy release rates. Eng Fract Mech 21:405–421
15. McMeeking RM (1999) Crack tip energy release rate for a piezoelectric compact tension specimen. Eng Fract Mech 64:217–244
16. Shindo Y, Narita F, Hirama M (2009) Effect of the electrical boundary condition at the crack face on the mode I energy release rate in piezoelectric ceramics. Appl Phys Lett 94:081902

This page intentionally left blank

Shape Memory Alloys: Material Modeling and Device Finite Element Simulations

Ferdinando Auricchio, Michele Conti, Simone Morganti, and Alessandro Reali

Abstract The use of shape memory alloys (SMA) in an increasing number of applications in many fields of engineering, and in particular in biomedical engineering, is leading to a growing interest toward an exhaustive modeling of their macroscopic behavior in order to construct reliable simulation tools for SMA devices. In this paper we review the properties of a robust three-dimensional model able to reproduce both pseudo-elastic and shape-memory effect; we then employ such as a model to perform the Finite Element Analysis of SMA-based devices such as self-expanding stents and spring actuators.

1 Introduction

The great and always growing interest in shape memory alloys (SMA) (cf. [7, 8]) and in their industrial applications in many branches of engineering is deeply stimulating the research on constitutive laws. As a consequence, many models able

F. Auricchio (✉)
Dipartimento di Meccanica Strutturale, Università degli Studi di Pavia, Italy
Centro di Simulazione Numerica Avanzata (CESNA), Pavia, Italy
Istituto di Matematica Applicata e Tecnologie Informatiche del CNR, Pavia, Italy
e-mail: auricchio@unipv.it

M. Conti
Dipartimento di Meccanica Strutturale, Università degli Studi di Pavia, Italy
IBiTech, Institute Biomedical Technology, Ghent, Belgium
e-mail: michele.conti@unipv.it

S. Morganti
Dipartimento di Meccanica Strutturale, Università degli Studi di Pavia, Italy
e-mail: simone.morganti@unipv.it

A. Reali
Dipartimento di Meccanica Strutturale, Università degli Studi di Pavia, Italy
European Centre for Training and Research in Earthquake Engineering, Pavia, Italy
Istituto di Matematica Applicata e Tecnologie Informatiche del CNR, Pavia, Italy
e-mail: alessandro.reali@unipv.it

M. Kuna and A. Ricoeur (eds.), *IUTAM Symposium on Multiscale Modelling of Fatigue, Damage and Fracture in Smart Materials*, IUTAM Bookseries 24,
DOI 10.1007/978-90-481-9887-0_4,

to reproduce one or both of the well-known SMA macroscopic behaviors, referred to as *pseudo-elasticity* and *shape-memory effect*, have been proposed in the literature in the last years (refer for instance to [5, 9–12, 14–16, 19, 20]). In particular, the constitutive law proposed in [22] and improved in [2] seems to be attractive. Developed within the theory of irreversible thermodynamics, this model is in fact able to describe both pseudo-elasticity and shape-memory effect and the corresponding solution algorithm is simple and robust as it is based on a plasticity-like return map procedure. The robustness of such a model makes it particularly suitable for implementation within finite element codes, allowing in this way the simulation of the behavior of complex SMA devices. In this paper we review the properties of this model and we report some results of its application in order to perform simulations of SMA-based devices such as self-expanding stents and spring actuators.

2 3D SMA Phenomenological Model

In this first part of the paper we present and discuss in detail the 3D phenomenological model for SMA introduced in [2, 3, 22], within the context of thermo-electromechanical coupling.

The model assumes the total strain $\boldsymbol{\varepsilon}$ and the absolute temperature T as control variables, the transformation strain $\mathbf{e}^{tr}$ as internal one. The second-order tensor $\mathbf{e}^{tr}$ describes the strain associated to the transformation between the two solid phases referred to as martensite and austenite. Here, this quantity should have a fully reversible evolution and should be completely recovered when unloading to a zero stress state. Moreover, we require that

$$\|\mathbf{e}^{tr}\| \leq \varepsilon_L, \tag{1}$$

where $\|\cdot\|$ is the usual Euclidean norm and ε_L is a material parameter corresponding to the maximum transformation strain reached at the end of the transformation during an uniaxial test.

Assuming a small strain regime, justified by the fact that the approximation of large deformations and small strains is valid for several applications, the following standard additive decomposition can be considered

$$\boldsymbol{\varepsilon} = \frac{\theta}{3}\mathbf{1} + \mathbf{e},$$

where $\theta = \mathrm{tr}(\boldsymbol{\varepsilon})$ and $\mathbf{e}$ are respectively the volumetric and the deviatoric part of the total strain $\boldsymbol{\varepsilon}$, while $\mathbf{1}$ is the second-order identity tensor. The free energy density function Ψ for a polycrystalline SMA material is then expressed as the convex potential

$$\Psi(\theta, \mathbf{e}, T, \mathbf{e}^{tr}) = \frac{1}{2}K\theta^2 + G\|\mathbf{e} - \mathbf{e}^{tr}\|^2 - 3\alpha K\theta(T - T_0) + \beta\langle T - M_f\rangle\|\mathbf{e}^{tr}\| + \frac{1}{2}h\|\mathbf{e}^{tr}\|^2 + (u_0 - T\eta_0) + c\left[T - T_0 - T\log\left(\frac{T}{T_0}\right)\right] + \mathscr{I}_{\varepsilon_L}(\mathbf{e}^{tr}),$$

where K and G are respectively the bulk and the shear modulus, α is the thermal expansion coefficient, β is a material parameter related to the dependence of the critical stress on the temperature, M_f is the temperature below which only martensite phase is stable, h defines the hardening of the phase transformation, c is the heat capacity, and u_0, η_0 and T_0 are, respectively, the internal energy, the entropy and the temperature at the reference state. Moreover, we make use of the indicator function

$$\mathscr{I}_{\varepsilon_L}(\mathbf{e}^{tr}) = \begin{cases} 0 & \text{if } \|\mathbf{e}^{tr}\| \leq \varepsilon_L \\ +\infty & \text{otherwise,} \end{cases}$$

in order to satisfy the transformation strain constraint of Eq. 1; we also introduce the positive part function $\langle\cdot\rangle$, defined as

$$\langle a\rangle = \begin{cases} a & \text{if } a > 0 \\ 0 & \text{otherwise.} \end{cases}$$

We remark that, since we use only a single internal variable second-order tensor to describe phase transformations, at most it is possible to distinguish between a generic parent phase (not associated to any macroscopic strain) and a generic product phase (associated to a macroscopic strain). Accordingly, the model does not distinguish between the austenite and the twinned martensite, as both these phases do not produce macroscopic strain

We furthermore highlight that, for the sake of simplicity, the present model does not reflect the differences existing between the austenite and the martensite elastic properties (see [4] on a way to include it in the model).

Starting from the free energy function Ψ and following standard arguments, we can derive the constitutive equations

$$\begin{cases} p = & \dfrac{\partial\Psi}{\partial\theta} = K\left[\theta - 3\alpha(T - T_0)\right], \\ \mathbf{s} = & \dfrac{\partial\Psi}{\partial\mathbf{e}} = 2G(\mathbf{e} - \mathbf{e}^{tr}), \\ \eta = & -\dfrac{\partial\Psi}{\partial T} = \eta_0 + 3\alpha K\theta - \beta\|\mathbf{e}^{tr}\|\dfrac{\langle T - M_f\rangle}{|T - M_f|} + c\log\left(\dfrac{T}{T_0}\right), \\ \mathbf{X} = -\dfrac{\partial\Psi}{\partial\mathbf{e}^{tr}} = & \mathbf{s} - \beta\langle T - M_f\rangle\dfrac{\mathbf{e}^{tr}}{\|\mathbf{e}^{tr}\|} - h\mathbf{e}^{tr} - \gamma\dfrac{\mathbf{e}^{tr}}{\|\mathbf{e}^{tr}\|}, \end{cases} \tag{2}$$

where $p = \mathrm{tr}(\boldsymbol{\sigma})/3$ and $\mathbf{s}$ are respectively the volumetric and the deviatoric part of the stress $\boldsymbol{\sigma}$, $\mathbf{X}$ is a thermodynamic stress-like quantity associated to the transformation strain $\mathbf{e}^{tr}$, and η is the entropy. The variable γ results from the indicator function subdifferential $\partial \mathscr{I}_{\varepsilon_L}(\mathbf{e}^{tr})$ and it is defined as

$$\begin{cases} \gamma = 0 & \text{if } \|\mathbf{e}^{tr}\| < \varepsilon_L, \\ \gamma \geq 0 & \text{if } \|\mathbf{e}^{tr}\| = \varepsilon_L, \end{cases}$$

so that $\partial \mathscr{I}_{\varepsilon_L}(\mathbf{e}^{tr}) = \gamma \mathbf{e}^{tr}/|\mathbf{e}^{tr}\|$.

To describe phase transformation and inelasticity evolution, we choose a limit function F defined as

$$F(\mathbf{X}) = \|\mathbf{X}\| - R \tag{3}$$

where R is the radius of the elastic domain in the deviatoric space.

Considering an associative framework, the flow rule for the internal variable takes the form

$$\dot{\mathbf{e}}^{tr} = \dot{\zeta} \frac{\partial F}{\partial \mathbf{X}} = \dot{\zeta} \frac{\mathbf{X}}{\|\mathbf{X}\|}, \tag{4}$$

where $\dot{\zeta}$ is the consistency parameter.

The model is then completed by the classical Kuhn–Tucker conditions

$$\begin{cases} \dot{\zeta} \geq 0, \\ F \leq 0, \\ \dot{\zeta} F = 0. \end{cases} \tag{5}$$

Following classical arguments [13], we can also compute the evolution of the current internal energy u, using the first principle of thermodynamics, as

$$\dot{u} = \dot{\Psi} + T\dot{\eta} + \dot{T}\eta = \boldsymbol{\sigma} : \dot{\boldsymbol{\varepsilon}} + r - \nabla \cdot \mathbf{q}, \tag{6}$$

being r and $\mathbf{q}$, respectively, the heat source and flux vector.

Observation 1 The proposed model is thermodynamically consistent since it satisfies the second principle of thermodynamics in the form of the Clausis–Duhem inequality (for more details see [2]).

Observation 2 By exploiting basic Convex Analysis tools (see, e.g., [6]) we can rewrite our constitutive model defined by Eqs. 2–5 in the equivalent form

$$\begin{pmatrix} -p \\ -\mathbf{s} \\ \eta \\ \partial D \dot{\mathbf{e}}^{tr} \end{pmatrix} + \partial \Psi \begin{pmatrix} \theta \\ \mathbf{e} \\ T \\ \mathbf{e}^{tr} \end{pmatrix} \ni \mathbf{0}. \tag{7}$$

Here ∂D stands for the subdifferential of the function D defined as

$$D(\mathbf{e}^{tr}) = \sup_{F(\mathbf{A})\leq 0} \left\{\mathbf{A} : \mathbf{e}^{tr}\right\}, \tag{8}$$

which is the dissipation function associated to the phase transformation mechanism ($\mathbf{A}$ is a generic thermodynamic stress-like tensor). It can be shown that $D(\mathbf{e}^{tr}) = R||\mathbf{e}^{tr}||$, as well as that it is the Fenchel–Legendre conjugate of the indicator function of the non-empty, convex, and closed domain

$$\mathscr{E} = \{\mathbf{A} \,:\, F(\mathbf{A}) \leq 0\}.$$

Hence, it is easy to check that D is positively 1-homogeneous, that is

$$D(\lambda \mathbf{e}^{tr}) = \lambda D(\mathbf{e}^{tr}) \quad \forall \lambda > 0.$$

Namely, the time-evolution of $\mathbf{e}^{tr}$ is of rate-independent type since we readily have that

$$\partial D(\lambda \mathbf{e}^{tr}) = \partial D(\mathbf{e}^{tr}) \quad \forall \lambda > 0.$$

The formulation of rate-independent evolution problems in terms of a doubly-nonlinear differential inclusion as in Eq. 7 has recently attracted a good deal of attention. In particular, the mathematical treatment of relations as Eq. 7 is nowadays fairly settled and existence, uniqueness, and time-discretization results are available. The interested reader is referred to the recent survey [17] where a comprehensive collection of mathematical results on doubly-nonlinear rate-independent problems is provided.

3 Numerical Simulations of SMA-Based Devices

In this section we highlight the numerical implementation of the model proposing two different finite element analyses: the first simulation reproduces a flexibility test of a SMA self-expanding stent exploiting the pseudo-elastic effect; the second one reproduces the action of the shape memory effect on the elongation of a spring.

3.1 Self-expandable SMA Stent: An Example of Pseudo-elastic Effect

The best example of the successful use of SMA in the biomedical field is Nitinol, a Nickel–Titanium SMA with excellent biocompatibility. In particular, the peculiar features of Nitinol are exploited to manufacture self-expanding stents which are small tube-like devices providing the internal scaffolding of diseased arteries. Stents are the core of a minimally invasive clinical technique, called stenting, often used

as follow-up of angioplasty, a procedure in which a vessel, narrowed by stenotic lesion, is mechanically enlarged by the inflation of a balloon.

Two types of stents based on different expansion strategies are available on the market: balloon-expandable (BX) and self-expandable (SX) stents.

On one hand, the BX stent is mounted on a catheter supporting a balloon and it is positioned by plastic deformation inflating the balloon in the site of blockage.

On the other hand, the SX stent is crimped within a protective sheath; when the sheath is retracted the stent expands by itself into the artery exploiting Nitinol pseudo-elasticity. Moreover, pseudo-elasticity is a key-feature for stenting of peripheral vessels, as carotid or femoral arteries, where BX stents usually fail due to undesired plastic deformations provided by complex loading conditions related to the body kinematics.

Although Nitinol SX stents accomplish both technical and biomechanical requirements (i.e. flexibility, kink resistance, low delivery profile, etc.), it has been observed that many of these stents fail once implanted in peripheral vessels [1, 21].

In the scientific literature, there has been an increasing effort to study the stent mechanics by Finite Element Analysis (FEA) to support stent design and enhance the related stenting performance. In the following, we exploit the proposed constitutive model to perform a FEA in order to assess the flexibility of a Nitinol self-expanding stent in open configuration. We design the numerical test to mimic the approach proposed by Muller–Hulsbeck [18]. We consider a geometry very similar to the tapered XACT stent (Abbott, IL, USA) with a structure characterized by tubular-like rings having the main function of sustaining the vessel after stent expansion, and bridging members (links) having the main function of assuring the stent flexibility by allowing mutual rotation between adjacent rings.

As shown in Fig. 1, we tie the stent ends to two rigid plates: the proximal rigid plate is fully constrained while the distal one is free to rotate around the X axis; we impose the stent bending by a displacement (11 mm) along the Y direction of the distal reference point and we monitor the relative reaction force. For this simulations, we use linear hexahedral (C3D8) elements for the stent mesh and the commercial code ABAQUS/STD (Dassault Systèmes Simulia Corp., Providence, RI, USA) as finite element solver. We implement the constitutive model within a user material subroutine (UMAT) using the typical NiTi material parameters reported in Table 1. Large deformations are included in the analysis to get a non-linear force/displacement response of the device as shown in Fig. 2. The simulation results are in qualitative agreement with experimental results provided by Muller–Hulsbeck et al. [18] and further investigations should address the validation of the numerical analysis especially with focus on the assessment of the SMA material properties.

We conclude that the proposed constitutive model can be exploited to assess the mechanical behavior of complex SMA-based biomedical devices as stents, thanks to its simple and robust numerical implementation.

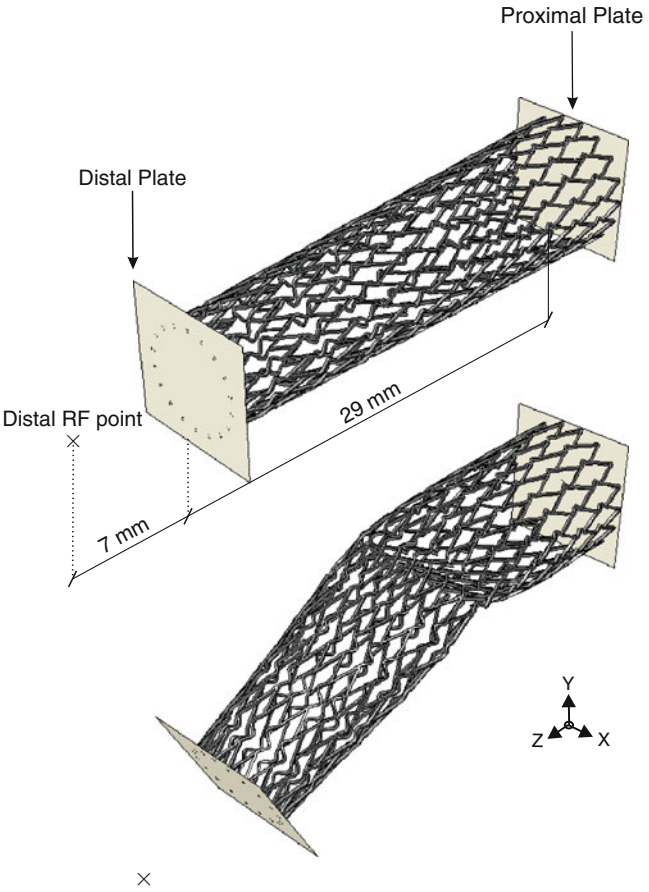

Fig. 1 Nitinol stent: initial configuration (*top*); final bent configuration (*bottom*)

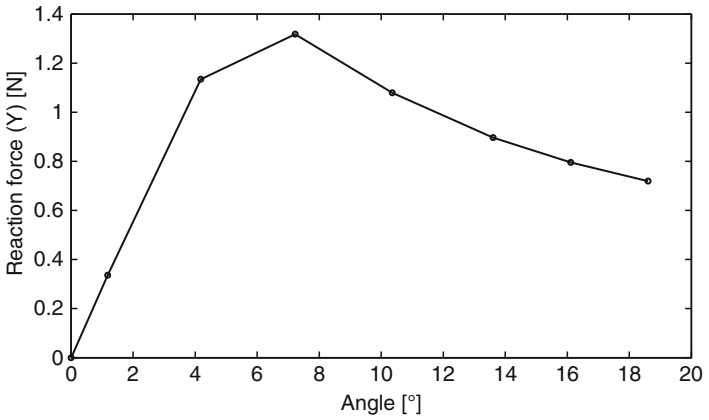

Fig. 2 Reaction force along the Y direction at the distal reference point versus the bending angle

Table 1 Adopted nitinol constitutive parameters

Symbol	Description	Value	Unit
E	Elastic modulus	51,700	MPa
ν	Poisson's ratio	0.3	–
ε^L	Maximum transformation strain	0.077	–
h	Stress-strain slope measure during transformation	707	MPa
β	Temperature dependence for transformation stress	5.33	$\text{MPa}^\circ\text{C}^{-1}$
M_f	Reference temperature	−28	°C
T	Working temperature	37	°C
R	Elastic domain radius	141	MPa

3.2 Temperature-Induced Recovery of Spring Elongation: An Example of Shape Memory Effect

The shape-memory effect allows to recover large strains by heating SMA materials; to reproduce an example of such an effect, we perform a FEA of a spring defined by the following steps:

1. Axial loading of the spring
2. Load release and elastic strain recovery
3. Heating and residual inelastic strain recovery

We apply the following boundary conditions: the top end of the spring (RF 1 in Fig. 3a) is constrained; the bottom end (RF 2) is allowed to move only along the axial direction (Y axis); during the first step we apply at RF 2 a force of 3.25 N to induce the spring elongation (see Fig. 3b).

The same material properties reported in Table 1 are used.

For the first two steps we set the working temperature equal to M_f (i.e. −28°C). Then, in the third step, we increase the temperature up to 40°C to allow the residual elongation recovery due to the shape memory effect.

Figure 3 illustrates the results of the simulation highlighting the complete recovery of the residual elongation after heating the material above A_f. The shape-memory phenomenon is clearly illustrated also in Fig. 4, where the force–displacement–temperature curve at RF 2 is reported.

Again, numerical results show the robustness of the proposed constitutive model, which can be successfully exploited also for the simulation of devices based on the shape memory effect, such as, e.g., spring actuators.

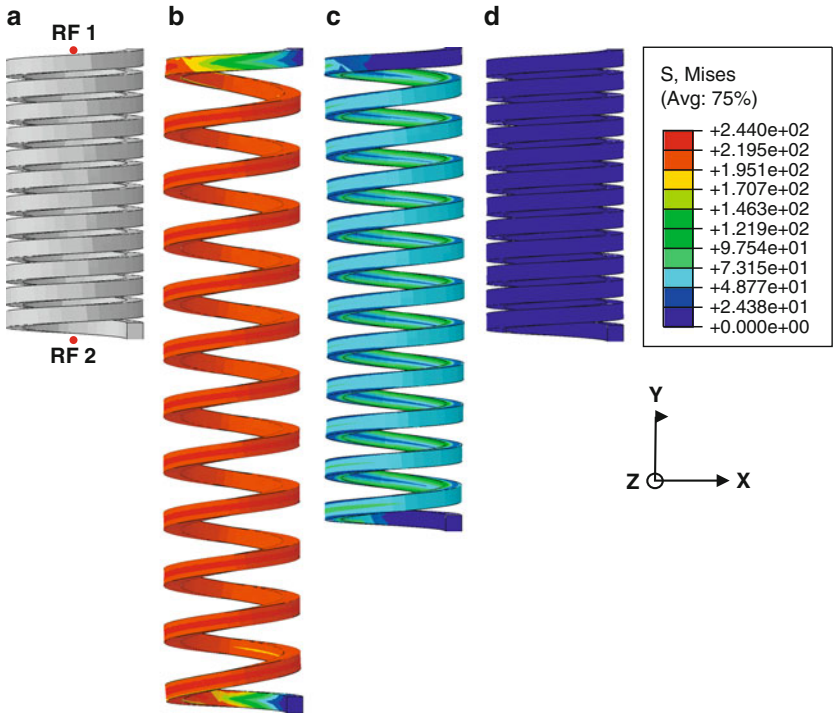

Fig. 3 Contour-plot of the VonMises stress [MPa] in the spring superimposed to the: (**a**) undeformed configuration; (**b**) deformed configuration after axial loading; (**c**) deformed configuration after load releasing; (**d**) deformed configuration after heating (residual elongation is recovered)

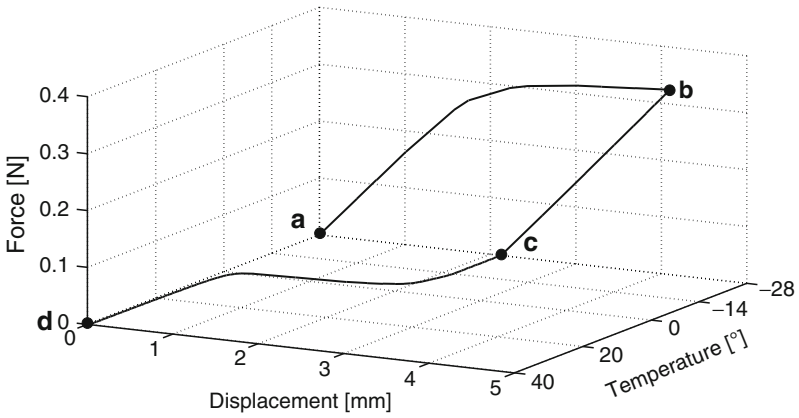

Fig. 4 Reaction force and axial displacement of RF 2 versus temperature. The labeled points refer to the steps illustrated in Fig. 3

References

1. Allie DE, Hebert CJ, Walker CM (2004) Nitinol stent fractures in the SFA. Endovasc Today 7(Jul/Aug):22–34
2. Auricchio F, Petrini L (2004) Int J Num Meth Eng 61:807–836
3. Auricchio F, Petrini L (2004) Int J Num Meth Eng 61:716–737
4. Auricchio F, Reali A, Stefanelli U (2009) Comput Methods Appl Mech Eng 198:1631–1637
5. Bouvet C, Calloch S, Lexcellent C (2004) Eur J Mech A/Sol 23:37–61
6. Clarke FH (1990) Optimization and nonsmooth analysis, 2nd edn. Classics in applied mathematics, 5. Society for Industrial and Applied Mathematics, SIAM
7. Duerig TW, Melton KN, Stoekel D, Wayman CM (1990) Engineering aspects of shape memory alloys. Butterworth-Heinemann, London
8. Duerig TW, Pelton A (2003) SMST-2003 proceedings of the international conference on shape memory and superelastic technology conference. ASM International
9. Govindjee S, Miehe C (2001) Comput Methods Appl Mech Eng 191:215–238
10. Helm D, Haupt P (2003) Int J Sol Struct 40:827–849
11. Lagoudas DC, Entchev P (2004) Mech Mater 36:865–892
12. Leclercq S, Lexcellent C (1996) J Mech Phys Sol 44:953–980
13. Lemaitre J, Chaboche JL (1990) Mechanics of solid materials. Cambridge University Press, Cambridge
14. Levitas VI (1998) Int J Sol Struct 35:889–940
15. Levitas VI, Preston DL (2002) Phys Rev B 66:134206:1–9
16. Levitas VI, Preston DL (2002) Phys Rev B Vol 66:134207:1–15
17. Mielke A (2005) In: Dafermos C, Feireisl E (eds) Handbook of differential equations. Elsevier, Amsterdam
18. Muller-Hulsbeck S, Schafer PJ, Charalambous N, Schaffner SR, Heller M, Jahnke T (2009) Comparison of carotid stents: An in-vitro experiment focusing on stent design. J Endovasc Ther 16:168–177
19. Peultier B, Benzineb T, Patoor E (2004) J Phys IV Fr 115:351–359
20. Raniecki B, Lexcellent C (1994) Eur J Mech A/Sol 13:21–50
21. Scheinert D, Scheinert S, Sax J, Piorkowski C, Bräunlich S, Ulrich M, Biamino G, Schmidt A (2005) Prevalence and clinical impact of stent fractures after femoropopliteal stenting. J Am Coll Cardiol 45:312–315
22. Souza AC, Mamiya EN, Zouain N (1998) Eur J Mech A/Sol 17:789–806

Effective Computational Methods for the Modeling of Ferroelectroelastic Hysteresis Behavior

Artem S. Semenov, Albrecht C. Liskowsky, Peter Neumeister, and Herbert Balke

Abstract Numerical methods for the solution of nonlinear electromechanically coupled boundary value problems are considered. A vector potential finite element formulation with return mapping algorithms and consistent tangent operators is developed. The accuracy and robustness of the algorithms are assessed with the help of numerical examples, including a ferroelectroelastic analysis of a notched specimen.

1 Introduction

Numerous modern applications of piezoelectric materials involve complex loading regimes with large input signals and complicated device geometries. The prediction of device performance or failure requires effective computational methods for the integration of constitutive equations and the solution of nonlinear coupled initial-boundary-value problems.

The computational methods considered below include three main ingredients:

- Return mapping (RM) algorithm [1–5]
- Consistent tangent matrix (CTM) [1, 3, 6]
- Vector potential (VP) formulation [8, 9]

The material models for ferroelectroelastic ceramics can be understood as a set of nonlinear differential-algebraic equations. Due to the switching condition, the differential equations for the evolution of the internal variables remanent polarization and remanent strain are unilaterally constrained by nonlinear algebraic equations. The RM algorithms [1–5] represent a well established scheme for the integration of nonlinear constitutive equations of evolution type with constraints.

A.S. Semenov (✉), A.C. Liskowsky, P. Neumeister, and H. Balk
Technische Universität Dresden, Institut für Festkörpermechanik, 01062 Dresden, Germany
e-mail: Semenov.Artem@googlemail.com; ACLi@gmx.de; Neumeister@mfk.mw.tu-dresden.de; Herbert.Balke@tu-dresden.de

M. Kuna and A. Ricoeur (eds.), *IUTAM Symposium on Multiscale Modelling of Fatigue, Damage and Fracture in Smart Materials*, IUTAM Bookseries 24,
DOI 10.1007/978-90-481-9887-0_5,

These constraints (switching conditions) are satisfied by a projection of the trial state onto the switching surface. Because of this interpretation, the method is called return mapping (RM). Examples of RM applications in ferroelectroelastic problems are given in [4, 5] for some special forms of constitutive equations. A systematic analysis of RM algorithms is presented in [3] considering stability conditions.

In order to achieve a quadratic rate of convergence of the Newton–Raphson (NR) method for the solution of nonlinear finite element (FE) equations, tangent moduli consistent with the utilized RM algorithm should be used for the global stiffness matrix computation. The algorithmic CTM [1, 3, 6] can be obtained by performing an exact linearization of the used RM algorithm. The CTM for ferroelectroelasticity was proposed in [3] for the first time.

The RM algorithms and CTM are considered for both the scalar potential (SP) [7] and the VP FE formulation [8, 9]. Numerical examples illustrate the accuracy and efficiency of the suggested algorithms for both formulations.

2 General Constitutive Equations of Ferroelectroelasticity

We take advantage of the fully coupled 3D macroscopic phenomenological model for ferroelectroelastic polycrystalline materials proposed by C.M. Landis in [10], which is thermodynamically consistent. Two potentials are required for the description of the constitutive equations. The Helmholtz free energy $\Psi = \Psi^s(\boldsymbol{\varepsilon}, \mathbf{D}, \boldsymbol{\varepsilon}^r, \mathbf{P}^r) + \Psi^r(\boldsymbol{\varepsilon}^r, \mathbf{P}^r)$ is introduced as a sum of the reversible (or stored) part and the contribution from internal variables (remanent polarization vector $\mathbf{P}^r$ and remanent strain tensor $\boldsymbol{\varepsilon}^r$) for the description of hardening and saturation effects [10, 11]:

$$\Psi = \tfrac{1}{2}\,(\boldsymbol{\Gamma} - \boldsymbol{\Gamma}^r) \cdot \mathrm{G}\,(\boldsymbol{\Gamma}^r) \cdot (\boldsymbol{\Gamma} - \boldsymbol{\Gamma}^r) + \Psi^r(\boldsymbol{\Gamma}^r), \tag{1}$$

where a compact notation combining a first and a second order tensor as components of one symbolic vector is used: $\boldsymbol{\Gamma} = \left\{ \begin{matrix} \boldsymbol{\varepsilon} \\ \mathbf{D} \end{matrix} \right\}$, $\boldsymbol{\Gamma}^r = \left\{ \begin{matrix} \boldsymbol{\varepsilon}^r \\ \mathbf{P}^r \end{matrix} \right\}$, $\boldsymbol{\Sigma} = \left\{ \begin{matrix} \boldsymbol{\sigma} \\ \mathbf{E} \end{matrix} \right\}$. The positive definite matrix of the extended ferroelectroelastic moduli G is therewith defined by the expression

$$\mathrm{G} = \left[\begin{array}{c|c} {}^4\mathbf{C}^D & -{}^3\mathbf{h}^T \\ \hline -{}^3\mathbf{h} & \boldsymbol{\beta}^{\varepsilon} \end{array} \right] = \left[\begin{array}{c|c} \partial^2_{\boldsymbol{\varepsilon}\boldsymbol{\varepsilon}}\Psi & \partial^2_{\boldsymbol{\varepsilon}\mathbf{D}}\Psi \\ \hline \partial^2_{\mathbf{D}\boldsymbol{\varepsilon}}\Psi & \partial^2_{\mathbf{D}\mathbf{D}}\Psi \end{array} \right] = \partial^2_{\boldsymbol{\Gamma}\,\boldsymbol{\Gamma}}\Psi. \tag{2}$$

Disregarding thermal effects, the second law of thermodynamics yields $\delta = \boldsymbol{\Sigma} \cdot \dot{\boldsymbol{\Gamma}} - \dot{\Psi} \geq 0$. The evaluation of the dissipation inequality leads to the expression $\delta = (\boldsymbol{\Sigma} - \partial_{\boldsymbol{\Gamma}}\Psi) \cdot \dot{\boldsymbol{\Gamma}} - \partial_{\boldsymbol{\Gamma}^r}\Psi \cdot \dot{\boldsymbol{\Gamma}}^r \geq 0$. This inequality has to be fulfilled for all possible thermodynamic processes. Thus, we obtain the constitutive equation

$$\boldsymbol{\Sigma} = \partial_{\boldsymbol{\Gamma}}\Psi = \mathrm{G} \cdot (\boldsymbol{\Gamma} - \boldsymbol{\Gamma}^r)\,. \tag{3}$$

Introducing the internal generalized forces $\hat{\boldsymbol{\Sigma}} = -\partial_{\boldsymbol{\Gamma}^r}\Psi$, which form a conjugate pair with the internal variables, leads to the reduced dissipation inequality

$$\delta = \hat{\boldsymbol{\Sigma}} \cdot \dot{\boldsymbol{\Gamma}}^r \geq 0. \tag{4}$$

The switching surface is defined by a smooth *convex* function [10]

$$\Phi(\hat{\boldsymbol{\Sigma}}, \boldsymbol{\Gamma}^r) = 0. \tag{5}$$

Applying the principle of maximum ferroelectroelastic dissipation introduces the Lagrangian functional $L(\hat{\boldsymbol{\Sigma}}, \lambda) = -\delta(\hat{\boldsymbol{\Sigma}}) + \lambda\Phi(\hat{\boldsymbol{\Sigma}})$ with the Lagrange multiplier $\lambda \geq 0$. The optimization conditions $\partial_{\hat{\boldsymbol{\Sigma}}} L = 0,\ \partial_\lambda L = 0$ lead to the *associated switching rule* (normality conditions) for the internal variables as well as the *loading/unloading conditions* (also known as Kuhn–Tucker conditions):

$$\dot{\boldsymbol{\Gamma}}^r = \lambda\partial_{\hat{\boldsymbol{\Sigma}}}\Phi \text{ as well as } \lambda \geq 0,\ \Phi \leq 0,\ \lambda\Phi = 0. \tag{6}$$

Note that $(6)_1$ ensures the dissipation inequality (4) for any convex Φ containing the origin of the coordinate system of the internal generalized forces.

3 Return Mapping Algorithms

RM algorithms represent a widely used effective integration scheme to integrate the nonlinear constitutive equations for unilaterally constrained problems. The objective of using the algorithms is to enforce the consistency condition defined by the switching condition.

The switching rule $(6)_1$ is integrated by employing the backward Euler implicit integration scheme, which is first-order accurate and unconditionally stable under some assumptions concerning material characteristics:

$$\boldsymbol{\Gamma}^r_{n+1} = \boldsymbol{\Gamma}^r_n + \Delta\lambda_{n+1}\partial_{\hat{\boldsymbol{\Sigma}}}\Phi\left(\hat{\boldsymbol{\Sigma}}_{n+1}, \boldsymbol{\Gamma}^r_{n+1}\right), \tag{7}$$

where $\Delta\lambda_{n+1} = \lambda_{n+1}\Delta t,\ \hat{\boldsymbol{\Sigma}}_{n+1} = -\partial_{\boldsymbol{\Gamma}^r}\Psi\left(\boldsymbol{\Gamma}_{n+1}, \boldsymbol{\Gamma}^r_{n+1}\right)$ and according with (3)

$$\boldsymbol{\Sigma}_{n+1} = \mathrm{G}\left(\boldsymbol{\Gamma}^r_{n+1}\right) \cdot \left(\boldsymbol{\Gamma}_{n+1} - \boldsymbol{\Gamma}^r_{n+1}\right). \tag{8}$$

In conclusion, the discrete counterparts of the Kuhn–Tucker conditions $(6)_2$ have to be enforced:

$$\Delta\lambda_{n+1} \geq 0,\ \Phi\left(\hat{\boldsymbol{\Sigma}}_{n+1}, \boldsymbol{\Gamma}^r_{n+1}\right) \leq 0,\ \Delta\lambda_{n+1}\Phi\left(\hat{\boldsymbol{\Sigma}}_{n+1}, \boldsymbol{\Gamma}^r_{n+1}\right) = 0. \tag{9}$$

Equations (7) and $(9)_3$ are nonlinear equations regarding the variables $\mathbf{\Gamma}^r_{n+1}$ and $\Delta\lambda_{n+1}$. We use the NR method for their solution [3]:

$$\Delta\lambda^{(k+1)}_{n+1} = \Delta\lambda^{(k)}_{n+1} + \frac{\Phi^{(k)}_{n+1} - \left(\partial_{\hat{\mathbf{\Sigma}}}\Phi^{(k)}_{n+1}\cdot \mathrm{B} - \partial_{\mathbf{\Gamma}^r}\Phi^{(k)}_{n+1}\right)\cdot \mathrm{J}\cdot\left(\mathbf{\Gamma}^r_n - \mathbf{\Gamma}^{r(k)}_{n+1} + \Delta\lambda^{(k)}_{n+1}\partial_{\hat{\mathbf{\Sigma}}}\Phi^{(k)}_{n+1}\right)}{\left(\partial_{\hat{\mathbf{\Sigma}}}\Phi^{(k)}_{n+1}\cdot \mathrm{B} - \partial_{\mathbf{\Gamma}^r}\Phi^{(k)}_{n+1}\right)\cdot \mathrm{J}\cdot\partial_{\hat{\mathbf{\Sigma}}}\Phi^{(k)}_{n+1}},$$

$$\mathbf{\Gamma}^{r(k+1)}_{n+1} = \mathbf{\Gamma}^{r(k)}_{n+1} + \mathrm{J}\cdot\left(\mathbf{\Gamma}^r_n - \mathbf{\Gamma}^{r(k)}_{n+1} + \Delta\lambda^{(k+1)}_{n+1}\partial_{\hat{\mathbf{\Sigma}}}\Phi^{(k)}_{n+1}\right), \tag{10}$$

where $\mathrm{B} = \left(\mathrm{I} + \mathrm{A}^T\right)\cdot\mathrm{G}\cdot(\mathrm{I}+\mathrm{A}) + \mathrm{H} - \mathrm{U}$, $\mathrm{H} = \partial^2_{\mathbf{\Gamma}^r\mathbf{\Gamma}^r}\Psi^r$, $\mathrm{U} = -\frac{1}{2}\mathbf{\Sigma}\mathbf{\Sigma}\cdot\cdot\,\partial^2_{\mathbf{\Gamma}^r\mathbf{\Gamma}^r}\mathrm{G}^{-1}$, $\mathrm{A} = -\mathbf{\Sigma}\cdot\partial_{\mathbf{\Gamma}^r}\mathrm{G}^{-1}$, $\mathrm{J} = \left[\mathrm{I} + \Delta\lambda^{(k)}_{n+1}\left(\partial_{\hat{\mathbf{\Sigma}}\hat{\mathbf{\Sigma}}^2}\Phi^{(k)}_{n+1}\cdot\mathrm{B} - \partial^2_{\hat{\mathbf{\Sigma}}\mathbf{\Gamma}^r}\Phi^{(k)}_{n+1}\right)\right]^{-1}$.

For ferroelectroelastic material, an RM algorithm represents a two-step-algorithm including the following steps:

- Piezoelectric (linear electroelastic) predictor $\mathbf{\Sigma}^{trial}_{n+1} = \mathrm{G}_n\cdot\left(\mathbf{\Gamma}_{n+1} - \mathbf{\Gamma}^r_n\right)$
- Ferroelectroelastic corrector

The piezoelectric *predictor* is used for checking the loading/unloading conditions. It also provides the initial conditions for the ferroelectroelastic *corrector*. The linearly predicted trial state is projected (corrected) onto a suitably updated switching surface. The consistency condition is ensured by "returning" the trial solution to the switching surface.

Equations (7)–(9) can be considered as optimality conditions associated with a convex optimization problem. The constrained convex minimization problem proposes the geometric interpretation of the RM as the closest point projection of the trial state onto the switching surface.

4 Algorithmic Consistent Tangent Moduli

In order to achieve a quadratic rate of convergence of the NR method for the solution of nonlinear FE equations, tangent moduli consistent with the constitutive equation integration algorithm has to be used for the global stiffness matrix computation. The ferroelectroelastic CTM $\bar{\mathrm{G}}_t = \frac{\partial\mathbf{\Sigma}^{(k)}_{n+1}}{\partial\mathbf{\Gamma}^{(k)}_{n+1}}$ is obtained by performing an exact linearization of the RM algorithm (7)–(9) [3]:

$$\bar{\mathrm{G}}_t = \bar{\mathrm{G}} - \frac{\bar{\mathrm{G}}\cdot\tilde{\mathbf{N}}\;\tilde{\mathbf{L}}\cdot\bar{\mathrm{G}}}{\tilde{\mathbf{L}}\cdot\bar{\mathrm{G}}\cdot\tilde{\mathbf{N}} + \bar{D}}, \tag{11}$$

where $\bar{\mathrm{G}} = \left[\mathrm{G}^{-1} + \Delta\lambda\,(\mathrm{I}+\mathrm{A})\cdot\mathrm{Q}\cdot\partial^2_{\hat{\boldsymbol{\Sigma}}\,\hat{\boldsymbol{\Sigma}}}\Phi\cdot\left(\mathrm{I}+\mathrm{A}^T\right)\right]^{-1}$, $\tilde{\mathbf{N}} = (\mathrm{I}+\mathrm{A})\cdot\mathrm{Q}\cdot\partial_{\hat{\boldsymbol{\Sigma}}}\Phi$,

$$\tilde{\mathbf{L}} = \left\{\partial_{\hat{\boldsymbol{\Sigma}}}\Phi - \left[\partial_{\hat{\boldsymbol{\Sigma}}}\Phi\cdot(\mathrm{H}-\mathrm{U}) - \partial_{\boldsymbol{\Gamma}^r}\Phi\right]\cdot\mathrm{Q}\cdot\Delta\lambda\partial^2_{\hat{\boldsymbol{\Sigma}}\,\hat{\boldsymbol{\Sigma}}}\Phi\right\}\cdot\left(\mathrm{I}+\mathrm{A}^T\right),$$

$$\mathrm{Q} = \left[\mathrm{I} + \Delta\lambda\partial^2_{\hat{\boldsymbol{\Sigma}}\,\hat{\boldsymbol{\Sigma}}}\Phi\cdot(\mathrm{H}-\mathrm{U}) - \Delta\lambda\partial^2_{\hat{\boldsymbol{\Sigma}}\,\boldsymbol{\Gamma}^r}\Phi\right]^{-1},$$

$$\bar{D} = \left[\partial_{\hat{\boldsymbol{\Sigma}}}\Phi\cdot(\mathrm{H}-\mathrm{U}) - \partial_{\boldsymbol{\Gamma}^r}\Phi\right]\cdot\mathrm{Q}\cdot\partial_{\hat{\boldsymbol{\Sigma}}}\Phi.$$

Note that the ferroelectroelastic CTM $\bar{\mathrm{G}}_t$ is non-symmetric in the general case. The symmetry conditions of the CTM are analyzed in [3].

5 Scalar and Vector Potential Weak Formulations

The Maxwell equations for static electromechanical problems with a vanishing volume density of free charges are: $\nabla\times\mathbf{E} = \mathbf{0}$, $\nabla\cdot\mathbf{D} = 0$. There are two formulations with different choices of the primary electric variables: The electric field intensity $\mathbf{E}$ is expressed by the electric SP ϕ: $\mathbf{E} = -\nabla\phi$ such that Faraday's law $\nabla\times\mathbf{E} = -\nabla\times\nabla\phi \equiv \mathbf{0}$ is satisfied, whereas the electric displacement $\mathbf{D}$ follows from the electric VP $\boldsymbol{\psi}$: $\mathbf{D} = -\nabla\times\boldsymbol{\psi}$, which fulfills Gauss's law $\nabla\cdot\mathbf{D} = -\nabla\cdot(\nabla\times\boldsymbol{\psi}) \equiv 0$.

Equations defining the SP and the VP find their counterparts in FE formulations of coupled electromechanical problems with corresponding choices of the electric nodal variables using ϕ in the standard SP formulation [7] and $\boldsymbol{\psi}$ in the VP formulation [8].

In the standard approach in piezoelectricity, the electric field is expressed by the SP [7] and the weak formulation is written as

$$\int_V (\boldsymbol{\sigma}\cdot\cdot\,\delta\boldsymbol{\varepsilon} - \mathbf{D}\cdot\delta\mathbf{E})\,dV = \int_V \mathbf{f}_V\cdot\delta\mathbf{u}\,dV + \int_V (\mathbf{n}\cdot\boldsymbol{\sigma}\cdot\delta\mathbf{u} + \mathbf{n}\cdot\mathbf{D}\delta\phi)\,dS. \quad (12)$$

In this case, the displacement $\mathbf{u}$ and the SP ϕ are the basic variables, $\delta\boldsymbol{\varepsilon} = (\nabla\delta\mathbf{u})^S$ and $\delta\mathbf{E} = -\nabla\delta\phi$.

In the alternative approach, the electric displacement is expressed by the VP [8,9]. The principle of virtual work can be stated in the form

$$\int_V (\boldsymbol{\sigma}\cdot\cdot\,\delta\boldsymbol{\varepsilon} + \mathbf{E}\cdot\delta\mathbf{D})\,dV = \int_V \mathbf{f}_V\cdot\delta\mathbf{u}\,dV + \int_S (\mathbf{n}\cdot\boldsymbol{\sigma}\cdot\delta\mathbf{u} + \mathbf{n}\times\mathbf{E}\cdot\delta\boldsymbol{\psi})\,dS, \quad (13)$$

where $\delta\mathbf{D} = -\nabla\times\delta\boldsymbol{\psi}$ and the components of the VP $\boldsymbol{\psi}$ are the basic electric variables.

From the thermodynamic point of view, the electric displacement $\mathbf{D}$ (and $\boldsymbol{\psi}$, respectively) as well as the strain $\boldsymbol{\varepsilon}$ (and the displacement $\mathbf{u}$, respectively) represent generalized thermodynamic displacements, while the electric field $\mathbf{E}$ (and ϕ, respectively) and the mechanical stress $\boldsymbol{\sigma}$ represent generalized thermodynamic forces.

Therefore, the weak formulation of coupled electromechanical problems using the SP ϕ is based on the variation of a mixed thermodynamic potential–energy in the mechanical sense, but enthalpy in the electrical sense. Hence, in the context of the FE method, using the SP leads to a *non-definite stiffness* matrix and the solution of a boundary value problem corresponds to a saddle point of the potential as a function of $\mathbf{u}$ and ϕ. In contrary, the weak formulation making use of the VP ψ is based on the balance of pure electromechanical energy variation and external work variation. Therefore, in the context of the FE method, using the VP leads to a *positive definite stiffness* matrix such that the solution of the boundary value problem lies in an actual minimum of the potential in the space of the nodal degrees of freedom $\mathbf{u}$ and ψ. This difference favors the electric VP especially for the solution of nonlinear electromechanical problems.

Another advantage of the VP formulation consists in less strict conditions for the convergence of the global NR method due to the shape of the "load-response" hysteresis curve. One of the convergence conditions by the Kantorovich theorem [12] for the NR method for finding the root of $f(x)$ is $c = 2 \max |f''| \cdot \max |1/f'| \cdot \max |f/f'| < 1$. Considering $f_{SP}(E) = D(E) - D^{ext}$ for the SP formulation and $f_{VP}(D) = E(D) - E^{ext}$ for the VP formulation applying typical material parameters, we obtain $c_{VP} << c_{SP}$ (more than 200 times for typical PZT). That leads to the necessity to apply very small load steps for the SP formulation.

In computational practice a disadvantage of the VP is the complexity of formulating Dirichlet's boundary condition (directly in terms of VP components) in the general case. However, there is no problem to set boundary conditions $\phi|_S = \phi_s$ and $\boldsymbol{n} \cdot \boldsymbol{D}|_S = D_n$. The latter condition is implemented by the penalty function method [13].

At first view, a disadvantage of the VP formulation seems to be the increase in the number of nodal degrees of freedom for 3D problems (six per node in comparison with four for the SP formulation). However, this increase can be compensated by the higher rate of convergence.

6 Numerical Examples

The RM algorithms and corresponding CTMs for the SP and the VP formulations have been implemented into the FE program PANTOCRATOR [3,9,13]. The examples reported below compare various integration methods, various CTMs as well as SP and VP formulations for ferroelectroelastic materials.

6.1 Simulation of Hysteresis Phenomena in Ferroelectric Ceramics

The intention of this example is a comparison between the RM algorithm representing the implicit method and explicit forward Euler method applied for the

integration of the constitutive Eq. $(6)_1$ for polycrystalline ferroelectric ceramics with material parameters corresponding to PZT-5H [3, 10]. The remanent part of the free energy Ψ^r from (1) is approximated by the power-type expression [10]

$$\Psi^r(|\mathbf{P}^r|) = \frac{H^e P_0^2}{m^e - 1}\left[\frac{1}{m^e - 2}\left(1 - \frac{|\mathbf{P}^r|}{P_0}\right)^{2-m^e} - \frac{|\mathbf{P}^r|}{P_0}\right] \tag{14}$$

with the material constants $H^e = 714{,}000\,\mathrm{m/F}$, $P_0 = 0.24\,\mathrm{C/m^2}$, $m^e = 1.4$.

The results of numerical simulations of one cycle subdivided into 60 increments are presented in Fig. 1. An electric field is given altering from -3 up to 3 MV/m. The coercive field is 0.82 MV/m. The results of the RM procedure strongly follow the exact solution curve, whereas the explicit method shows a drift. For the latter, the dielectric hysteresis and butterfly loop are not closed.

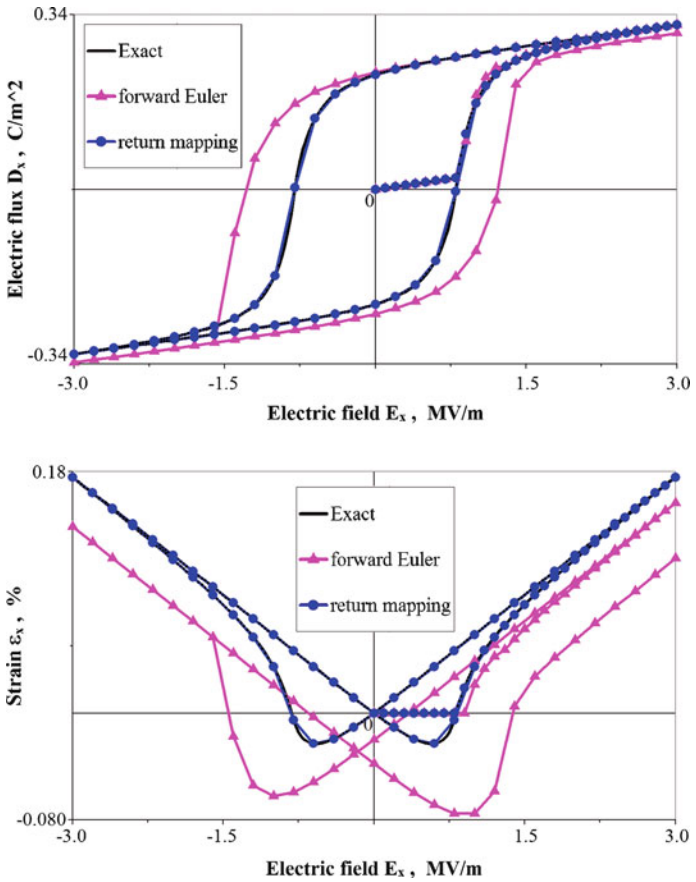

Fig. 1 Comparison of the RM procedure and the forward Euler method

Table 1 Number of iterations corresponding to SP and VP formulations for various load levels (tolerance $\varepsilon = 10^{-5}$)

ϕ_0 (kV)	10	15	20	25	30
Scalar potential formulation	5	4	4	No convergence	No convergence
Vector potential formulation	4	5	6	6	7

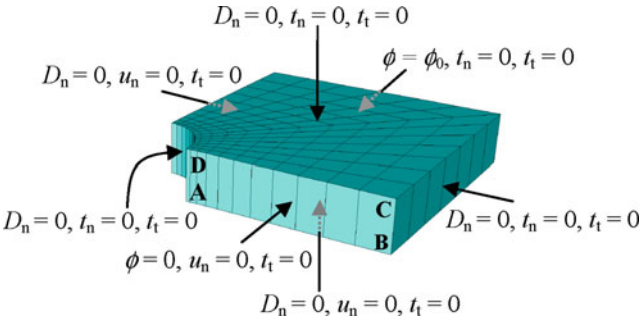

Fig. 2 FE model and boundary conditions in the problem of a hexahedron with a centered hole

6.2 Radial Poling of a Hollow Cylinder

An infinitely long thick-walled cylinder (see details in [3]) is charged by a constant potential ϕ_0 on the inner surface, while ϕ is zero on the outer surface. The convergence properties for the SP and the VP formulation under various load levels are shown in Table 1. At high load levels, divergence is observed for the SP formulation.

6.3 Hexahedron with a Centered Cylindrical Hole

A $0.02\,\text{m} \times 0.02\,\text{m} \times 0.006\,\text{m}$ hexahedron with a centered cylindrical hole of 0.004 m diameter is considered. Due to its symmetry in geometry and mechanical load as well as symmetry and antisymmetry in electrical load, only one eighth of the specimen is discretized with 154 eight-node 3D FEs (see Fig. 2). The displacement along the symmetry planes is fixed in perpendicular direction to the corresponding plane. The electric SP is set to zero at the front side (ABCD in Fig. 2), whereas the SP $\phi = \phi_0$ is prescribed at the back side. Material parameters correspond to PZT-5H [3, 10].

The convergence of the global NR iteration procedure for different stiffness matrixes is shown in Fig. 3. Note the advantage of the method with the CTM, which becomes more considerable with an increase of the load level (see Table 2).

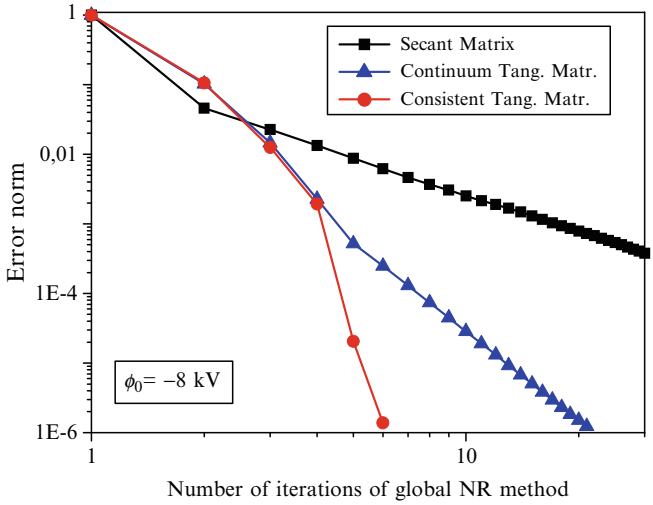

Fig. 3 Comparison of the convergence rate of global Newton–Raphson iterations

Table 2 Cumulative number of iterations corresponding to procedures with continuum and consistent tangent matrixes for various load levels (tolerance $\varepsilon = 10^{-4}$)

ϕ_0 (kV)	−5	−8	−9	−10	−15
Number of load steps	1	1	2	3	6
Continuum tangent matrix	7	8	15	No convergence	No convergence
Consistent tangent matrix	5	6	11	16	29

6.4 Four Point Bending Specimen with a Notch

The simulation of switching in a four bending specimen with a central notch under combined non-proportional load is presented. Realistic material parameters, specimen geometry, and loads as used and measured in [14] are considered. A 3D ferroelectroelastic FE analysis based on the VP formulation has been performed with the aim to evaluate the size and shape of the global switching zones at critical loads. The loading program includes: (i) initial poling of the unnotched sample parallel to the long axis; (ii) after changing the boundary condition along the notch (notching), applying an electric field parallel as well as antiparallel to the poling direction (perpendicular to the notch surface); and (iii) increasing the mechanical load under constant electric load. The notch surfaces are assumed to be traction free and impermeable. The latter is justified by the fact that the specimen is deeply notched and that only the global behavior is considered. Material properties correspond to PZT PIC 151 [14].

The evolution of the switching zones is presented in Fig. 4 for an electric field of $E = -0.15\,\mathrm{MV/mm}$ and various levels of the applied force up to the critical value $F_{cr} = 20\,\mathrm{N}$. The solution is obtained with the help of the VP formulation. Utilizing

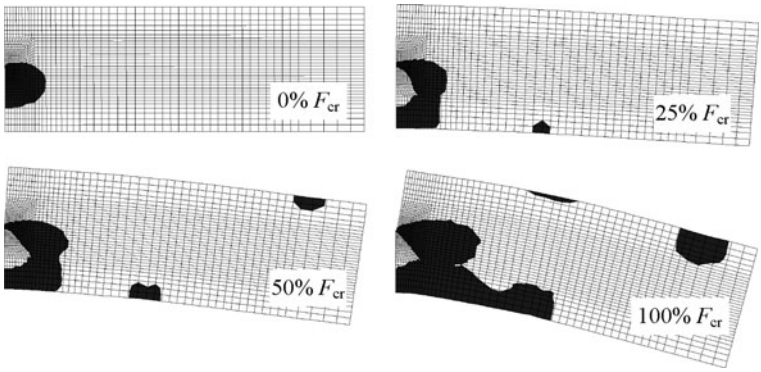

Fig. 4 Switching zones in a four-point bending specimen with a notch under various loads

the SP causes divergence under the same conditions. Also, an acceleration of the convergence of the NR iteration procedure is observed if the CTM is used.

With regard to fracture mechanics, the example impressively illustrates that, under the measured critical loads, switching occurs in large regions. Hence, predicting crack growth using linear piezoelectric fracture mechanics is questionable.

7 Conclusions

The VP FE formulation with RM and CTM represents an efficient tool to solve nonlinear coupled electromechanical problems. Using the CTM avoids divergence in the global NR iteration process and allows to apply large load steps.

Another approach to improve the convergence of the iterations for the nonlinear solution of ferroelectroelastic boundary value problems is considered in the article of S. Roth et al. in these proceedings of the IUTAM symposium.

Acknowledgements The authors are thankful for the support of this work by the DFG.

References

1. Simo JC, Hughes TJR (1998) Computational inelasticity. Mechanics and materials, vol 7, Springer, New York
2. Simo JC (1998) Numerical analysis and simulation of plasticity. In: Ciarlet P, Lions J (eds) Handbook of numerical analysis, vol 4. North-Holland, Amsterdam, New York, Oxford, pp 183–499
3. Semenov AS, Liskowsky AC, Balke H (2010) Return mapping algorithms and consistent tangent operators in ferroelectroelasticity. Int J Numer Methods Eng 81:1298–1340
4. Klinkel S (2006) A phenomenological constitutive model for ferroelastic and ferroelectric hysteresis effects in ferroelectric ceramics. Int J Solids Struct 43:7197–7222

5. Kamlah M, Laskewitz B, Zhou D (2007) Ferroelectric ceramics: basic properties and modeling methods. In: Schroeder J, Lupascu D, Balzani D (eds) Proceedings of the 1st seminar on the mechanics of multifunctional materials, Bad Honnef, Germany, pp. 60–63
6. Simo JC, Taylor RL (1985) Consistent tangent operators for rate-independent elastoplasticity. Comput Methods Appl Mech Eng 48:101–118
7. Allik H, Hughes TJR (1970) Finite element method for piezoelectric vibration. Int J Numer Methods Eng 2:151–157
8. Landis CM (2002) A new finite-element formulation for electromechanical boundary value problems. Int J Numer Methods Eng 55:613–628
9. Semenov AS, Kessler H, Liskowsky AC, Balke H (2006) On a vector potential formulation for 3D electromechanical finite element analysis. Commun Numer Methods Eng 22:357–375
10. Landis CM (2002) Fully coupled, multi-axial, symmetric constitutive laws for polycrystalline ferroelectric ceramics. J Mech Phys Solids 50:127–152
11. McMeeking RM, Landis CM (2002) A phenomenological multiaxial constitutive law for switching in polycrystalline ferroelectric ceramics. Int J Eng Sci 40:1553–1577
12. Kantorovich LV, Akilov GP (1964) Functional analysis in normed spaces. Pergamon, Oxford
13. Semenov AS (2003) PANTOCRATOR – the finite element program specialized on the nonlinear problem solution. In: Melnikov BE (ed) Proceedings of the Vth international conference on scientific and engineering problems of predicting the reliability and service life of structures, St.-Petersburg, pp. 466–480
14. Jelitto H, Kessler H, Schneider GA, Balke H (2005) Fracture behavior of poled piezoelectric PZT under mechanical and electrical loads. J Eur Ceram Soc 25:749–757

This page intentionally left blank

Finite Element Simulation of the Non-remanent Straining Ferroelectric Material Behaviour Based on the Electrostatic Scalar Potential: Convergence and Stability

Stephan Roth, Peter Neumeister, Artem S. Semenov, and Herbert Balke

Abstract The applicability of the Newton–Raphson iteration scheme to an electric scalar potential formulation of a ferroelectric/ferroelastic constitutive model within the framework of a finite element simulation is analysed methodically. Since the specific shape of the polarisation hysteresis is recognised as the principal reason of numerical problems, the considerations given here are limited to the non-remanent straining ferroelectric material model. Three approaches to gain convergence are discussed. Besides the known Line Search two other methods are presented, which are applied locally for each integration point. While the main idea of the first is to modify the vector of the internal dielectric displacement, the second approach affects the tangent modulus. An additional scaling of the tangent modulus is proposed in order to suppress numerical instabilities which may arise as a consequence of an over-compensation of numerical errors. To identify the remanent polarisation an enhanced Return Mapping algorithm based on an implicit backward Euler method is used. The applicability of the modified numerical iteration procedure is demonstrated by two examples.

1 Introduction

Ferroelectric ceramics are used for actuation and sensing applications with increasing complexity of part geometry and loading conditions. Detailed simulations of their nonlinear ferroelectric response during poling or in large-signal operation are necessary, for example to predict the resulting piezoelectric coupling properties or residual stresses. This requires appropriate material models together with numerical

S. Roth (✉)
TU Bergakademie Freiberg, Institute of Mechanics and Fluid Dynamics, Lampadiusstraße 4, 09599 Freiberg, Germany
e-mail: Stephan.Roth@imfd.tu-freiberg.de

P. Neumeister, A.S. Semenov, and H. Balke
Fakultät Maschinenwesen, Technische Universität Dresden, Mommsenstraße 13, 01062 Dresden, Germany

M. Kuna and A. Ricoeur (eds.), *IUTAM Symposium on Multiscale Modelling of Fatigue, Damage and Fracture in Smart Materials*, IUTAM Bookseries 24,
DOI 10.1007/978-90-481-9887-0_6,

solution techniques such as the finite element method (FEM). The latter incorporates an additional solution procedure to account for the nonlinear effects, most commonly based on the Newton–Raphson method. While various material models have been developed in preceding years, their implementation to FEM is tedious. The FE discretisation used for electromechanical problems is typically based on the mechanical displacements and the electrostatic scalar potential (SP). However, in combination with the Newton–Raphson method, the specific nonlinear ferroelectric material behaviour causes numerical problems, which from experience lead to divergence. An alternative FE formulation based on the electrostatic vector potential (VP) has proven suitable [5], but requires additional numerical treatment to assure accurate results. In addition, the electrostatic boundary conditions cannot be formulated in terms of SP or charges directly.

The object of the present work is to analyse methodically the applicability of the SP formulation together with the Newton–Raphson method in connection with the ferroelectric material model of Landis [3]. As the reasons leading to divergence are expected to be related to the constitutive relation of electric field E_i and dielectric displacement D_i, only the special case of non-remanent straining ferroelectrics without piezoelectric coupling and with isotropic permittivity is considered. Thus, the problem reduces to purely electrostatic. The internal variables, which define the material state as consequence of the load history, are the coordinates of the remanent polarisation vector P_i^{r}. Due to the choice of the electric scalar potential φ as the independent nodal variable, the coordinates of the electric field $E_i = -\varphi_{,i}$ are recognised as independent variables of the material formulation. The governing equations of the constitutive model are outlined in Section 2. In Section 3, the solution procedure for nonlinear problems is discussed briefly.

A total of three causes inducing numerical problems have been identified emerging on different levels through the numerical solution process. Section 4 presents additional measures that have to be taken to detect and avoid non-physical solutions for the internal variables, while the stability of the Newton–Raphson method and potential modifications are discussed in Section 5. At last, a directional instability of the remanent polarisation, which is observed during the iterative solution, is described in Section 6. Again, modifications are derived gaining stability. The so modified material routines have been implemented to the commercial FE code ANSYS utilising user elements. In Section 7, the applicability of the here proposed modifications is demonstrated, including a comparison with results obtained using a VP formulation.

2 Constitutive Model

The constitutive equations of the nonlinear behaviour of ferroelectric ceramics are derived from the phenomenological model of Landis [3], by applying the limitations given in Section 1. The dielectric displacement D_i is related to the electric field E_i taking into account the remanent polarisation state of the material point defined by P_i^{r} with

$$D_i = \kappa\, E_i + P_i^{\mathrm{r}}, \tag{1}$$

where κ denotes the isotropic dielectric constant. Switching is governed by the switching surface Φ with

$$\Phi = \hat{E}_i \, \hat{E}_i - E_0^2 = 0, \quad \hat{E}_i = E_i - E_i^{\mathrm{B}}(P_j^{\mathrm{r}}) \tag{2}$$

in terms of the effective electric field $\hat{E}_i$, which is in turn derived from E_i and the back electric field E_i^{B}. The switching surface Φ, which is a sphere of the constant material specific radius E_0 in the electric field space with centre at E_i^{B}, encloses the dielectric domain. The collinear vectors of back electric field and remanent polarisation are related as follows:

$$E_i^{\mathrm{B}} = E^{\mathrm{B}} \frac{P_i^{\mathrm{r}}}{P^{\mathrm{r}}}, \quad E^{\mathrm{B}} = \frac{H_0^{\mathrm{e}} \, P_0}{m^{\mathrm{e}} - 1} \left[\left(1 - \frac{P^{\mathrm{r}}}{P_0} \right)^{1-m^{\mathrm{e}}} - 1 \right], \quad P^{\mathrm{r}} = \sqrt{P_i^{\mathrm{r}} \, P_i^{\mathrm{r}}}, \tag{3}$$

where $H_0^{\mathrm{e}} > 0$ and $m^{\mathrm{e}} > 1$ are hardening parameters and $P_0 > 0$ denotes the intrinsic saturation level of the remanent polarisation. The associated switching rule

$$\dot{P}_i^{\mathrm{r}} = \lambda \frac{\partial \Phi}{\partial \hat{E}_i} = 2 \lambda \, \hat{E}_i \,, \quad \lambda \geq 0 \tag{4}$$

with the non-negative multiplier λ implies that increments of P_i^{r} are normal to the switching surface. The relation between increments of electric field and increments of dielectric displacement is defined by the tangent modulus κ_{ij}^{t}

$$\dot{D}_i = \kappa_{ij}^{\mathrm{t}} \, \dot{E}_j \,. \tag{5}$$

The shape of the normalised uniaxial $D(E)$-hysteresis in Fig. 1 is characterised by κ, H_0^{e} and m^{e}. It has two turning points where the curvature changes from convex to concave. Saturation is accounted for by means of nonlinear hardening, Eq. 3, ensuring $P^{\mathrm{r}} < P_0$. However, due to the structure of Eqs. 2 and 3, additional non-physical solutions exist associated with a non-positive lambda or violating the saturation condition (see Fig. 1).

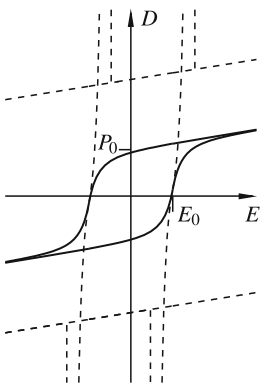

Fig. 1 $D(E)$-hysteresis (*solid line*) and non-physical solutions violating the saturation condition (*dashed line*) for PZT5H (Table 1)

Table 1 Material parameters of PZT5H [3] and 8/65/35 PLZT [2]

κ (nA s/MV mm)		E_0 (MV/mm)	P_0 (nA s/mm^2)	H_0^{e} (MV mm/nA s)	m^{e}
PZT5H	42000	0.82×10^{-3}	240	7.14×10^{-7}	1.4
PLZT	56300	0.36×10^{-3}	250	1.44×10^{-8}	2.0

3 Solution Procedure

To gain equilibrium between applied loads and internal reactions with the help of the Newton–Raphson method, an iteration is initiated. Each iteration step consists of two principal parts: In the first part, here referred to as equilibrium iteration step, the FE model is brought into equilibrium using a linear extrapolation of the nonlinear relation between independent nodal variables and nodal reactions. In a SP formulation of electrostatic problems these are φ and nodal charges Q, respectively. Here, this linearisation follows directly from the linearisation of the nonlinear material response, i.e. κ_{ij}^{t} defined in Eq. 5. The result is an increment $\Delta\varphi$ at the nodes and thus an increment ΔE_i of the electric field. In the second part, the actual material response in terms of the dielectric displacement as consequence of the derived ΔE_i is computed at each evaluation point. If switching is recognised, the identification of the internal variables P_i^{r} is required. Here the Return Mapping algorithm proposed by Wilkins [1, 7] is used: Equations 2 and 4 are discretised with respect to the three internal variables P_i^{r} and the multiplier λ starting from the last equilibrium configuration applying the implicit Euler backward method. The new P_i^{r} and λ corresponding to the current E_i are computed iteratively using again a Newton–Raphson method.

4 Enhancement of Return Mapping Algorithm

Within the Return Mapping algorithm, it is essential to include a check of the constraints concerning saturation as well as the branch of the hysteresis, which both are not accounted for so far, to distinguish between physical and mathematically induced solutions (see Fig. 1): Firstly, all results with $P^{\mathrm{r}} \geq P_0$ have to be treated as invalid as consequence of the saturation condition. In theses cases a sub-division of the increment of the electric field, which is defined by the equilibrium iteration, inside the Return Mapping procedure yield admissible solutions. It is important to notice that the reference configuration used in the discretisation of Eqs. 2 and 4 remains the latest known equilibrium configuration at all times. The results of a sub-increment are merely used as starting values for the next sub-increment. Secondly, false hysteresis branches can be identified by a non-positive λ, i.e. $\lambda < 0$, which is associated with negative dissipation. If $\lambda < 0$ is recognised, a restart of the entire equilibrium iteration with a smaller change of the applied loads is suggested.

5 Convergence Study and Modification to Newton–Raphson Method

The convergence behaviour of the Newton–Raphson method is considered for the case of uniformly directed electric loads. Indices related to this direction are omitted. Depending on the choice of the independent field variable the application of the Newton–Raphson method may yield divergence, which as we show below is due to the character of the turning points of the hysteresis. For an VP formulation [5] the independent field variables are the components D_i of the dielectric displacement. The curvatures of the $E(D)$-hysteresis change from concave to convex at the turning points. As Fig. 2 illustrates the Newton–Raphson iteration converges. Here, the subscript $(\,)_{(n)}$ and the superscript $(\,)^{(m)}$ denote the current equilibrium iteration step and the last equilibrium configuration, respectively. The tangent $\beta^t = 1/\kappa^t$ follows from the VP rate formulation $\dot{E} = \beta^t \dot{D}$.

On the other hand the curvature of the $D(E)$-hysteresis of the SP formulation with the electric field E_i as independent field variable changes from convex to concave at the turning points. This means that the dielectric slope as well as the slopes of the hysteresis close to saturation are lower than those in the vicinity of the turning points. Thus, the equilibrium iteration diverges (see Fig. 3). Thereby, the problem does not arise from the overshoot of E due to the dielectric extrapolation as result of the first equilibrium iteration step. In fact, the decreasing slope of the hysteresis causes a strong correction of E back into the dielectric domain or even further leading to switching in the opposite direction. Figure 4 illustrates such a scenario in more detail for an increased load starting from $E^{(m)}$, $D^{(m)}$ with constant applied D^{ext}. There, ΔE denotes the correction of E in the second equilibrium step. It can be stated empirically that divergence is avoided if E is kept larger than the critical electric field E^c which marks the transition between dielectric and ferroelectric behaviour with the reference polarisation state:

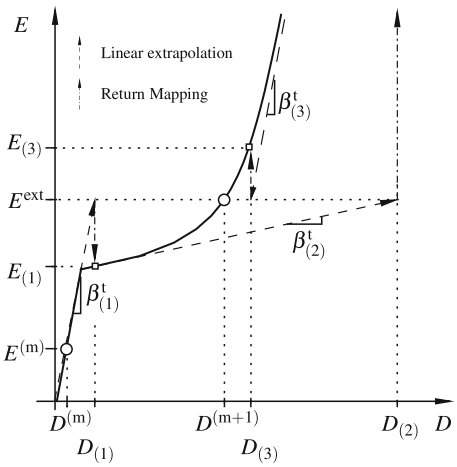

Fig. 2 Vector potential formulation – converging Newton–Raphson iteration

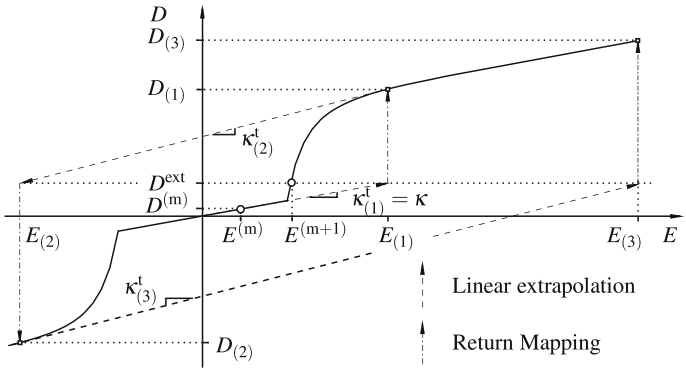

Fig. 3 Scalar potential formulation – diverging Newton–Raphson iteration

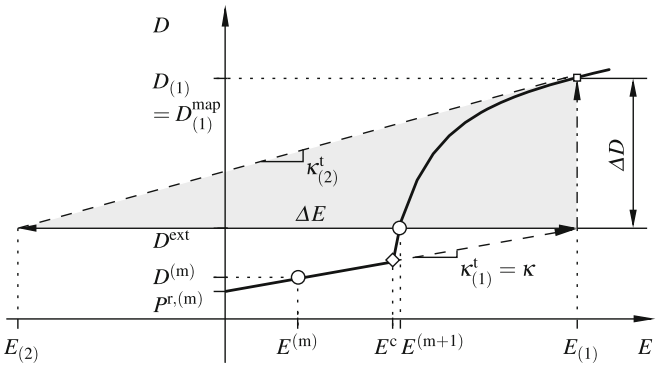

Fig. 4 Scalar potential formulation – first two iteration steps

$$E_{(\mathrm{n}+1)} > E^{\mathrm{c}}\left(P^{\mathrm{r},(\mathrm{m})}\right). \tag{6}$$

One possibility to reduce ΔE is its direct manipulation by scaling the increment of the independent nodal variable $\Delta\varphi$. This method is known as Underrelaxation or Line Search and was developed for the treatment of magnetostatic hysteresis problems also based on a SP formulation, e.g. [4]. It is considered as a global method because the scaling of $\Delta\varphi$ is equal for the entire FE model. In addition, a global criterion, which is usually work-related, is used to compute the scaling factor. It is thus obvious that the condition formulated in Eq. 6 is met at all evaluation points. Therefore, two different approaches are proposed here, acting locally in each evaluation point independently. There, the correction of E is damped by scaling either the tangent modulus κ^{t} (τ-method) or the change of the dielectric displacement D as result of the Return Mapping algorithm (γ-method). Both methods are highly adaptive as they use a local measure of convergence, namely the difference ΔD between the

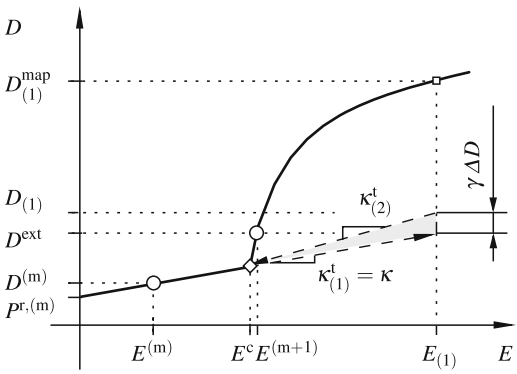

Fig. 5 Converging equilibrium iteration: γ-method

result of the linear extrapolation D^{ext} and D^{map} computed by the Return Mapping algorithm. The former, which is generally not constant, has to be determined by a local repetition of the preceding equilibrium iteration step:

$$\Delta D = \left| D^{\mathrm{map}}_{(\mathrm{n})} - D^{\mathrm{ext}}_{(\mathrm{n})} \right| \quad \text{with} \quad D^{\mathrm{ext}}_{(\mathrm{n})} = D_{(\mathrm{n}-1)} + \kappa^{\mathrm{t}}_{(\mathrm{n})}\, \Delta E. \tag{7}$$

5.1 The γ-Method

The γ-method bases on a scaling of the dielectric displacement as dependent variable as shown in Fig. 5 according to

$$D_{(\mathrm{n})} = D^{\mathrm{ext}}_{(\mathrm{n})} + \gamma \left(D^{\mathrm{map}}_{(\mathrm{n})} - D^{\mathrm{ext}}_{(\mathrm{n})} \right) \quad \text{with} \quad 0 < \gamma \leq 1. \tag{8}$$

An empirical relation between scaling factor γ and measure of convergence ΔD is derived by evaluating Eq. 6 for various external loads and initial remanent polarisations incorporating two material specific iteration parameters (γ approaches 1 as $\Delta D \to 0$). For general loading, the difference vector $\Delta D_i = D^{\mathrm{map}}_i - D^{\mathrm{ext}}_i$ is scaled, while its norm is used as measure of convergence.

5.2 The τ-Method

According to the modified Newton–Raphson method, the τ-method involves changing the tangent modulus so that Eq. 6 is met at the next iteration step:

$$\kappa^{\mathrm{t}}_{(\mathrm{n}+1)} = \tau\, \kappa^{\mathrm{t,map}}_{(\mathrm{n}+1)} \quad \text{with} \quad 0 < \tau \leq 1, \tag{9}$$

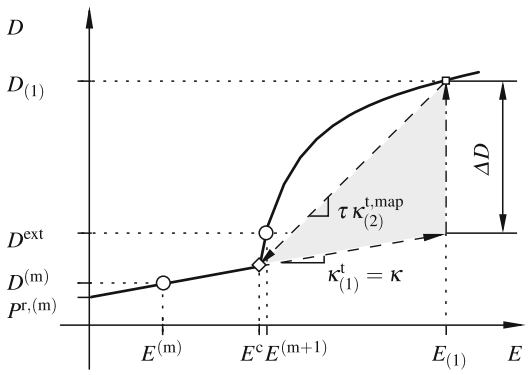

Fig. 6 Converging equilibrium iteration: τ-method

where $\kappa^{\mathrm{t,map}}$ denotes the tangent modulus evaluated for the current polarisation state (see Fig. 6). Again an empirical relation between scaling factor τ and ΔD is used. For general loading, τ is only applied to the components of the tangent modulus in the direction of ΔD_i, which requires a transformation of the tangent modulus into a coordinate system parallel to ΔD_i.

6 Directional Stability

Beside the overcorrection of E_i as consequence of the SP formulation, another numerical problem is observed that is characterised by a growing remanent polarisation with alternating sign transverse to the expected direction of the remanent polarisation. This phenomenon originates from the effort of the Newton–Raphson method to compensate minor numerically induced fluctuations of E_i or D_i. The iteration process indicates that this compensation overreacts, increasing the magnitude of the erroneous values. In the following, this scenario is illustrated on a square loaded homogeneously with the surface charges ω^{ext} as shown in Fig. 7.

The solution $D_x = 0$ and $D_y = -\omega^{\mathrm{ext}}$ is found easily from the boundary conditions. For $|\omega^{\mathrm{ext}}|$ of the same order of magnitude as P_0, the Newton–Raphson method converges without modifications (providing that no directional instability occurs). Figure 8 shows the evolution of D_y and of the oscillating erroneous D_x for PZT5H with $\omega^{\mathrm{ext}} = -280\ \mathrm{nAs/mm^2}$ during the iteration process, derived with the assumption that $P_x^{\mathrm{r}} \ll P_y^{\mathrm{r}}$.

Stable behaviour can be achieved if the magnitude of the erroneous value becomes smaller, giving rise to the stability condition

$$\left|E_{x,(\mathrm{n})}\right| = \left|E_{x,(\mathrm{n}-1)} + \Delta E_x\right| < \left|E_{x,(\mathrm{n}-1)}\right|, \tag{10}$$

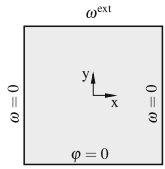

Fig. 7 Square with electric boundary conditions

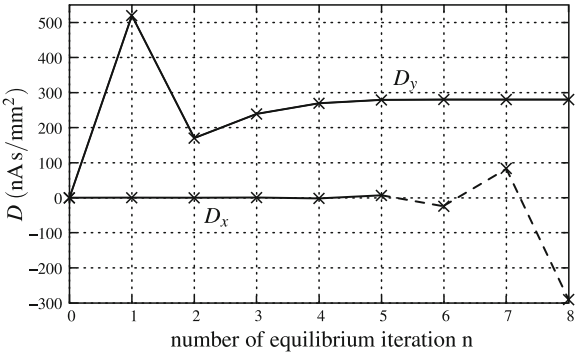

Fig. 8 Development of dielectric displacement during equilibrium iteration, material PZT5H, $D_y^{\text{ext}} = -\omega^{\text{ext}} = 280\,\text{nA s/mm}^2$: D_y (stable), D_x (unstable)

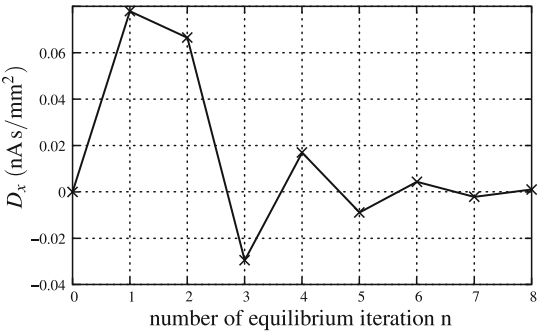

Fig. 9 Development of dielectric displacement during equilibrium iteration, material PZT5H, $D_y^{\text{ext}} = -\omega^{\text{ext}} = 280\,\text{nA s/mm}^2$: D_x (stabilised with $\rho = 3$)

where ΔE_x represents the increment of E_x as result of the n-th equilibrium iteration step. To satisfy this condition a further scaling factor $\rho > 1$ is introduced to increase the tangent modulus in the x-direction according to

$$\kappa_{xx}^{\text{t,scal}} = \rho\, \kappa_{xx}^{\text{t}}. \tag{11}$$

Figure 9 shows the stabilised development of D_x with $\rho = 3$. The generalisation of Eq. 11 again uses the direction of evolution of the internal variables.

7 Examples

The capability of the presented enhancements and modifications is demonstrated at two examples. Firstly, the radial poling of a circular ring made of PLZT (Table 1) is considered (see Fig. 10 a), for which an analytical solution is available [6]. The ring is loaded with $\varphi = \varphi^{\text{ext}}$ and $\varphi = 0$ at the outer and inner radius, respectively. The rotationally symmetrical distribution of the field variables is reproduced exactly by the numerical solution within the numerical tolerance. Figure 10 b shows the numerically obtained results of the radial coordinates E_r, D_r and P_r^{r} at an arbitrary angle for $\varphi^{\text{ext}} = -10\,\text{kV}$. The maximum deviation from the analytical solution is found at the inner radius with $\delta E_r = 0.08\%$ and $\delta D_r = 0.05\%$.

In a second example, the inhomogeneous poling of a square plate with centred circular hole made of PZT5H (Table 1) is presented. Due to symmetry only one fourth of the plate is modelled as shown in Fig. 11 a. The edge length to hole radius ratio is $L/R = 40$. At the top edge an electrostatic scalar potential $\varphi^{\text{ext}} < 0$ is applied, corresponding to the nominal electric field $E^{\text{ext}} = -\varphi^{\text{ext}}/L$. Results for two different load levels are presented: firstly, (a) $E^{\text{ext}}/E_0 = 0.98$ just under the coercive field and, secondly, (b) $E^{\text{ext}}/E_0 = 2.4$ causing switching even in the undisturbed regions. Thereby, the load is applied in one step only to prove the robustness of the iteration procedure.

Figure 12 depicts D_y and E_y along x at $y = 0$. A concentration of D_y can be seen close to the hole. For loading case (a), this is accompanied only by a small elevation of E_y due to the abrupt evolution of remanent polarisation P_y^{r} as E_y reaches E_0. The plot of P_i^{r} around the hole (see Fig. 11 b) confirms this argumentation. For loading case (b) on the other hand, the elevation of D_y arises from dielectric polarisation mainly and is thus connected with a more pronounced increase of E_y.

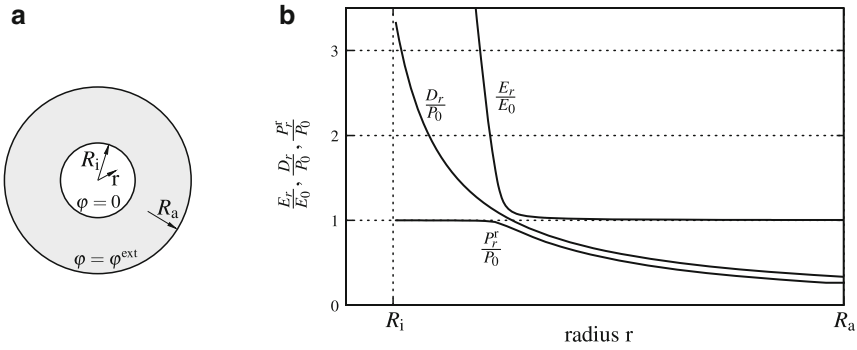

Fig. 10 Circular ring, material PLZT: (**a**) Geometry and boundary conditions, $R_i = 1\,\text{mm}$, $R_a = 10\,\text{mm}$, $\varphi^{\text{ext}} = -10\,\text{kV}$; (**b**) Distribution of field variables after radial poling

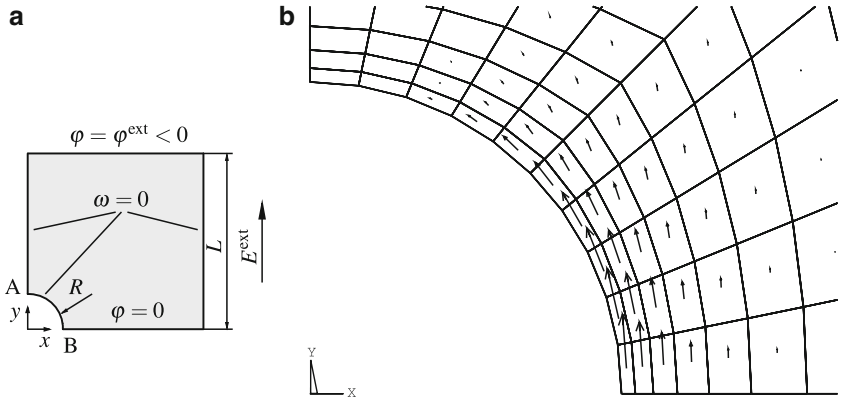

Fig. 11 (**a**) Square plate with centred circular hole, electric boundary conditions; (**b**) Vector plot of P_i^{r}, material PZT5H, $E^{\text{ext}}/E_0 = 0.98$, results obtained using γ-method

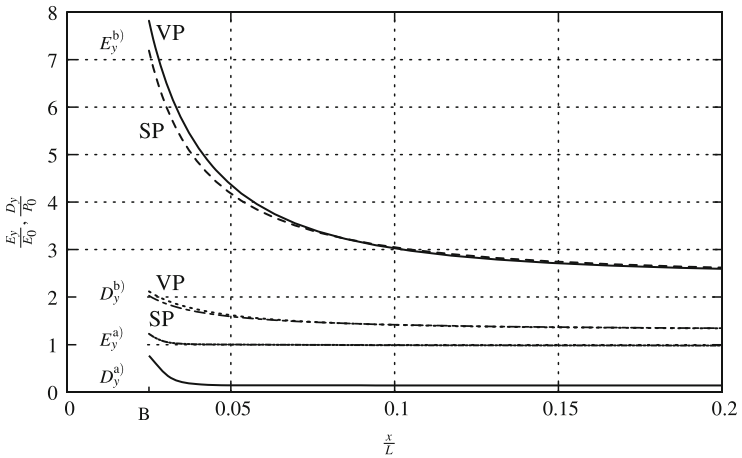

Fig. 12 Comparison between scalar potential and vector potential formulation, field variables at $y = 0$, material PZT5H, SP results obtained using γ-method: (**a**) $E^{\text{ext}}/E_0 = 0.98$; (**b**) $E^{\text{ext}}/E_0 = 2.4$

For comparison, Fig. 12 also shows results obtained by solving the problem based on the VP formulation, computed with the FE software PANTOCRATOR [5]. For load case (a), there is a satisfying agreement with a maximum relative deviation of $\delta D_y = 0.03\%$ and $\delta E_y = 0.02\%$. In contrast, maximum relative deviations of $\delta D_y = 4\%$ and $\delta E_y = 8\%$ are observed for load case (b). Since there is no analytical solution, a further assessment of the correctness of either SP or VP formulation is complex and requires a more detailed analysis.

8 Conclusion

The reason for divergence of the Newton–Raphson method in its application to the ferroelectric material behaviour in connection with the SP formulation could be deduced from the shape of the $D(E)$-hysteresis. The combination of a reliable Return Mapping, an effective algorithm to prevent directional instability, and an appropriate enhancement of the Newton–Raphson method yields convergence depending on a set of scaling parameters, which, in turn, depend on the material, the load level, and the current field variables. Due to these scaling parameters, the solution of complex problems requires a great number of equilibrium iteration steps to gain equilibrium. However, in comparison to certain divergence this is an acceptable cost.

Acknowledgements The authors greatly acknowledge the support from the Deutsche Forschungsgemeinschaft (DFG) under Contract No. Ba 1411/12.

References

1. Belytschko T (2000) Nonlinear finite elements for continua and structures. Wiley, New York
2. Huber JE, Fleck NA (2001) Multi-axial electrical switching of a ferroelectric: Theory versus experiment. J Mech Phys Solids 49:785–811
3. Landis CM (2002) Fully coupled multi-axial, symmetric constitutive laws for polycristalline ferroelectric ceramics. J Mech Phys Solids 50:127–152 (2002)
4. Nakata T, et al (1992) Improvements of convergence characteristics of newton-raphson method for nonlinear magnetic field analysis. IEEE Trans Magn 28(2):1048–1051
5. Semenov AS, Kessler H, Liskowsky AC, Balke H (2006) On a vector potential formulation for 3d electromechanical finite element analysis. Commun Num Meth Eng 22:357–375
6. Semenov AS, Liskowsky AC, Balke H (2010) Return mapping algorithms and consistent tangent operators in ferroelectroelasticity. Int J Num Meth Eng 81(10):1298–1340
7. Simo JC, Hughes TJR (1998) Computational inelasticity. Springer, New York

Constitutive Behavior of Nano-particle Ferroelectric Ceramics

Li Yu, Shouwen Yu, and Dietmar Gross

Abstract Due to the characteristic of the microstructure, nanoparticle ferroelectric ceramics display a considerable different behavior than ordinary ferroelectric ceramics. In this paper a model is proposed from which the constitutive relation of nanoparticle ferroelectric ceramics is deduced. The model is based on the micro structure of the nanoparticles which consist on the ferroelectric phase and a non-ferroelectric matrix phase. The results show that the effective electro-elastic parameters and the constitutive behavior are size dependent. The size effect is most dominant when the grain size is in the range of dozens of nanometers to several nanometers.

1 Introduction

Due to the particularity of the microstructure, nanoparticle ferroelectric ceramics shown some outstanding properties that ordinary ferroelectric ceramics don't have. Among others superplasticity [1], low thermal conductivity [2] and optical permeability shall be mentioned which have continuously expanded the potential applications of nanoparticle ferroelectric ceramics, e.g. in MEMS. In recent years, with the development of ferroelectric thin films and ferroelectric ultrafine powders, the research on nanoparticle ferroelectric materials has been intensified. At the same time the ferroelectric size effect became a practical problem.

Beside the electro-mechanical coupling, ferroelectric materials have the specific physical property that their phase transition behavior is grain size dependent. In a review paper Ahn [3] discussed the outstanding performance and attractive

L. Yu and S. Yu (✉)
Department of Mechanics, Tsinghua University, Beijing, China
e-mail: yusw@mail.tsinghua.edu.cn

D. Gross
Universität Darmstadt, Germany
e-mail: gross@mechanik.tu-darmstadt.de

M. Kuna and A. Ricoeur (eds.), *IUTAM Symposium on Multiscale Modelling of Fatigue, Damage and Fracture in Smart Materials*, IUTAM Bookseries 24,
DOI 10.1007/978-90-481-9887-0_7,

application prospects of nanoparticle ferroelectric materials. He summarized recent research on the behavior of these materials and discussed some new directions regarding the size effect. Experimental results indicate that the size effect is influenced by a number of different factors. For example, some studies [4–6] show that the size effect depends on the crystalline microstructure, the ferroelectric domain structure, the crystal defects and grain boundaries, etc. Other works [7–9] indicate that the size effect is related to the surface of the interfacial layers (interphase) of the grains. With decreasing size of the nanoparticles, the relative number of surface atoms, i.e. the grain surface area, increases. Thus, the volume of the interfacial layer should be taken into account. Based on these observations, in-depth studies on the behavior of ferroelectric materials from the macro and microscopic point of view have been carried out. For example, the dependence of the phase transition temperature and permittivity on the grain size has been modelled and the respective theories have successfully been applied for the prediction of critical grain sizes of typical ferroelectrics such as barium titanate and lead titanate. The results guided the design of integrated ferroelectric devices and stimulated the development of the ferroelectric theory for small sizes. However, a theory describing the constitutive behavior of nanoparticle ferroelectric ceramics has not been reported yet. Starting from the microscopic structure of nanoparticles ferroelectric ceramic, this paper investigates the role of the interphase and its influence on the effective electro-elastic properties of these materials and their constitutive behavior. The contents of the paper is arranged as follows: in Section 2 the microscopic model of nanoparticle ferroelectrics based on the interfacial layer is described; Section 3 discusses how the effective electro-elastic properties change with the grain size. The corresponding constitutive relations are given in Section 4 while in Section 5 results for a specific material are discussed. Finally, Section 6 will provide a brief summary.

2 Nanoparticle Ferroelectric Model

The structure of nanoparticle materials is particular. When the size of the particles decrease, the number of atoms appearing in the transition zone between the different grains increase, i.e. the number of interface atoms form a considerable portion of the volume. These interface atoms can be considered as one constituent of a two-phase composite while the grain itself acts as the other constituent [9]. The interfacial layer between the active grains is called dead layer or interphase.

Experimental results [10, 11] show that the permittivity and the phase transition temperature of nanoparticle ferroelectric materials differ considerably from those of conventional materials. The reasons for this phenomenon are mainly devoted to the large portion of the grain boundaries or the dead layer [11, 12]. Frey [12] studied experimentally the microstructure of nanoparticle barium titanate; a typical micrograph is depicted in Fig. 1. He clearly showed that the structures of the grain phase and the dead layer phase of classical and nanoparticle barium titanate are

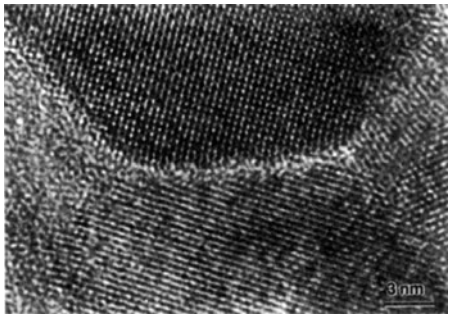

Fig. 1 Dead layer phase of barium titanate, after [12]

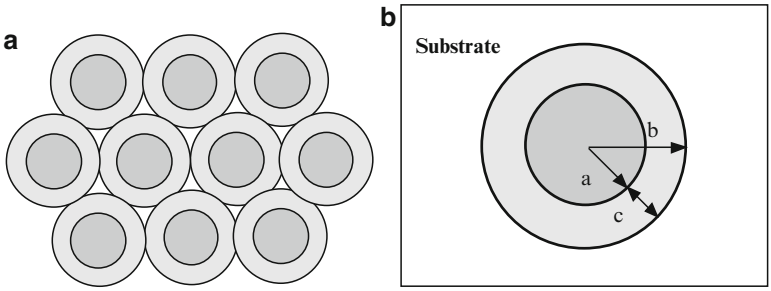

Fig. 2 Two phase model of a nanoparticle ferroelectric material

different and that the dead layer phase has no ferroelectric properties. Experimental observations [14, 15] support the picture that ferroelectric materials with a small crystal size can be considered as a multi-phase material.

Based on the described experimental evidence, a simplified two-phase model of nanoparticle ferroelectric ceramics is proposed as shown in Fig. 2. The grain of nanoparticle ferroelectric ceramic is assumed as a sphere with ferroelectric properties. Each ferroelectric phase grain is surrounded by a layer of the grain boundary with non-ferroelectric properties (interphase), see Fig. 2a. One cell of the model is shown in the enlarged Fig. 2b where a is the radius of the active inner ferroelectric phase and b characterizes the total size of the grain including the non-ferroelectric phase. The thickness of the latter is $c = b - a$.

3 Electro-elastic Parameters

Different from conventional poly-crystals, in the model shown in Fig. 2, the electro-elastic and phase transition behavior of the material will depend on the thickness on account of the included dead layer phase. As a first approximation, no interaction between the adjacent particles is assumed. As a consequence, the behavior of the whole ferroelectric material is the same as the behavior of one individual cell.

Furthermore, the thickness of dead layer phase c is assumed to be fixed, so that the outer radius b of the cell is the control parameter that reflects changes of the relevant behavior. The made assumptions are equivalent to the so-called dilute distribution assumption in micromechanics.

According to Fig. 2b the volumes V_I and V_{II} of the inner grain phase and outer interfacial phase, respectively, are given by

$$V_I = \frac{4\pi a^3}{3}, \qquad V_{II} = \frac{4\pi(b^3 - a^3)}{3}. \tag{1}$$

The behavior of the whole composite ferroelectric particles is derived by volume averaging the components. In the following this is done for the spontaneous polarization, the permittivity and the elastic behavior.

Denoting the spontaneous polarization of the inner and outer phase as $\mathbf{P}_I$ and $\mathbf{P}_{II}$, respectively, the overall (surplus) spontaneous polarization is assumed to be given by the simple average value

$$\mathbf{P} = \frac{V_I \mathbf{P}_I + V_{II} \mathbf{P}_{II}}{V_I + V_{II}}. \tag{2}$$

Because the outer grain boundary phase behaves non-ferroelectric, i.e. $\mathbf{P}(II) = 0$, and introducing the phase volumes, we receive the overall spontaneous polarization

$$\mathbf{P}(b) = \left(\frac{a}{b}\right)^3 \mathbf{P}_I = \left(\frac{b-c}{b}\right)^3 \mathbf{P}_I = \left(1 - \frac{c}{b}\right)^3 \mathbf{P}_I. \tag{3}$$

In the same way, assuming that the non-ferroelectric phase exhibit no spontaneous strain, the total spontaneous strain is described by

$$\varepsilon(b) = \left(1 - \frac{c}{b}\right)^3 \varepsilon_I. \tag{4}$$

The permittivity, piezoelectric coefficient and elastic compliance can be derived analogously but with the difference that these coefficients may be nonzero in the dead layer. Assuming again that the total permittivity tensor $\mathbf{k}$ of the ferroelectric particles is given by the average value

$$\mathbf{k} = \frac{V_I \mathbf{k}_I + V_{II} \mathbf{k}_{II}}{V_I + V_{II}} \tag{5}$$

we receive by introducing the phase volumes

$$\mathbf{k}(b) = \frac{a^3 \mathbf{k}_I + (b^3 - a^3)\mathbf{k}_{II}}{b^3} = (\mathbf{k}_I - \mathbf{k}_{II}) \left(1 - \frac{c}{b}\right)^3 + \mathbf{k}_{II}. \tag{6}$$

Here, as before, I and II indicate the inner phase and the outer phase, respectively. In the exact same manner the piezoelectric tensor $\mathbf{d}$ and the elastic compliance tensor $\mathbf{S}$ are obtained:

$$\mathbf{d}(b) = (\mathbf{d}_I - \mathbf{d}_{II}) \left(1 - \frac{c}{b}\right)^3 + \mathbf{d}_{II} \,, \tag{7}$$

$$\mathbf{S}(b) = (\mathbf{S}_I - \mathbf{S}_{II}) \left(1 - \frac{c}{b}\right)^3 + \mathbf{S}_{II} \,. \tag{8}$$

4 Constitutive Relations

In the literature exist a number of constitutive models that are able to simulate the ferroelectric hysteresis behavior. One example is the phenomenological macroscopic model proposed by Mehling et al. [16] which has a microscopic basis and which is well adapted for the implementation in a finite element program. Another phenomenological model is that of Yu et al. [17] which provides an accurate but still simple constitutive framework based on gradual domain switching. For the sake of simplicity, the model [17] is used as a basis to study the changes of the constitutive behavior of nanoparticle ferroelectrics and to establish a constitutive model for these materials. In order to be self-contained, the model [17] briefly is described in what follows.

Consider a ferroelectric ceramics whose poling direction coincides with the x_3-direction. When the material is subjected to an external electric field parallel to the poling direction, the constitutive equation in x_3-direction can be written as

$$D_3 = k_{33} E_3 + \overline{P}^r_3 \,, \tag{9}$$

$$\varepsilon_{33} = \overline{d}_{333} E_3 + \overline{\varepsilon}^r_{33} \,. \tag{10}$$

Here, k_{33} denotes the dielectric permittivity, ε_{33} the strain, D_3 the electric displacement, E_3 the electric field, $\overline{d}_{333}$, $\overline{P}^r_3$ and $\overline{\varepsilon}^r_3$ are the current value of piezoelectric coefficient, remanent polarization and remanent strain, respectively.

According to the Landau–Devonshire theory [23], the remanent strain of a ferroelectric ceramic is approximately proportional to the square of the remanent polarization, that is,

$$\overline{\varepsilon}^r_{33} = Q_{eff} (\overline{P}^r_3)^2 \tag{11}$$

where Q_{eff} is the effective electrostriction coefficient. According to the domain nucleation theory the evolution of the remanent polarization $\overline{P}^r_3$ and the piezoelectric tensor component $\overline{d}_{333}$ is directly related to the domain switching volume fraction f^E_d through

$$\overline{P}^r_3 = f^E_d P^r_3 \,, \tag{12}$$

$$\overline{d}_{333} = f^E_d d_{333} \,. \tag{13}$$

The domain switching volume fraction f_d^E under cyclic electric loading approximately is given by [17]

$$f_d^E = \exp\left(-\frac{b^E}{|E_3 \pm E_c|}\right) \tag{14}$$

where the material constant b^E is the activation field under electric loading. The evolution of f_d^E in one electrical loading cycle is explicitly expressed by

$$f_d^E(E_3) = \begin{cases} \exp[-b^E/(E_3 + E_c)] & -E_c \le E_3 \le E_{max}\,, \\ \exp[b^E/(E_3 + E_c)] & -E_{max} \le E_3 < -E_c\,, \\ \exp[b^E/(E_3 - E_c)] & -E_{max} \le E_3 < E_c\,, \\ \exp[-b^E/(E_3 - E_c)] & E_c < E_3 \le E_{max} \end{cases} \tag{15}$$

where E_{max} is the saturation polarization field.

Thus, substituting Eqs. 11–14 into 9 and 10 yields the uniaxial relations

$$D_3 = k_{33}E_3 + f_d^E P_3^r\,, \tag{16}$$

$$\varepsilon_{33} = d_{333} f_d^E E_3 + f_d^E \varepsilon_{33}^r = d_{333} f_d^E E_3 + Q_{eff}(f_d^E P_3^r)^2\,. \tag{17}$$

In three dimensions the constitutive relation for the electrical and mechanical response can be written as

$$D_i = d_{ikl}\frac{P^{r'}}{|P_s^r|}\sigma_{kl} + k_{ik}E_k + f_d^L P_i^r\,, \tag{18}$$

$$\varepsilon_{ij} = s_{ijkl}\sigma_{kl} + d_{kij}\frac{P^{r'}}{|P_s^r|}E_k + f_d^L \varepsilon_{ij}^r\,. \tag{19}$$

From the discussion in Section 3 we know that the microscopic structure of the nanoparticle material differs from the classical material which gives rise to changes of the effective material constants and polarization behavior. Therefore, if the characteristic particle size b of the nanoparticle ferroelectric ceramic is introduced into the constitutive relations above, the changed constitutive relations of nanoparticle ferroelectric ceramic with the particle size b are obtained:

$$D_i(b) = d_{ikl}(b)\frac{P^{r'}}{|P_s^r|}\sigma_{kl} + k_{ik}(b)E_k + f_d^L(b)P_i^r\,, \tag{20}$$

$$\varepsilon_{ij}(b) = s_{ijkl}(b)\sigma_{kl} + d_{kij}(b)\frac{P^{r'}}{|P_s^r|}E_k + f_d^L(b)\varepsilon_{ij}^r(b)\,. \tag{21}$$

In the uniaxial case nanoparticle ferroelectric ceramic which is poled and loaded in x_3-direction we obtain from (16–17)

$$D_3(b) = k_{33}(b)E_3 + f_d^E(b)P_3^r(b)\,, \tag{22}$$

$$\varepsilon_{33}(b) = d_{333}(b)f_d^E E_3 + f_d^E(b)\varepsilon_{33}^r(b)\,. \tag{23}$$

It shall be mentioned that the domain switching volume fraction $f_d^E(b)$, strictly speaking, depends on the particle size b. The respective relation initially is not known. Experimental results [12] for nanoparticle ferroelectric ceramic indicate that the coercivity of the material does not noticeable change with grain size. Therefore, since f_d^E is mainly related to coercivity [16], the evolution of $f_d^E(b)$ in this paper is assumed to be the same as Eq. 14.

In case when the nanoparticle ferroelectric ceramics after the polarization is mechanically loaded by the stress σ_{33}, the ferroeleastic constitutive response is given by

$$\varepsilon_{33}(b) = s_{333}(b)\sigma_{33} + f_d^\sigma(b)\varepsilon_{33}^r(b)\,, \tag{24}$$

$$D_3(b) = d_{333}(b)f_d^\sigma(b)\sigma_{33} + f_d^\sigma(b)P_3^r(b)\,. \tag{25}$$

5 Results

In order to study the size effect, the material data of PLZT8/65/35 have been introduced into the model as basic parameters, see [17] and Table 1.

The remaining parameters were determined as follows: according to experimental results in [12], the thickness of the interface phase has been determined as approximately $c = 2\,\text{nm}$. In addition, the permittivity of the interface phase is much lower than of inner ferroelectric phase. Taking the results in [12], $k_{33}(II) = 0.03\,k_{33}(I)$ is obtained. Applying the relationship between the piezoelectric coefficient and permittivity, the relationship of piezoelectric coefficient between interface phase and ferroelectric phase has been determined as $d_{333}(II) = 0.1\,d_{333}(I)$. According to the calculation of the effective elastic modulus of general nanoparticle materials by Wang [18], the elastic compliance is estimated as $s_{3333}(II) = 3\,s_{3333}(I)$ in this paper. Using these data, the dependence of the effective constants and the constitutive relations on the grain size b have been calculated. The results are shown in Figs. 3–6.

Table 1 Material parameters

Piezoelectric coefficient	d_{33}	$1188 \cdot 10^{-12}$ m/V
Dielectric permittivity	k_{33}	$5.625 \cdot 10^{-8}$ F/m
Coercive electric field	Eco	0.36 MV/m
Remanent polarization	P_0^r	0.25 C/m^2
Remanent strain	ε_{33}^r	0.00144
Activation electric field	b^E	0.0117 MV/m

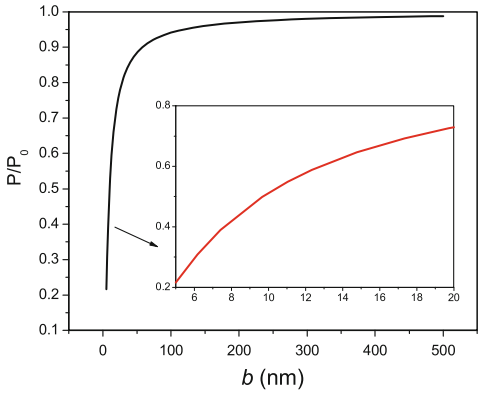

Fig. 3 The relation between spontaneous polarization and grain size

In Fig. 3 the dependence of the spontaneous polarization P on b is displayed in the grain size range of 5–500 nm. Here P is normalized by the macroscopic value P_0 where no interface phase is taken into account. With decreasing grain size the spontaneous polarization decreases what agrees well with experimental observations [18, 19]. In the grain size range from 500 to 100 nm, the decrease of P is relatively small while in the range from 100 to 20 nm the decrease is considerable. In the the grain size range from 20 to 5 nm, spontaneous polarization changes rapidly, the size effect here is most dominant.

The dependence of normalized permittivity, piezoelectric coefficient and elastic compliance on b are shown in Fig. 4a–c. Again, k_{33}^0, d_{33}^0 and s_{3333}^0 are the respective macroscopic (size-independent) values. The permittivity and piezoelectric coefficient decrease with decreasing grain size what is in qualitative agreement with experimental results [14]. In contrast, the compliance increases with decreasing grain size. The reason for that is the higher compliance of the outer interface phase compared to the inner ferroelectric phase and the assumed constant thickness of the outer phase. Up to now there are no experimental results available which may be used for a verification of this trend. The theoretical results imply that the size effect is most significant when the grain size of the material is less than 20 nm.

In Fig. 5 the dielectric hysteresis D_3 versus E_3 is depicted for three different grain sizes. For the grain size of 200 nm the hysteresis loop virtually coincides with the macroscopic one in [17]. With decreasing grain size, the loop shrinks significantly. The height decrease is mainly caused by the decrease of remanent polarization. Since also the permittivity decreases with decreasing grain size, the slope at $E_3=0$, which is determined by the permittivity, decreases too, i.e. the loops become more flat. These effects are most visible at the grain size of 5 nm when the remanent polarization and permittivity are reduced to 21.6 and 23.6 percent of their macroscopic values. Similar dependencies of the hysteresis loop on the grain size have been observed in experiments [12].

The butterfly curve ε_{33} versus E_3 and anti-butterfly curve ε_{11} versus E_3 are shown in Figs. 6b, c. The trends are more or less the same as at the dielectric hysteresis loop. For $b = 200$ nm the curves represent essentially the macroscopic case.

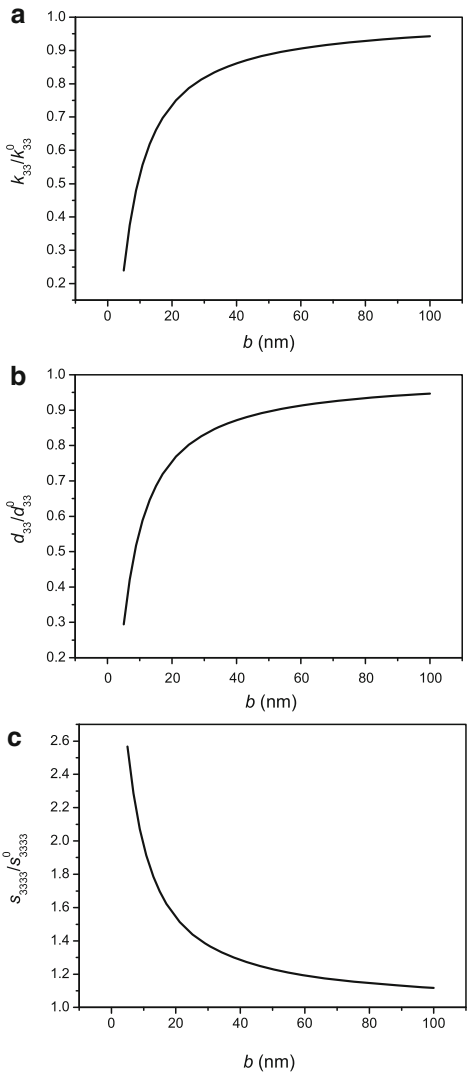

Fig. 4 Dependence on grain size: (**a**) permittivity, (**b**) piezoelectric coefficient, (**c**) compliance

With decreasing grain size the butterfly curve continuously shrinks and its center is shifted downwards. Furthermore, the "long tail" disappears at $b = 5$ nm. Similar tendencies can be observed at the anti-butterfly curve.

As already mentioned, there are no experimental data available regarding the dependence of the ferroelastic behavior on grain size. The corresponding predictions of the model are shown in Fig. 7a, b. The nonlinear part of the stress-strain relationship in Fig. 7a for a grain size of 200 nm is nearly the same as on the

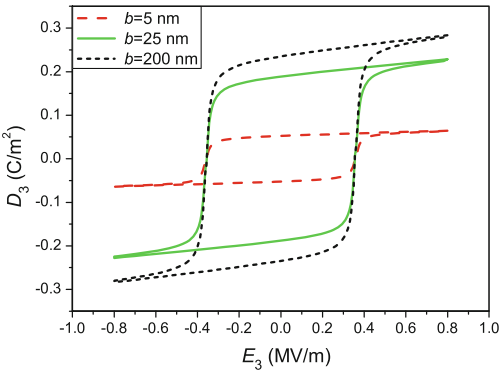

Fig. 5 Dependence on grain size: Dielectric hysteresis

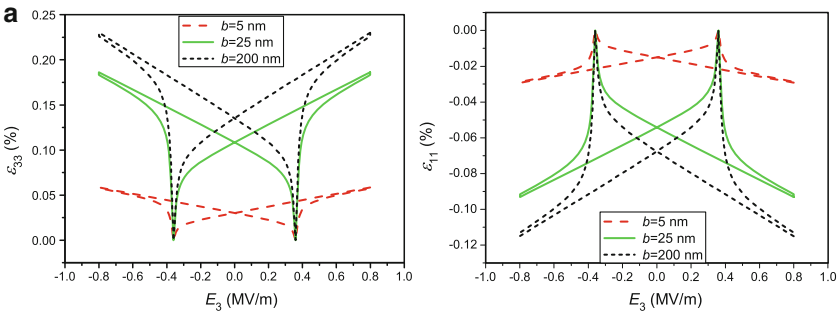

Fig. 6 Dependence on grain size: (**a**) butterfly curve, (**b**) anti-butterfly

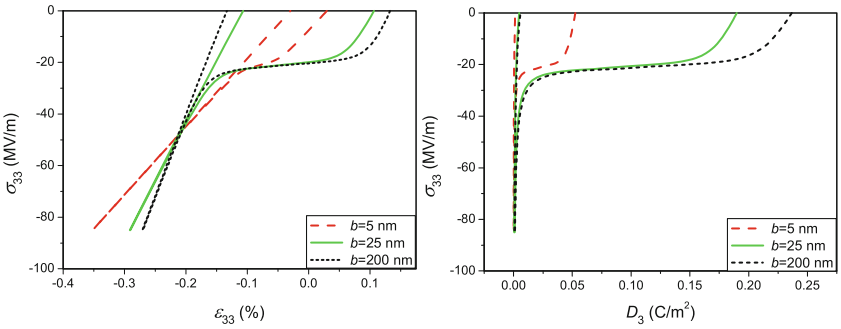

Fig. 7 Dependence on grain size: (**a**) stress-strain curve, (**b**) depolarization curve

macro-scale. With decreasing grain size the spontaneous strain decreases, resulting in a weaker nonlinearity. From the depolarization curves in Fig 7b it can be seen that the electric displacement caused by strain decreases with decreasing grain size. Thus, the nonlinearity of the curves will be weakened. Both, the stress-strain and the depolarization curves, clearly show that with decreasing grain size the saturation stress will be reduced.

Summarizing all results for this specific example, the size effect is small and negligible for grain sizes larger than 200 nm. In this case the volume fraction of the interface phase may be disregarded and the constitutive relations of ferroelectric ceramics coincide approximately with those on the macro-scale. In contrast, when the grain size is dozens of nanometers to several nanometers, the size effect is most significant. With decreasing grain size ferroelectricity, permittivity and piezoelectric coefficient decrease while elastic compliance increases and the nonlinear response of the resulting hysteresis loop, butterfly curve, stress-strain curve and electric displacement curve become weaker.

Finally it shall be mentioned that the grain size also influences the domain structure of the ferroelectric ceramic. While in conventional ferroelectric ceramics there are usually more than one domains in a grain, the number of domains may be reduced to only one for small grain sizes. This is supported by experiments on barium titanate ceramics [21]. It is well known that the domains have a remarkably impact on the ferroelectric phase transition behavior. The existence of domain walls may lead to a decrease of the Curie temperature and a reduction of the spontaneous polarization [22]. These effects have not been taken into account in this paper. In addition, the interaction of the neighboring grains has been ignored which might be influential. Therefore, the proposed model is only of qualitative or semi-quantitative nature and must be improved and linked to further experiments in future work.

6 Summary

This paper is based on the micro structure of nanoparticle ferroelectric ceramic. The important role of the interfacial layer has been taken into account in a two-phase model consisting of a ferroelectric phase and a non-ferroelectric phase. From the model, the constitutive relation of nanoparticle ferroelectric ceramics have been deduced. The results show that the effective electro-elastic constants and the constitutive behavior of nanoparticle ferroelectric ceramics exhibit size effect. When the grain size is dozens of nanometers to several nanometers, the size effect is most dominant. Under electric loading, with decreasing grain size, the hysteresis loop and butterfly curve of the material continuously shrinks, and the nonlinearity is gradually weakened. The predicted results are consistent with the experimental trends. Also the constitutive behavior under the mechanical loading has been studied. The results show that the stress-strain curve and the electric displacement curve are strongly dependent on the grain size.

Acknowledgements This project was supported by the Alexander von Humboldt Foundation, FRG, by the NSFC-No. 10572067, 10772093 and the NBRPC 973 program 2007-CB-936803, China.

References

1. Ye L (1998) Achievement of research and respect of the application of superplasticity for ceramic materials. Guide Report Mater 5:33–36 (in Chinese)
2. Chen IW, Wang XH (2000) Sintering dense nano-crystalline ceramics without final stage grain growth. Nature 404:168–171
3. Ahn CH, Rabe KM, JM Triscone (2004) Ferroelectricity at the nanoscale: Local polarization in oxide thin films and heterostructures. Science 303:488–491
4. Kanno I, Kotera H, Matsunaga T et al (2005) Intrinsic crystalline structure of epitaxial $Pb(Zr,Ti)O_3$ thin films. J Appl Phys 97:074101
5. Yashima M, Hoshina T, Shimura D et al (2005) Size effect on the crystal structure of barium titanate nanoparticles. J Appl Phys 98:014313
6. Kim YK, Kim SS, Shin H et al (2004) Thickness effect of ferroelectric domain switching in epitaxial $PbTiO_3$ thin films on Pt(001)/MgO(001). Appl Phys Lett 84:5085–5087
7. Svalov AV, Vas'kovskiy VO, Kurlyandskaya GV et al (2006) Structural peculiarities and magnetic properties of nanoscale terbium in Tb/Ti and Tb/Si multilayers. Chin Phys Lett 23(1):196–199
8. Sepliarsky M, Stachiotti MG, Migoni RL (2005) Surface reconstruction and ferroelectricity in $PbTiO_3$ thin films. Phys Rev B 72:014110
9. Wang GF (2001) Some problems of interfacial mechanics by strain gradient theory. PhD Thesis, Tsinghua University, Beijing (in Chinese, Abstract in English)
10. Hoshina T (2006) Size and temperature induced phase transition behaviors of barium titanate nanoparticles. J Appl Phys 99(3):054311
11. Shaw TM, McKinstry ST, McIntyre PC (2000) The properties of ferroelectric films at small dimensions. Annu Rev Mater Sci 30:263–298
12. Frey MH, Xu Z, Han P et al (1998) The role of interfaces on an apparent grain size effect on the dielectric properties for ferroelectric barium titanate ceramics. Ferroelectrics 206 (1–4):337–353
13. Shaw TM, McKinstry ST, McIntyre PC (2000) The properties of ferroelectric films at small dimensions. Annu Rev Mater Sci 30:263–298
14. Arlt G (1985) Dielectric properties of fine grained barium titanate ceramics. J Appl Phys 58:1619–1625
15. Deng X (2006) An investigation of processing-microstructure-performance for nan0-$BaTiO_3$ ceramics. PhD Thesis, Tsinghua University, Beijing (in Chinese, Abstract in English)
16. Mehling V, Tsakmakis Ch, Gross D (2007) Phenomenological model for the macroscopical material behavior of ferroelectric ceramics. J Mech Phys Solids 55:2106–2141
17. Yu L,Yu S and Feng X (2007) Effects of electric fatigue on the butterfly curves of ferroelectric ceramics. Mater Sci Engg A A459:273–277
18. Ishikawa K, Yoshikawa K, Okada N (1988) Size effect on the ferroelectric phase transition in $PbTiO_3$ ultrafine particles. Phys Rev B 37(10):5852–5855
19. Zhong WL, Jiang B, Zhang PL et al (1993) Phase transition in $PbTiO_3$ ultrafine particles of different sizes. J Phys Condensed Matter 5:2619–2624
20. Wang GF, Feng XQ, Yu SW (2002) Effective elastic moduli and interface effects of nanocrystalline materials. Chinese Sci Bull 47(17):1493–1496
21. Buscaglia MT, Viviani M, Buscaglia V et al (2006) High dielectric constant and frozen macroscopic polarization in dense nanocrystalline $BaTiO_3$ ceramics. Phys Rev B 73:064114
22. Lupascu DC, Verdier C (2004) Fatigue anisotropy in lead-zirconate-titanate. J Eur Ceram Soc 24:1663–1667
23. Lines ME, Glass AM (1977) Principles and applications of ferroelectrics and related materials. Oxford University Press, Oxford

An Optimization-Based Computational Model for Polycrystalline Ferroelastics

Faxin Li

Abstract An optimization-based computational model is proposed for domain reorientation in polycrystalline ferroelastics. In this model, a polycrystalline ferroelastics is made up of numerous, random oriented grains, with each grain consisting of N types of domains. Under any prescribed loading condition, the fraction of each domain in a specific grain is obtained via an optimization process to minimize the free energy of the total grain. The mechanical constraint from neighboring grains is considered in an Eshelby inclusion manner. This model has the similar superiority as the phase field model that does not impose any priori domain-switching criterion. Meanwhile, the computational complexity of this model is fairly small and affordable in 3-D cases using numerous grains. Furthermore, this model can reproduce very well the Taylor's rule of plasticity. Simulation results on tetragonal, rhombohedral and morphotropic PZT ceramics show the superiority and efficiency of this model. The domain texture evolution can also be calculated.

1 Introduction

Ferroelastics, including shape memory alloy (SMA), ferroelectrics, ferromagnetics, etc, are such materials in which multi-variants or multi-domains (each having a distinct spontaneous strain) can arise below a certain temperature and the domains can be oriented by applied stress. In SMA [1], the ferroelastic property is exhibited by the martensitic–austenitic phase transformations and martensitic variants reorientations under applied stress. The shape memory effect (SME) is actually generated by the ferroelastic properties although we usually do not use the terminology "ferroelastic" in SMA. While in ferroelectrics or ferromagnetics, the ferroelastic property usually accompanies ferroelectricity or ferromagnetism, thus it may sometimes be considered as a secondary effect.

F. Li (✉)
State Key Lab for Turbulence and Complex Systems, College of Engineering,
Peking University, Beijing, 100871, China
e-mail: lifaxin@pku.edu.cn

M. Kuna and A. Ricoeur (eds.), *IUTAM Symposium on Multiscale Modelling of Fatigue, Damage and Fracture in Smart Materials*, IUTAM Bookseries 24,
DOI 10.1007/978-90-481-9887-0_8,

Note that even in ferroelectrics or ferromagnetics, the ferroelastic properties can also exist independently and exhibit without the aids of ferroelectricity or ferromagnetism. The ferroelastic property is very important for sure because of the well-known SME in SMA. Besides, as the ferroelastic property is directly related to strain variations in materials, it is quite important in various actuator applications.

As ferroelastics is usually not mentioned independently, specific studies on it are very few. While modeling domain evolutions in ferroelectrics has received intensive attentions in recent years [2–5], among which the phase field model (PFM) [4, 5] seems more promising. The phase field model does not impose any priori domain switching criterion and domain switching is a natural process during minimizing the total free energy of the whole material system. The PFM had achieved great success in modeling domain evolution in ferroelectric single crystals, while applications in polycrystalline ferroelectrics are very few [5], probably because of the difficulties in addressing the complicated interactions between grains and the computational complexity in three dimensional cases.

In single-crystal ferroelastics, domain reorientation is relatively easy to accomplish thus a single domain state can exist, while this may be quite difficult in polycrystalline because of the mechanical constraint from neighboring grains. The recoverable strain in SMA of various crystal symmetries have been systematically addressed by Bhattacharya and Kohn [6], for both single crystals and polycrystals. The elastic interactions between grains are also crystal symmetry dependent. In our recent works [7], the elastic interactions in both tetragonal and rhombohedral ferroelectric ceramics are addressed by an analytical, constrained domain switching model. Note that in that model, a priori domain switching criterion and switching path must be prescribed and only uni-axial loading is allowed to get the analytical solution, thus it is not suitable for a general computational study of domain evolution in polycrystalline under arbitrary loading.

In this work, we propose an optimization-based computational model to study the domain evolution process in polycrystalline ferroelastics of arbitrary crystal symmetries. The total free energy in each grain is set as the optimization objective using the fractions of each type of domains as optimization variables. The optimization process is realized by the Complex Method for constrained optimization problem [8]. Like the PFM, this model also does not impose any priori domain switching criterion. Simulation results of this model can well fit the existing experiments. Furthermore, the model can reproduce the Taylor's rule of plasticity [9] very well.

2 Material Model

In this model, a polycrystalline ferroelastics is made up of numerous randomly oriented grains each of which contains N types of domains ($N = 3$ for the tetragonal case and $N = 4$ for the rhombohedral case), the fraction of each type of domains is denoted by f_i ($i = 1, 2, \ldots, N$) and obviously we have $\sum_{i=1}^{N} f_i = 1$.

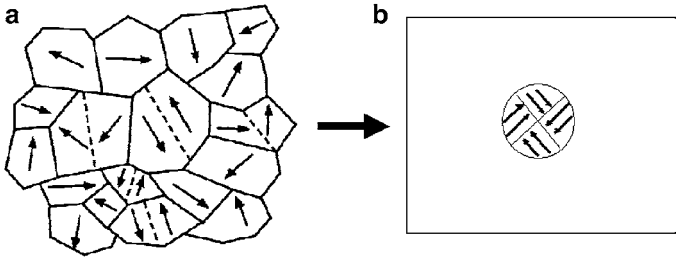

Fig. 1 2-D Illustration of material model: grains in polycrystalline ferroelastics (**a**), and spherical inclusion in a matrix (**b**)

The interactions between grains are considered in a self-consistent inclusion manner [10]. That is, each grain is regarded as an inclusion surrounded by an infinite large matrix with the materials properties same as the whole material, as shown in Fig. 1. As the spherical inclusion case is the simplest and no evidence can prove that other shapes of inclusion are more accurate than the spherical, we use the spherical inclusion case in this model.

Furthermore, to grasp the major characteristics of domain switching and to make the computational complexity affordable, in the present model we also assume that a ferroelastic polycrystalline is elastically isotropic and shows linear elastic behavior unless domain switching occurs (i.e., all the nonlinear strains are caused by domain switching).

3 Free Energy of a Single Grain

We use the free energy of each grain as the optimization objective and repeat the optimization process over all grains to get the domain structures and properties of the whole material system. The free energy of a specific grain is expressed as

$$\begin{aligned} U(\mathbf{E},\boldsymbol{\sigma}) = &-\boldsymbol{\sigma} : \boldsymbol{\varepsilon}^r + \frac{1}{2}\frac{1}{2\mu(1+\nu)}\boldsymbol{\sigma} : \boldsymbol{\sigma} \\ &+\frac{1}{2}\cdot 2\mu\frac{7-5\nu}{15(1-\nu)}(\boldsymbol{\varepsilon}^r - \overline{\boldsymbol{\varepsilon}}):(\boldsymbol{\varepsilon}^r - \overline{\boldsymbol{\varepsilon}}) + f_{sw}\cdot W_{sw} \end{aligned} \tag{1}$$

Where σ is the applied stress, μ, ν the isotropic shear modulus and possion ratio. $\overline{\boldsymbol{\varepsilon}}$ is the mean strain of the whole material system or the matrix. W_{sw} and f_{sw} are the energy barrier (per volume) and fractions for ferroelastic domain switching, respectively. Note that in this paper, except for the case in morphotropic ferroelastics [11], the energy barrier for all types of ferroelastics switching is set as the same expression, i.e., $W_{sw} = S_0\sigma_C$, where S_0 is the single crystal deformation, $S_0 = S_{lattice} = c/a - 1$ for the tetragonal, while $(8/9)S_0 = S_{lattice} = d_{[111]}/d_{[11\bar{1}]} - 1$ for the rhombohedral [7], σ_C is the nominal coercive stress. In ferroelastics near the morphotropic phase boundary (MPB), the energy barrier for all types of domain

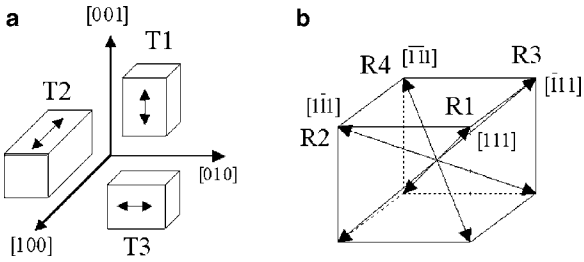

Fig. 2 Domains in (**a**) tetragonal and (**b**) rhombohderal ferroelastics

switching is set as the same value as that in the rhombohedral. The domain switching fraction, f_{sw}, is calculated as follows:

$$f_{sw} = \frac{1}{2}\sum_{i=1}^{N}\left|f_i - f_i^0\right| \tag{2}$$

where f_i^0 is the fraction of the ith domain calculated at last loading step.

$\boldsymbol{\varepsilon}^r$ is the remnant strain of a grain which can be expressed as linear functions of the domain fractions.

$$\boldsymbol{\varepsilon}^r = \sum_{i=1}^{N} f_i \boldsymbol{\varepsilon}^i \tag{3}$$

Where $\boldsymbol{\varepsilon}^i$ is the spontaneous strain tensor of the ith domain, the three types of domains in tetragonal ferroelastics and four types of domains in the rhombohderal are illustrated in Fig. 2.

In the expression of the Free Energy Eq. (1), the first item on the right side is the potential energy, the second item is the linear elastic strain energy; the third item is the inclusion strain energy or misfit strain energy; and the last item is the dissipation energy for domain switching.

4 Optimization Methodology

The optimization problem in this model can be written as:

$$\begin{aligned} &\text{Min} && U(f_1, f_2, \cdots, f_N) \\ &\textbf{Problem I } s.t. && 0 \le f_i \le 1 \ (i = 1, 2, \cdots, N) \\ &&& \sum_{i=1}^{N} f_i = 1 \end{aligned}$$

As the free energy is a nonlinear function of domain fractions, **Problem I** turns to be a constrained nonlinear optimization problem. To solve this type of optimization

problem, the Complex Method by Box [8] is a very effective algorithm with high accuracy and quick convergence. As the expression of the free energy varies from grain to grain and depends on the applied loading, at each loading step, the optimization process is repeated over all grains and the domain structures as well as the switching strain are calculated.

5 Results and Discussions

Both tetragonal and rhombohdral single-phase PZT ceramics, and PZT ceramics near the morphotropic phase boundary (MPB) where tetragonal phase and rhombohedal phase coexist, under uniaxial compression/tension are simulated using the proposed optimization model. The materials constants used in the simulations are listed in table referring to Ref. [12] but with slight modifications because of the isotropic elastic assumptions. For a better comparison, the elastic properties and the nominal coercive stress of all types of ceramics are taken to be the same as they did not differ much in reality.

5.1 Tetragonal PZT

Figure 3 shows the switching strain vs. stress curves of tetragonal PZT ceramics under uniaxial tension and compression up to 350 MPa ($5\sigma_C$). The switching strain under tension and compression is symmetric and very small. The maximum switching strain in both cases is about 0.1% and the remnant strain is only about

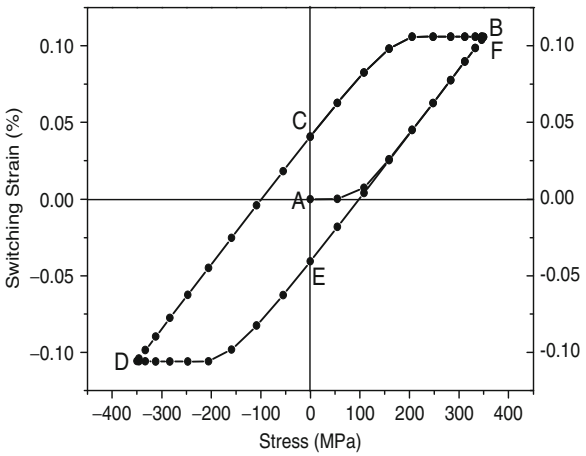

Fig. 3 Switching strain–stress curves of tetragonal PZT ceramics under uniaxial tension and compression

0.04%. The switching strain even under a high stress ($5\sigma_C$) is far from saturation, indicating that ferroelastic domain switching in tetragonal PZT ceramics is very difficult. These results fit well with the experimental results on tetragonal PZT ceramics and $BaTiO_3$ ceramics [13].

To show the domain texture evolution process, the pole figure [14] of the elongation axis, i.e., (001) for the tetragonal grains is calculated at each loading step. Under electric loading or uni-axial compression (tension), the pole figure of the elongation axis is axisymmetric around the loading axis and thus can be described by an angular distribution function $g(\theta)$ $(0 \leq \theta \leq \pi/2)$ [15], $g(\theta) \equiv 1$ for the random uniform distribution and the normalization condition requires

$$\int_0^{\pi/2} g(\theta) \sin\theta d\,\theta = 1 \tag{4}$$

From its definition, it can be seen that $g(\theta)$ completely depends on ferroelastic domain switching. In this paper, $g(\theta)$ is calculated using 10,000 grains and dividing the interval of [0, 90°] into eighteen subintervals each with equal length 5°. The accumulated domain fractions at all these subintervals give rise to $g(\theta)$ at discrete values of θ.

Figure 4 shows the calculated pole figure of (001) axis in tetragonal PZT ceramics under different loading points referring to Fig. 3. For convenience, in Figs. 3 and 4, we name State A as Initial State, B-Tension Saturated State, C-Tension Remnant State, D-Compression Saturated State, E-Compression Remnant State, F-Repeated Tension Saturated State. Compared to the initial random state A, the domain textures at the saturated states (B, D and F) changed to some extent but is still far from the saturated domain texture [15]. The remnant domain textures at State C and State E does not change much from the initial State A, which coincides

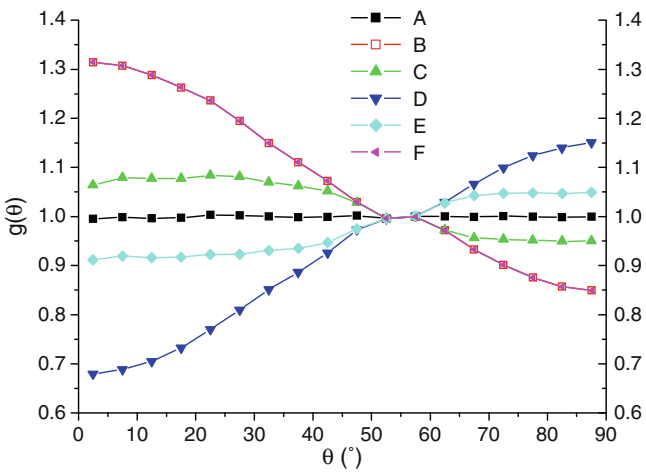

Fig. 4 Domain textures of tetragonal PZT ceramics under uniaxial tension and compression

well with the little remnant strain in Fig. 3. The symmetric domain textures under tension and compression in Fig. 4 are also consistent with the symmetric switching strains in Fig. 3.

5.2 *Rhombohedral PZT*

Figure 5 shows the switching strain–stress curve and domain textures of rhombohedral PZT ceramics under uniaxial tension and compression up to 350 MPa. Quite different from that in the tetragonal PZT ceramics, considerable amount of switching strain can be realized in rhombohedral PZT ceramics. Moreover, the switching strains under uniaxial tension and compression are not symmetric. The positive switching strain under maximum tension is about 0.25% while the negative strain under maximum compression is only about −0.16%. The asymmetric deformation of ferroelastic materials under tension and compression is due to the asymmetric spontaneous strain of ferroelastic domains which is $2S_0/3$ for elongation and $-S_0/3$ for contraction. The asymmetry of mathematically saturated strains under uniaxial tension and compression has been shown before [15]. Since the switching strains under maximum stress in Fig. 5a is approaching the mathematically saturated values (0.31% for tension and −0.21% for compression) [15], they should share the similar asymmetric properties. However, in Fig. 5a, the remnant strains under tension and compression are almost the same, which is about 0.12%.

The domain textures of rhombohedral PZT ceramics, seen in Fig. 5b, are also quite different from that in tetragonal PZT ceramics in Fig. 4. The domain textures of rhombohedral PZT ceramics changed a lot from its initial unpoled state. The domain texture $g(\theta)$ reaches the saturated value 4 at the Tension Saturated State B and the Repeated Tension Saturated State F. After removing the tensile stress, some fractions of back switching occurs, which can be clearly seen from the domain texture evolution from State B to State C. When under maximum uniaxial compression,

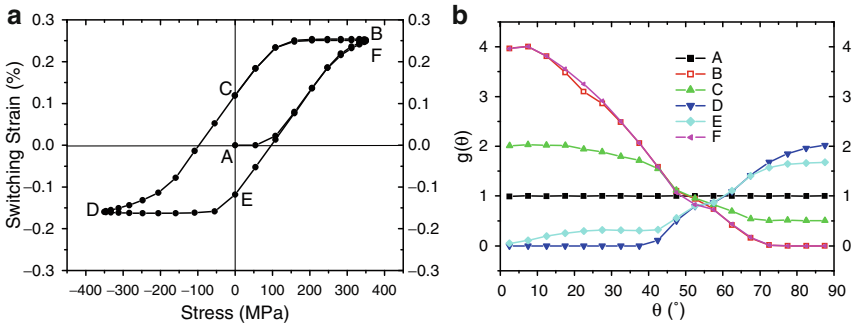

Fig. 5 (**a**) Switching strain–stress curve and (**b**) domain textures of rhombohedral PZT ceramics under uniaxial tension and compression

most domains switch to a state with its elongation axis forming a large acute angle to the compressive direction. When removing the compressive stress, the domain texture at State E does not change much from that at the Compression Saturated State D, indicating little back ferroelastic switching occurs, which is consistent with the small strain variations from Point D to Point E in Fig. 5a.

5.3 *Morphotropic PZT*

Figure 6 shows the simulated switching strain-curve and domain textures of morphotropic PZT under uniaxial tension and compression. It can be seen from Fig. 6a that, similar with the rhombohedral case in Fig. 5a, the switching strain under maximum tension (about 0.62%) is considerably larger than that under maximum compression (0.4%). While different from that in Fig. 5a, the remnant switching strain under tension (about 0.5%) is also larger than that under compression (about 0.35%). The back ferroelastic switching in morphotrpic PZT ceramics upon removing the applied stress is not so evident as that in the rhombohedral and tetragonal PZT which may indicates that the internal stress caused by ferroelastic switching in morphotropic PZT ceramics is not very large.

The domain textures of morphotropic PZT ceramics under applied stress in Fig. 6b shows that under maximum tension at State B and F, as expected, most domains will switch to a state with their elongation axis as close as possible to the tensile direction. After removing the uniaxial tension, some domains lie down to their initial states, making the curve C slightly lower than Curve B within the small angle range (say $\theta < 30°$). Under maximum uniaxial compression, the maximum value of $g(\theta)$ at 90° is only about 3, considerably smaller than the mathematically saturated value of 7, which may indicate that it is more difficult to approach the saturated domain orientation state under uniaxial compression.

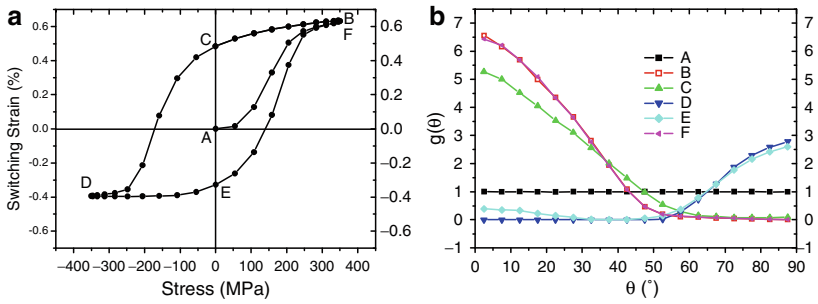

Fig. 6 (**a**) Switching strain–stress curve and (**b**) domain textures in morphotropic PZT ceramics under uniaxial tension and compression

Table 1 Material constants of tetragonal and rhombohedral PZT used in the model

Material constants	Rhombohedral	Tetragonal
Shear modulus μ (GPa)		30
Poisson's ratio v		0.3
Single crystal deformation S_0 in single-phase PZT	0.73%	2.77%
Single crystal deformation S_0 in morphotropic PZT	1.0%	2.0%
Coercive stress σ_C (MPa)		70

5.4 Reproduction of the Taylor Rule of Plasticity

It can be seen from Figs. 3, 5a, and 6a that the remnant switching strain of the morphotropic PZT (0.5% under tension and 0.35% under compression) is much larger than that of the tetragonal (0.04%) and rhombohedral PZT (0.12%). The remnant strain in polycrystalline ferroelastics is crystal symmetry dependent. According to the Taylor's rule of plasticity [9], a crystal must have at least five slip systems for a polycrystalline to be ductile. In terms of the deformation modes, a tetragonal ferroelastic crystal has two independent slip systems and a rhombohedral ferroelastic crystal has three. Thus the tetragonal and rhombohedral PZT ceramics are brittle materials from this sense. While in PZT ceramics near the MPB, there are totally six independent deformation modes, which make the material to be ductile. Then ferroelastic domain switching does not generate very large internal stress from neighboring grains and can be almost completely accomplished [11].

According to Taylor's rule of plasticity, the remnant switching strain for tetragonal and rhombohedral PZT ceramics should be zero. The simulation results can follow this rule very well. In fact, the existence of the remnant strain in the tetragonal and rhombohedral PZT is due to the large coercive stress (70 MPa). If using a very small switching stress, the simulated remnant strain will reduce to almost zero, leading to the vanishing strain–stress hysteresis curves. The remnant strain of the morphotropic PZT ceramics, however, is not zero and can be estimated from the Taylor bound [6] which give the lower limit. The Taylor bound of remnant strain can be calculated using the proposed model by prescribing the isotropic elastic modulus to be infinitely large and the coercive stress to be infinitely small. For the morphotropic PZT ceramics with material parameters listed in Table 1, the Taylor bound of remnant switching strain is 0.32% under tension and 0.22% under compression, which, as expected, are smaller than the remnant strain in real cases. The proposed model can thus reproduce the Taylor's rule of plasticity very well.

6 Conclusions

In summary, we proposed an optimization-based computational model for domain evolution in polycrystalline ferroelastics. The model has the similar superiority as the PFM and a much smaller computational complexity thus is affordable in 3-D

cases using numerous grains. The domain textures evolution can also be calculated. Furthermore, the proposed model can reproduce the Taylor's rule of plasticity very well. Simulation results on tetragonal, rhombohedral and morphotropic PZT ceramics validate the superiority and efficiency of this model.

Acknowledgments This work is supported by the National Natural Science Foundation (Grant No.10872002) and the 985 Project Foundation of Peking University.

References

1. Otsuka K, Ren X (2005) Physical metallurgy of Ti-Ni-based shape memory alloys. Progress Mater Sci 50(5):511–678
2. Huber JE, Fleck NA, Landis CM et al (1999) J Mech Phys Solids 47:1663–1697
3. Li FX, Fang DN (2004) Simulations of domain switching in ferroelectrics by a three-dimensional finite element model. Mech Mater 36:959–973
4. Chen LQ (2002) Phase field models for microstructure evolution. Annu Rev Mater Res 32: 113–140
5. Schrade D, Mueller R, Xu B et al (2007) Domain evolution in ferroelectric materials: a continuum phase field model and finite element implementation. Comp Meth Appl Mech Eng 196(41–44):4365–4374
6. Bhattacharya K, Kohn RV (1996) Symmetry, texture and the recoverable strain of shape-memory polycrystals. Acta Mater 44:529–542
7. Li FX, Rajapakse RKND (2007) A constrained domain switching model for polycrystalline ferroelectric ceramics. Acta Mater 55, Part I-Model formulation and application to tetragonal materials, 6472–6480; Part II-Combined switching and application to rhombohedral materials, 6481–6488
8. Box MJ (1965) A new method of constrained optimization and a comparison with other methods. Comput J 8:42–52
9. Taylor GI (1938) Plastic strain in metals. J Inst Metals 62:307–324
10. Eshelby JD (1957) The determination of the elastic field of an ellipsoidal inclusion and related problems. Proc R Soc Lond A 241:376–396
11. Li JY, Rogan RC, Üstündag E et al (2005) Domain switching in polycrystalline ferroelectric ceramics. Nat Mater 4:776–781
12. Hoffmann MJ, Hammer M, Endriss A et al (2001) Correlation between microstructure, strain behavior, and acoustic emission of soft PZT ceramics. Acta Mater 49:1301–1310
13. Berlincourt D, Krueger HHA (1959) Domain processes in lead titanate zirconate and barium titanate ceramics. J Appl Phys 30:1804–1810
14. Bunge HJ (1982) Texture analysis in materials science. Butterworth, Berlin
15. Li FX, Rajapakse RKND (2007) Analytically saturated domain orientation textures and electromechanical properties of ferroelectric ceramics due to electric/mechanical loading. J Appl Phys 101:054110

Modeling of Domain Structure Evolution in Ferroelectric Materials*

Ralf Müller, Bai Xiang Xu, David Schrade, and Dietmar Gross

Abstract A continuum phase field model is presented to simulate domain structures in ferroelectric single crystals. Special attention is given to domain structure evolution in the vicinity of crack tips. Using the spontaneous polarization as an order parameter the model is set up and implemented into a 2D finite element method. To evaluate crack driving forces the theory of configurational forces is extended to the phase field continuum and numerically realized within the finite element method.

Simulations show the influence of boundary conditions and system parameters on the development of certain domain structures. Calculations with combined electric and mechanical loadings display the complex interaction of the loading with the domain structure and the crack driving force.

1 Introduction

In ferroelectric materials the mechanical and electric fields are coupled by the constitutive behavior, which makes these materials highly interesting for actuator and sensor applications. A typical example are piezoelectric stack actuators, which are frequently used in automotive and machining applications. The microstructure of these materials manifests itself in so called domain structures, which are decisive for their electrical and electro-mechanical properties and thus for the application. These microstructures have been analyzed extensively in the literature (e.g. [4, 6, 10]). There are phenomenological material models which describe the

*The authors R. Müller and D. Schrade acknowledge the German Research Foundation for its financial support on the Collaborate Research Center 595. The author B.X. Xu is thankful for the financial support by the Alexander-von-Humboldt Foundation.

R. Müller (✉) and B.X. Xu
Chair of Applied Mechanics, Department of Mechanical and Process Engineering,
TU Kaiserslautern, Germany
e-mail: ram/baxiaxu@rhrk.uni-kl.de

D. Schrade and D. Gross
Division of Solid Mechanics, Department of Civil Engineering and Geodesy,
TU Darmstadt, Germany
e-mail: schrade/gross@mechanik.tu-darmstadt.de

M. Kuna and A. Ricoeur (eds.), *IUTAM Symposium on Multiscale Modelling of Fatigue, Damage and Fracture in Smart Materials*, IUTAM Bookseries 24,
DOI 10.1007/978-90-481-9887-0_9,

macroscopic material response by treating the remanent polarization in an average sense as an internal variable [6, 7, 10, 11]. Other models aim at resolving microstructural aspects by treating the domain wall as a sharp interface with zero thickness [15].

In this paper, a continuum phase field method is employed to model microstructure and ferroelectric behavior. Special focus is on simulating domain structures in the vicinity of cracks. The phase field model is a regularization of the sharp interface model presented in [15]. Therefore the main assumption is the choice of the spontaneous polarization as an independent order parameter. A thermodynamical analysis reveals the constitutive relations and an evolution law of Ginzburg–Landau type. A rigorous numerical implementation of the phase field model is achieved via the Finite Element Method in combination with an implicit time integration and nonlinear Newton iteration. Other works of phase field models for ferroelectric materials can be found in e.g. [1, 2, 19, 20, 22, 23].

In the fracture analysis the concept of configurational forces is extended to the phase field continuum, and this generalization enables us to evaluate the crack driving force in a ferroelectric material.

2 Modelling of Domain Structures and Cracks in Ferroelectric Materials

2.1 Continuum Phase Field Model

We assume that the body $\mathscr{B}$ with boundary $\partial\mathscr{B}$ is occupied by a ferroelectric solid. For the mechanical problem under quasi-static conditions the stress $\boldsymbol{\sigma}$ fulfills the equilibrium equation

$$\operatorname{div}\boldsymbol{\sigma} = \mathbf{0}. \tag{1}$$

Using linearized kinematics the strain is defined by

$$\boldsymbol{\varepsilon} = \frac{1}{2}\left(\operatorname{grad}\boldsymbol{u} + \operatorname{grad}^{\mathrm{T}}\boldsymbol{u}\right). \tag{2}$$

Two types of mechanical boundary conditions can be considered

$$\boldsymbol{\sigma}\boldsymbol{n} = \boldsymbol{t}^{*} \qquad \text{or} \qquad \boldsymbol{u} = \boldsymbol{u}^{*}, \tag{3}$$

where $\boldsymbol{t}^{*}$ and $\boldsymbol{u}^{*}$ are prescribed surface tractions and prescribed displacements.

The electrical field quantities satisfy the electrostatic equations. We introduce the electric displacement $\mathbf{D}$ which is governed by the Gauß law

$$\operatorname{div}\boldsymbol{D} = 0, \tag{4}$$

and the electric field $\boldsymbol{E}$ which is defined by

$$\boldsymbol{E} = -\text{grad}\varphi, \tag{5}$$

where φ is the electric potential. Possible electric boundary conditions are

$$\boldsymbol{D}\cdot\boldsymbol{n} = -Q^* \qquad \text{or} \qquad \varphi = \varphi^*, \tag{6}$$

where Q^* and φ^* are the prescribed surface charge density and electric potential, respectively.

To model the microstructures, which consist of domains and interfaces between them, the potential of the phase field model is additively split into three parts,

$$H = H^{\text{ent}} + H^{\text{sep}} + H^{\text{int}}, \tag{7}$$

where H^{ent} is the modified electric enthalpy, and H^{sep} and H^{int} are called the domain separation energy and the interface energy, respectively.

The electric enthalpy of the phase field potential reads

$$H^{\text{ent}} = \frac{1}{2}(\boldsymbol{\varepsilon}-\boldsymbol{\varepsilon}^0) : [\boldsymbol{C}(\boldsymbol{\varepsilon}-\boldsymbol{\varepsilon}^0)] - (\boldsymbol{\varepsilon}-\boldsymbol{\varepsilon}^0) : [\boldsymbol{b}^{\mathrm{T}}\boldsymbol{E}] - \frac{1}{2}\boldsymbol{E}\cdot(\boldsymbol{A}\boldsymbol{E}) - \boldsymbol{P}\cdot\boldsymbol{E}, \tag{8}$$

where $\boldsymbol{C}$ is the elastic stiffness tensor, $\boldsymbol{b}$ the piezoelectric tensor, and $\boldsymbol{A}$ the dielectric tensor. It is crucial that the spontaneous strain $\boldsymbol{\varepsilon}^0$ and the piezoelectric tensor $\boldsymbol{b}$ depend on the spontaneous polarization $\boldsymbol{P}$, see e.g. [5].

$$\boldsymbol{\varepsilon}^0(\boldsymbol{P}) = \frac{3}{2}\varepsilon_0\frac{\|\boldsymbol{P}\|}{P_0}\left(\boldsymbol{e}\otimes\boldsymbol{e} - \frac{1}{3}\mathbf{1}\right), \tag{9}$$

$$\begin{aligned} b_{kij}(\boldsymbol{P}) = \frac{\|\boldsymbol{P}\|}{P_0}\Big\{ & b_{\parallel}e_ie_je_k + b_{\perp}(\delta_{ij}-e_ie_j)e_k \\ & + b_{=}\frac{1}{2}\left[(\delta_{ki}-e_ke_i)e_j + (\delta_{kj}-e_ke_j)e_i\right]\Big\}, \end{aligned} \tag{10}$$

where $\boldsymbol{e} = \boldsymbol{P}/\|\boldsymbol{P}\|$ is the unit vector along $\boldsymbol{P}$, and $\varepsilon_0, P_0, b_{\parallel}, b_{\perp}, b_{=}$ are material parameters. In Eq. 10 index notation has been used for compact notation.

The domain separation energy term H^{sep} is mainly responsible for the formation of domains in the material. It allows for the representation of the ferroelectric states, as the four (six) energetically favorable variants in the case of 2D (3D) problems. To achieve this, H^{sep} is chosen to be a sixth order polynomial with respect to the spontaneous polarization. In the case of 2D problems the following expression is assumed:

$$H^{\text{sep}} = \kappa_{\text{s}}\frac{G}{\lambda}\left[1 + a_1\left(P_1^2+P_2^2\right) + a_2\left(P_1^4+P_2^4\right) + a_3P_1^2P_2^2 + a_4\left(P_1^6+P_2^6\right)\right], \tag{11}$$

where P_1 and P_2 are the Cartesian components of the spontaneous polarization $\boldsymbol{P}$ and a_i $(i = 1, 2, \ldots, 4)$ are parameters which specify the energy landscape, i.e. determine the energy for domains to switch from one variant to another. The domain separation energy achieves local minima at the four variants $(\pm P_0, 0)$ and $(0, \pm P_0)$. With a proper choice of the coefficient κ_s the parameter G represents the 180° domain wall energy, while λ is associated with the domain wall width. The choice of κ_s is related to the polynomial structure in Eq. 11. For details the reader is referred to [17, 18].

The domain wall energy H^{int} takes into account the energy stored in the domain walls due to the variation of the polarization in this localized zone. This energy contribution is assumed to have the form

$$H^{\mathrm{int}} = \kappa_\mathrm{i} \frac{G\lambda}{P_0^2} \|\mathrm{grad}\, \boldsymbol{P}\|^2, \tag{12}$$

where again a coefficient κ_i is introduced to relate G to the domain wall energy and λ to the domain wall width, see [17, 18]. Standard thermodynamic arguments yield the constitutive relations for the stress and electric displacement

$$\boldsymbol{\sigma} = \boldsymbol{C}(\boldsymbol{\varepsilon} - \boldsymbol{\varepsilon}^0) - \boldsymbol{b}^{\mathrm{T}} \boldsymbol{E}\,, \qquad \boldsymbol{D} = \boldsymbol{b}(\boldsymbol{\varepsilon} - \boldsymbol{\varepsilon}^0) + \boldsymbol{A}\boldsymbol{E} + \boldsymbol{P}. \tag{13}$$

Using the total energy (7), the following expression for the evolution of the order parameter $\boldsymbol{P}$ is obtained

$$\dot{\boldsymbol{P}} = -M \left(\frac{\partial H^{\mathrm{ent}}}{\partial \boldsymbol{P}} + \frac{\partial H^{\mathrm{sep}}}{\partial \boldsymbol{P}} - 2\kappa_\mathrm{i} \frac{G\lambda}{P_0^2} \Delta \boldsymbol{P} \right), \tag{14}$$

with Δ being the Laplace operator.

2.2 Finite Element Implementation

The numerical implementation remains similar to that presented in [16], except the phase field parameters need to be interpreted in a different way. The 2D implementation into a finite element method uses bi-linear plane elements which take two displacements components u_1, u_2, the electric potential φ and the spontaneous polarization P_1, P_2 as nodal degrees of freedom. Thus a four-node element possesses 20 degrees of freedom. The evolution equation (Ginzburg–Landau equation) is integrated implicitly in time. Details on this numerical integration in conjunction with a Newton method can be found in [16].

2.3 Configurational Force Method

To evaluate the driving force on a crack tip, we will utilize the concept of configurational forces. Following the ideas outlined in [3] and keeping in mind that the phase field potential depends on mechanical strain $\boldsymbol{\varepsilon}$, electric field $\boldsymbol{E}$ and spontaneous polarization $\boldsymbol{P}$, i.e.

$$H = H(\boldsymbol{\varepsilon}, \boldsymbol{E}, \boldsymbol{P}, \mathrm{grad}\boldsymbol{P}) \tag{15}$$

the gradient of H can be rearranged in the following way

$$\mathrm{div}\boldsymbol{\Sigma} + \boldsymbol{g} = \boldsymbol{0}, \tag{16}$$

in which the generalized configurational stress tensor $\boldsymbol{\Sigma}$ and the generalized configurational force $\boldsymbol{g}$ have the following form

$$\boldsymbol{\Sigma} = H\boldsymbol{1} - (\mathrm{grad}\boldsymbol{u})^{\mathrm{T}}\boldsymbol{\sigma} - \mathrm{grad}\varphi \otimes \boldsymbol{D} - (\mathrm{grad}\boldsymbol{P})^{\mathrm{T}}\frac{\partial H}{\partial \mathrm{grad}\boldsymbol{P}} \tag{17}$$

$$\boldsymbol{g} = -\left.\frac{\partial H}{\partial \boldsymbol{x}}\right|_{\mathrm{expl.}} - (\mathrm{grad}\boldsymbol{u})^{\mathrm{T}}\boldsymbol{f} + q\mathrm{grad}\varphi + \frac{1}{M}(\mathrm{grad}\boldsymbol{P})^{\mathrm{T}}\dot{\boldsymbol{P}}. \tag{18}$$

In the derivation of Eq.16 the other balance laws (1), (2) and (4), (5) together with the constitutive equation (13) and the evolution equation (14) have been used. It is possible to put the last term of Eq.18 as a pseudo momentum like quantity, see e.g. [9] on the left hand side to get a configurational force balance which resembles the structure of the balance of (physical) linear momentum. However in the following we will study only crack problems with stationary microstructures, i.e domain arrangements that had sufficient time to finish evolution. For these situations the last term involving $\dot{\boldsymbol{P}}$ can be neglected. Furthermore we will only analyze situations which are free of volume forces $\boldsymbol{f}$ and free of volume charges q, such that only the explicit derivative remains in Eq. 18. At the crack tip this is equivalent to the J-integral in its vectorial form, c.f. [9]. The computation of the discrete configurational force follows the techniques outlined for example in [13, 14]. After discretization with finite elements the discrete configurational force $\boldsymbol{G}^I$ at node I becomes

$$\boldsymbol{G}^I = \bigcup_{e=1}^{n_{el}} \int_{\Omega_e} \boldsymbol{\Sigma} : \mathrm{grad}N^I \, d\Omega, \tag{19}$$

where the assembly operation is performed over all elements adjacent to node I, and Ω_e is the corresponding area of these elements. The derivatives of the shape functions N^I can be computed in the same manner as for standard finite element techniques.

3 Numerical Results

3.1 Domain Structures in Single Crystals

In agreement with other works, it is found that the electric boundary conditions play an important role in the evolution and occurrence of certain microstructures. In Fig. 1d an initially random polarization distribution was prescribed. The boundary is assumed to be charge free, which forces the polarization vector to be aligned tangentially to the boundary. A non-aligned polarization vector causes extremely strong electric fields to satisfy the condition of charge free boundaries, which is energetically less favorable. Therefore the domain structure arranges in a vortex like structure, with four 90° domain walls and one 180° domain wall in the center. However with increasing the domain wall energy G the system is gradually going from the vortex structure to a structure with a reduced domain wall length, see Fig. 1a–c. The influence of the parameter λ which can be understood as the domain wall width, or the width of the regularized zone with a transition of the polarization vector, is depicted in Fig. 2. All simulations started from an arrangement with a 180° domain wall as sharp interface. The system is than relaxed until it reaches a stationary state. It is observed that the width of the transition layer between the

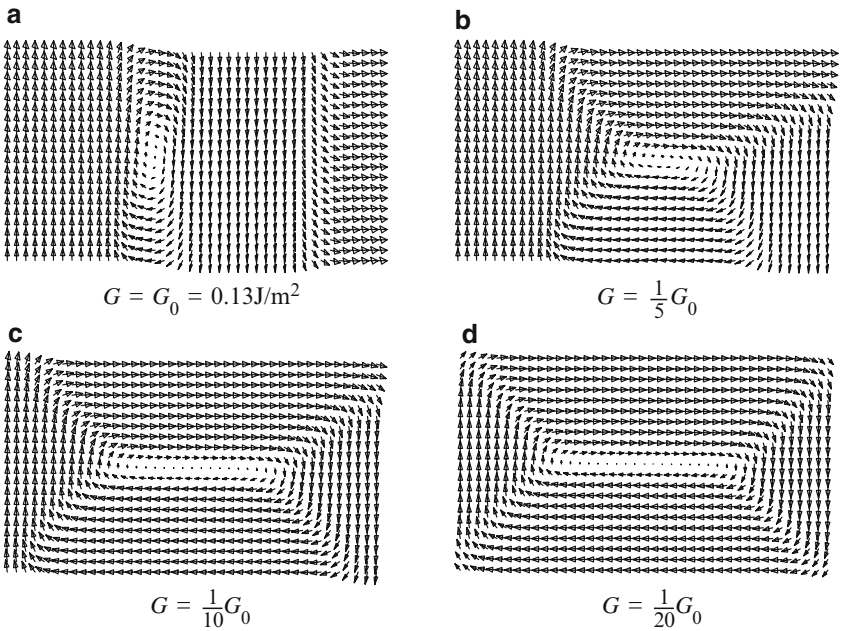

Fig. 1 Stationary domain structures for different domain wall energies. All simulations started from the same initial random distribution of polarizations

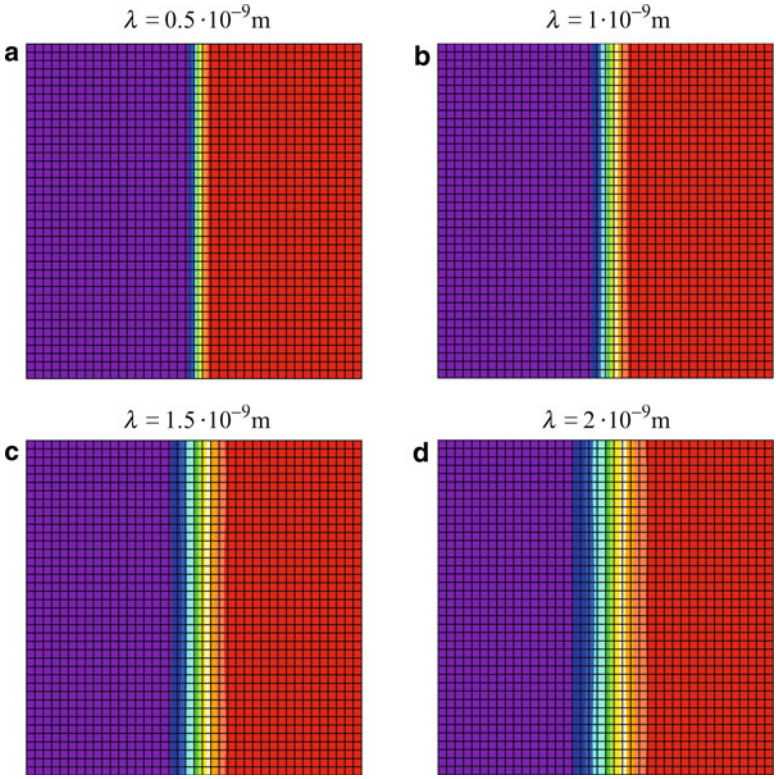

Fig. 2 Influence of the regularization parameter ε on the width of a 180° domain wall

two domains increases with the parameter λ. Especially from a computational point of view this is important, as the finite element mesh has to be sufficiently fine to resolve the gradients in the transition layer.

3.2 Domain Structures in the Vicinity of Crack Tips

In the vicinity of crack tips the domain structure is strongly influenced by the boundary conditions at the crack faces. In the following we will assume traction and charge free conditions on the crack surfaces. The electric boundary conditions on cracks in ferroelectric materials are subject to current research. However, this topic is not addressed here, as the main focus of the work is on the domain structures. Figure 3a shows the domain structure around a center crack. Initially the material was poled to the right. The crack is compatible with this poling state. By applying a mechanical tensile load in the vertical direction switching was initiated to produce the microstructure which is depicted in Fig. 3a. The mechanical load equally favors

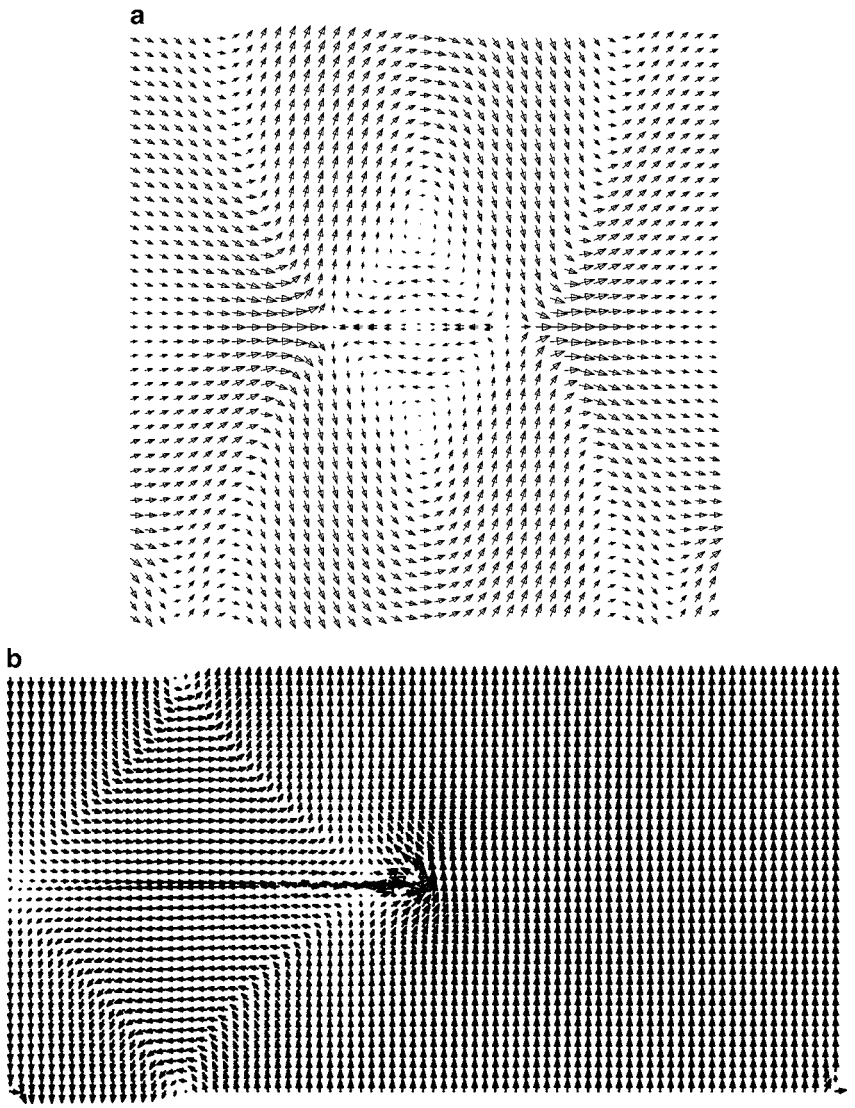

Fig. 3 Domain structures in the vicinity of crack tips: (**a**) center crack, and (**b**) edge crack

polarization vectors pointing up or down is equally, as both states are associated with the same spontaneous strain. Thus a microstructure of 90° domain walls at the crack tips and 180° domain walls in the top and bottom region is formed.

In Fig. 3b the domain structure at an edge crack is studied. Initially the material was poled downwards. By introduction of the edge crack and the application of an upward electric field, the polarization in front of the crack is switched. In conjunction with the charge free boundary conditions on the crack faces, again

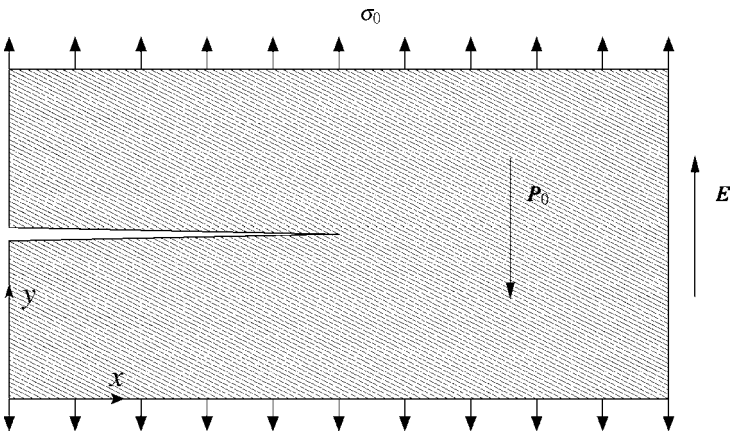

Fig. 4 Domain structures under combined electric and mechanical loading

four 90° domain walls appear. Only the very left part of the specimen still shows the initial downward polarization. Both examples show the fact that due to the presence of cracks the local switching behavior of the materials is strongly reduced or altered.

The third example is now taken to analyze the effect of an additionally applied vertical mechanical load. This introduces again mechanically triggered switching and leads to the domain structure shown in Fig. 4. To investigate a possible dependence of the domain structure on the finite element mesh in Fig. 5a–c different discretizations were used. It can be seen, that the rather complex stationary domain structure remains very similar for all three discretizations. The value of the configurational force at the crack tip, i.e. the crack driving force, is plotted in Fig. 6a for different meshes of Fig. 5. It is observed that the crack driving force is only moderately influenced by the mesh size. Thus the coarse discretization of $40 \times 80 = 3{,}200$ elements was chosen for the following analysis.

The crack driving force for an edge crack loaded in mode I by mechanical stresses is analyzed. Figure 6 depicts the crack driving force with and without an additional electric field. The cases of a field in the direction of initial polarization (parallel) and in the opposite direction of poling (anti-parallel) are studied. Figure 6b shows that a parallel electric field reduces the crack driving force, while an anti-parallel electric field promotes crack growth. This qualitative behavior is in agreement with the experimental results on single crystals documented in [21]. It can be explained by the following reasoning: By the piezoelectric effect a parallel electric field leads to an elongation of unit cells in front of the crack tip, thereby reducing the stresses and the crack tip loading. On the contrary, an anti-parallel field leads to enhanced stresses as the unit cells in front of the crack contract by the application of the electric field.

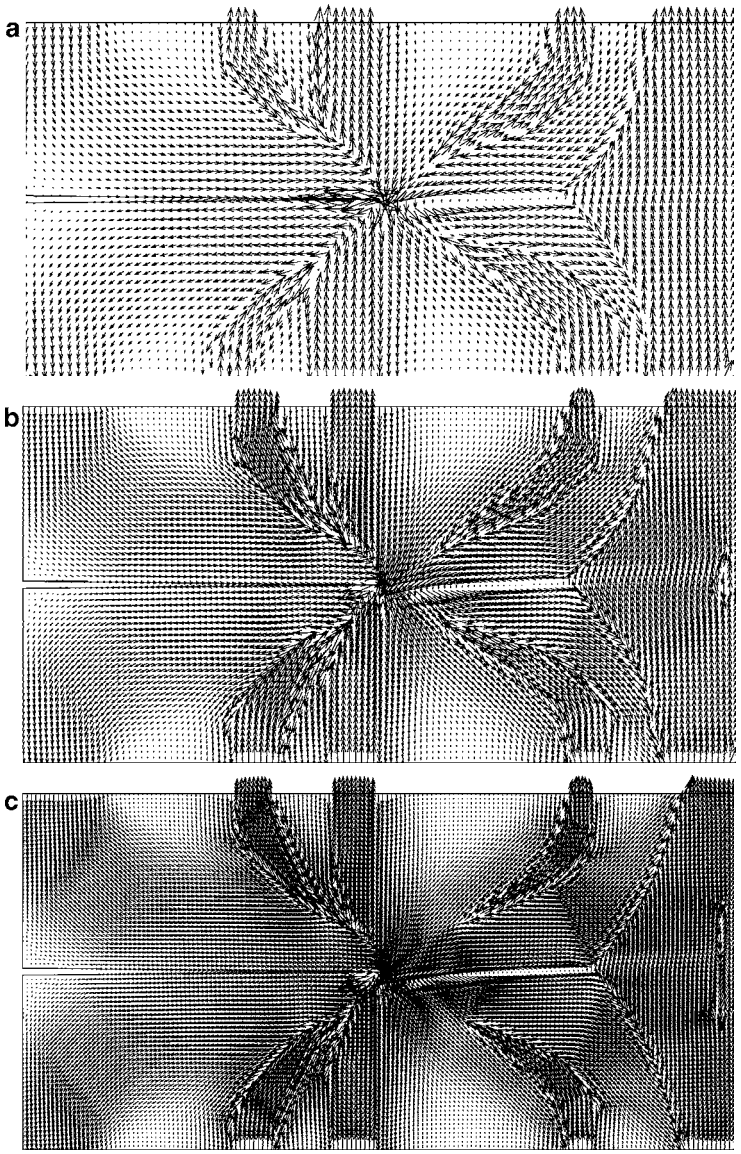

Fig. 5 Domain structures under combined electric and mechanical loading for different finite element meshes: (**a**) 40×80 elements, (**b**) 60×120 elements, and (**c**) 80×160 elements

4 Conclusion

The domain structures in the vicinity of the crack are strongly influenced by the electric boundary conditions at the crack flanks. The proposed continuum

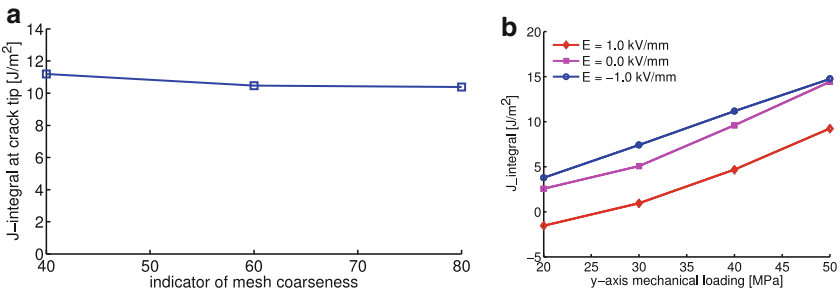

Fig. 6 Crack driving force: Influence of (**a**) mesh, and (**b**) applied electric field

phase field model can capture these microstructural effects. The implementation for two dimensional problems was carried out using the finite element method. The numerical scheme is robust and efficient due to an implicit time integration.

The concept of configurational forces was extended to the phase field continuum in order to compute discrete configurational forces. By this technique the crack driving force is readily available. The analysis of combined electric and mechanical loadings on an edge crack showed the formation of complex domain structures. Furthermore, the enhancement and reduction of the crack driving force by an antiparallel or a parallel electric field is investigated.

References

1. Bhattacharya K, Ravichandran G (2003) Ferroelectric perovskites for electromechanical actuation. Acta Mater 51:5941–5960
2. Chen LQ (2008) Phase-field method of phase transitions/domain structures in ferroelectric thin films: A review. J Am Ceram Soc 91(6):1835–1844
3. Eshelby JD (1970) Energy relations and the energy-momentum tensor in continuum mechanics. In: Kanninen MF (ed) Inelastic behaviour of solids. McGraw Hill, New York, pp 77–115
4. Hwang SC, Huber JE, McMeeking RM, Fleck NA (1998) The simulation of switching in polycrystalline ferroelectric ceramics. J Appl Phys 84(3):1530–1540
5. Kamlah M (2001) Ferroelectric and ferroelastic piezoceramics – Modeling of electromechanical hysteresis phenomena. Continuum Mech Thermodyn 13:219–268
6. Kamlah M, Bohle U (2001) Finite element analysis of piezoceramic components taking into account ferroelectric hysteresis. Int J Solids Struct 38(4):605–633
7. Kamlah M, Liskowsky AC, McMeeking RM, Balke H (2005) Finite element simulation of a polycrystalline ferroelectric based on a multidomain single crystal switching model. Int J Sol Struct 42(9–10):2949–2964
8. Kienzler R, Herrmann G (2000) Mechanics in material space with applications in defect and fracture mechanics. Springer, Berlin, ISBN 3-540-66965-5
9. Maugin GA (1993) Material inhomogeneities in elasticity. Chapman & Hall, London
10. McMeeking RM, Landis CM (2002) A phenomenological multi-axial constitutive law for switching in polycrystalline ferroelectric ceramics. Int J Engng Sci 40(14):1553–1577
11. Mehling V, Tsakmakis Ch, Gross D (2007) Phenomenological model for the macroscopical material behavior of ferroelectric materials. J Mech Phys Sol 55(10):2106–2141

12. Mueller R (2005) Configurational forces in defect mechanics and in computational methods. Habilitation thesis, Institute of Mechanics, TU Darmstadt, Germany, ISBN 3-935868-13-8
13. Mueller R, Maugin GA (2002) On material forces and finite element discretizations. Comp Mech 29(1):52–60
14. Mueller R, Kolling S, Gross D (2002) On Configurational forces in the context of the Finite Element Method. Int J Numer Meth Engng 53:1557–1574
15. Schrade D, Mueller R, Gross D, Utschig T, Shur V, Lupascu D (2007) Interaction of domain walls with defects in ferroelectric materials. Mech Mater 39:161–174
16. Schrade D, Mueller R, Xu BX, Gross D (2007) Domain evolution in ferroelectric materials: A continuum phase field model and finite element implementation. Comp Meth Appl Mech Eng 196:4365–4374
17. Schrade D, Xu BX, Mueller R, Gross D (2009) On phase field simulations of ferroelectrics: Parameter identification and verification. Proceedings of the ASME 2008 smart materials. Adaptive structures and intelligent systems (SMASIS 2008), pp 301–308
18. Schrade D, Mueller R, Gross D (2009) Parameter identification in phase field models for ferroelectrics. Proceedings in applied mathematics and mechacnics (submitted)
19. Soh A, Song Y, Ni Y (2006) Phase field simulations of hysteresis and butterfly loops in ferroelectrics subjected to electro-mechanical coupled loading. J Am Ceram Soc 89:652–661
20. Su Y, Landis C (2007) Continuum thermodynamics of ferroelectric domain evolution: Theory, finite element implementation, and application to domain wall pinning. J Mech Phys Sol 55:280–305
21. Wang H, Singh RN (1997) Crack propagation in piezoelectric ceramics: Effect of applied electric fields. J Appl Phys 81:7471–7479
22. Wang J, Shi S-Q, Chen L-Q, Li Y, Zhang T-Y (2004) Phase field simulations of ferroelectric/ferroelastic polarization switching. Acta Mater 52:749–764
23. Zhang W, Bhattacharya K (2005) A computational model of ferroelectric domains. Part I: model formulation and domain switching. Acta Mater 53:185–198

Micromechanical Simulation of Ferroelectric Domain Switching at Cracks

Qun Li, Marco Enderlein, and Meinhard Kuna

Abstract A micromechanical nonlinear constitutive model is embedded into a finite element algorithm to simulate domain switching in tetragonal ferroelectrics. Each Gaussian integration point of finite elements is considered as a grain comprising a set of distinct domain variants. It is found that a large scale ferroelectric domain switching zone exists in the vicinity of crack tip even under a small magnitude of electromechanical loading. Linear fracture mechanics based on small scale domain switching theory would be inappropriate for the crack problems in ferroelectric ceramics. In addition, the crack opening displacement δ_t of an electrically permeable crack is numerically calculated. The results indicate that the effect of electric fields on δ_t depends on the degree of domain switching.

1 Introduction

Over the last decades, polycrystalline ferroelectric ceramics have been widely used in many electromechanical devices due to their excellent electromechanical coupling property [1, 2]. An applied electric field induces a preferred orientation in the initially randomly oriented ferroelectric domains through domain switching.

A macroscopic polarization develops and in turn enables the macroscopic piezoelectric effect [3]. Generally speaking, there exists a threefold hierachical microstructure in ferroelectrics. That is, the polycrystalline ceramic is composed of *grains*, and each grain is subdivided into *domains*, where each domain is an assembly of *unit cells* all having the same electrical dipole orientation. A nonlinear constitutive model is proposed by Huber et al. [4] based on the above microstructural mechanism. It assumes that each grain comprises a set of distinct domain variants with their own volume fractions. Within each grain the switching

Q. Li (✉), M. Enderlein, and M. Kuna
TU Bergakademie Freiberg, Institute of Mechanics and Fluid Dynamics,
Lampadiusstrasse 4, 09596 Freiberg, Germany
e-mail: qunli@imfd.tu-freiberg.de or liqunxjtu@hotmail.com;
Macro.Enderlein@imfd.tu-freiberg.de; Meinhard.Kuna@imfd.tu-freiberg.de

M. Kuna and A. Ricoeur (eds.), *IUTAM Symposium on Multiscale Modelling of Fatigue, Damage and Fracture in Smart Materials*, IUTAM Bookseries 24,
DOI 10.1007/978-90-481-9887-0_10,

event, which converts one domain variant into another, gives rise to a progressive change in remanent strain and polarization and to a corresponding change in volume fraction. The finite element algorithm is successfully used to simulate domain switching by considering each Gaussian integration point of finite elements as a grain in tetragonal ferroelectrics. Many efforts have been focused on this field and some significant achievements are obtained. Kamlah et al. [5] computed the constitutive behavior of a ferroelectric ceramic by a plane strain finite element model. They discussed the response of a polycrystalline array of ferroelectric grains to poling by electric fields under plane strain constraint. Haug et al. [6] studied the influence of grain-to-grain interactions on the overall and local switching behavior by a similar 2-dimensional finite element technique. They compared the results of self-consistent calculations and multi-grain finite element calculations and found excellent agreements of macroscopic response between numerical simulations and experimental observations four different loading situations. Pathak and McMeeking [7] developed a 3-dimensional finite element method to simulate a polycrystalline ferroelectric under electric and mechanical loading.

On the other hand, ferroelectric ceramics are brittle and susceptible to cracking at all scales. The limited reliability of ferroelectric devices due to cracking constitutes a major impediment to large-scale usage. Fracture behavior of ferro/piezoelectric ceramics has received much attention due to its complexity. Exhaustive theoretical and experimental investigations have been performed in the field of fracture mechanics of ferroelectric devices. However, there still exist some controversial results in both experimental observations and theoretical predictions [8–16]. Most complexity of fracture behavior of ferroelectric ceramics is attributed to the nonlinear constitutive properties due to domain switching. The concentration of stress or electric field near the crack tip may cause domain switching, thereby changing the local ferroelectric domain structure. The change of the domain structure affects the internal electric field near the crack tip and the internal stress field because spontaneous strains are accompanied with polarizations. The internal fields induced by domain switching may shield or anti-shield the crack tip from the applied electromechanical load, resulting in strengthening or weakening the apparent fracture toughness [11]. Based on a small-scale-switching model, Ricoeur and Kuna [12] investigated the fracture process zone near the tip of an electromechanically loaded crack. The influence of the switching induced field changes on the mechanical ΔK_I and dielectric intensity factors ΔK_{IV} was calculated via piezoelectric weight functions. Actually, many theoretical and numerical studies [13, 14] have been conducted to understand and predict the fracture behavior induced by domain switching under mechanical and electrical loading. Therefore, the main purpose of this paper is devoted to report on domain switching induced fracture behavior for a crack in ferroelectric ceramics by the micromechanical FEM simulation.

2 FEM Simulation Methodology

Considering the non-linear behavior in ferroelectrics, the total strain ε_{ij}^{tot} and the total electric displacement D_i^{tot} are the summation of the reversible (linear) and irreversible (nonlinear) components,

$$\begin{aligned} \varepsilon_{ij}^{tot} &= \varepsilon_{ij} + \varepsilon_{ij}^{irr}, \\ D_i^{tot} &= D_i + P_i^{irr}. \end{aligned} \tag{1}$$

where the irreversible parts ε_{ij}^{irr} and P_i^{irr} are known as the remanent strain and polarization. Starting from the linear constitutive equations, the ferroelectric material behavior is described considering Eq. (1)

$$\begin{aligned} \sigma_{ij} &= c_{ijkl}\left(\varepsilon_{kl}^{tot} - \varepsilon_{kl}^{irr}\right) - e_{kij}E_k, \\ D_i^{tot} &= e_{ikl}\left(\varepsilon_{kl}^{tot} - \varepsilon_{kl}^{irr}\right) + \kappa_{ij}E_j + P_i^{irr}, \end{aligned} \tag{2}$$

where σ_{ij} and E_k are the stresses and the electric field components. c_{ijkl}, e_{ikl} and κ_{ij} are the elastic, piezoelectric and dielectric constants of the material, respectively.

The basic laws are the balance equations for the mechanical momentum and the electric charges

$$\begin{aligned} \sigma_{ij,j} + b_i &= 0 \\ D_{i,i} - \omega_V &= 0 \end{aligned} \tag{3}$$

Here b_i denotes the volume forces and ω_V the volume charges.

A finite element algorithm of the nonlinear model can be obtained by the generalized principle of virtual work. Without further elaboration the resulting variational principle may be stated in matrix notations as [17, 18]

$$\begin{aligned} &\int_{V^E} \left[-\{\delta\boldsymbol{\varepsilon}^{\mathbf{tot}}\}^{\mathrm{T}}\left([\mathbf{c}]\{\boldsymbol{\varepsilon}^{\mathbf{tot}}\} - [\mathbf{e}]\{\mathbf{E}\}\right) + \{\delta\mathbf{E}\}^{\mathrm{T}}\left([\mathbf{e}]^{\mathrm{T}}\{\boldsymbol{\varepsilon}^{\mathbf{tot}}\} + [\boldsymbol{\kappa}]\{\mathbf{E}\}\right)\right]dV \\ &+ \int_{V^E} \{\delta\boldsymbol{\varepsilon}^{\mathbf{tot}}\}^{\mathrm{T}}[\mathbf{c}]\{\boldsymbol{\varepsilon}^{\mathbf{irr}}\}dV + \int_{V^E} \{\delta\mathbf{E}\}^{\mathrm{T}}\left(\{\mathbf{P}^{\mathbf{irr}}\} - [\mathbf{e}]\{\boldsymbol{\varepsilon}^{\mathbf{irr}}\}\right)dV \\ &+ \int_{V^E} \{\delta\mathbf{u}\}^{\mathrm{T}}\{\mathbf{b}\}dV + \int_{S_t^E} \{\delta\mathbf{u}\}^{\mathrm{T}}\{\mathbf{t}\}dS - \int_{S_\omega^E} \delta\phi\,\omega_s dS = 0. \end{aligned} \tag{4}$$

Equation (4) can be discretized in the usual manner of a finite element formulation, i.e. the mechanical displacements and electric potential are expressed in terms of nodal values via interpolation functions. The discretized result is the algebraic equation system

$$\begin{aligned} [\mathbf{K_{uu}}]\{\mathbf{u}\} + [\mathbf{K_{u\phi}}]\{\boldsymbol{\phi}\} &= \{\mathbf{f_b}\} + \{\mathbf{f_s}\} + \{\mathbf{f_e}\}, \\ [\mathbf{K_{\phi u}}]\{\mathbf{u}\} + [\mathbf{K_{\phi\phi}}]\{\boldsymbol{\phi}\} &= \{\mathbf{q_s}\} + \{\mathbf{q_e}\}, \end{aligned} \tag{5}$$

where $\{\mathbf{u}\}$ and $\{\boldsymbol{\phi}\}$ are the nodal values of the mechanical displacement and electric potential, respectively. $[\mathbf{K_{uu}}]$, $[\mathbf{K_{u\phi}}]$, $[\mathbf{K_{\phi\phi}}]$ are the mechanical, dielectric and

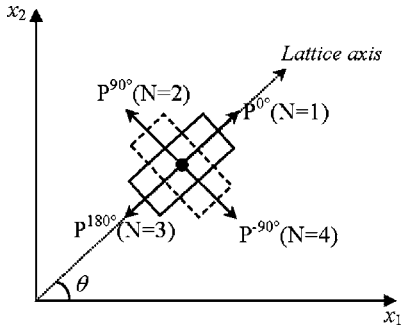

Fig. 1 Illustration of four types of domains in tetragonal ferroelectrics

piezoelectric element stiffness matrices. $\{\mathbf{f_b}\}$, $\{\mathbf{f_s}\}$, $\{\mathbf{f_e}\}$, $\{\mathbf{q_s}\}$, and $\{\mathbf{q_e}\}$ are the electrical and mechanical load vectors and the nonlinear contributions as described in the reference of Enderlein [18, 19].

A polycrystalline ferroelectrics is composed of multiple grains. Due to strain incompatibilities and depolarization fields, each grain is divided into many domains having their own orientation. When all considerations of switching events are restricted to the x_1–x_2 plane, there are four allowable polarization directions for a tetragonal ferroelectric crystal. Figure 1 illustrates the four different domain types in each grain, where the lattice axis of the grain is indicated by an angle θ with the global coordinate x_1. Based on the micro polycrystalline model, it is assumed that every domain type corresponds to a volume fraction of $v^{(N)}$ ($N = 1, 2, 3, 4$). It is noted that $v^{(N)}$ satisfies the conditions [4]

$$0 \le v^{(N)} \le 1, \qquad \sum_{N=1}^{4} v^{(N)} = 1. \tag{6}$$

Thus, the average of the linear, irreversible and total quantities can be given as

$$\begin{aligned} &\varepsilon_{ij} = \sum_{N=1}^{4} \varepsilon_{ij}^{(N)} v^{(N)}, \qquad \varepsilon_{ij}^{irr} = \sum_{N=1}^{4} \varepsilon_{ij}^{irr(N)} v^{(N)}, \quad \varepsilon_{ij}^{tot} = \sum_{N=1}^{4} \varepsilon_{ij}^{tot(N)} v^{(N)}, \\ &D_i = \sum_{N=1}^{4} D_i^{(N)} v^{(N)}, \qquad P_i^{irr} = \sum_{N=1}^{4} P_i^{irr(N)} v^{(N)}, \quad D_i^{tot} = \sum_{N=1}^{4} D_i^{tot(N)} v^{(N)}. \end{aligned} \tag{7}$$

Let $\mathbf{P}^{(N)}$ and $\boldsymbol{\varepsilon}^{(N)}$ denote the spontaneous polarization vectors and spontaneous strain tensors of the Nth type of domains with the volume fraction $v^{(N)}$. Then [20]

$$\begin{aligned} &\mathbf{P}^{(1)} = -\mathbf{P}^{(3)} = P_0(\cos\theta, \sin\theta)^{\mathrm{T}}, \quad \mathbf{P}^{(2)} = -\mathbf{P}^{(4)} = P_0(-\sin\theta, \cos\theta)^{\mathrm{T}}, \\ &\boldsymbol{\varepsilon}^{(1)} = \boldsymbol{\varepsilon}^{(3)} = \frac{S_0}{6} \begin{bmatrix} 1 + 3\cos 2\theta & -3\sin 2\theta \\ -3\sin 2\theta & 1 - 3\cos 2\theta \end{bmatrix}, \\ &\boldsymbol{\varepsilon}^{(2)} = \boldsymbol{\varepsilon}^{(4)} = \frac{S_0}{6} \begin{bmatrix} 1 - 3\cos 2\theta & 3\sin 2\theta \\ 3\sin 2\theta & 1 + 3\cos 2\theta \end{bmatrix}, \end{aligned} \tag{8}$$

where P_0 is the amount of spontaneous polarization of a unit cell, S_0 is the single crystal deformation or lattice deformation in tetragonal crystals.

When domain switching is activated by the electromechanical loading, three different switching events have to be distinguished. In Fig. 1 one can recognize three distinct possible switching variants. That is, unit cell can switch 90° (e.g., domain-1→domain-2), 180° (e.g., domain-1→domain-3), or −90° (e.g., domain-1→domain-4). Thus, the change of spontaneous polarization can be described by the polarization switch vector

$$\Delta \mathbf{P_i^{sp}} = bP_0 \begin{pmatrix} \sin\left(\theta + \frac{1}{2}\beta\right) \\ -\cos\left(\theta + \frac{1}{2}\beta\right) \end{pmatrix}, \tag{9}$$

where

$$b = \begin{cases} \pm\sqrt{2} & \mp 90°\text{domain switching} \\ -2 & 180°\text{domain switching} \end{cases}, \quad \beta = \begin{cases} \pm\pi/4 & \mp 90°\text{domain switching} \\ \pi/2 & 180°\text{domain switching} \end{cases}. \tag{10}$$

The change of spontaneous strain can be described as

$$\begin{aligned} \Delta \boldsymbol{\varepsilon}_{\mathbf{ij}}^{\mathbf{sp}} &= -S_0 \begin{pmatrix} \cos 2\theta & \sin 2\theta \\ \sin 2\theta & -\cos 2\theta \end{pmatrix} && \pm 90°\text{domain switching}, \\ \Delta \boldsymbol{\varepsilon}_{\mathbf{ij}}^{\mathbf{sp}} &= 0 && 180°\text{domain switching}, \end{aligned} \tag{11}$$

Thus, the changes of irreversible strain and polarization in one grain are computed by summing over all domain switching events with their volume fractions

$$d\varepsilon_{ij}^{irr} = \sum_{N=1}^{4} \Delta\varepsilon_{ij}^{sp(N)} dv^{(N)}, \quad dP_i^{irr} = \sum_{N=1}^{4} \Delta P_i^{sp(N)} dv^{(N)}. \tag{12}$$

Moreover, polarization domain switching relies on the balance between energy release and energy dissipation in domains. Energy dissipation is responsible for switching barriers such as the critical energy release density to switch a crystallite. The total differential of the internal energy density for nonlinear ferroelectrics can be formulated as:

$$\begin{aligned} du = \; & \sigma_{ij} \sum_{N=1}^{4} d\left(\varepsilon_{ij}^{(N)} v^{(N)}\right) + E_i \sum_{N=1}^{4} d\left(D_i^{(N)} v^{(N)}\right) + \sigma_{ij} \sum_{N=1}^{4} \Delta\varepsilon_{ij}^{sp(N)} dv^{(N)} \\ & + E_i \sum_{N=1}^{4} \Delta P_i^{sp(N)} dv^{(N)}. \end{aligned} \tag{13}$$

Expanding the first two terms of the right hand side and separating Eq. (13) into two parts, one reversible part (ω^{rev}) and the other dissipative part (ω^{diss}), yields

$$du = \sum_{N=1}^{4} \underbrace{\left(\sigma_{ij} d\varepsilon_{ij}^{(N)} + E_i dD_i^{(N)}\right) v^{(N)}}_{du^{rev(N)}} + \sum_{N=1}^{4} \underbrace{\left(\sigma_{ij}\varepsilon_{ij}^{(N)} + E_i D_i^{(N)} + \sigma_{ij}\Delta\varepsilon_{ij}^{sp(N)} + E_i \Delta P_i^{sp(N)}\right) dv^{(N)}}_{\omega^{diss(N)} dv^{(N)}}. \quad (14)$$

A switching criterion can be proposed relating the sum of dissipative mechanical and electric works for a variant N to a threshold value [21]

$$\omega^{diss(N)} \geq \omega^{crit}. \quad (15)$$

The critical work possesses different values for $\pm 90°$ and $180°$ domain switching

$$\omega_{\pm 90^o}^{crit} = \sqrt{2} P^0 E_c \qquad \omega_{180^o}^{crit} = 2 P^0 E_c \quad (16)$$

where the coercive field is denoted by E_c.

3 An Electrically Permeable Crack in Ferroelectric Ceramics

The configuration of the crack problem and FEM mesh are depicted in Fig. 2a, b and the FEM mesh is restricted to the lower right part of the model due to symmetry. A crack of length $2a$ is represented by the line OA, where the electric potential and the tractions are zero. The upper edge AB is electrically grounded and the vertical displacement u_2 is vanishing due to symmetry. Thus, the potential along the crack surface OA is the same as on the upper edge AB. An electric field will not be disrupted meaning that the crack is electrically 'permeable'. An electric field load along x_2 is applied by imposing a magnitude of electric potential on the bottom DC.

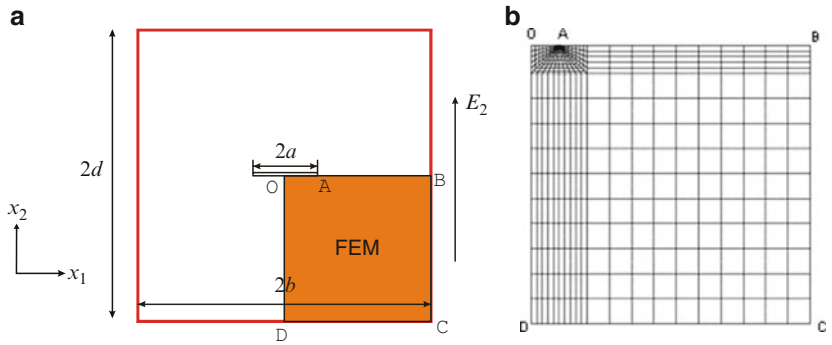

Fig. 2 (**a**) Schematic configuration of a crack and (**b**) finite element mesh

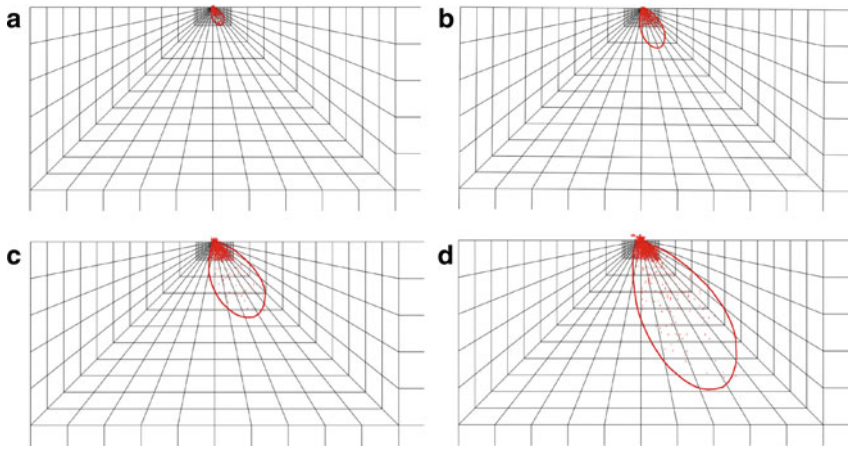

Fig. 3 Evolution of domain switching zone near the crack tip under different mechanical loads (**a**) 6 (**b**) 8 (**c**) 10 and (**d**) 12 MPa

A uniform mechanical tensile load of 10 MPa is prescribed on the bottom of the specimen before imposing the electric field. Because of symmetry, the left surface OD is constrained in the x_1 direction. A typically tetragonal $BaTiO_3$ (mm2 point group) is used in the present analysis.

Domain switching zones induced by a purely mechanical load perpendicular to the crack are considered in unpoled ferroelectrics. In the unpoled case, domains are randomly distributed in the ferroelectric body by means of a random number generator. The configuration and size of domain switching zone is depicted in Fig. 3a–d under different mechanical loads. Smaller switching zone scales under 6 and 8 MPa are shown in Fig. 3a, b and larger switching scales under 10 and 12 MPa are shown in Fig. 3c, d. To clearly show the detailed domain switching structure, the scale in Fig. 3a–d is about two times of crack length. Due to the concentration of stress or electric field in the vicinity of the crack tip, a maximum dissipative switching energy is obtained and causes domain switching to occur firstly near the crack tip. The larger the applied mechanical load is, the larger the switching zone will be. Even a full field switching zone is formed under a high enough applied mechanical load. Thereafter, domain switching grows to be saturated and remains a steady state. Of great significance is that even under a small mechanical load, the size of switching zone is large compared to small domain switching assumption widely adopted in linear fracture mechanics.

It indicates that small scale domain switching assumption would be inappropriate to analyze the crack problems in ferroelectrics. Furthermore, although the switching zone becomes larger and larger with the increase of mechanical loads, the basic shape of switching zone is found to be similar for all of cases. The switching zone direction is approximately along $-45°$ to x_1-axis, where the maximum value of stress exists and induces the maximum dissipative switching energy.

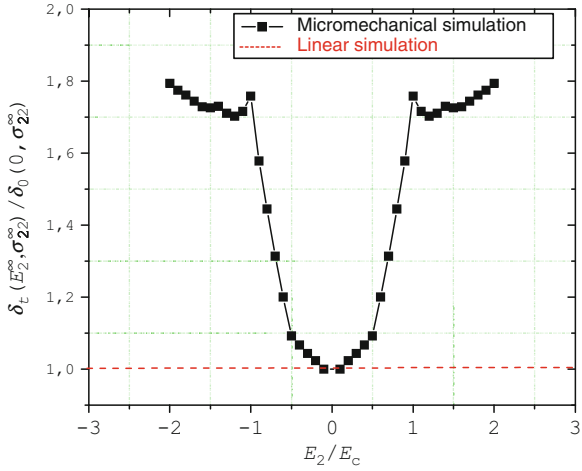

Fig. 4 Normalized crack opening displacement $\delta_t\left(E_2^\infty, \sigma_{22}^\infty\right)$ by\in unpoled ferroelectric ceramics

Since the linear piezoelectric strain due to the electric field is much smaller than the strain associated with the domain switching, the concentration of spontaneous strain induced by domain switching would play a significant role near the crack tip. Polarization switching generates an internal stress field and it can weaken or strengthen fracture parameters. It is known that the crack opening displacement occasionally is used as a fracture parameter, which is equivalent to the J-integral or energy release rate. Here, we pay more attention to the influence of domain switching on the crack opening displacement under the combined mechanical and electric loading.

Numerical computations of the crack opening displacement $\delta_t\left(E_2^\infty, \sigma_{22}^\infty\right)$ are performed in an unpoled ferroelectrics normalized by the value $\delta_0\left(0, \sigma_{22}^\infty\right)$ under pure mechanical load $\sigma_{22}^\infty = 10\,\text{MPa}$. Numerical results of δ_t as function of the applied electric fields are plotted in Fig. 4. The red dashed straight line in Fig. 4 means the results from the traditional linear equation without considering domain switching. Figure 4 demonstrates that both positive and negative electric fields have a significant but identical effect on δ_t. It is evident that the invariance towards the sign of the electric load results from the initial isotropic property of the unpoled material. With the increase of the electric field, the characteristic of δ_t vs. E_2 is divided into three different parts, as shown in Fig. 4. The slope of δ_t vs. E_2 is low until $0.5\,E_\text{c}$. A larger effect of electric field is found between 0.5 and $1\,E_\text{c}$. Thereafter, there is a slower enlargement of δ_t. Moreover, a peak value of δ_t is obtained when the electric field approaches the coercive strength E_c or $-E_\text{c}$.

A physical mechanism may be established to explain the influence of the electric field on δ_t based on the intrinsic correlation between the magnitude of spontaneous strain and the degree of domain switching. The increasing degree of

domain switching leads to a prominent spontaneous strain and thus can enhance the magnitude of residual stress near the crack tip. If E_2 is much lower than E_c, only small-scale-switching events occur, producing minor effect on δ_t. The blunting of the crack increases about proportionally with the square of the applied electric field, which reminds to the relation $\delta_t \sim K_I^2$ in elastic-plastic fracture mechanics under small-scale-yielding conditions. With increasing electric field, the transition from small- to large-scale switching zones happens. Near E_c a threshold is reached resulting in the peak effect of switching-induced crack opening δ_t. If E_2 is much larger than E_c, most domains around the crack tip have already completely switched. This leads to the saturation of the crack tip opening δ_t as can be observed in Fig. 4. This rigorous limitation of crack tip opening means an essential difference if compared to large scale yielding in ductile fracture, where the δ_t growth unrestrained after limit load.

4 Conclusions

This paper reports an investigation of an electrically permeable crack in tetragonal ferroelectric ceramics based on the micromechanical FEM simulation. Each Gaussian point in finite elements is representative of a grain with different lattice orientation and comprises a set of distinct domain variants. It is concluded that the electric field has a significant influence on the crack opening displacement. These findings are different from those based on the traditional linear piezoelectric fracture mechanics, where the electric field has no effect on the fracture behavior of an electrically permeable crack. Results show that the characteristic of δ_t vs. E_2 depends on the degree of domain switching and is divided into three different parts. The slope of δ_t vs. E_2 is low and quadratic until 0.5 E_c. A larger effect of electric field is found between 0.5 and 1 E_c. Thereafter, a saturation is reached with much slower enlargement of δ_t.

Acknowledgments The author Qun Li appreciates the financial support by the Alexander von Humboldt Foundation in Germany.

References

1. Uchino K (1997) Piezoelectric actuators and ultrasonic motors. Kluwer, Boston, MA
2. Setter N (2002) Piezoelectric materials in devices. Ceramics Laboratory EPFL, Lausanne
3. Jones JL, Kounga AB, Aulbach E, GranzowT (2008) Domain switching during electromechanical poling in lead zirconate titanate ceramics. J Am Ceram Soc 91:1586–1590
4. Huber JE, Fleck NA, Landis CM, McMeeking RM (1999) A constitutive model for ferroelectric Polycrystals. J Mech Phys Solids 47:1663–1697
5. Kamlah M, Liskowsky AC, McMeeking RM, Balke H (2005) Finite element simulation of a polycrystalline ferroelectric based on a multidomain single crystal switching model. Int J Solids Struct 42:2949–2964

6. Haug A, Huber JE, Onck PR, Giessen E (2007) Multi-grain analysis versus self-consistent estimates of ferroelectric polycrystals. J Mech Phys Solids 55:648–665
7. Pathak A, McMeeking RM (2008) Three-dimensional finite element simulations of ferroelectric polycrystals under electrical and mechanical loading. J Mech Phys Solids 56:663–683
8. Chen YH, Lu TJ (2003) Cracks and fracture in piezoelectrics. Adv Appl Mech 39:121–215
9. Zhang TY, Zhao MH, Tong P (2002) Fracture of piezoelectric ceramics. Adv Appl Mech 38:147–289
10. Kuna M (2009) Fracture mechanics of piezoelectric materials – where are we right now? Engng Fract Mech. doi:10.1016/j.engfracmech.2009.03.016
11. Wang J, Zhang TY (2007) Phase field simulations of polarization switching-induced toughening in ferroelectric ceramic. Acta Materialia 55:2465–2477
12. Ricoeur A, Kuna M (2003) A micromechanical model for the fracture process zone in ferroelectrics. Comput Mater Sci 27:235–249
13. Shindo Y, Narita F, Saito F (2007) Electroelastic intensification and domain switching near a plane strain crack in rectangular piezoelectric material. J Mech Mater Struct 2(8):1525–1540
14. Huber JE, Fleck NA (2001) Multi-axial electrical switching of a ferroelectric: theory versus experiment. J Mech Phys Solids 49:785–811
15. Park SB, Sun CT (1995a) Fracture criteria for piezoelectric ceramics. J Am Ceram Soc 78:1475–1480
16. Park SB, Sun CT (1995b) Effect of electric fields on fracture of piezoelectric ceramics. Int J Fract 70:203–216
17. Allik H, Hughes TJT (1970) Finite element method for piezoelectric vibration. Int J Num Meth Eng 2:151–157
18. Enderlein M, Ricoeur A, Kuna M (2005) Finite element techniques for dynamic crack analysis in piezoelectrics. Int J Fract 127:131–143
19. Enderlein M (2007) Finite-Elemente-Verfahren zur bruchmechanischen Analyse von Rissen in piezoelektrischen Strukturen bei transienter elektromechanischer Belastung. Dissertation, TU Bergakademie Freiberg (in German)
20. Li FX, Rajapakse RKND (2007) A constrained domain-switching model for polycrystalline ferroelectric ceramics. Part I: Model formulation and application to tetragonal materials. Acta Mat 55:6472–6480
21. Hwang SC, McMeeking RM (1999) A finite element model of ferroelectric polycrystals. Int J Solids Struct 36:1541–1556

A Phenomenological Constitutive Model for Ferroelectric Ceramics and Ferromagnetic Materials

Sven Klinkel and Konrad Linnemann

Abstract This Contribution is concerned with a macroscopic nonlinear constitutive law for ferromagnetic alloys and ferroelectric ceramics. It accounts for the hysteresis effects which occur in the considered class of materials. The uniaxial model is thermodynamically motivated and based on the definition of a specific free energy function and a switching criterion. The strains and the magnetic or electric field strength are additively split into a reversible and an irreversible part. Analogous to plasticity, the irreversible quantities serve as internal variables. A one-to-one-relation between the two internal variables provides conservation of volume during polarization or magnetization process. The material model is able to approximate the ferromagnetic or ferroelectric hysteresis curves and the related butterfly hysteresis curves. An extended approach for ferrimagnetic behavior which occurs in ferromagnetic materials is presented. A main aspect of the constitutive model is its numerical treatment. The model is embedded in a three dimensional finite element formulation. The usage of the irreversible field strength permits the application of algorithms known from the treatment of computational inelasticity.

1 Introduction

Ferromagnetic materials show an inherent coupling between magnetic field and deformation. Ferroelectric ceramics are characterized by a coupling between electric field and deformation. Both materials show similar nonlinear behavior. The purpose of this paper to develop a constitutive model which accounts for the nonlinear behavior and hysteresis effects of ferromagnetic alloys and ferroelectric ceramics.

S. Klinkel (✉)
Statik und Dynamik der Tragwerke, TU Kaiserslautern, Paul-Ehrlich-Str. 14,
67663 Kaiserslautern, Germany
e-mail: klinkel@rhrk.uni-kl.de

K. Linnemann
Institut für Baustatik, Universität Karlsruhe (TH), Kaiserstr. 12, 76131 Karlsruhe, Germany
e-mail: Konrad.Linnemann@bs.uka.de

M. Kuna and A. Ricoeur (eds.), *IUTAM Symposium on Multiscale Modelling of Fatigue, Damage and Fracture in Smart Materials*, IUTAM Bookseries 24,
DOI 10.1007/978-90-481-9887-0_11,

Constitutive models which are in accordance with the principles of thermodynamics are determined with the definition of a specific free energy function. For ferroelectric ceramics the strains, the polarization, and the temperature often serve as independent variables. For ferromagnetic materials the magnetization is used instead of the polarization. Here, a common approach are higher order energy functions, see e.g. [1, 13–15]. Alternatively a definition of the free energy function in sections is used, see [13] and [12]. The independent variables are split in a reversible and an irreversible part for the approximation of the hysteresis behavior. The irreversible quantities serve as internal variables and represent the polarization or magnetization state. The development of the internal variables is determined with the definition of a switching criterion. The model of [4] for ferromagnetic materials is based on these assumptions. More often, thermodynamically motivated models are applied for ferroelectric ceramics. The approaches of [6] use multiple switching criterions to specify begin and end of the irreversible behavior. The multiaxial models of [8] and [10] get along with only one switching criterion. The domain processes are restricted by a hardening function. In [11] an orientation distribution function is introduced which serves as additional internal variable to approximate coupled electromechanical loadings.

In the present paper a thermodynamically motivated constitutive model is developed which accounts for hysteresis effects in ferroelectric ceramics and ferromagnetic alloys. The uniaxial model is embedded in a three dimensional formulation. This benefits an efficient numerical treatment of the model but prevents a reorientation of magnetization or polarization during the simulation. The main aspects of the model may by summarized as follows:

- A thermodynamically consistent constitutive model is presented. The formulation is based on the definition of a free energy function and a switching criterion. The switching criterion controls domain switching. The center of the switching surface moves in the sense of kinematic hardening in plasticity.
- The strains, the magnetic and the electric field strength respectively are decomposed additively in a reversible and an irreversible part. The split of the field strength is an alternative approach to the decomposition of the magnetization or polarization. Its application is motivated by the numerical treatment of the constitutive model with the finite element method. Here the field strength is described by a scalar potential which serves as nodal degree of freedom. Thus, no change of variables is necessary. Furthermore, one may draw on algorithms of computational inelasticity.
- The model is able to reproduce the ferroelectric and butterfly hysteresis of ferroelectric ceramics. Besides, the typical hysteresis of ferromagnetic alloys can be simulated. The occurring ferrimagnetic hysteresis behavior of these materials is approximated by an expanded approach which is based on a transformation of the independent variables in a local description. Ferroelastic switching and mechanical depolarization are not considered within this work.

2 Governing Equations

2.1 Magnetomechanical Field Equations

The balance equations of magnetomechanical coupled problems are the strong form of equilibrium and the Maxwell equation considering solenoidality of the magnetic field. The local forms are given as

$$\boldsymbol{S}\,\nabla + \rho\boldsymbol{b} = \boldsymbol{0} \qquad\qquad \vec{\boldsymbol{B}} \cdot \nabla = 0. \tag{1}$$

Here, $\boldsymbol{S}$ stands for the stress tensor, $\rho\boldsymbol{b}$ for the mechanical body forces and $\vec{\boldsymbol{B}}$ for the magnetic flux density. Thus the influence of ponderomotive forces is minor, they are neglected in this paper. Consequently the stress tensor is symmetric. The mechanical and magnetic boundary conditions read $\boldsymbol{S}\cdot\boldsymbol{n} = \boldsymbol{t}$ on $\partial_t\mathscr{B}_0$ and $\vec{\boldsymbol{B}}\cdot\boldsymbol{n} = \varsigma_M$ on $\partial_\varsigma\mathscr{B}_0$. The vector $\boldsymbol{t}$ denotes the prescribed traction on the surface $\partial_t\mathscr{B}_0$ and the scalar value ς_M the magnetic surface charge on $\partial_\varsigma\mathscr{B}_0$. The vector $\boldsymbol{n}$ gives the outward unit normal on $\partial\mathscr{B}_0$. The linear strain tensor $\boldsymbol{E}$ and the magnetic field strength $\vec{\boldsymbol{H}}$ are defined as

$$\boldsymbol{E} = \frac{1}{2}(\nabla \otimes \boldsymbol{u} + \boldsymbol{u} \otimes \nabla) \qquad\qquad \vec{\boldsymbol{H}} = -\nabla\,\phi_M, \tag{2}$$

where $\boldsymbol{u}$ is the displacement vector and ϕ_M the magnetic scalar potential. The scalar potential is used instead of the magnetic vector potential, because only fields without curl are considered. For the constitutive model the total strains and the magnetic field strength are additively decomposed as

$$\boldsymbol{E} = \boldsymbol{E}^r + \boldsymbol{E}^i \qquad\qquad \vec{\boldsymbol{H}} = \vec{\boldsymbol{H}}^r + \vec{\boldsymbol{H}}^i. \tag{3}$$

The superscript r denotes the reversible part. The irreversible quantities, indexed by i, serve as internal variables and describe the dissipative part. Equation 3 is in full accordance with small strain plasticity theory. Due to conservation of volume, which is claimed for the irreversible strains, a one-to-one relation is assumed as $\boldsymbol{E}^i = \frac{E_s}{(\vec{H}_s^i)^2}\,\vec{\boldsymbol{H}}^i \cdot \vec{\boldsymbol{H}}^i\,\boldsymbol{I}$, see e.g. [10]. The quantity $\boldsymbol{I}$ denotes the projection tensor of rank two given as $\boldsymbol{I} = \frac{3}{2}\left(\boldsymbol{e}\otimes\boldsymbol{e} - \frac{1}{3}1\right)$ with magnetization direction $\boldsymbol{e} = \vec{\boldsymbol{H}}^i / \|\vec{\boldsymbol{H}}^i\|$.

2.2 Electromechanical Field Equations

The balance equations of the electromechanical coupled problem are given by Eq. 1 and the local form of the Gauss' law $\vec{\boldsymbol{D}} \cdot \nabla = 0$. The vector $\vec{\boldsymbol{D}}$ stands for the dielectric displacements. In case of dielectrics free volume charges are not considered.

The boundary conditions are supplemented with $\vec{\boldsymbol{D}} \cdot \boldsymbol{n} = \varsigma_E$ on $\partial_\varsigma \mathscr{B}_0$, where ς_E is the electric surface charge. The electric field $\vec{\boldsymbol{E}}$ is described via $\vec{\boldsymbol{E}} = -\nabla \phi_E$, $\vec{\boldsymbol{E}} = \vec{\boldsymbol{E}}^r + \vec{\boldsymbol{E}}^i$ with the electric scalar potential ϕ_E. Similar to [7] the total electric field is additively decomposed, where $\vec{\boldsymbol{E}}^i$ is the irreversible electric field. It serves as internal variable and replaces $\vec{\boldsymbol{H}}^i$. Additionally the saturation parameter $\vec{E}_s^i$ is applied instead of $\vec{H}_s^i$ and $\vec{P}_c$ instead of $\vec{M}_c$. The similarities of magnetomechanical and electromechanical coupling are obvious. Further the formulation is exclusively formulated for ferromagnetic problems.

3 Thermodynamic Framework

The constitutive model is based on a free energy function

$$\rho\psi = \frac{1}{2}(\boldsymbol{E} - \boldsymbol{E}^i) : \quad : (\boldsymbol{E} - \boldsymbol{E}^i) + \frac{\vec{\boldsymbol{H}}^i \cdot \boldsymbol{e}}{\vec{H}_s^i} (\boldsymbol{E} - \boldsymbol{E}^i) : \quad \cdot \vec{\boldsymbol{H}} - \frac{1}{2}(\vec{\boldsymbol{H}} - \vec{\boldsymbol{H}}^i) \cdot \mu\, (\vec{\boldsymbol{H}} - \vec{\boldsymbol{H}}^i) + \rho\bar{\psi}(\vec{\boldsymbol{H}}^i). \tag{4}$$

which serves as thermodynamic potential. Here, , , and μ are the elasticity tensor, the coupling tensor and the permeability. In the present work a second order potential is used. Thus Eq. 4 is quadratic in $\boldsymbol{E}$ und $\vec{\boldsymbol{H}}$. The last term $\rho\bar{\psi}(\vec{\boldsymbol{H}}^i)$ represents the energy stored in the internal variable $\vec{\boldsymbol{H}}^i$. With respect to plasticity it is called hardening function. According to the second law of thermodynamics and with neglecting thermal effects the Clausium–Duhem inequality reads

$$\mathscr{D} = \boldsymbol{S} : \dot{\boldsymbol{E}} - \vec{\boldsymbol{B}} \cdot \dot{\vec{\boldsymbol{H}}} - \rho\dot{\psi} \geq 0 \tag{5}$$

The scalar $\mathscr{D}$ names the dissipated energy. Using standard arguments of rational continuum mechanics, the stress and the magnetic flux density can be derived as

$$\boldsymbol{S} := \frac{\partial \rho\psi}{\partial \boldsymbol{E}} = \quad : (\boldsymbol{E} - \boldsymbol{E}^i) + \frac{\vec{\boldsymbol{H}}^i \cdot \boldsymbol{e}}{\vec{H}_s^i} \cdot \vec{\boldsymbol{H}} \tag{6}$$

$$-\vec{\boldsymbol{B}} := \frac{\partial \rho\psi}{\partial \vec{\boldsymbol{H}}} = \frac{\vec{\boldsymbol{H}}^i \cdot \boldsymbol{e}}{\vec{H}_s^i}^T : (\boldsymbol{E} - \boldsymbol{E}^i) - \mu\, (\vec{\boldsymbol{H}} - \vec{\boldsymbol{H}}^i). \tag{7}$$

Applying these definitions and the derivation in time the dissipation reduces to

$$\mathscr{D} = -\underbrace{\left(2\frac{E_s}{(\overrightarrow{H}_s^{\,i})^2}\,\frac{\partial \rho\psi}{\partial \boldsymbol{E}^i} : \boldsymbol{I}\,\overrightarrow{\boldsymbol{H}}^{\,i} + \frac{\partial \rho\psi}{\partial \overrightarrow{\boldsymbol{H}}^{\,i}} \right)}_{\boldsymbol{\Xi}} \cdot \dot{\overrightarrow{\boldsymbol{H}}}^{\,i} \geq 0, \tag{8}$$

in which $\boldsymbol{\Xi}$ is defined as the work conjugated variable to the internal variable $\overrightarrow{\boldsymbol{H}}^{\,i}$. The partial derivatives are given by

$$\frac{\partial \rho\psi}{\partial \boldsymbol{E}^i} = \boldsymbol{S}, \quad \frac{\partial \rho\psi}{\partial \overrightarrow{\boldsymbol{H}}^{\,i}} = \frac{1}{\overrightarrow{H}_s^{\,i}} \left[(\boldsymbol{E} - \boldsymbol{E}^i) : \quad \cdot \overrightarrow{\boldsymbol{H}} \right] \boldsymbol{e} - \mu\,(\overrightarrow{\boldsymbol{H}} - \overrightarrow{\boldsymbol{H}}^{\,i}) - \frac{\partial \rho\bar{\psi}}{\partial \overrightarrow{\boldsymbol{H}}^{\,i}}. \tag{9}$$

A switching criterion is introduced to signify the begin of irreversible domain processes

$$\Phi = \frac{\boldsymbol{\Xi} \cdot \boldsymbol{\Xi}}{\overrightarrow{M}_c^{\,2}} - 1 \leq 0. \tag{10}$$

Here the parameter $\overrightarrow{M}_c$ serves as coercive value. Reversible wall movements in the domains are assumed for $\Phi < 0$. For irreversible wall movements it holds $\Phi = 0$. The postulate of maximum dissipation is formulated by a Lagrange functional with Φ as constraint. It reads $\mathscr{L} = -\mathscr{D}(\boldsymbol{\Xi}) + \lambda\Phi(\boldsymbol{\Xi})$, where λ is the Lagrange multiplier. The solution requires $\frac{\partial \mathscr{L}}{\partial \boldsymbol{\Xi}} = 0$ and $\frac{\partial \mathscr{L}}{\partial \lambda} = \Phi(\boldsymbol{\Xi}) = 0$. The necessary conditions for the existence of a local minimum are given by the Kuhn–Tucker conditions $\lambda \geq 0$, $\Phi \leq 0$, $\lambda\Phi = 0$. The evolution equation for the internal variable $\overrightarrow{\boldsymbol{H}}^{\,i}$ is derived as

$$\dot{\overrightarrow{\boldsymbol{H}}}^{\,i} = 2\,\lambda\,\frac{\boldsymbol{\Xi}}{\overrightarrow{M}_c^{\,2}}. \tag{11}$$

The presented constitutive model is applied almost unmodified for ferroelectric ceramics. Here an additive split is done for the electric field with $\overrightarrow{\boldsymbol{E}} = \overrightarrow{\boldsymbol{E}}^{\,r} + \overrightarrow{\boldsymbol{E}}^{\,i}$. Furthermore, $\overrightarrow{\boldsymbol{E}}$ and $\overrightarrow{\boldsymbol{E}}^{\,i}$ replaces $\overrightarrow{\boldsymbol{H}}$ and $\overrightarrow{\boldsymbol{H}}^{\,i}$ in the free energy function Eq. 4. The switching criterion depends on the coercive polarization $\overrightarrow{P}_c$.

4 Ferrimagnetic Hysteresis Effects

The ferrimagnetic lattice consists of two interleaving lattices with contrary magnetization. For an applied magnetic field $\boldsymbol{H}$, one of these lattices switches in the direction of $\boldsymbol{H}$, the other one remains unchanged. The mechanical prestress hampers

the switching process. As a result the characteristic hysteresis curves are separated in two hysteresis respectively, see Fig. 3. A local coordinate system is introduced. Its origin is in the center of the partial hysteresis. The horizontal offset is defined with the parameter $\vec{H}_0$. The local field quantities marked with superscript L are defined as

$$\vec{\boldsymbol{H}}^{L} = \vec{\boldsymbol{H}} - \vec{H}_0\, g\, \boldsymbol{e} \qquad\qquad \vec{\boldsymbol{H}}^{Li} = \vec{\boldsymbol{H}}^{i} + \vec{H}_s^{\,i}\, g\, \boldsymbol{e}. \tag{12}$$

The scalar valued variable $g = \operatorname{sign}(\vec{\boldsymbol{H}} \cdot \boldsymbol{e})$ gives the sign of the offset. The offset $\vec{B}_0$ has not to be specified, because the magnetic flux density is determined by the constitutive equations. With $\vec{\boldsymbol{H}}^{L}$, $\vec{\boldsymbol{H}}^{Li}$ a local free energy function is introduced as

$$\begin{aligned}\rho\psi^L =& \frac{1}{2}(\boldsymbol{E}-\boldsymbol{E}^i) : \quad : (\boldsymbol{E}-\boldsymbol{E}^i) + \frac{\vec{\boldsymbol{H}}^{i} \cdot \boldsymbol{e}}{H_s^i}\,(\boldsymbol{E}-\boldsymbol{E}^i) : \quad \cdot \vec{\boldsymbol{H}}^{L} \\ & - \frac{1}{2}(\vec{\boldsymbol{H}}^{L} - \vec{\boldsymbol{H}}^{Li}) \cdot \mu\, (\vec{\boldsymbol{H}}^{L} - \vec{\boldsymbol{H}}^{Li}) + \rho\bar{\psi}(\vec{\boldsymbol{H}}^{Li})\end{aligned} \tag{13}$$

which leads to local dissipation inequality $\mathscr{D} = \boldsymbol{\Xi}^{L} \cdot \vec{\boldsymbol{H}}^{Li} \geq 0$ with

$$\boldsymbol{\Xi}^{L} = -\left(2\frac{E_s}{(\vec{H}_s^{\,i})^2}\,\frac{\partial\rho\psi^L}{\partial\boldsymbol{E}^i} : \boldsymbol{I}\,(\vec{\boldsymbol{H}}^{Li} - \vec{H}_s^{\,i}\, g\, \boldsymbol{e}) + \frac{\partial\rho\psi^L}{\partial\vec{\boldsymbol{H}}^{Li}} \right), \tag{14}$$

see also [9]. The yield criterion is modified to provide reversible behavior in the global origin $\vec{\boldsymbol{H}} = \boldsymbol{0}$. Here the sign of g changes. The modified yield criterion reads

$$\Phi^L = \operatorname{sign}(\vec{M}_{max} - \|\vec{\boldsymbol{M}}^{L}\|)\,\frac{\boldsymbol{\Xi}^{L} \cdot \boldsymbol{\Xi}^{L}}{(\vec{M}_c)^2} - 1 \leq 0 \tag{15}$$

with $\vec{M}_{max} = \vec{M}_c + k\vec{H}_s^{\,i} + a/\operatorname{arctanh}(1/b)$. The vector $\vec{\boldsymbol{M}}^{L} = \boldsymbol{\mu}(\vec{\boldsymbol{H}}^{L} - \vec{\boldsymbol{H}}^{Li})$ denotes the uncoupled magnetization. For $\|\vec{\boldsymbol{M}}\| > \vec{M}_c$ the sign function is negative and reversible behavior is ensured. With the Eqs. 13, 15, and the arguments of Section 3 the evolution equation $\dot{\vec{\boldsymbol{H}}}^{Li} = 2\,\lambda\,\operatorname{sign}(\vec{M}_{max} - \|\vec{\boldsymbol{M}}^{L}\|)\boldsymbol{\Xi}^{L}/\vec{M}_c$ is developed. The implicit Euler scheme is applied for the time integration.

5 Variational Formulation and Finite Element Approximation

In this section the weak form of the coupled boundary value problem is derived. The boundary value problem is given by the balance equations (1), the Neumann boundary conditions, and Dirichlet boundary conditions $\boldsymbol{u} = \bar{\boldsymbol{u}}$on $\partial_u \mathscr{B}_0$, $\phi = \bar{\phi}$on $\partial_\phi \mathscr{B}_0$. It holds $\partial\mathscr{B}_0 = \partial_t \mathscr{B}_0 \bigcup \partial_u \mathscr{B}_0$, $\emptyset = \partial_t \mathscr{B}_0 \bigcap \partial_u \mathscr{B}_0$, $\partial\mathscr{B}_0 = \partial_\varsigma \mathscr{B}_0 \bigcup \partial_\phi \mathscr{B}_0$ and $\emptyset = \partial_\varsigma \mathscr{B}_0 \bigcap \partial_\phi \mathscr{B}_0$. The weak form $\delta\pi$ is obtained by multiplying Eqs. 1 with the test functions $\delta\boldsymbol{u}$ and $\delta\phi$. Integration by part and application of the divergence theorem lead to

$$\begin{aligned}\delta\pi = \int_{\mathscr{B}_0} \frac{\partial\rho\psi}{\partial \boldsymbol{E}} : \delta\boldsymbol{E} + \frac{\partial\rho\psi}{\partial \vec{\boldsymbol{H}}} \cdot \delta\vec{\boldsymbol{H}} - \rho\boldsymbol{b}\cdot\delta\boldsymbol{u}\,\mathrm{d}V \\ - \int_{\partial_t\mathscr{B}_0} \boldsymbol{t}\cdot\delta\boldsymbol{u}\,\mathrm{d}A - \int_{\partial_\varsigma\mathscr{B}_0} \varsigma_M\delta\phi\,\mathrm{d}A = 0.\end{aligned} \tag{16}$$

The virtual gradient fields are given by $\delta\boldsymbol{E} = \frac{1}{2}(\nabla\otimes\delta\boldsymbol{u} + \delta\boldsymbol{u}\otimes\nabla)$ and $\delta\vec{\boldsymbol{H}} = -\nabla\,\delta\phi_{\boldsymbol{M}}$. The finite element approximation is based on the discretization of the domain $\mathscr{B}_0$ in *nelem* finite elements $\mathscr{B}_e$ with $\mathscr{B}_0 = \bigcup_{e=1}^{nelem} \mathscr{B}_e$. Here, an hexahedral element with tri-linear shape function is employed.

6 Numerical Simulations

6.1 Ferromagnetic Hysteresis

A simple example is used to illustrate the ability of the presented constitutive model to account for ferromagnetic hysteresis phenomena. Here a cube of Terfenol-D with an edge length of $L = 20\,\mathrm{mm}$ is considered. The boundary and loading conditions are given in Fig. 1.

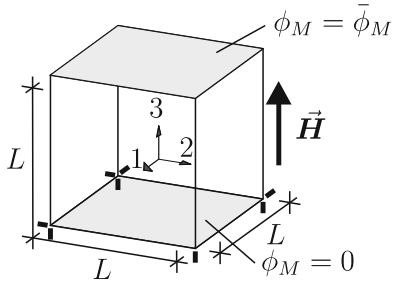

Fig. 1 Boundary and loading conditions for the Terfenol-D specimen

Table 1 Applied material parameters

Terfenol-D
$E_1 = E_3 = 29\ \mathrm{GN/m^2}$, $\nu_{12} = \nu_{13} = 0.25$, $G_{12} = G_{13} = 11.6\ \mathrm{GN/m^2}$
$e_{33} = 40.9\,\mathrm{Vs/Am^2}$, $e_{13} = -43.95\,\mathrm{Vs/Am^2}$, $e_{51} = 28.3\,\mathrm{Vs/Am^2}$
$\mu_1 = \mu_2 = \mu_3 = 2.8025 \cdot 10^{-6}\,\mathrm{Vs/Am}$
$\vec{M}_c = 8.2 \cdot 10^{-3}\,\mathrm{T}$, $E_s^i = 1.08 \cdot 10^{-3}$, $\vec{H}_s^i = 185\,\mathrm{kA/m}$, $k = 1.03\,\mu_3$
$a = 0.15/\mathrm{arctanh}(1/b)\,\mathrm{T}$, $b = 1.04$

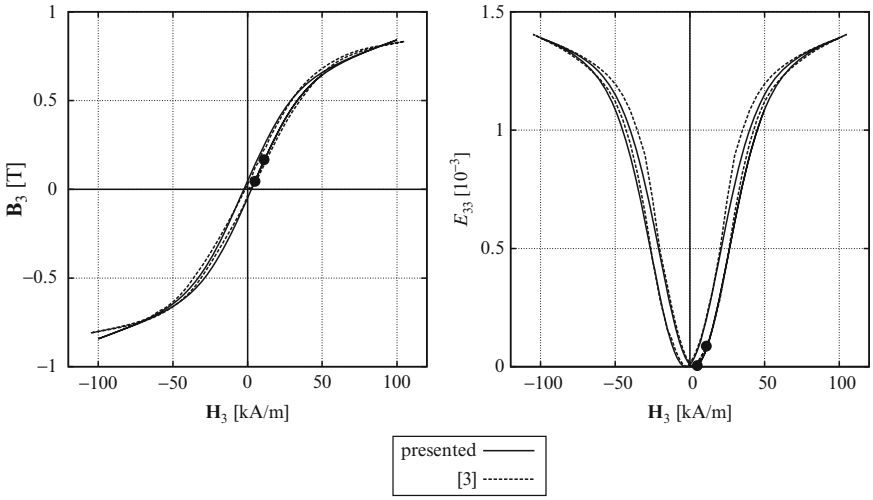

Fig. 2 Ferromagnetic and butterfly hystereses compared to experimental data and the load step for convergence evaluation

The magnetic loading is set with the scalar potential $\bar{\phi}_M$ resulting in a homogeneous magnetic field in 3-direction. The field strength is oscillated in a zigzag function between $\vec{H}_3 = -100\,\mathrm{kA/m}$ and $\vec{H}_3 = 100\,\mathrm{kA/m}$. The applied material parameters based on [2] are given in Table 1.

The resulting hysteresis curves compared with the experimental data of [3] are depicted in Fig. 2. Terfenol-D is a soft magnetic material. Thus, the range of linear behavior is very small. Raising the magnetic field beyond the coercive value $\vec{M}_c$ results in an intense increase of $\vec{B}_3$ and E_{33}.

The growth slows down for values $\vec{H}_3 > 50\,\mathrm{kA/m}$, because of the arctanh-term in the hardening function. This leads to a saturation of the irreversible quantity α for magnetic fields higher 80 kA/m. After unloading only low remanent values of $\vec{B}_3$ and E_{33} are noticed. The ferromagnetic and butterfly hystereses in Fig. 2 show good agreement with the experimental data. It confirms that the model is able to approximate the typical behavior of Terfenol-D.

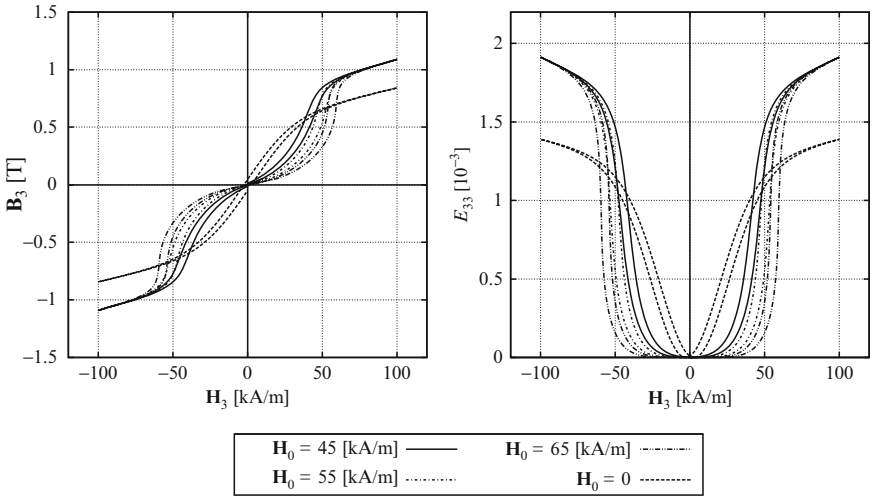

Fig. 3 Ferrimagnetic and butterfly hysteresis for different parameters $\overrightarrow{H}_0$

Table 2 Applied material parameters for PLZT

PLZT
$E_1 = E_3 = 68\ \mathrm{GN/m^2}$, $\nu_{12} = \nu_{13} = 0.35$, $G_{13} = 25.19\ \mathrm{GN/m^2}$
$\mathfrak{e}_{33} = 50.116\,\mathrm{C/m^2}$, $\mathfrak{e}_{13} = -14.96\,\mathrm{C/m^2}$, $\mathfrak{e}_{51} = 38.148\,\mathrm{C/m^2}$
$\varepsilon_1 = \varepsilon_2 = \varepsilon_3 = 1.125\,\mathrm{C/kN\,m^2}$
$\overrightarrow{P}_c = 0.405 \cdot 10^{-3}\,\mathrm{C/m^2}$, $E_s^i = 1.44 \cdot 10^{-3}$, $\overrightarrow{E}_s^i = 0.215\,\mathrm{kV/m}$, $k = 0.9998\,\varepsilon_3$
$a = 0.0005/\mathrm{arctanh}(1/b)\,\mathrm{C/m^2}$, $b = 1.04$

Terfenol-D shows ferrimagnetic behavior for mechanical prestresses. The presented simulations account for different values of the parameter $\overrightarrow{H}_0$. The remaining parameters are modified according to $E_s^i = 0.35 \cdot 10^{-3}$, $\overrightarrow{H}_s^i = 125\,\mathrm{kA/m}$, $k = 1.1\,\mu_3$, $a = 0.1/\mathrm{arctanh}(1/b)\,\mathrm{T}$, $b = 1.05$. The results are given in Fig. 3. Depending on the offset $\overrightarrow{H}_0$ the separated hysteresis curves are shifted differently, which qualitatively represents the occurring material behavior. As mentioned before the model does not include the influence of the mechanical prestress. For this reason the curves are not compared with experimental data.

6.2 Ferroelectric Hysteresis

This example is concerned with the simulation of ferroelectric ceramics. A cubic specimen of lead lanthanum zirconate titanate (PLZT) is simulated. The edge

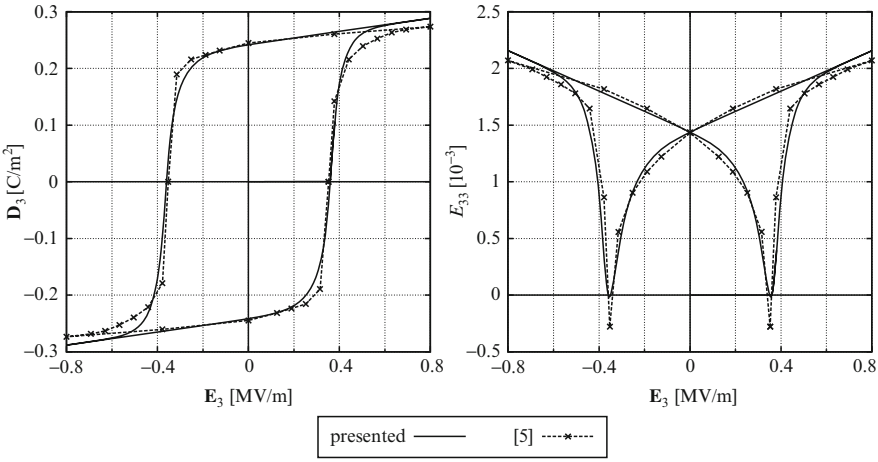

Fig. 4 Ferroelectric und butterfly hysteresis compared to experimental data

length is $L = 10\,\text{mm}$. The boundary conditions are analogue to Fig. 1 but ϕ_E is used instead of ϕ_M. The scalar potential $\bar{\phi}_E$ at the topside is oscillating between $\pm 800\,\text{V}$. The material parameters are given in Table 2. Figure 4 shows the resulting ferroelectric und butterfly hysteresis compared with the results of [5]. A good agreement for both curves is observed. PLZT has a much higher coercive value than Terfenol-D which results in distinctive remanent values of $\vec{D}_3$ and E_{33}.

References

1. Carman GP, Mitrovic M (1995) Nonlinear constitutive relations for magnetostrictive materials with applications to 1-d problems. J Int Mat Sys Struc 6(5):673–683
2. Dapino MJ, Flatau AB, Calkins FT (2006) Statistical analysis of terfenol-d material properties. J Int Mat Sys Struc 17(7):587–599
3. Engdahl G (2000) Handbook of giant magnetostrictive materials. Academic, San Diego
4. Fang DN, Feng X, Hwang KC (2004) Study of magnetomechanical non-linear deformation of ferromagnetic materials: Theory and experiment. Proc Inst Mech Eng Part C J Mech Eng Sci 218(12):1405–1410
5. Hwang SC, Lynch CS, McMeeking RM (1995) Ferroelectric/ferroelastic interactions and a polarization switching model. Acta Metal Mater 43(5):2073–2084
6. Kamlah M Ferroelectric and ferroelastic piezoceramics – Modeling of electromechanical hysteresis phenomena. Continuum Mech Thermodyn 13:219–268
7. Klinkel S (2006) A phenomenological constitutive model for ferroelastic and ferroelectric hysteresis effects in ferroelectric ceramics. Int J Solid Struct 43(22–23):7197–7222
8. Landis CM (2002) Fully coupled multi-axial, symmetric constitutive laws for polycrystalline ferroelectric ceramics. J Mech Phys Solid 50:127–152
9. Linnemann K, Klinkel S, Wagner W (2009) A constitutive model for magnetostrictive and piezoelectric materials. Int J Solid Struct 46:1149–1166
10. McMeeking RM, Landis CM (2002) A phenomenological multi-axial constitutive switching in polycrystalline ferroelectric ceramics. Int J Eng Sci 40:1553–1577

11. Mehling V, Tsakmakis Ch, Gross D (2007) Phenomenological model for the macroscopic material behavior of ferroelectric ceramics. Int J Mech Phys Solids 55:2106–2141
12. Smith RC, Dapino MJ, Seelecke S (2003) Free energy model for hysteresis in magnetostrictive transducers. J Appl Phys 93(1):458–466
13. Wan YP, Fang DN, Hwang KC (2003) Non-linear constitutive relations for magnetostrictive materials. Int J Non-Linear Mech 38(7):1053–1065
14. Zheng XJ, Sun L (2007) A one-dimension coupled hysteresis model for giant magnetostrictive materials. J Magnet Magnet Mater 309(2):263–271
15. Zheng XJ, Liu XE (2005) A nonlinear constitutive model for terfenol-d rods. J Appl Phys 97(5):053901

This page intentionally left blank

The Concept of Material Forces in Nonlinear Electro-elastostatics

Duc Khoi Vu and Paul Steinmann

Abstract In this work we review the application of material forces in electro-elastostatics, especially in the computation of the so-called vectorial J-integral in crack problems. The formulations of material forces take into account the contribution of the outer space surrounding the body under consideration. It is shown that the contribution of the outer space is of importance when the polarization is relatively weak, for example in the case of electronic electro-active polymers, and that this contribution can be ignored if the polarization is much higher than that of the surrounding space like in most piezoelectric materials.

1 Introduction

The problem of nonlinear electro-elastostatics has been recently the subject of many researches due to the interesting application of electroelastic materials in developing artificial muscles, especially the so-called electronic electroactive polymers. In this work, attention is paid to the computation of the J-integral in structures made of electroactive materials using the concept of material forces. We restrict ourself to the static cases in which both the electric field and the deformation field are considered as static. It should be noted that here the concept of the J-integral is an extension of the J-integral in elasticity to electro-elasticity. This extension using the theory of material forces was given by, for example, Pak and Herrmann [1,2], and Epstein and Maugin [3]. In order to maintain the similitude with the formulation of the J-integral

D. Khoi Vu (✉) and P. Steinmann
Lehrstuhl für Technische Mechanik, Friedrich-Alexander-Universität,
Erlangen-Nürnberg, Egerlandstrasse 5, 91058 Erlangen, Germany
e-mail: vu@ltm.uni-erlangen.de; Paul.Steinmann@ltm.uni-erlangen.de

M. Kuna and A. Ricoeur (eds.), *IUTAM Symposium on Multiscale Modelling of Fatigue, Damage and Fracture in Smart Materials*, IUTAM Bookseries 24,
DOI 10.1007/978-90-481-9887-0_12,

in pure mechanics, or in other words, for the J-integral to be path-independent, some special conditions must be specified, namely on the crack faces traction and charge must be zero, see for example, the work of Dascalu and Maugin [4] or Abendroth et al. [5]. The boundary condition on the crack faces increases the complication in analyzing crack problems in electro-elasticity. In order to properly model cracks in electro-elasticity, special attention should be paid to the effect of the medium filling the crack [6, 7]. In this work, material forces are used to compute the so-called vectorial J-integral. The formulations of these material forces take into account the contribution of the outer space surrounding body. This contribution is expressed in the form of the boundary condition at the boundary of the body under consideration. Here the numerical computation is realized with the help of the coupling between the finite element method and the boundary element method.

2 Governing Equations of Nonlinear Electrostatics

The behavior of electric and magnetic fields, as well as their interactions with matter are governed by: (1) Gauss' law for electricity that describes how electric charges produce electric fields; (2) Gauss' law for magnetism that describes the experimental absence of magnetic charges; (3) Ampere's law that describes how currents produce magnetic fields and (4) Faraday's law of induction that describes how changing magnetic fields produce electric fields. To facilitate the formulation process, let us denote the material configuration of the body in the absence of electric and magnetic fields and mechanical loads by $\mathscr{B}_0$. The spatial configuration of the body is denoted by $\mathscr{B}_t$. In the spatial motion problem, the position vector x of a point in the spatial configuration $\mathscr{B}_t$ is described by the nonlinear spatial motion map $x = \varphi(X)$ and the deformation is characterized by the spatial motion deformation gradient $F = \nabla_X \varphi$ wherein $\nabla_X \varphi$ denotes $\partial \varphi_i / \partial X_j$. In the material motion problem, the position vector X of a point in the material configuration $\mathscr{B}_0$ is described by the nonlinear material motion map $X = \Phi(x)$ and the deformation is characterized by the material motion deformation gradient $f = \nabla_x \Phi$.

In reference to the deformed configuration $\mathscr{B}_t$, the Faraday's law is written as:

$$\nabla_x \times \mathbb{e} = \mathbf{0} \tag{1}$$

and the electric Gauss' law:

$$\nabla_x \cdot \mathbb{d} = 0 \tag{2}$$

where $\mathbb{e}$ is the electric field vector and $\mathbb{d}$ is the electric displacement vector in spatial configuration.

At the boundary of the considered body or across a surface of discontinuity within the body, in the absence of surface charges, the electric field vector and the electric displacement vector must satisfy the jump conditions:

$$n \times [\![\mathbb{e}]\!] = \mathbf{0} \quad \text{and} \quad [\![\mathbb{d}]\!] \cdot n = 0 \tag{3.1-2}$$

where at the boundary: $[\![\bullet]\!] = \bullet_{outside} - \bullet_{inside}$.

In order to solve the problem and because the electric field vector $\mathbb{e}$ is conservative, this vector is defined as the gradient of some scalar electric potential ψ:

$$\mathbb{e} = -\nabla_x \psi \tag{4}$$

As constitutive equation, the electric displacement $\mathbb{d}$ can be computed from the electric field vector $\mathbb{e}$ by:

$$\mathbb{d} = \varepsilon_0 \mathbb{e} + \mathbb{p} \tag{5}$$

where $\mathbb{p}$ is the electric polarization density and ε_0 is the vacuum electric permittivity.

The electric body force b_t^e that the electric field exerts on matter can be computed by:

$$b_t^e = [\nabla_x \mathbb{e}] \cdot \mathbb{p} \tag{6}$$

which can be rewritten in the format:

$$b_t^e = \nabla_x \cdot \left[\mathbb{e} \otimes \mathbb{d} - \frac{1}{2} \varepsilon_0 [\mathbb{e} \cdot \mathbb{e}] \boldsymbol{I} \right] \tag{7}$$

wherein $\otimes$ denotes the dyadic product.

In reference to the material configuration $\mathscr{B}_0$, the Faraday's law (1) and the electric Gauss' law (2) are expressed as:

$$\nabla_X \times \mathbb{E} = \mathbf{0} \tag{8}$$

and:

$$\nabla_X \cdot \mathbb{D} = 0 \tag{9}$$

where $\mathbb{E}$ and $\mathbb{D}$ denote the electric field vector and the electric displacement vector, respectively, in the material configuration $\mathscr{B}_0$. The two vectors $\mathbb{E}$ and $\mathbb{D}$ are considered as the pull-back versions of $\mathbb{e}$ and $\mathbb{d}$ in $\mathscr{B}_0$:

$$\mathbb{E} = F^t \cdot \mathbb{e} \quad \text{and} \quad \mathbb{D} = JF^{-1} \cdot \mathbb{d} \tag{10.1-2}$$

and the jump conditions of these quantities in the material configuration $\mathscr{B}_0$ are written in the form:

$$N \times [\![\mathbb{E}]\!] = \mathbf{0} \quad \text{and} \quad [\![\mathbb{D}]\!] \cdot \boldsymbol{N} = 0 \tag{11.1-2}$$

in which, the electric field vector $\mathbb{E}$, as counter part to Eq. 4, can be expressed as the gradient of some scalar electric potential Ψ:

$$\mathbb{E} = -\nabla_X \Psi \tag{12}$$

where Ψ can be computed as the composition of ψ and $\boldsymbol{\varphi}$: $\Psi = \psi \circ \boldsymbol{\varphi}$ and the constitutive equation (5) is now written in the form:

$$\mathbb{D} = \varepsilon_0 J \boldsymbol{C}^{-1} \cdot \mathbb{E} + \mathbb{P} \tag{13}$$

where $\mathbb{P} = J\boldsymbol{F}^{-1} \cdot \mathbb{p}$.

In reference to the material configuration $\mathscr{B}_0$, the electric body force b_t^e can be written as:

$$b_0^e = J b_t^e = \nabla_X \left[\boldsymbol{F}^{-t} \cdot \mathbb{E}\right] \cdot \mathbb{P} \tag{14}$$

or:

$$b_0^e = \nabla_X \cdot \left[\boldsymbol{F}^{-t} \cdot \mathbb{E} \otimes \mathbb{D} - \frac{1}{2}\varepsilon_0 J \left[\mathbb{E} \cdot \boldsymbol{C}^{-1} \cdot \mathbb{E}\right] \boldsymbol{F}^{-t}\right] \tag{15}$$

3 Spatial and Material Motion Problem

In nonlinear electro-elastostatics, we study the deformation of bodies made of hyperelastic material undergoing large deformation and interacting with a static electric field in the absence of magnetic fields, free currents and free electric body charges. In the spatial motion problem, given the geometry, the boundary condition and loading condition, we look for the deformation of the body under consideration. In the material motion problem, given the deformed state of the body, the task is to find back the original configuration of the body.

For the spatial motion problem, the balance equation of linear momentum is the same as that of a normal nonlinear elastic system except the fact that the Cauchy stress tensor $\boldsymbol{\sigma}$ is not symmetric. This is due to the existence of the electric body force. In order to overcome this nonsymmetry we define a total stress tensor $\hat{\boldsymbol{\sigma}}$:

$$\hat{\boldsymbol{\sigma}} = \boldsymbol{\sigma} + \mathbb{e} \otimes \mathbb{d} - \frac{1}{2}\varepsilon_0 \left[\mathbb{e} \cdot \mathbb{e}\right] \boldsymbol{I} \tag{16}$$

and require this total stress tensor to be symmetric and the balance equation of linear momentum is written in the form:

$$\nabla_{\boldsymbol{x}} \cdot \hat{\boldsymbol{\sigma}} + b_t = \mathbf{0} \tag{17}$$

In reference to the material configuration $\mathscr{B}_0$, the counterpart of the balance equation (17) is:

$$\nabla_X \cdot \hat{\boldsymbol{P}} + \boldsymbol{b}_0 = \boldsymbol{0} \tag{18}$$

where $\hat{\boldsymbol{P}}$ is the counterpart of the spatial motion stress tensor $\boldsymbol{P}$ in nonlinear elastostatics and is considered as the pull-back version of the total stress tensor $\hat{\boldsymbol{\sigma}}$:

$$\hat{\boldsymbol{P}} = J\hat{\boldsymbol{\sigma}} \cdot \boldsymbol{F}^{-t} \tag{19}$$

At the boundary of the considered body or across a surface of discontinuity within the body, the jump conditions for $\hat{\boldsymbol{\sigma}}$ and $\hat{\boldsymbol{P}}$ are:

$$[\![\hat{\boldsymbol{\sigma}}]\!] \cdot \boldsymbol{n} = \boldsymbol{0} \quad \text{and} \quad [\![\hat{\boldsymbol{P}}]\!] \cdot \boldsymbol{N} = \boldsymbol{0} \tag{20.1-2}$$

To simplify the problem, let us assume that we only have the jump conditions (3), (11) and (20) at the boundary of the body under consideration and that these conditions can be cast in the form: $\mathbb{D} \cdot \boldsymbol{N} = -q_0$, $\mathbb{d} \cdot \boldsymbol{n} = -q_t$, $\hat{\boldsymbol{P}} \cdot \boldsymbol{N} = \hat{\boldsymbol{t}}_0$, $\hat{\boldsymbol{\sigma}} \cdot \boldsymbol{n} = \hat{\boldsymbol{t}}_t$. In this case, the spatial motion problem can be rewritten as:

$$\begin{aligned} \nabla_X \cdot \hat{\boldsymbol{P}} + b_0 = \boldsymbol{0} \quad &\text{and} \quad \nabla_X \cdot \mathbb{D} = 0 \quad \text{in } \mathscr{B}_0 \\ \hat{\boldsymbol{P}} \cdot \boldsymbol{N} = \hat{\boldsymbol{t}}_0 \quad &\text{and} \quad \mathbb{D} \cdot \boldsymbol{N} = -q_0 \quad \text{on } \partial\mathscr{B}_0 \end{aligned} \tag{21}$$

in reference to the material configuration $\mathscr{B}_0$, or:

$$\begin{aligned} \nabla_x \cdot \hat{\boldsymbol{\sigma}} + \boldsymbol{b}_t = \boldsymbol{0} \quad &\text{and} \quad \nabla_x \cdot \mathbb{d} = 0 \quad \text{in } \mathscr{B}_t \\ \hat{\boldsymbol{\sigma}} \cdot \boldsymbol{n} = \hat{\boldsymbol{t}}_t \quad &\text{and} \quad \mathbb{d} \cdot \boldsymbol{n} = -q_t \quad \text{on } \partial\mathscr{B}_t \end{aligned} \tag{22}$$

in reference to the spatial configuration $\mathscr{B}_t$.

In order to formulate the governing equations of the material problem, we assume the existence of some energy densities $W_{0\mathbb{e}}(\boldsymbol{F}, \mathbb{e}; \boldsymbol{X})$, $W_{0\mathbb{E}}(\boldsymbol{F}, \mathbb{E}; \boldsymbol{X})$, $W_{0\mathbb{e}}|_{\boldsymbol{F},\mathbb{e},\boldsymbol{X}} = W_{0\mathbb{E}}|_{\boldsymbol{F},\mathbb{E},\boldsymbol{X}}$ such that the stress tensor $\boldsymbol{\sigma}$ and the electric polarization density $\mathbb{p}$ can be computed by:

$$\boldsymbol{\sigma} = J^{-1}\boldsymbol{P} \cdot \boldsymbol{F}^t = J^{-1}[\partial_{\boldsymbol{F}} W_{0\mathbb{e}}] \cdot \boldsymbol{F}^t \quad \text{and} \quad \mathbb{p} = -J^{-1}\partial_{\mathbb{e}} W_{0\mathbb{e}} \tag{23.1-2}$$

With this assumption, in the material motion problem, the balance equation of the material motion problem in reference to the spatial configuration $\mathscr{B}_t$ can be shown to be:

$$\nabla_X \cdot \hat{\boldsymbol{\Sigma}} + \boldsymbol{B}_0 = \boldsymbol{0} \qquad \text{in } \mathscr{B}_0 \tag{24}$$

where the material stress tensor $\hat{\boldsymbol{\Sigma}}$ and the material body force $\hat{\boldsymbol{B}}_0$ are defined as:

$$\hat{\boldsymbol{\Sigma}} := \hat{W}_{0\boldsymbol{F}}\boldsymbol{I} - \boldsymbol{F}^t \cdot \hat{\boldsymbol{P}} + \mathbb{E} \otimes \mathbb{D} \tag{25}$$

and:

$$\hat{\boldsymbol{B}}_0 := -\partial_{\boldsymbol{\Phi}} \hat{W}_{0f} - \boldsymbol{f}^{-t} \cdot \boldsymbol{b}_0 \tag{26}$$

In the above formulations, $\hat{W}_{0f}$ is defined by: $\hat{W}_{0f} = \hat{W}_{0f}(\boldsymbol{f}, \mathbb{e}, \boldsymbol{\Phi})$, $\hat{W}_{0f}\Big|_{\boldsymbol{f},\mathbb{e},\boldsymbol{\Phi}} = \hat{W}_{0\boldsymbol{F}}\Big|_{\boldsymbol{F},\mathbb{E},\boldsymbol{X}}$ and:

$$\hat{W}_{0\boldsymbol{F}}(\boldsymbol{F}, \mathbb{E}; \boldsymbol{X}) = W_{0\mathbb{E}}(\boldsymbol{F}, \mathbb{E}; \boldsymbol{X}) - \frac{1}{2}\varepsilon_0 J \boldsymbol{C}^{-1} : [\mathbb{E} \otimes \mathbb{E}] \tag{27}$$

In reference to the deformed configuration, the counterpart of Eq. 24 is:

$$\nabla_{\boldsymbol{x}} \cdot \hat{\boldsymbol{p}} + \boldsymbol{B}_t = \boldsymbol{0} \tag{28}$$

where the material stress tensor $\hat{\boldsymbol{p}}$ and the material body force $\hat{\boldsymbol{B}}_t$ are defined as:

$$\hat{\boldsymbol{p}} := \hat{W}_{tf} \boldsymbol{F}^t - \boldsymbol{F}^t \cdot \hat{\boldsymbol{\sigma}} + \boldsymbol{F}^t \cdot \mathbb{e} \otimes \mathbb{d} \tag{29}$$

and:

$$\hat{\boldsymbol{B}}_t = -\partial_{\boldsymbol{\Phi}} \hat{W}_{tf} - \boldsymbol{f}^{-t} \cdot \boldsymbol{b}_t \tag{30}$$

in which $\hat{W}_{tf}$ is defined by: $\hat{W}_{tf} = \hat{W}_{tf}(\boldsymbol{f}, \mathbb{e}, \boldsymbol{\Phi})$, $\hat{W}_{tf}\Big|_{\boldsymbol{f},\mathbb{e},\boldsymbol{\Phi}} = J^{-1}\, \hat{W}_{0\boldsymbol{F}}\Big|_{\boldsymbol{F},\mathbb{E},\boldsymbol{X}}$.

4 Material Forces in Fracture Mechanics

One application of material forces in fracture mechanics is the computation of the so-called vectorial J-integral. In order to show how the material forces can be used in computing this vectorial J-integral, let us consider a structure with a crack that lies in a subdomain $\mathscr{V}_0$ of $\mathscr{B}_0$. If we divide the boundary $\partial\mathscr{V}_0$ of V_0 into two parts: a regular part and a singular part, which denotes the crack tip, then the vectorial J-integral $\mathfrak{J}$ is defined as:

$$\mathfrak{J} = \lim_{\partial V_0^r \to \boldsymbol{0}} \int_{\partial \mathscr{V}_0^r} \hat{\boldsymbol{\Sigma}} \cdot \boldsymbol{N} dS \tag{31}$$

where $\partial\mathscr{V}_0^r$ is the regular part and $\partial\mathscr{V}_0^s$ is the singular part of the boundary. By denoting the material force acting on the regular part as $\mathfrak{f}^{sur,r}$ and the material force acting on the singular part as $\mathfrak{f}^{sur,s}$, we see that these two forces must be in equilibrium:

$$\mathfrak{f}^{sur,s} + \mathfrak{f}^{sur,r} = \boldsymbol{0} \tag{32}$$

where:

$$\mathfrak{f}^{sur,s} = \int_{\partial \mathscr{V}_0^s} \hat{\boldsymbol{\Sigma}} \cdot \boldsymbol{N} dS \quad \text{and} \quad \mathfrak{f}^{sur,r} = \int_{\partial \mathscr{V}_0^r} \hat{\boldsymbol{\Sigma}} \cdot \boldsymbol{N} dS \tag{33.1-2}$$

As result, the vectorial J-integral $\mathfrak{J}$ can be computed as:

$$\mathfrak{J} = -\mathfrak{f}^{sur,s} = -\int_{\partial \mathscr{V}_0^s} \hat{\boldsymbol{\Sigma}} \cdot \boldsymbol{N} dS \tag{34}$$

By using the finite element method, this material force can be discretized as:

$$\mathfrak{J}^h = -\mathop{\mathsf{A}}_{e=1}^{nel} \int_{\mathscr{B}_0^e} \hat{\boldsymbol{\Sigma}} \cdot \nabla_X N^n dV \tag{35}$$

where n is the crack tip node, $\mathscr{B}_0^e$ is the domain of element e, nel is the number of elements inside the subdomain $\mathscr{V}_0$ and N is element shape functions.

5 Numerical Example

As numerical example, we consider an rectangular plate (width $\times$ height $= 30\,\mu\text{m} \times 60\,\mu\text{m}$) with a crack-like notch at the center of the plate. Between the upper and lower edge of the plate we put an electric potential difference of 1,000 V. The displacement of the upper and lower edge of the plate is fixed in the vertical direction. To fix the rigid body motion, the displacement of one of the corners is fixed in horizontal direction. The material property of the plate is given by the energy density function $W_{0\mathbb{E}}(\boldsymbol{F}, \mathbb{E})$, which is defined as:

$$\begin{aligned} W_{0\mathbb{E}}(\boldsymbol{F}, \mathbb{E}) = \frac{\mu}{2}[\boldsymbol{C} : \boldsymbol{I} - 3] - \mu \ln J + \frac{\lambda}{2}[\ln J]^2 + \alpha \boldsymbol{I} : [\mathbb{E} \otimes \mathbb{E}] \\ + \beta \boldsymbol{C} : [\mathbb{E} \otimes \mathbb{E}] - \tfrac{1}{2}[\varepsilon_1 - \varepsilon_0] J \boldsymbol{C}^{-1} : [\mathbb{E} \otimes \mathbb{E}] \end{aligned} \tag{36}$$

in which ϵ_1 is the electric permittivity of the plate, $\alpha = 0.2\varepsilon_0$, $\beta = 2\varepsilon_0$, $\varepsilon_1 = 5\varepsilon_0$, $\varepsilon_0 = 8.854 \times 10^{-12} \left[\frac{\mathsf{F}}{\mathsf{m}}\right]$. The plate is modeled using 2,000 quadrangle 4-node linear finite elements and the outer space surrounding the plate is modeled using 220 2-node linear boundary elements. The finite element mesh is presented in Fig. 1. Boundary elements are linked to the finite element mesh on the boundary of the plate.

The result is presented in Fig. 2 for the case only the plate is modeled using finite elements and in Fig. 3 when the contribution of the outer space is taken into account with the help of boundary elements. It is observed that in the case considered here,

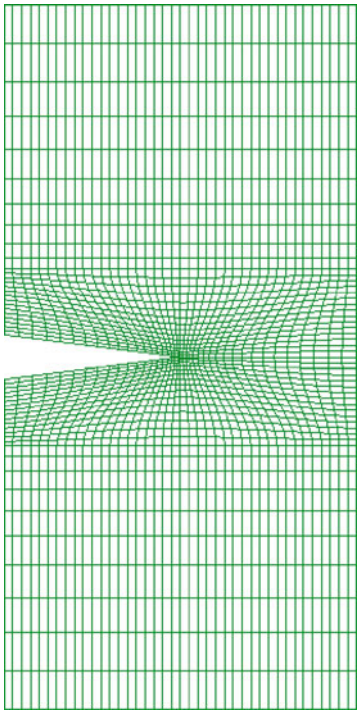

Fig. 1 Finite element mesh used in the computation of the vectorial J-integral. The outer space is modeled by boundary elements (not shown here in this Figure)

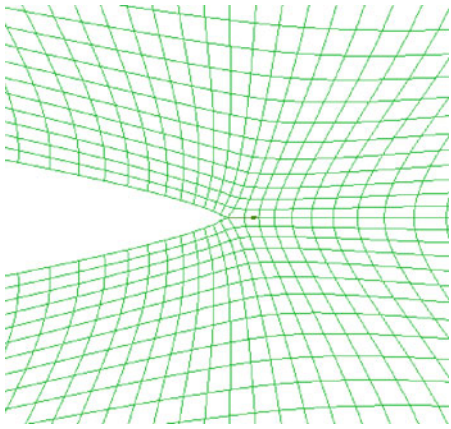

Fig. 2 Vectorial J integral at crack tip node by using only finite elements ignoring the contribution of the outer space: $|\mathfrak{J}| = 5.17 \times 10^{-3}\,\mathrm{Nm}^{-1}$

the influence of outer space is significant and should be taken into account. It can also be proven that in the case where the electric permittivity of the plate is much higher than that of the outer space, the two results are practically the same, which means that the contribution of the outer space is negligible and can be conveniently ignore.

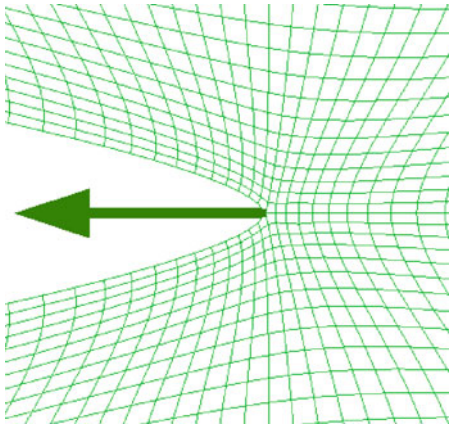

Fig. 3 Vectorial J integral at crack tip node by using finite elements and boundary elements: $|\mathfrak{J}| = 42.08 \times 10^{-3}\mathrm{Nm}^{-1}$

6 Conclusion

In this work, the application of material forces in computing the vectorial J-integral is considered. It is observed that special attention should be paid to the outer space surrounding the body of interest. The contribution of the outer space is of importance when the polarization is relatively weak, for example in the case of electronic electro-active polymers, and that this contribution can be ignored if the polarization is much higher than that of the surrounding space like in most piezoelectric materials. In the case contribution of the outer space is of importance, boundary element method or other methods should be used in order to get the correct result.

References

1. Pak YE, Herrmann G (1986) Conservation laws and the material momentum tensor for the elastic dielectric. Internat J Engrg Sci 24:1365–1374
2. Pak YE, Herrmann G (1986) Crack extension force in a dielectric medium. Internat J Engrg Sci 24:1375–1388
3. Epstein M, Maugin GA (1991) Energy-momentum tensor and J-integral in electrodeformable bodies. Internat J Appl Electromagn Mater 2:141–145
4. Dascalu C, Maugin GA (1994) Energy-release rates and path-independent integrals in electroelastic crack propagation. Int J Engng Sci 32(5):755–765
5. Abendroth M, Groh U, Kuna M, Ricoeur A (2002) Finite element-computation of the electromechanical J-integral for 2-D and 3-D crack analysis. Int J Fract 114:359–378
6. Qi H, Fang D, Yao Z (2001) Analysis of electric boundary condition effects on crack propagation in piezoelectric ceramics. Acta Mech Sinica 17(1):59–70
7. Wang XD, Jiang LY (2003) The effective electroelastic property of piezoelectric media with parallel dielectric cracks. Internat J Solid Struct 40:5287–5303

This page intentionally left blank

Permeable Interfacial Crack in Electrostrictive Materials

Cun-Fa Gao and Yiu-Wing Mai

Abstract This paper studies the two-dimensional problem of an interface crack between two dissimilar electrostrictive materials under electric loads based on complex variable method. The solutions of complex potentials are derived by use of the permeable crack model. It is found that the singular structure of total stress is the same as that in traditional bi-materials, and the intensity of total stress is dependent on the electric boundary conditions adopted on the crack faces, and the Maxwell stresses on the crack faces and at infinity.

1 Introduction

Layered composites consisting of electrostrictive materials have important application in engineering. Cracking may occur at the interface when the materials are subjected to electrical loads. McMeeking [5] studied the electrostrictive stresses near crack-like flaws, and gave comprehensive discussions about the effects of applied electric fields on crack growth. Ru et al. [10] addressed the electric-field induced interfacial cracking in multilayer electrostrictive actuators based on the small-scale saturation solutions. Recently, McMeeking and Landis [6] and Kuang [3] pointed out that the Maxwell stresses in the space surrounding should be taken into account since the electric field exists in every non-conducting material. More recently, Ricoeur and Kuna [8,9] examine the effects of Maxwell stresses on fracture of piezoelectric materials. In the present work, we study a permeable interface crack between two dissimilar electrostrictive materials by using the complex variable

C.-F. Gao (✉)
College of Aerospace Engineering, Nanjing University of Aeronautics & Astronautics, Nanjing 210016, China
e-mail: cfgao@nuaa.edu.cn

Y.-W. Mai
Centre for Advanced Materials Technology (CAMT), School of Aerospace, Mechanical and Mechatronic Engineering J07, University of Sydney, Sydney, NSW 2006, Australia
e-mail: yiu-wing.mai@sydney.edu.au

M. Kuna and A. Ricoeur (eds.), *IUTAM Symposium on Multiscale Modelling of Fatigue, Damage and Fracture in Smart Materials*, IUTAM Bookseries 24,
DOI 10.1007/978-90-481-9887-0_13,

approach. Emphasis is placed on the investigation of the effects of Maxwell stresses on the singularity of total stresses. Following the introduction, in Section 2 we outline the basic equations required for this study. In Sections 3 we derive the general solutions for a permeable interface crack in order to discuss the effects of Maxwell stresses and finally conclusions are given in Section 4.

2 Basic Equations

Consider an isothermal and isotropic electrostrictive material, and neglect the piezoelectricity, the constitutive equations of the material can be expressed as [4, 11]:

$$\sigma_{ij} = 2Ge_{ij} + \lambda e_{kk}\delta_{ij} - \frac{1}{2}(a_1 E_i E_j + a_2 E_k E_k \delta_{ij}), \tag{1}$$

$$D_i = (\varepsilon\delta_{ij} + a_1 e_{ij} + a_2 e_{kk}\delta_{ij})E_j, \tag{2}$$

where, $i, j = 1, 2, 3$. σ_{ij}, e_{ij}, D_i and E_j are stress, strain, electric displacement and electric field intensity, respectively. a_1 and a_2 are two independent electrostrictive coefficients in isotropic materials. ε is the permittivity at the state without any strain. δ_{ij} is Kronecker delta. λ and G are Lame constants expressed in terms of Young's modulus E and Poisson ratio ν by: $\lambda = E\nu/[(1+\nu)(1-2\nu)]$, and $G = E/[2(1+\nu)]$.

When the strain is so small, the coupling effects between strain and electric field can be neglected, so the electric field may be obtained directly from the theory of electrostatics. In this case, the components of electric fields and electric displacement can be expressed as

$$E_1 = -\mathrm{Re}[w'(z)],\ E_2 = \mathrm{Im}[w'(z)], \tag{3}$$

$$D_1 = -\varepsilon\mathrm{Re}[w'(z)],\ D_2 = \varepsilon\mathrm{Im}[w'(z)]. \tag{4}$$

After $w(z)$ is determined subject to given electric boundary conditions, all the fields of stresses can be obtained as below [2]:

2.1 Pseudo Total Stresses $\tilde{\sigma}_{ij}$

$$\tilde{\sigma}_{22} + \tilde{\sigma}_{11} = \kappa w'(z)\overline{w'(z)} + 2\left[\varphi'(z) + \overline{\varphi'(z)}\right], \tag{5}$$

$$\tilde{\sigma}_{22} - \tilde{\sigma}_{11} + 2i\tilde{\sigma}_{12} = \kappa w''(z)\overline{w(z)} + 2\left[\bar{z}\varphi''(z) + \psi'(z)\right], \tag{6}$$

Where $\kappa = -(1-2\nu)(a_1+2a_2)/[4(1-\nu)]$, and $\varphi(z)$ and $\psi(z)$ are two complex functions to be determined.

2.2 Maxwell Stresses σ_{ij}^{M}

$$\sigma_{22}^{M} + \sigma_{11}^{M} = 0, \tag{7}$$

$$\sigma_{22}^{M} - \sigma_{11}^{M} + 2i\sigma_{12}^{M} = -\varepsilon_m \Omega'(z), \tag{8}$$

where

$$\Omega'(z) = \left[w'(z)\right]^2. \tag{9}$$

2.3 Electroelastic Stresses σ_{ij}

$$\sigma_{22} + \sigma_{11} = \kappa w'(z)\,\overline{w'(z)} + 2\left[\varphi'(z) + \overline{\varphi'(z)}\right], \tag{10}$$

$$\sigma_{22} - \sigma_{11} + 2i\sigma_{12} = \kappa w''(z)\,\overline{w(z)} + 2\left[\bar{z}\varphi''(z) + \psi'(z)\right] + \varepsilon_m \Omega'(z). \tag{11}$$

Similarly, the displacement field can be finally obtained as:

$$\left[K\varphi(z) - z\overline{\varphi'(z)} - \overline{\psi(z)} + \chi\overline{\Omega(z)} - \frac{\kappa}{2} w(z)\,\overline{w'(z)}\right] = 2\mu\left(u_1 + iu_2\right), \tag{12}$$

where $K = 3 - 4\nu$ and $\chi = (a_1 - 2\varepsilon_m)/4$.

2.4 Boundary Equations

From Eqs. (5) and (6) we have:

$$\tilde{\sigma}_{22} - i\tilde{\sigma}_{12} = \frac{1}{2}\kappa w'(z)\,\overline{w'(z)} + \frac{1}{2}\kappa\overline{w''(z)}w(z) + \varphi'(z) + \overline{\varphi'(z)} + z\overline{\varphi''(z)} + \overline{\psi'(z)} \tag{13}$$

Introduce a new function,

$$W(z) = \frac{1}{2}\kappa[\bar{w}'(z)\,w'(\bar{z}) + \bar{w}''(z)\,w(\bar{z})] + \bar{\varphi}'(z) + z\bar{\varphi}''(z) + \bar{\psi}'(z). \tag{14}$$

Then, we have

$$W(\bar{z}) = \frac{1}{2}\kappa[\overline{w'(z)}w'(z) + \overline{w''(z)}w(z)] + \overline{\varphi'(z)} + \bar{z}\overline{\varphi''(z)} + \overline{\psi'(z)}. \tag{15}$$

Eq. (15) gives:

$$\frac{1}{2}\kappa[\overline{w'(z)}w'(z) + \overline{w''(z)}w(z)] + \overline{\varphi'(z)} + \overline{\psi'(z)} = W(\bar{z}) - \bar{z}\overline{\varphi''(z)}. \tag{16}$$

Substituting Eq. (16) into Eq (13) yields:

$$\tilde{\sigma}_{22} - i\tilde{\sigma}_{12} = \Phi(z) + W(\bar{z}) + (z - \bar{z})\overline{\Phi'(z)}, \tag{17}$$

where $\Phi(z) = \varphi'(z)$.

Similarly, we have from Eq. (12) that:

$$2G(u_{1,1} + iu_{2,1}) = K\Phi(z) - W(\bar{z}) - (z - \bar{z})\overline{\Phi'(z)} + \chi\overline{\Omega'(z)}, \tag{18}$$

where $u_{i,1} = \partial u_i / \partial x_1$.

3 Analysis

Consider an interface crack between two dissimilar electrostrictive half-planes S_1 and S_2, as shown in Fig. 1. Assume that the upper and lower planes are surrounded by free space with a dielectric constant ε_∞ and electric field D_2^∞.

In this case, the potential functions D_2^∞ can be expressed as

$$w_k(z) = c_k^\infty z + w_{k0}(z), \; k = 1, 2, \; z \in S_k, \tag{19}$$

where c_k^∞ are complex constants to be obtained, and $w_{k0}(\infty) = 0$.

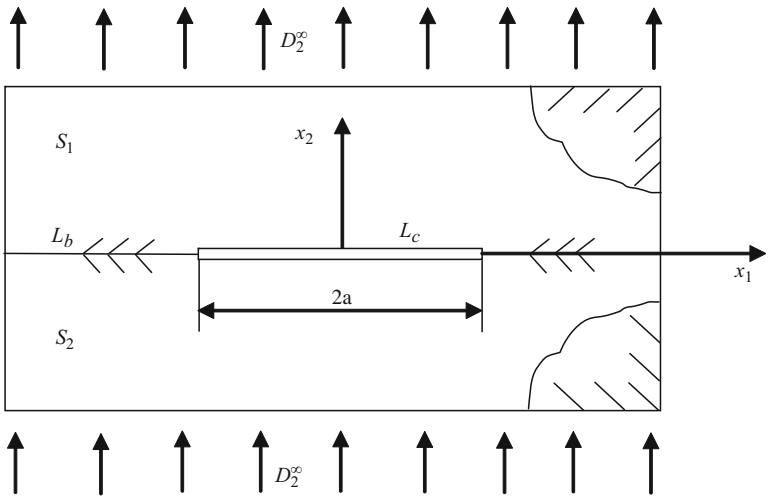

Fig. 1 An interface crack in two dissimilar electrostrictive materials

For the case of a permeable crack, the electric continuous conditions on the crack faces require:

$$D_2^+(x_1) = D_2^-(x_1),\ E_1^+(x_1) = E_1^-(x_1). \tag{20}$$

Omitting some details we finally have

$$c_k^\infty = iE_2^\infty,\ w_{k0}(z) = 0,\ w_k(z) = iE_2^\infty z,\ \Omega_k'(z) = -\left(E_2^\infty\right)^2. \tag{21}$$

Also, along the x_1 axis

$$[\tilde{\sigma}_{22} - i\tilde{\sigma}_{12}]_1 = [\tilde{\sigma}_{22} - i\tilde{\sigma}_{12}]_2,\ -\infty < x_1 < +\infty \tag{22}$$

From Eq. (17) we obtain

$$[\tilde{\sigma}_{22} - i\tilde{\sigma}_{12}]_1 = [\tilde{\sigma}_{22} - i\tilde{\sigma}_{12}]_1^\infty + \Phi_{10}^+(x_1) + W_{10}^-(x_1), \tag{23}$$

$$[\tilde{\sigma}_{22} - i\tilde{\sigma}_{12}]_2 = [\tilde{\sigma}_{22} - i\tilde{\sigma}_{12}]_2^\infty + \Phi_{20}^-(x_1) + W_{20}^+(x_1). \tag{24}$$

Substituting Eqs. (23) and (24) into Eq. (22) leads to

$$\left[\Phi_{10}^+(x_1) - W_{20}^+(x_1)\right] - \left[\Phi_{20}^-(x_1) - W_{10}^-(x_1)\right] = 0_{,-\infty<x_1<+\infty},$$

which results in

$$\Phi_{10}(z) - W_{20}(z) = 0,\ z \in S_1, \tag{25}$$

$$\Phi_{20}(z) - W_{10}(z) = 0, z \in S_2. \tag{26}$$

Using Eqs. (18), (25) and (26), we have

$$\Delta u_{,1} = (u_{1,1} + iu_{2,1})_1 - (u_{1,1} + iu_{2,1})_2 = \frac{1}{2}\left[\lambda_{12}\Phi_{10}^+(x_1) - \lambda_{21}\Phi_{20}^-(x_1)\right], \tag{27}$$

where

$$\lambda_{12} = \frac{K_1}{G_1} + G_2, \quad \lambda_{21} = \frac{K_2}{G_2} + G_1.$$

Define a new function as

$$M_0(z) = \begin{cases} \lambda_{12}\Phi_{10}(z), z \in S_1 \\ \lambda_{21}\Phi_{20}(z),\ z \in S_2 \end{cases}. \tag{28}$$

Then, Eq. (27) becomes

$$2\Delta u_{,1} = M_0^+(x_1) - M_0^-(x_1). \tag{29}$$

It is obvious that $M_0(z)$ is an analytic function in the whole plane except the crack. Moreover, on the crack faces the total stresses can be expressed as

$$[\tilde{\sigma}_{22} - i\tilde{\sigma}_{12}]_1 = [\tilde{\sigma}_{22} - i\tilde{\sigma}_{12}]_2 = \left(\sigma_{22}^M - i\sigma_{12}^M\right)_c, \tag{30}$$

where σ_{22}^M and σ_{12}^M stand for the Maxwell stress inside the crack.

In addition, we have from Eq. (23) that

$$[\tilde{\sigma}_{22} - i\tilde{\sigma}_{12}]_1 = [\tilde{\sigma}_{22} - i\tilde{\sigma}_{12}]_1^{\infty} + \lambda_{12}^{-1} M_0^+(x_1) + \lambda_{21}^{-1} M_0^-(x_1). \tag{31}$$

Inserting Eq. (30) in Eq. (31) produces

$$M_0^+(x_1) + \frac{\lambda_{12}}{\lambda_{21}} M_0^+(x_1) = m_0, \tag{32}$$

where

$$m_0 = \lambda_{12}\left[\left(\sigma_{22}^M - i\sigma_{12}^M\right)_c - (\tilde{\sigma}_{22} - i\tilde{\sigma}_{12})^{\infty}\right]. \tag{33}$$

It can be found from Eq. (32) that the singular structure of the total stresses at the tip of the interface crack is the same as that in the case of traditional bi-materials.

For a crack in a single material, $\lambda_{12} = \lambda_{21}$ and Eqs. (32) and (33) become

$$\Phi_0^+(x_1) + \Phi_0^-(x_1) = m_0, \tag{34}$$

$$m_0 = \left(\sigma_{22}^M - i\sigma_{12}^M\right)_c - \left(\sigma_{22}^M - i\sigma_{12}^M\right)^{\infty} = \left(\frac{1}{2\varepsilon_0} - \frac{1}{2\varepsilon_\infty}\right)\left(D_2^{\infty}\right)^2. \tag{35}$$

The solution of Eq. (34) is [7]

$$\Phi_0(z) = \frac{1}{2}\left[1 - \frac{z}{\sqrt{z^2 - a^2}}\right] m_0. \tag{36}$$

Define the intensity factor of the total stress as

$$K_I + iK_{II} = \lim_{r \to 0} \sqrt{2\pi r}\,[\tilde{\sigma}_{22} + i\tilde{\sigma}_{12}]. \tag{37}$$

Using Eqs. (37), (17), (25) and (36) we finally obtain

$$K_I = \sqrt{\pi a}\left(\frac{1}{2\varepsilon_\infty} - \frac{1}{2\varepsilon_0}\right)\left(D_2^{\infty}\right)^2, K_{II} = 0. \tag{38}$$

This result is consistent with that obtained in [1], that is, the applied electric field may enhance or retard crack growth, which is dependent on the electric boundary conditions adopted on the crack faces, and the Maxwell stresses on the crack faces and at infinity.

4 Conclusions

We studied the 2D problem of an interface crack between two dissimilar electrostrictive solids by using the complex variable method combined with the analytical extension of complex functions. The general solutions are presented for the complex potentials based on the permeable crack model. It is found that the singular structure of total stress is the same as that in traditional materials with an interface crack. Especially, for a crack in a homogeneous electrostrictive material, it can be seen that the total stresses have the classical $r^{-1/2}$ crack tip singularity, and that the applied electric field may enhance or retard crack growth, which is dependent on the electric boundary conditions adopted on the crack faces, and the Maxwell stresses on the crack faces and at infinity.

Acknowledgments CFG thanks the financial support from the National Natural Science Foundation of China (10672076) and the Australian Research Council (ARC) as Visiting Professor to the CAMT at Sydney University. YWM also thanks the ARC for supporting this research project (DP0665856).

References

1. Gao CF, Mai Y-W, Zhang N (2009) Solution of a crack in an electrostrictive solid. Int J Solids Struct 47:444–453
2. Jiang Q, Kuang ZB (2004) Stress analysis in two dimensional electrostrictive material with an elliptic rigid conductor. Eur J Mech A Solids 23:945–956
3. Kuang ZB (2008) Some variational principles in elastic dielectric and elastic magnetic materials. Eur J Mech A Solids 27:504–514
4. Landau LD, Lifshitz EM (1960) Electrodynamics of continous media, Pergamon Press, Oxford
5. McMeeking RM (1989) Electrostrictive stresses near crack-like flaws. Zeitschrift fur Angewandte Mathematik und Physik 40:615–627
6. McMeeking RM, Landis CM (2005) Electrostatic forces and stored energy for deformable dielectric materials. ASME, J Appl Mech 72:581–590
7. Muskhelisvili NI (1975) Some basic problems of mathematical theory of elasticity. Noordhoff, Gronigen
8. Ricoeur A, Kuna M (2009) Electrostatic tractions at crack faces and their influence on the fracture mechanics of piezoelectrics. Int J Fract 157:3–12
9. Ricoeur A, Kuna M (2009) Electrostatic tractions at dielectric interfaces and their implication for crack boundary conditions. Mech Res Commun 36:330–335
10. Ru CQ, Mao X, Epstein M (1998) Electric-field induced interfacial cracking in multilayer electrostrictive actuators. J Mech Phys Solids 46:1301–1318
11. Stratton JA (1941) Electromagnetic theory. McGraw-Hill, New York

This page intentionally left blank

Some Numerical Studies with X-FEM for Cracked Piezoelectric Media

Éric Béchet and Meinhard Kuna

Abstract Piezoelectric materials are increasingly used in actuators and sensors. New applications can be found as constituents of smart composites for adaptive electromechanical structures. Under in service loading, phenomena of crack initiation and propagation may occur due to high electromechanical field concentrations. In the past few years, the extended finite element method (X-FEM) has been gained much attention to model cracks in structural materials. This paper presents the application of X-FEM to the coupled electromechanical crack problem in two-dimensional piezoelectric structures. The convergence of solutions is investigated in the energy norm and for the stress intensity factors. Then, some studies about inaccuracies in the stresses near the crack tip are reported.

1 Introduction

The Extended Finite Element Method (X-FEM) [9] has been originally designed for crack growth analysis in isotropic elastic materials. In conjunction with level-sets [10] as a mean for representing the crack geometry, it is a powerful way to get rid of the costly constrained remeshing needed with conventional finite element techniques. Under certain circumstances, this method is also able to achieve regular convergence rates in the energy error even for a cracked domain [3].

Piezoelectric materials exhibit a coupling between mechanical and electrical variables, as well as transversely isotropic material characteristics. This leads to completely different near-crack tip fields of the mechanical and electrical quantities.

É. Béchet (✉)
Department of Aerospace and Mechanical Engineering, Université de Liége,
Chemin des Chevreuils 1, 4000 Liége, Belgium
e-mail: eric.bechet@ulg.ac.be

M. Kuna
Institut für Mechanik und Fluiddynamik, Technische Universität Bergakademie Freiberg,
Lampadiusstraße 4, 09596 Freiberg, Germany
e-mail: meinhard.kuna@imfd.tu-freiberg.de

M. Kuna and A. Ricoeur (eds.), *IUTAM Symposium on Multiscale Modelling of Fatigue, Damage and Fracture in Smart Materials*, IUTAM Bookseries 24,
DOI 10.1007/978-90-481-9887-0_14,

Moreover, the electrical variables show a singularity as well. Comprehensive reviews about the analytical and experimental developments in fracture mechanics of piezoelectric and ferroelectric materials can be found in [4, 8, 12]. During last two decades, special finite element algorithms for crack analysis (such as crack tip elements, J-integrals or crack closure techniques) have been adopted to cracks in piezoelectric materials quite well, which was summarized in [7]. To treat this new crack analysis problems by means of the X-FEM, specific crack analysis tools and changes in the enrichment functions are needed, which allow to represent the crack – both in the mechanical and electrical functional spaces. It is worth noting that the methodology presented here may be applied to anisotropic elastic materials such as composites as well.

2 Piezoelectric Model

We recall the linear material equations of piezoelectricity under assumption of small strains. The material (PZT4) considered here for the numerical experiments may be either part of an actuator or a sensor (see e.g. [6]). However, devices that usually withstand higher loads are actuators. The cracked domain is denoted by Ω and its boundary $\partial\Omega \cup C^+ \cup C^-$ by B. The boundary B is subjected to boundary conditions: At the part B_n tractions or the electric field are imposed (natural boundary conditions), whereas at part B_e the displacement u_i or the electrical potential φ are prescribed (essential boundary conditions). The crack faces C^+ and C^- are assumed to be both traction-free and electrically impermeable. Throughout the paper, the international system of units (SI) is chosen.

$$\left.\begin{array}{l}\sigma_{ij}n_j = 0\\ D_i n_j = 0\end{array}\right\} \text{ on } C^- \cup C^+ , \quad \left.\begin{array}{l}\sigma_{ij}n_j = t_j\\ D_i n_j = q\end{array}\right\} \text{ on } B_n , \quad \left.\begin{array}{l}u_i = u_i^0\\ \varphi = \varphi^0\end{array}\right\} \text{ on } B_e \tag{1}$$

In the following equation, the Cauchy stress tensor σ_{ij} and the electric displacement D_j satisfy the equilibrium equations and the constitutive law:

$$\left.\begin{array}{l}\sigma_{ij,j} = 0\\ D_{j,j} = 0\end{array}\right\} \text{ in } \Omega, \quad \begin{array}{l}\sigma_{ij} = c_{ijkl}\varepsilon_{kl} - e_{kij}E_k\\ D_i = e_{ikl}\varepsilon_{kl} + \kappa_{ik}E_k\end{array} \tag{2}$$

Here, c_{ijkl} is Hooke's elasticity tensor, κ_{ij} is the dielectric tensor and e_{ijk} is the piezoelectric tensor. The strain tensor ε_{ij} and the electric field vector E_j are derived from the displacement field u_i and the electric potential φ:

$$\varepsilon_{ij} = \frac{1}{2}(u_{i,j} + u_{j,i}) \tag{3}$$

$$E_j = -\varphi_{,j} \tag{4}$$

3 Analytical Solutions

The analytical solutions mentioned in the sequel are eigenfunction related to a semi-infinite crack in an infinite piezoelectric domain. They are used to generate enrichment functions that span the exact solution at crack tips for every loading case. These have been calculated by the extended Lekhnitskii-formalism (see e.g. [11]) and can be found in a detailed fashion in [2]. Also, to assess the numerical accuracy of the method, one needs a distinct reference problem, where the asymptotical expansion used to build the new enrichment functions is not part of the solution. For this purpose, an analytical solution for a Griffith–Irwin crack was developed in the aforementioned reference, too.

Moreover, exact values of the K-factors are required for the Griffith–Irwin crack to prove the efficiency of the numerical technique for determining the K-factors. The exact K-factors are extracted for different inclined cracks (angle α) with respect to the σ_{yy}^{∞}-D_{y}^{∞}-loading ($\sigma_{xy}^{\infty} = 0$) along the poling direction, see Fig. 1. The results of the calculations are based on the analytical solutions found in [2].

4 The Classical X-FEM Formulation

The idea of partition of unity methods (PUM) [1] is to enrich an approximation field coming from standard finite elements with functions that are able to describe

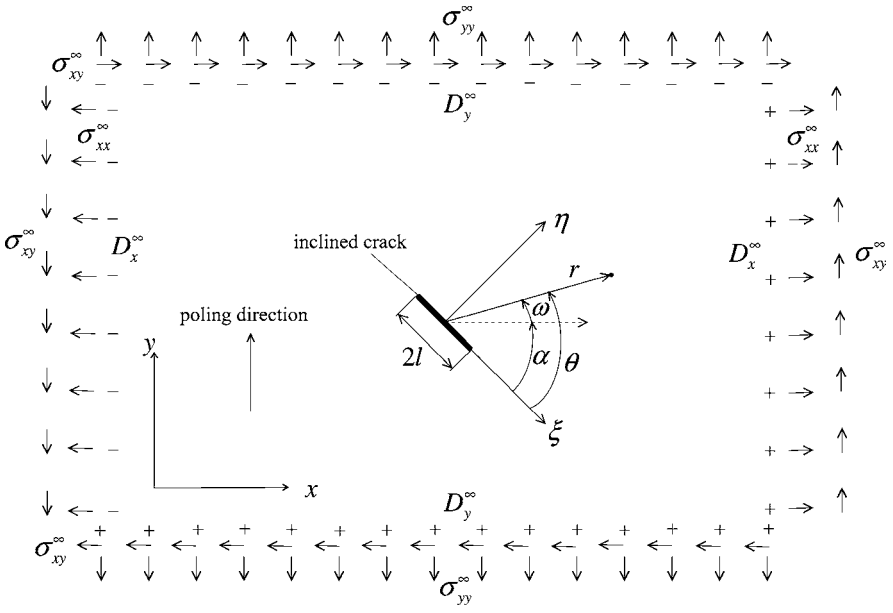

Fig. 1 Cracked body with a description of the angles appearing in the enrichment functions

some specific behavior of the exact solution field. The X-FEM is based on the local PUM [9]. In the sequel, we explain first the application to cracks in linear isotropic materials. In this case, one uses elementary displacement fields obtained from an asymptotic solution at the crack tip.

4.1 Crack Description

As in the original article from Moës et al. [9], the crack is described by a pair of level set functions. In the following, the local polar coordinates (r, θ) at the crack tip, introduced in [2], are used. They are computed from the values of the level set functions lsn and lst in the vicinity of the crack. These level sets are interpolated on the same mesh used for the finite element computation. This is of course not mandatory but may ease the fast computation of r and θ. The dependence of r and θ is the following:

$$\begin{cases} r = \sqrt{lsn^2 + lst^2} \\ \theta = \text{atan2}\,(lst, lsn) \end{cases} \tag{5}$$

where atan2 is the four-quadrant inverse tangent function.

4.2 Enrichment Functions

The classical enrichment functions used for isotropic elastic materials can be found in [9] and are as following.

$$g_i^e\,(r, \theta) = \left\{ \sqrt{r} \sin \frac{\theta}{2}, \sqrt{r} \cos \frac{\theta}{2}, \sqrt{r} \sin \frac{\theta}{2} \sin \theta, \sqrt{r} \cos \frac{\theta}{2} \sin \theta \right\} \tag{6}$$

Only elements immediately around the crack tip are usually enriched with these functions, but in the sequel we will deal with geometrical and topological enrichment schemes as in [3]. For the elements that are completely cut by the crack, the enrichment is chosen to be the modified Heaviside discontinuous function.

$$h\,(lst) = \begin{cases} +1 & \text{if } lst \geq 0, \\ -1 & \text{if } lst < 0 \end{cases} \tag{7}$$

In this function, lst is the level set representing the signed distance to the crack plane. In the remaining portion of the domain, there is no enrichment, so the conventional finite element basis is the only one existing. In the sequel, the conventional finite element used is a linear three node triangle except otherwise mentioned.

5 New Enrichment Functions for Cracks in Piezoelectric Media

The asymptotic expansion for a crack in an infinite piezoelectric medium can be determined. From this expansion, we can determine a set of elementary functions that span the same functional space for any supposed orientation of the crack and any loading. For plane problems, there are three independent eigenmodes (only two in isotropic elasticity). These modes are combined linearly for each spatial variable x or y. It should be noted that these functions depend on the inclination of the crack with respect to the material axes α (given by poling direction), contrary to the isotropic case. Altogether, one needs six functions to describe all the possible states at the crack tip, as opposed to the only four functions used to span the Westergaard–Williams–Sneddon solution in the isotropic elastic case. These independent functions are extracted from the asymptotic singular solution found in [2].

$$g_i^p(r,\theta) = \left\{\sqrt{r}\,f_1(\theta), \sqrt{r}\,f_2(\theta), \sqrt{r}\,f_3(\theta), \sqrt{r}\,f_4(\theta), \sqrt{r}\,f_5(\theta), \sqrt{r}\,f_6(\theta)\right\} \quad (8)$$

where:

$$\begin{aligned} f_i(\theta) &= \phi\left(\omega(\theta,\alpha), a_i^{(\mathrm{re})}, a_i^{(\mathrm{im})}\right) \\ &= \begin{cases} \rho\left(\omega, a_i^{(\mathrm{re})}, a_i^{(\mathrm{im})}\right)\cos\dfrac{\psi\left(\omega, a_i^{(\mathrm{re})}, a_i^{(\mathrm{im})}\right)}{2} & \text{if } a_i^{(\mathrm{im})} > 0 \\ \rho\left(\omega, a_i^{(\mathrm{re})}, a_i^{(\mathrm{im})}\right)\sin\dfrac{\psi\left(\omega, a_i^{(\mathrm{re})}, a_i^{(\mathrm{im})}\right)}{2} & \text{if } a_i^{(\mathrm{im})} \le 0 \end{cases} \end{aligned} \quad (9)$$

The complex numbers $a_i = a_i^{(\mathrm{re})} + \mathrm{i}a_i^{(\mathrm{im})}$ are the six roots of the characteristic equation. The angle α defines the orientation of the material axes with respect to the crack. The angles ω and ψ as well as the modified radius ρ have the form:

$$\omega = \theta - \alpha \quad (10)$$

$$\begin{aligned} \psi\left(\omega, a_i^{(\mathrm{re})}, a_i^{(\mathrm{im})}\right) &= \frac{\pi}{2} + \pi\,\mathrm{int}\left(\frac{\omega}{\pi}\right) \\ &\quad - \arctan\left(\frac{\cos\left(\omega - \pi\,\mathrm{int}\left(\frac{\omega}{\pi}\right)\right) + a_i^{(\mathrm{re})}\sin\left(\omega - \pi\,\mathrm{int}\left(\frac{\omega}{\pi}\right)\right)}{\left|a_i^{(\mathrm{im})}\right|\sin\left(\omega - \pi\,\mathrm{int}\left(\frac{\omega}{\pi}\right)\right)}\right) \end{aligned} \quad (11)$$

$$\begin{aligned} &\rho\left(\omega, a_i^{(\mathrm{re})}, a_i^{(\mathrm{im})}\right) = \\ &\frac{1}{\sqrt{2}}\sqrt[4]{\left(a_i^{(\mathrm{re})}\right)^2 + \left(a_i^{(\mathrm{im})}\right)^2 + a_i^{(\mathrm{re})}\sin 2\omega - \left[\left(a_i^{(\mathrm{re})}\right)^2 + \left(a_i^{(\mathrm{im})}\right)^2 - 1\right]\cos 2\omega} \end{aligned} \quad (12)$$

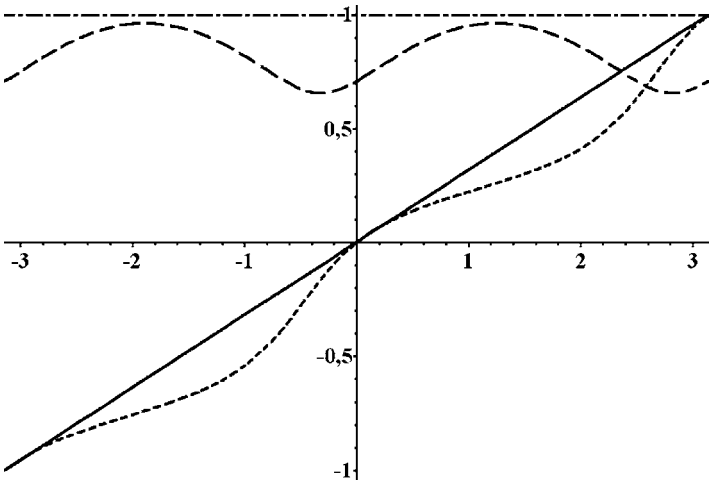

Fig. 2 Comparison between $\rho(\theta)$ (*dashed line*) and $r(\theta) = 1$ (*dotted-dashed line*) appearing respectively in the sixfold piezoelectric enrichment and the usual fourfold enrichment, and between $\psi(\theta)$ (*dotted line*) and θ (*solid line*)

The setting with labeled angles is depicted in Fig. 1 for the case of a Griffith crack. Of course, in the case of a Griffith crack, these expansions are a limiting case where the crack length is infinite. It is worth noting that the same enrichment functions are used for the displacements and the electric potential. In Fig. 2, we show the transformation between the pseudo polar coordinates (ρ, ψ) used in the sixfold enrichment, and the raw geometrical polar coordinates (r, θ) at the crack tip as a function of θ.

6 Convergence Study in the Energy Norm

The convergence is studied by comparing exact solutions for a reference problem to the actual results of a numerical model. The total (internal) energy of the system is given by:

$$W = \frac{1}{2} \int \left(c_{ijkl} \varepsilon_{ij} \varepsilon_{kl} + \kappa_{ij} E_i E_j \right) dV \tag{13}$$

The error in the (total) energy norm is then given by:

$$err_W = \sqrt{\frac{1}{2} \int c_{ijkl} \left(\varepsilon_{ij} - \varepsilon_{ij}^{ex} \right) \left(\varepsilon_{kl} - \varepsilon_{kl}^{ex} \right) + \kappa_{ij} \left(E_i - E_i^{ex} \right) \left(E_j - E_j^{ex} \right) dV}, \tag{14}$$

where ε_{ij}^{ex} and E_j^{ex} are obtained from the exact displacements u_i^{ex} and electric potential fields φ^{ex}, which can be found in [2]. The error energy norm err_W does not contain terms involving the piezoelectric coupling e_{ijk}, because of symmetries.

This would not have been the case if we had used the enthalpy H as reference, but convergence results shown in the sequel are also valid for H.

The example problem is that of a Griffith–Irwin crack in an infinite medium. Boundary conditions are applied at infinity. Those are $D_\eta^\infty = 10^{-3}$ and $\sigma_{\eta\eta}^\infty = 10^7$. If needed, the boundary conditions can be expressed in the $x - y$ axes as follows by simple rotations:

$$\sigma_{xx}^\infty = \sigma_{\eta\eta}^\infty \cdot (\cos\alpha)^2,\ \sigma_{xy}^\infty = -\sigma_{\eta\eta}^\infty \cdot \sin\alpha\cos\alpha,\ \sigma_{yy}^\infty = \sigma_{\eta\eta}^\infty \cdot (\sin\alpha)^2$$
$$D_y^\infty = D_\eta^\infty \cdot \cos\alpha,\ D_x^\infty = -D_\eta^\infty \cdot \sin\alpha. \tag{15}$$

The computations were made with a FEM-model, whose mesh is structured and has been gradually refined. Of course the computational domain is finite, so we apply the exact solution for an infinite domain as boundary condition for the finite computational domain. The length of the crack is 2 and the size of the domain is 8-by-8 and all units are SI. The material axes have been rotated by an angle of 30 degrees with respect to the plane of the crack to avoid trivial symmetry of the solution. Except for enriched degrees of freedom, the finite element discretization is linear for both displacements u_i and potential φ. We use three noded linear triangles as regular finite element basis.

Five sets of simulations have performed with various enrichment strategies:

1. Topological enrichment done with six functions
2. Geometrical enrichment done with six functions (radius of the enriched domain is 0.24)
3. Geometrical enrichment done with six functions and a bigger enriched domain (radius of the enriched domain is 0.48)
4. Geometrical enrichment done with the four functions used in linear elasticity (radius of the enriched domain is 0.24)
5. And no enrichment at all

Figure 3 shows the relation between the mesh density and the error in the energy norm in a log-log scale. It should be stressed that any enrichment strategy allows better results than conventional finite elements without enrichment. This fact has been explained in earlier papers [3, 9] extensively, so we will not discuss it further. Thus, these results without enrichment are for reference only. A comparison of results obtained using a specifically designed sixfold enrichment with the standard fourfold enrichment of the isotropic elasticity in similar settings shows almost no difference. It means that the classical fourfold enrichment spans a functional space that is large enough to represent well the more complex crack tip behavior found in piezoelectric materials. While this may be surprising, one should keep in mind that piezoelectric materials are not very far from having an isotropic behavior both in the mechanical and electrical variables. Furthermore, the coupling which is clearly anisotropic has a very weak magnitude. Thus, the additional degrees of freedom and shape of the sixfold enrichment may be of little advantage for piezoelectric materials. This is not a bad news, since it means that reliable piezoelectric simulations can be made using the much simpler fourfold enrichment.

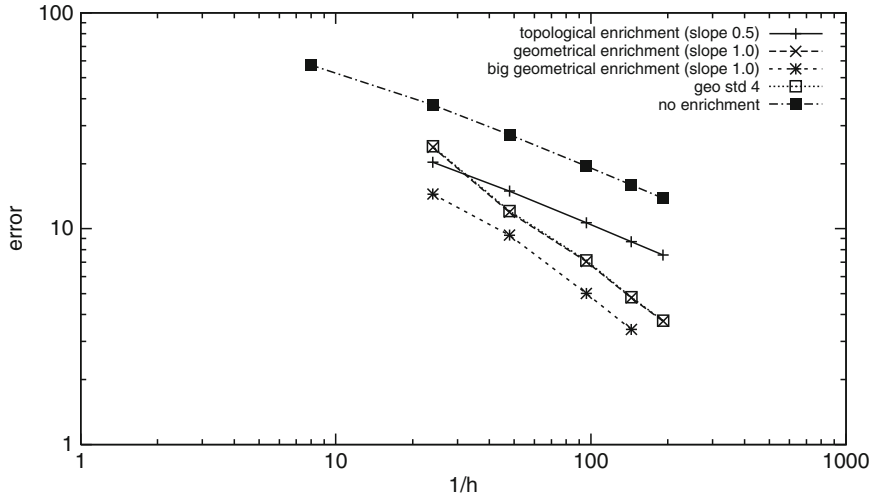

Fig. 3 Convergence for various enrichment strategies, with a mixed loading ($D_\eta^\infty = 10^{-3}$, $\sigma_{\eta\eta}^\infty = 10^7$)

7 Convergence of the Stress Intensity Factors

We consider the case of a Griffith–Irwin crack in an infinite piezoelectric medium. The computational domain is actually finite (a 4-by-4 square) but loaded along its boundaries with those fields, corresponding to the exact solution that is sought for numerically. In both cases, the numerical values of the K-factors are determined using the equivalent domain integrals for a given contour (the radius of this domain is set to 0.8). The radius of the enriched domain in the case of a geometrical enrichment is 0.24 . In Fig. 4, a comparison is made between topological and geometrical piezoelectric enrichment (sixfold) as well as with the classical fourfold enrichment. The results without enrichment (regular finite elements) are also shown. We should stress that, results for $1/h < 50$ are not very interesting because the mesh is very coarse with regard to the characteristic length of the problem and the area where the domain integrals are computed. However, we kept these results for the sake of completeness. We consider the problem of a Griffith–Irwin crack with boundary conditions given at infinity. The boundary conditions are $\sigma_{\eta\eta}^\infty = 10^7$, $\sigma_{\xi\eta}^\infty = 0$, $\sigma_{\xi\xi}^\infty = 0$, $D_\xi^\infty = 0$ and $D_\eta^\infty = 10^{-3}$. As before, the computational domain is finite. Therefore the exact solution is applied on the actual boundary of the domain. The exact values of the stress intensity factors in this setting are found in [2]. These are $K_I = 1.772454 \cdot 10^7$ and $K_{IV} = 1.772454 \cdot 10^{-3}$. The results depicted in Fig. 4 show that the fourfold enrichment is sufficient, while a geometrical enrichment strategy is substantially superior to a topological enrichment. We have presented results for K_I only, but the same applies to the other intensity factors K_{II}, K_{IV}.

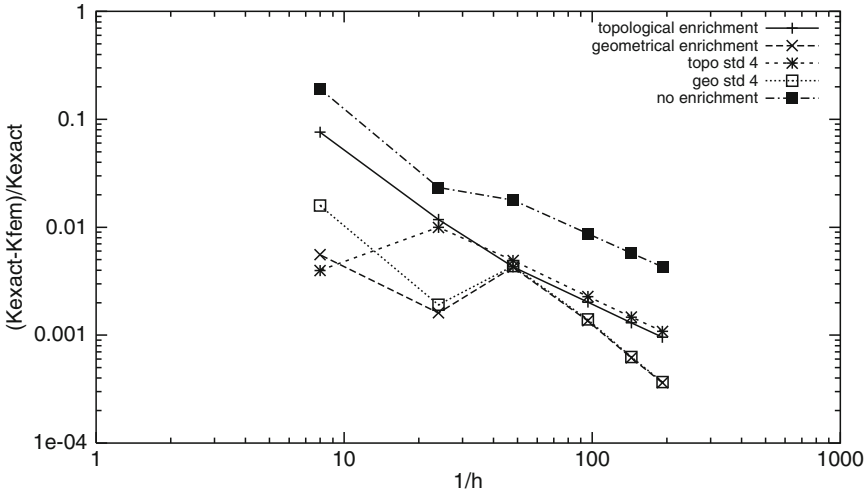

Fig. 4 Convergence of K_I for a Griffith–Irwin crack

8 About the Accuracy in the Vicinity of the Crack Tip

In the case of a vanishing mechanical loading, with electrical boundary conditions only, a huge numerical error in the Cauchy stresses can be observed around the crack tip (see Fig. 5). This is the consequence of the way stresses are computed, where variables with moderate relative errors (mostly interpolation error) may cancel each other:

$$\sigma_{ij} = c_{ijkl}\varepsilon_{kl} - e_{kij}E_k \tag{16}$$

The knowledge of stresses at the crack tip is important, even when no mechanical loadings are applied, because it can be shown that crack propagation still happens in that case. To lessen the numerical error, we tried (i) to increase the mesh density, (ii) to change the order of interpolation, and (iii) to use the X-FEM at the crack tip, respectively. Here, we present some qualitative results. In Fig. 5, right, the mesh density has been doubled (with a fourfold increase of computational expense). Figure 6 shows what happens when using order 2 and 3 interpolations instead of just linear elements. Finally, Fig. 7 shows the results when a linear interpolation is augmented with a crack tip enrichment. From these examples, it is clear that the best choice to improve numerical accuracy is to increase the polynomial order of the interpolation. However, the actual error made on the stresses is still much higher than what could be expected for such interpolations.

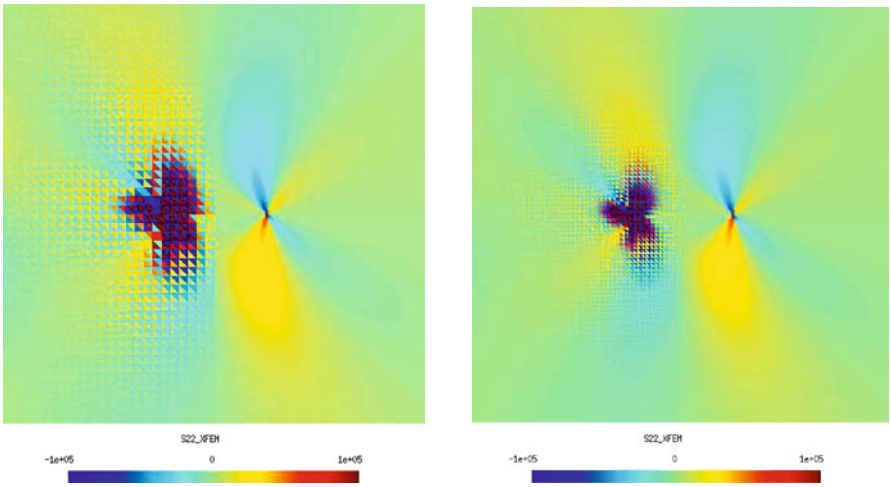

Fig. 5 Computation of σ_{yy} made with vanishing mechanical loadings (*left*), and same while doubling the mesh density (*right*). On each frame, the left side is the result of a numerical computation, and the right side is the exact solution

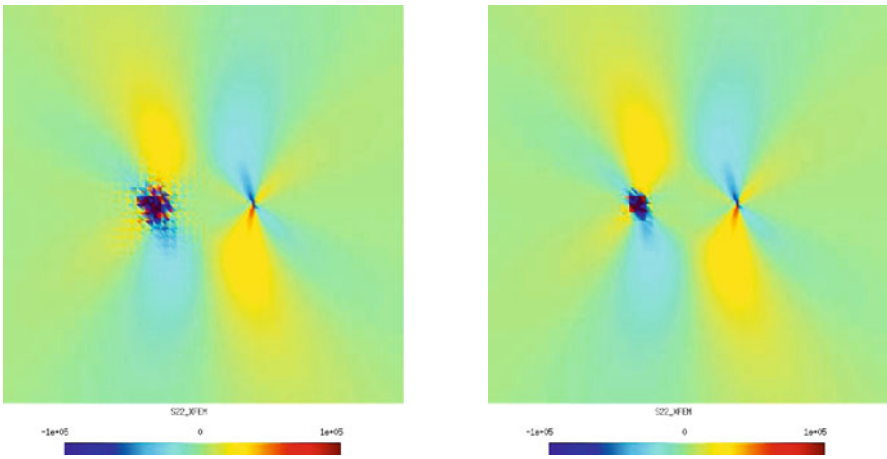

Fig. 6 Same as figure 5-left with order of interpolation p = 2 (*left*) and p = 3 (*right*)

9 Conclusions

We have devised an enrichment scheme based on the asymptotic expansion around a crack tip in piezoelectric materials. This enrichment scheme uses the six eigenfunctions of the asymptotic expansion. As such, it is optimal with regard to the problem to be solved (it contains the exact solution for a semi-infinite crack in an infinite body). However, a comparison made with the classical fourfold enrichment used for

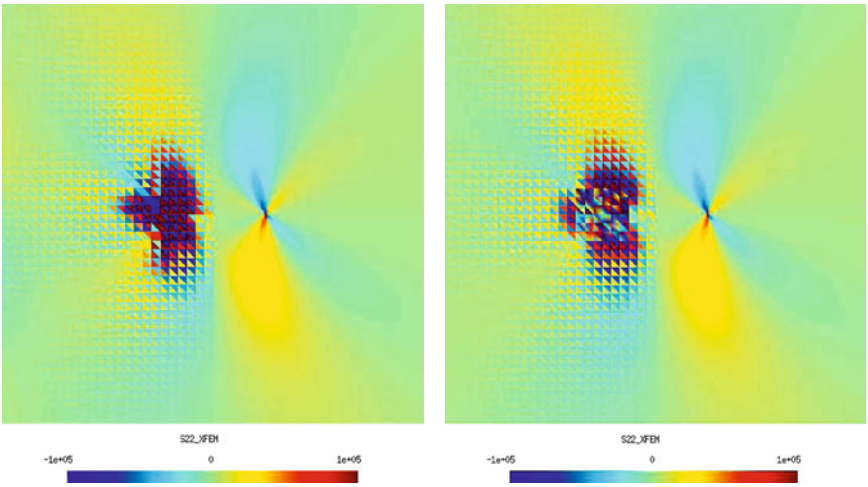

Fig. 7 Same as Fig. 5-left, without enrichment (*left*), with enrichment (*right*)

isotropic elasticity is interesting. It shows that, with an accuracy higher than usually expected for engineering problems, the fourfold enrichment gives almost the same efficiency, concerning accuracy both in energy and in the SIFs. The good news is that it is simpler to implement and involves less computational overhead, because it adds only four degrees of freedom (dofs) per regular dof, instead of six. For piezoelectric problems, it is therefore advisable to use the regular enrichment functions stemming from the isotropic elasticity. It should be mentioned that similar results have been obtained independently [5] with alternative enrichment functions for cracks in confined plasticity problems. Moreover, some qualitative results about the accuracy of Cauchy stresses in the crack tip vicinity were presented. The best performance was obtained by increasing the polynomial order if some specific boundary conditions are met.

References

1. Babuska I, Melenk JM (1997) The partition of unity method. Int J Numer Method Eng 40:727–758
2. Béchet E, Scherzer M, Kuna M (2009) Application of the x-fem to the fracture of piezoelectric materials. Int J Numer Method Eng 77(11):1535–1565
3. Béchet E, Minnebo H, Moës N, Burgardt B (2005) Convergence and conditioning issues with x-fem in fracture mechanics. Int J Numer Method Eng 64:1033–1056
4. Chen YH, Hasebe N (2005) Current understanding on fracture behavior of ferroelectric / piezoelectric materials. J Intel Mater Syst Struct 16:673–687
5. Elguedj T, Gravouil A, Combescure A (2005) Appropriate extended functions for x-fem simulation of plastic fracture mechanics. Comput Method Appl Mech Eng 195(7-8):501–515

6. Koy YL, Chiu KW, Marshall IH, Rajic N, Galea SC (2001) Detection of disbonding in a repair patch by means of an array of lead zirconate titanate and polyvinylidene fluoride sensors and actuators. Smart Mater Struct 10:946–962
7. Kuna M (2006) Finite element analyses of cracks in piezoelectric structures: A survey. Arch Appl Mech 76:725–745
8. Kuna M (2010) Fracture mechanics of piezoelectric materials – Where are we right now? Eng Fract Mech 77:309–326
9. Moës N, Dolbow J, Belytschko T (1999) A finite element method for crack growth without remeshing. Int J Numer Method Eng 46:131–150
10. Osher S, Sethian JA (1988) Fronts propagating with curvature-dependent speed: Algorithms based on hamilton-jacobi formulations. J Comput Phys 79:12–49
11. Scherzer M, Kuna M (2004) Combined analytical and numerical solution of 2d interface corner configurations between dissimilar piezoelectric materials. Int J Fract 127(1):61–99
12. Zhang TY, Zhao M, Tong P (2002) Fracture of piezoelectric ceramics. Adv Appl Mech 38:147–289

Singularity Analysis of Electro-mechanical Fields in Angularly Inhomogeneous Piezoelectric Composites Wedges

Jian-Shan Wang, Xiaoqiao He, and Qing-Hua Qin

Abstract An analytical solution is presented to study the singularity behavior of electroelastic fields in a wedge with angularly graded piezoelectric material (AGPM) and under anti-plane deformation. The analysis is based on the mixed-variable state space formulation developed in this paper. The characteristic equation containing the singular order is derived using the method of variable separation. The results presented demonstrate the effects of the angular variation of material properties on the singularities of the AGPM wedge systems. The analysis indicates that the material inhomogeneity degree η can be used to control the singularities of AGPM wedge systems.

1 Introduction

Singular behaviour of stresses and electric fields in a wedge structure with piezoelectric composites has caused a great concern due to their wide use as sensors and actuators in the field of smart structures in the past years. In the engineering practice, piezoelectric elements are often bonded to other materials, and thus they form a wedge shaped structure. Due to the discontinuities of material properties and geometry, the stresses and electric fields at the apex of a wedge may become infinity, which often induce cracking, fracture or debonding in the wedge composite. Xu and Rajapakse [1] investigated the inplane stress singularities of piezoelectric composite wedges by extending Lekhnitskii's complex potential functions. Later, studies on various singularity problems of a piezoelectric wedge have continuously been presented [2–6], in which effects of the parameters such as the wedge angles, material properties, graphite fiber orientation, and piezoelectric poling direction on the

J.-S. Wang (✉)
Department of Mechanics, Tianjin University, Tianjin, China
e-mail: wjs_tju@163.com

X. He
Department of Building and Construction, City University of Hong Kong, Hong Kong, China

Q.-H. Qin
Department of Engineering, Australian National University, Canberra, Australia

M. Kuna and A. Ricoeur (eds.), *IUTAM Symposium on Multiscale Modelling of Fatigue, Damage and Fracture in Smart Materials*, IUTAM Bookseries 24,
DOI 10.1007/978-90-481-9887-0_15,

stress singularity order are discussed in detail. These studies showed that boundary conditions and continuity conditions imposed on the edges and bonded interfaces of piezoelectric wedges play an important role on the stress and displacement singularities. Recently, Wang and Qin [7] presented a symplectic model for piezoelectric wedges and applied this model to the analysis of electro-elastic singularities of multi-wedge under anti-plane deformation. It should be noted that most previous studies concerned with the homogeneous piezoelectric wedges while the singularity problem for the angularly inhomogeneouse piezoelectric wedge has not been reported in the literature.

We noted that a new class of material, i.e. the functionally grading piezoelectric materials (FGPM) whose properties vary along layer-thickness direction only, has been developed recently and widely investigated [8–12]. It is well-known that functionally grading material can reduce the high stress concentration at the layer interface of a laminate structure. But how this can be reduced and what is its mechanism is still a challenging topic. In particular, the reduction of stress concentration and singular behavior of angularly graded piezoelectric material (AGPM) wedges have not been investigated theoretically.

Recently, Carpinteri and Paggi [13] presented a singularity analysis for the angularly inhomogeneous elastic wedges in plane deformation and investigated the potentials of the angularly graded materials (AGM) in joining technology. They consider a general angular grading on the Young's modulus $E = E(\theta)$, and this inhomogeneity can lead to a continuous and rapidly varying elastic modulus at the proximity of interface between two wedges, which is more accordance with the engineering practice than the analytical assumption for homogeneous elastic materials. Their study shows that the angular inhomogeneity has an important influence on the singular behaviour of AGM elastic wedges. However, in their work, only the Young's modulus varies angularly and it cannot be extended to the case of AGPM directly.

In this paper, a mixed-variable state space formulation is developed for analyzing singular behaviour of stresses and electric fields at the apex of AGPM wedges under anti-plane deformation. The AGPM wedge considered is assumed to be with angularly varying materials properties including shear modulus, piezoelectric constant and dielectric constant. Using the polar coordinate system, the governing equations is first transformed into a state space equation by choosing appropriate fields (w, φ, S_r, D_r in this work) as independent state variables. Then the method of variable separation is used to find the singular order of electroelastic fields for an AGPM wedge. As an application of the proposed mixed-variable state space formulation, explicit expressions for the singular order of a two-material wedge subjected to given boundary conditions are presented. Brief discussion is conducted to identify the influence of angular inhomogeneity on the singular behaviour of stresses and electric fields. This analysis shows that the angular material inhomogeneity can be used to control the singularity of stresses and electric fields in AGPM wedges.

2 Basic Formulations and the State Space Equation for Single AGPM Wedge

Consider an AGPM wedge with angular inhomogeneous material properties such as shear modulus, piezoelectric constant and dielectric constant shown in Fig. 1 under anti-plane deformation. The poling direction orientated along the z-axis and perpendicular to the $r-\theta$ plane, where r and θ are polar coordinates. The constitutive relation equations can be given as [14]:

$$\begin{Bmatrix} \tau_{\theta z} \\ \tau_{rz} \\ D_r \\ D_\theta \end{Bmatrix} = \begin{bmatrix} c_{44}(\theta) & 0 & 0 & -e_{15}(\theta) \\ 0 & c_{44}(\theta) & -e_{15}(\theta) & 0 \\ 0 & e_{15}(\theta) & \varepsilon_{11}(\theta) & 0 \\ e_{15}(\theta) & 0 & 0 & \varepsilon_{11}(\theta) \end{bmatrix} \begin{Bmatrix} \gamma_{\theta z} \\ \gamma_{rz} \\ E_r \\ E_\theta \end{Bmatrix} \tag{1}$$

where τ_{ij}, D_i, γ_{ij} and E_i ($i = r$, θ and $j = z$) are the shear stresses, electric displacements, shear strain and electric fields, respectively. The parameters $c_{44}(\theta)$, $e_{15}(\theta)$ and $\varepsilon_{11}(\theta)$ are the shear modulus, piezoelectric constant and dielectric constant, respectively. The material constants are assumed to vary in the following exponential form:

$$c_{44}(\theta) = c_{44}^* e^{\eta\theta},\ e_{15}(\theta) = e_{15}^* e^{\eta\theta},\ \varepsilon_{11}(\theta) = \varepsilon_{11}^* e^{\eta\theta} \tag{2}$$

in which η are the inhomogeneity degree of the material gradient along the angular direction, and η can be written as $\eta = 1/\theta_0 \ln(\zeta(\theta_0)/\zeta^*)$, where ζ represents shear modulus, piezoelectric constant or dielectric constant, depending on which one material constant being considered, and ζ^* represents c_{44}^*, e_{15}^*, or ε_{11}^* which is the associated material property at $\theta = 0$. Here and after c_{44}^*, e_{15}^*, and ε_{11}^* are known as the reference material parameters.

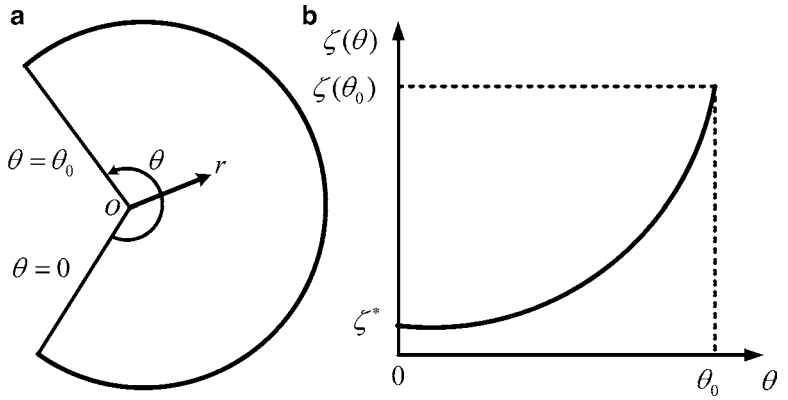

Fig. 1 (**a**) A diagram of an AGPM wedge and (**b**) the variation of the inhomogeneity of material properties including shear modulus, piezoelectric constant and dielectric constant

The equilibrium equation and Maxwell's equation can be written as [15]:

$$\frac{1}{r}\frac{\partial \tau_{\theta z}}{\partial \theta}+\frac{\partial \tau_{rz}}{\partial r}+\frac{\tau_{rz}}{r}=0,\ \frac{1}{r}\frac{\partial D_{\theta}}{\partial \theta}+\frac{\partial D_r}{\partial r}+\frac{D_r}{r}=0 \tag{3}$$

Equations of shear strain-displacement and electric field-electric potential relations are:

$$\gamma_{rz}=\frac{\partial w}{\partial r},\ \gamma_{\theta z}=\frac{1}{r}\frac{\partial w}{\partial \theta},\ E_r=-\frac{\partial \Phi}{\partial r},\ E_{\theta}=-\frac{1}{r}\frac{\partial \Phi}{\partial \theta} \tag{4}$$

To transform the governing Eqs. (1)–(4) into a state space equation, the variable ξ is introduced through use of $\xi=\ln(r)$.

The following state variables are also introduced to simplify the derivation

$$S_{\theta}=e^{-\eta\theta}r\tau_{\theta z},\ SD_{\theta}=e^{-\eta\theta}rD_{\theta},\ S_r=e^{-\eta\theta}r\tau_{rz},\ SD_r=e^{-\eta\theta}rD_r \tag{5}$$

From Eqs. (1), (3)–(5), we can arrive at

$$\left\{\dot{w},\dot{\varphi},\dot{S}_r,S\dot{D}_r\right\}^T=H\left\{w,\varphi,S_r,SD_r\right\}^T \tag{6}$$

where "$\cdot$" denotes the differentiation with respect to ξ, $\Delta=e_{15}^{*2}+c_{44}^{*}\varepsilon_{11}^{*}$ and $\mathbf{H}$ is the operator matrix with four order,

$$\begin{aligned}&H_{13}=\varepsilon_{11}^{*}/\Delta, H_{14}=H_{23}=e_{15}^{*}/\Delta, H_{24}=-c_{44}^{*}/\Delta\\&H_{31}=-c_{44}^{*}H_0, H_{32}=H_{41}=-e_{15}^{*}H_0, H_{42}=\varepsilon_{11}^{*}H_0, H_0=\frac{\partial^2}{\partial\theta^2}+\eta\frac{\partial}{\partial\theta}\end{aligned} \tag{7}$$

and other elements of $\boldsymbol{H}$ are zero.

Further, By introducing the notation $\boldsymbol{p}=\{w,\varphi\}^T$ and $\boldsymbol{v}=\{\boldsymbol{p},\boldsymbol{q}\}^T$, Eq. (6) can be simplified into the state space equation as

$$\dot{\boldsymbol{v}}=\boldsymbol{H}\boldsymbol{v} \tag{8}$$

If we assume $\boldsymbol{v}(\xi,\theta)=\boldsymbol{\kappa}(\xi)\boldsymbol{\psi}(\theta)$, and here $\boldsymbol{\psi}(\theta)=\{\boldsymbol{q}(\theta),\boldsymbol{p}(\theta)\}^T$, using the separate variables method, we have

$$\boldsymbol{\kappa}(\xi)=e^{\mu\,\xi}=r^{\mu},\ \boldsymbol{H}\boldsymbol{\psi}=\mu\,\boldsymbol{\psi} \tag{9}$$

Thus, the following equations can be obtained,

$$\{w,\varphi\}^T=r^{\mu}\left\{w^{(\theta)}(\theta),\varphi^{(\theta)}(\theta)\right\}^T,\ \{\tau_{rz},D_r\}^T=r^{\mu-1}e^{\eta\theta}\left\{\tau_{rz}^{(\theta)}(\theta),D_r^{(\theta)}(\theta)\right\}^T \tag{10}$$

where superscript '(θ)' represents the quantity being the function of variable θ only. It can be seen from Eq. (10) that the stress and electric field have the $\mathrm{Re}(\mu-1)$ singularity at the apex of the AGPM wedge when $r\to 0$.

It should be mentioned that for the case of homogeneous piezoelectric material ($\eta = 0$) the operator matrix $\boldsymbol{H}$ is a Hamiltonian operator matrix and Eq. (8) is a Hamiltonian equation [7], while for the case of inhomogeneous piezoelectric material ($\eta \neq 0$), $\boldsymbol{H}$ is not the Hamiltonian operator matrix due to the material inhomogeneity, thus the governing equation can not be directed into the Hamiltonian system, and it is difficult to find the adjoint symplectic orthonormailzation eigenvector $\boldsymbol{\psi}$ to obtain the electroelastic fields using the procedure similar to that in [7]. However, the singular order can still be obtained which also corresponds to the non-zero eigenvalue of the operator matrix. The singular order k is given as $k = \mathrm{Re}(\mu - 1)$ and μ must satisfy with the condition $0 < \mathrm{Re}(\mu) < 1$ [7]. We can obtain the solutions of $(\lambda^2 + \eta\lambda + \mu^2)^2 = 0$ as follows,

$$\lambda_{1,2} = -0.5\eta + 0.5\sqrt{\eta^2 - 4\mu^2},\ \lambda_{3,4} = -0.5\eta - 0.5\sqrt{\eta^2 - 4\mu^2} \tag{11}$$

where $\lambda = \mathrm{d}/\mathrm{d}\theta$ and $\lambda = \mathrm{d}^2/\mathrm{d}\theta^2$.

In the case of $\eta^2 - 4\mu^2 \leq 0$, one can easily obtain:

$$\begin{aligned} X_i(\theta) = {} & A_i e^{-\frac{\eta}{2}\theta} \cos(\frac{m}{2}\theta) + B_i e^{-\frac{\eta}{2}\theta} \sin(\frac{m}{2}\theta) + C_i \theta e^{-\frac{\eta}{2}\theta} \cos(\frac{m}{2}\theta) \\ & + D_i \theta e^{-\frac{\eta}{2}\theta} \sin(\frac{m}{2}\theta) \end{aligned} \tag{12}$$

in which $\boldsymbol{X}(\theta) = \{w(\theta), \varphi(\theta), S_r(\theta), SD_r(\theta)\}^T$, and A_i, B_i, C_i and $D_i (i = 1\text{–}4)$ are unknown constants to be determined and $m = \sqrt{4\mu^2 - \eta^2}$.

Substituting Eq. (12) into Eq. (9) leads to the following relationships between the unknown constants:

$$\begin{aligned} & A_3 = \mu(c_{44}^* A_1 + e_{15}^* A_2),\ A_4 = \mu(e_{15}^* A_1 - \varepsilon_{11}^* A_2), \\ & B_3 = \mu(c_{44}^* B_1 + e_{15}^* B_2),\ B_4 = \mu(e_{15}^* B_1 - \varepsilon_{11}^* B_2),\ D_i = C_i = 0. \end{aligned} \tag{13}$$

From Eqs. (1), (12) and (13) we can have:

$$\begin{aligned} S_\theta(\theta) &= c_{44}^* P(\theta) A_1 + e_{15}^* P(\theta) A_2 - c_{44}^* N(\theta) B_1 - e_{15}^* N(\theta) B_2 \\ SD_\theta(\theta) &= e_{15}^* P(\theta) A_1 - \varepsilon_{11}^* P(\theta) A_2 - e_{15}^* N(\theta) B_1 + \varepsilon_{11}^* N(\theta) B_2 \end{aligned} \tag{14}$$

where

$$\begin{aligned} P(\theta) &= -0.5 e^{-\frac{\eta}{2}\theta} \left[m \sin(0.5m\theta) + \eta \cos(0.5m\theta) \right], \\ N(\theta) &= -0.5 e^{-\frac{\eta}{2}\theta} \left[m \cos(0.5m\theta) - \eta \sin(0.5m\theta) \right] \end{aligned} \tag{15}$$

Considering the AGPM wedge shown in Fig. 1, the conditions at the boundary edges are assumed to be free of traction and electrically insulated, and the eigenvalue can be obtained as follows:

$$m = 2n\pi/\theta_0\ (n = 0,\ 1,\ 2, \cdots),\ \mu = \sqrt{\eta^2/4 + \pi^2/\theta_0^2} \tag{16}$$

Using the condition: $0 < \mu < 1$, it can be obtained that the wedge angle θ_0 must satisfy with the following condition if there exist singular electro-elastic fields at the apex of the single AGPM wedge:

$$\sqrt{\pi^2 + 0.25 \ln^2 (c_{44}(\theta_0)/c_{44}^*)} < \theta_0 \leq 2\pi \tag{17}$$

3 Two AGPM Wedges

For a bi-material wedge system consisting two AGPMs as shown in Fig. 2, consider the traction free and electrically insulated, the boundary conditions are as follows:

$$\tau_{\theta z}^{(1)}(r, \alpha) = \tau_{\theta z}^{(2)}(r, -\beta) = D_{\theta}^{(1)}(r, \alpha) = D_{\theta}^{(2)}(r, -\beta) = 0 \tag{18}$$

in which the superscripts "(1)" and "(2)" denote the AGPM1 and AGPM2, respectively, and $\alpha = \theta_2 - \theta_1$, $\beta = \theta_1 - \theta_0$. If the two AGPMs are fully bonded at the interface, the continuity conditions on the interface are:

$$\begin{aligned} &\tau_{\theta z}^{(1)}(r, 0) = \tau_{\theta z}^{(2)}(r, 0),\ w^{(1)}(r, 0) = w^{(2)}(r, 0), \\ &D_{\theta}^{(1)}(r, 0) = D_{\theta}^{(2)}(r, 0),\ E_r^{(1)}(r, 0) = E_r^{(2)}(r, 0). \end{aligned} \tag{19}$$

Combination of Eqs. (14), (18) and (19), we have the characteristic equation governing the singular order:

$$[M] \left\{ F^{(1)} \right\} = 0 \tag{20}$$

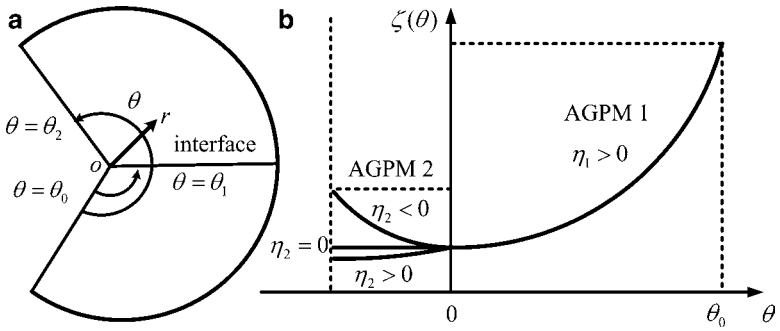

Fig. 2 A diagram of a bi-AGPM wedge system and the variation of the materials inhomogeneity of AGPM1 and AGPM2, (**a**) geometry configuration of the AGPM1-AGPM2 wedge system and (**b**) variation of material properties with the angle variable θ

where

$$F^{(1)} = \left\{ A_1^{(1)} \; A_2^{(1)} \; B_1^{(1)} \; B_2^{(1)} \right\}^T \tag{21}$$

$$[M] = \begin{bmatrix} c_{44}^{(1)} P^{(1)}(\alpha) & e_{15}^{(1)} P^{(1)}(\alpha) & -c_{44}^{(1)} N^{(1)}(\alpha) & -e_{15}^{(1)} N^{(1)}(\alpha) \\ e_{15}^{(1)} P^{(1)}(\alpha) & -\varepsilon_{11}^{(1)} P^{(1)}(\alpha) & -e_{15}^{(1)} N^{(1)}(\alpha) & \varepsilon_{11}^{(1)} N^{(1)}(\alpha) \\ b_{11} & b_{12} & b_{13} & b_{14} \\ b_{21} & b_{22} & b_{23} & b_{24} \end{bmatrix} \tag{22}$$

where b_{1i} and b_{2i} $(i = 1\text{–}4)$ are given as

$$\begin{aligned}
b_{11} &= c_{44}^{(2)} P^{(2)}(-\beta) - N^{(2)}(-\beta) \left(a_{11} c_{44}^{(2)} + a_{21} e_{15}^{(2)} \right), \\
b_{12} &= e_{15}^{(2)} P^{(2)}(-\beta) - N^{(2)}(-\beta) \left(a_{12} c_{44}^{(2)} + a_{22} e_{15}^{(2)} \right) \\
b_{13} &= -N^{(2)}(-\beta) \left(a_{13} c_{44}^{(2)} + a_{23} e_{15}^{(2)} \right), \\
b_{14} &= -N^{(2)}(-\beta) \left(a_{14} c_{44}^{(2)} + a_{24} e_{15}^{(2)} \right) \\
b_{21} &= e_{15}^{(2)} P^{(2)}(-\beta) - N^{(2)}(-\beta) \left(a_{11} e_{15}^{(2)} - a_{21} \varepsilon_{11}^{(2)} \right), \\
b_{22} &= -\varepsilon_{11}^{(2)} P^{(2)}(-\beta) - N^{(2)}(-\beta) \left(a_{12} e_{15}^{(2)} - a_{22} \varepsilon_{11}^{(2)} \right) \\
b_{23} &= -N^{(2)}(-\beta) \left(a_{13} e_{15}^{(2)} - a_{23} \varepsilon_{11}^{(2)} \right), \\
b_{24} &= -N^{(2)}(-\beta) \left(a_{14} e_{15}^{(2)} - a_{24} \varepsilon_{11}^{(2)} \right)
\end{aligned} \tag{23}$$

and a_{1i} and a_{2i} $(i = 1\text{–}4)$ are

$$\begin{aligned}
&a_{11} = \left[\eta^{(1)} \left(e_{15}^{(1)} e_{15}^{(2)} + c_{44}^{(1)} \varepsilon_{11}^{(2)} \right) - \eta^{(2)} \left(e_{15}^{(2)2} + c_{44}^{(2)} \varepsilon_{11}^{(2)} \right) \right] \Big/ \Delta_0, \\
&a_{12} = \eta^{(1)} \left(e_{15}^{(1)} \varepsilon_{11}^{(2)} - e_{15}^{(2)} \varepsilon_{11}^{(1)} \right) / \Delta_0, \; a_{13} = m^{(1)} \left(-e_{15}^{(1)} e_{15}^{(2)} - c_{44}^{(1)} \varepsilon_{11}^{(2)} \right) \Big/ \Delta_0, \\
&a_{14} = m^{(1)} \left(e_{15}^{(2)} \varepsilon_{11}^{(1)} - e_{15}^{(1)} \varepsilon_{11}^{(2)} \right) / \Delta_0, \; \Delta_0 = -m^{(2)} \left(e_{15}^{(2)2} + c_{44}^{(2)} \varepsilon_{11}^{(2)} \right)
\end{aligned} \tag{24}$$

Here, the superscripts "(1)" and "(2)" denote the AGPM1 and AGPM2, respectively, and $\alpha = \theta_2 - \theta_1$, $\beta = \theta_1 - \theta_0$.

4 Discussion

Using the definition $\rho = c_{44}(\theta_0)/c_{44}^* = e_{15}(\theta_0)/e_{15}^* = \varepsilon_{11}(\theta_0)/\varepsilon_{11}^*$, single AGPM wedge with $\rho = 1.0$ $(\eta = 0.)$ is a homogenous piezoelectric wedge and thus there is no singularity for the piezoelectric half plane $(\theta_0 = 180°)$. Hence,

there exists classic root for the singularity of a semi-infinite crack ($\theta_0 = 360°$). In addition, the singularity disappears when $\theta_0 \leq 180°$. These results consist with those of [4, 5, 7]. The range of wedge angle in which there exist singularity is given in Eq. (17) for inhomogeneous piezoelectric materials but the singular order for the semi-infinite crack ($\theta_0 = 360°$) is no longer to be -0.5. The angular material inhomogeneity leads to a smaller singular order than that of the homogenous material, and a larger inhomogeneity parameter η can produce a less singularity. For a single AGPM wedge, the singular order only relates to the value of η, wedge angle and boundary conditions. Due to the limitation of paper length, we here only give a theoretical analysis for single AGPM wedge. However, the model presented in this paper can be easily extended to cases of multi-AGPM-wedge systems.

5 Conclusion

In this paper, an analytical solution is presented to study the singularity of the AGPM wedge systems. In particular, the mixed variable state space formulation for the AGPM wedge under anti-plane deformation is developed for analyzing the singular behaviour of stresses and electric fields at the apex of AGPM wedges under anti-plane deformation. Using the boundary conditions and the interface continuous conditions, the characteristic equation governing the singular order is obtained and solved numerically. The effects of angular material inhomogeneity on the singularity of electro-elastic fields are investigated for single AGPM wedge. The theoretical results show that the angular material inhomogeneity has an important influence on the singular order of the electro-elastic fields compared to the homogeneous material. Hence, the material inhomogeneity can be used to control the singularity of the AGPM wedge systems.

Acknowledgments This work was supported by the National Natural Science Foundation of China (Grant Nos. 10802041) and Yong Teacher Foundation of Tianjin University and a grant from City University of Hong Kong (Project No. 7001922). Jianshan Wang was financially supported by IUTAM and TU Bergakademie Freiberg to participate the IUTAM Symposium 2009.

References

1. Xu XL, Rajapakse PKND (2002) On singularities in composite piezoelectric wedges and junctions. Int J Solids Struct 37:3253–3275
2. Chen CD (2006) On the singularities of the thermo-electro-elastic fields near the apex of a piezoelectric bonded wedge. Int J Solids Struct 43:957–981
3. Chue C.H., Chen CD (2002) Decoupled formulation of piezoelectric elasticity under generalized plane deformation and its application to wedge problems. Int J Solids Struct 39:3131–3158
4. Chue CH, Chen CD (2003) Antiplane stress singularities in a bonded bimaterial piezoelectric wedge. Arch Appl Mech 72:673–685
5. Chen CD, Chue CH (2003) Singular electro-mechanical fields near the apex of a piezoelectric bonded wedge under antiplane shear. Int J Solids Struct 40:6513–6526

6. Chen MC, Zhu JJ, Sze, KY (2006) Electroelastic singularities in piezoelectric-elastic wedges and junctions. Eng Fract Mech 73:855–868
7. Wang JS, Qin QH (2007) Symplectic model for piezoelectric wedges and its application in analysis of electroelastic singularities. Philos Mag 87(2):225–251
8. Chue CH, Ou YL.(2005) Mode III crack problems for two boned functionally graded piezoelectric materials. Int J Solids Struct 42:3321–3337
9. Ma L, Wu LZ, Zhou ZG, Guo LC (2005) Fracture analysis of a functionally graded piezoelectric strip. Compos Struct 69:294–300
10. Lu P, Lee HP, LuC (2006) Exact solutions for simply supported functionally graded piezoelectric laminates by Stroh-like formailism. Compos Struct 72:352–363
11. Chen J, Liu Z, Zou Z (2003) Dynamic response of a crack in a functionally graded interface of two dissimilar piezoelectric half-planes. Arch Appl Mech 72:686–696
12. Wang BL (2001) A mode III crack in functionally graded piezoelectric materials. Mech Res Comm 30:151–159
13. Carpinteri A, Paggi M (2005) On the asymptotic stress field in angularly nonhomogeneous materials. Int J Fract 135:267–283
14. Qin QH (2003) Solving anti-plane problems of piezoelectric materials by the Trefftz finite element approach. Comput Mech 31:461–468
15. Qin QH (2001) Fracture Mechanics of Piezoelectric Materials. WIT Press, Southampton

This page intentionally left blank

Crack Propagation Simulations in Piezoelectric Structures with an Efficient Adaptive Finite Element Tool

Łukasz Jański, Peter Steinhorst, and Meinhard Kuna

Abstract The first part of the publication concerns the special program πCRACK for crack propagation simulations in piezoelectric structures. In the kernel of the program, the piezoelectric boundary value problem is solved with the adaptive finite element method. The solution is applied, inter alia, to the computation of the dielectric and mechanical intensity factors with the interaction integral technique. The intensity factors are used in the fracture criterion of the maximum modified hoop stress intensity factor. The criterion takes into account the anisotropic behaviour of the fracture toughness of piezoelectric ceramics. In the second part of the publication, computation results obtained with the program πCRACK are presented. Thereby crack propagation starts in one of the crack tips of a straight crack located in an electromechanically loaded plate. The influence of both the isotropic and anisotropic fracture toughness is considered and analysed.

1 Introduction

Nowadays many sensors and actuators, constituting the kernel of smart structures, are made of piezoelectric ceramics [4]. The smart structures and their mentioned piezoelectric components are usually exposed under service conditions to

Ł. Jański (✉)
Institute of Mechanics and Fluid Dynamics, Technische Universität Bergakademie Freiberg, Lampadiusstr. 4, 09599 Freiberg, Germany
e-mail: Lukasz.Janski@imfd.tu-freiberg.de

P. Steinhorst
Faculty of Mathematics, Chemnitz University of Technology, Reichenhainer Str. 41, 09107 Chemnitz, Germany
e-mail: peter.steinhorst@mathematik.tu-chemnitz.de

M. Kuna
Institute of Mechanics and Fluid Dynamics, Technische Universität Bergakademie Freiberg, Lampadiusstr. 4, 09599 Freiberg, Germany
e-mail: Meinhard.Kuna@imfd.tu-freiberg.de

M. Kuna and A. Ricoeur (eds.), *IUTAM Symposium on Multiscale Modelling of Fatigue, Damage and Fracture in Smart Materials*, IUTAM Bookseries 24,
DOI 10.1007/978-90-481-9887-0_16,

severe mechanical and/or electrical, internal and/or external, static and/or dynamic loads. This is crucial considering reliability and durability of the smart structures. Exceeding a certain critical load level can lead for example to destructive fracture. For this reason, a better understanding and deeper investigation of the influence of various loading conditions on fracture of piezoelectric materials and components are necessary. A crack can either propagate or arrest. If the crack propagates, the prediction of the propagation direction is an important task.

Because of the complexity of propagating cracks and finiteness of the domains in which cracks propagate, only numerical strategies are applicable in practice for crack growth modeling. The well known advantages justify the choice of the finite element method. If a crack-like defect has to be considered in the domain of the analysed boundary value problem, special numerical methods for crack analysis are usually used e.g. special finite elements are chosen for the accurate representation of the singularity of the mechanical and electrical fields at crack tips or/and efficient algorithms are implemented for the computation of fracture-controlling parameters. An overview of these special numerical methods for piezoelectric materials can be found in the article [6].

To represent a propagating crack in a finite element model, at least three algorithms can be used. The first, being the simplest from the algorithmic point of view, is based on an update of the geometrical model with subsequent remeshing of the whole domain after each propagation step. Despite simplicity, the algorithm has high numerical cost. In the second, a domain remains continuous at that spot where the crack is localized and the behaviour of the discontinuity is described with discontinuous functions. In practice, the standard, continuous displacement interpolation functions basis has to be enriched (X-FEM) with leading terms of the near-tip asymptotic expansion for the displacement field. If the crack propagates, the enrichment is accordingly extended in space. In the third algorithm, only those finite elements are modified, which are cut by a new crack segment in the crack growth process. The above discussed algorithms are used for example in the publications [1], [2] and [9], respectively. The publications deal with crack propagation in elastic bodies. Since the third from the mentioned algorithms avoids excessive complexity on the one hand and guarantees low numerical cost on the other, it is the one used in the finite element tool πCRACK described in Section 2. In addition, the choice of the third algorithm and rejection of the second considerably simplifies the implementation of the finite element adaptivity [3].

One of the tasks of a fracture criterion is to predict the crack propagation direction. Since suitable fracture criteria for piezoelectric materials are still being searched for, the prediction of the propagation direction is not as easy as for the elastic case. Application of the well known maximal energy release rate criterion to piezoelectric problems leads to the conclusion that the electric field always impedes crack growth regardless of the direction of the electric field applied [7]. This conclusion is not consistent with experimental observations. On the other hand, the maximal mechanical energy release rate criterion, proposed in the publication [7], is doubtful due to different treatment of mechanical and electrical energies. No profound explanation exists, why the electrical energy part in the total energy release

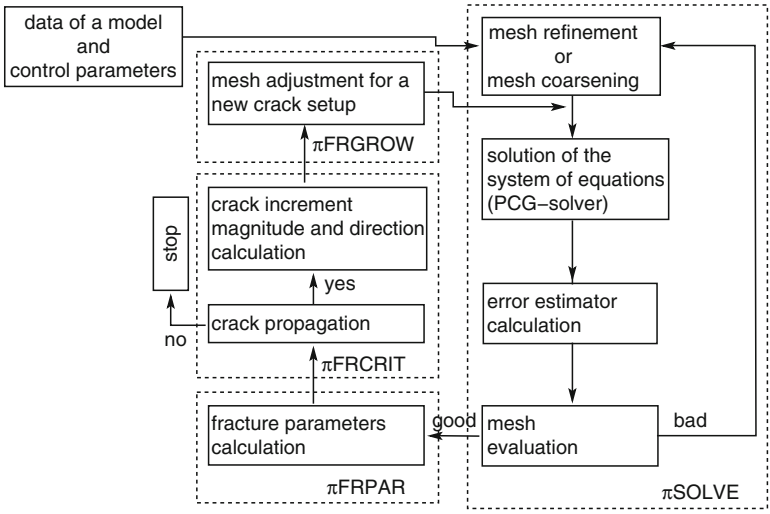

Fig. 1 Structure of the programm πCRACK

rate may be extraordinarily neglected. The criterion of the maximal modified hoop stress intensity factor, presented in the publication [10], fails e.g. in the case of pure electrical loading. For this loading, no crack propagation is predicted with the fracture criterion under consideration, whereas experimental findings are opposite. In order to test the criterion of the maximal modified hoop stress intensity factor more carefully, it has been implemented in the finite element tool πCRACK.

In Section 2, the structure of the specially developed finite element program πCRACK for crack propagation simulations in piezoelectric structures is presented. Sections 3 and 4 are devoted to adaptive remeshing and crack propagation algorithm, respectively. In Section 5, the fracture criterion implemented in the present version of the module πFRCRIT is described. To prove efficiency of the developed finite element tool, crack propagation simulation results in a plate being an approximation of Griffith's problem are presented in Section 6. Both the isotropic and anisotropic fracture toughnesses are assumed.

2 Structure of the Program πCRACK

The structure of the adaptive finite element programm πCRACK for crack propagation simulations in two-dimensional components is presented in Fig. 1. The module πSOLVE, which has been developed at the Faculty of Mathematics of Technical University of Chemnitz, solves the piezoelectric boundary value problem with the adaptive finite element method. The finite element solution is used in the module πFRPAR for the computation of the dielectric and mechanical intensity factors with

the interaction integral technique, see e.g. [6] or [5]. On the basis of the intensity factors, in the module πFRCRIT, the decision is undertaken if the crack propagates or not. In the case of crack growth, the fracture direction is computed. This direction is used for the finite element mesh adjustment in the module πFRGROW. After the finite element mesh modification, a new finite element solution is searched in the module πSOLVE. The fracture mechanical algorithms and computer routines have been developed at the Institute of Mechanics and Fluid Dynamics of Technical University of Freiberg. The description of the modules: πSOLVE, πFRPAR and πFRGROW can be found in the publication [5]. Some information on the modules: πSOLVE and πFRGROW is included in Sections 3 and 4, respectively.

3 Adaptive Remeshing (Module πSOLVE)

Even though locations of crack tips are usually known during crack propagation simulation, the density of the finite element mesh in the computer program under consideration is automatically adapted to the spatial distribution of the electrical and mechanical fields to model the spots of high gradients more accurately. Thereby h-adaptivity is chosen. According to this adaptivity type, finite element sizes are changed in dependency on the a posteriori computed local error in the former iteration. As the exact solution of the investigated problem is not known in the general case, the error of the finite element solution can not be quantified absolutely. Consequently, instead of exact errors, error estimators

$$R_{E,\sigma} = |E| \int_E \left\| \lceil \sigma_{\alpha\beta}\, n_\beta \rceil_E \right\|_2^2 ds, \quad R_{E,D} = |E| \int_E \lceil D_\alpha\, n_\alpha \rceil_E^2 \, ds \tag{1}$$

are used. These quantities characterise stress $\sigma_{\alpha\beta}$ and electric displacement D_α jumps along edges E of adjacent finite elements. In the Eqs. 1, $\lceil \quad \rceil_E$ means the mentioned jump, $\| \quad \|_2$, $| \quad |$ and n_α are the Euclidean vector norm, the length and the normal vector to E, respectively. Comparison of $R_{E,D}$ and $R_{E,\sigma}$ with maximal values allows to identify the regions where finite element sizes should be modified.

4 Crack Propagation Algorithm (Module πFRGROW)

To model a crack propagation on the finite element level, in the general case, generation of new nodes, edges and elements is necessary. In the finite element program under consideration, they are generated by the node and edge duplication technique as well as by the element splitting algorithm, which is graphically presented in Fig. 2. Thereby, S_1 corresponds to the tip of an initial crack of length a_0 and S_2 to the tip of the crack after the crack propagation with length $a = a_0 + \Delta a$. ω describes the propagation angle with respect to the direction of the initial crack and Δa is

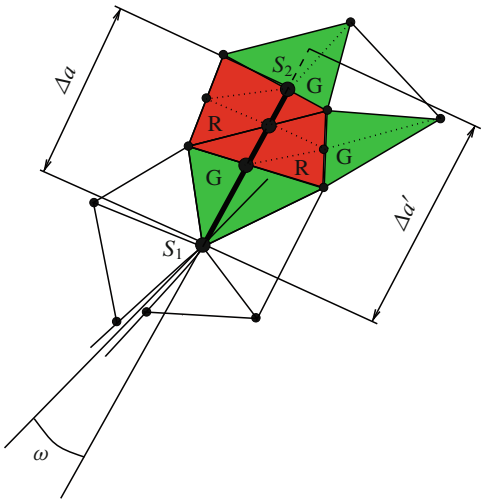

Fig. 2 Edge duplication and element splitting algorithm

the propagation length. During the edge duplication process, intersection points between a test segment of length $\Delta a' > \Delta a$ and finite element edges are searched in the first step. In the intersection points, new finite element nodes are pairwise defined. Then, the new nodes are used by the definition of pairs of finite element edges. Having introduced the additional nodes and edges, the concerned finite elements must be splitted according to the principle in Fig. 2. Thereby, two splitting variants can be distinguished. The first variant (green) pertains to those finite elements where only one edge is cut by the test segment, the second one (red) to those finite elements where two edges are cut by the mentioned segment. The corresponding description G (green) and R (red) is used in Fig. 2. The green splitting of an initial finite element creates two new elements, and the red one four new elements.

5 Implemented Fracture Criterion (Module πFRCRIT)

The criterion of the maximal modified hoop stress intensity factor [10] is implemented in the present version of the module πFRCRIT. Measurements of the fracture toughness of polarized piezoceramics show that the toughness $K_c^{||}$ in direction parallel to the poling direction is higher than the toughness $K_c^{\perp}$ in direction perpendicular to the poling direction [8]. The reported ratio $K_c^{||}/K_c^{\perp}$ ranges from 1.15 to 2.36 for different piezoceramics. To obtain the fracture toughness in any direction, the interpolation formula can be used [10]. Thereby (r, θ) is a polar

$$K_c(\theta) = K_c^{\perp} cos^2(\theta + \alpha) + K_c^{||} sin^2(\theta + \alpha) \tag{2}$$

coordinate system with the origin in the crack tip. $\theta = 0$ defines the tangential ray to the crack path in direction opposite to the crack. The angle α depends on the local orientation of the coordinate system (r, θ) with respect to the poling direction of the probe. The hoop stress intensity factor is defined as

$$K_{\theta\theta}(\theta) = \lim_{r \to 0} \sqrt{2\pi r}\, \sigma_{\theta\theta}(\theta) \tag{3}$$

and the modified hoop stress intensity factor as

$$K^*(\theta) = K_{\theta\theta}(\theta) / K_c(\theta). \tag{4}$$

In Eq. 3, $\sigma_{\theta\theta}(\theta)$ represents the hoop stress. Using the criterion of the modified hoop stress intensity factor, the crack growth direction θ_{max} is predicted which guarantees maximal modified hoop stress intensity factor. The crack propagates in this direction if the condition

$$K_{\theta\theta}(\theta_{max}) \geq K_c(\theta_{max}) \tag{5}$$

is satisfied.

6 Numerical Example

In the present section, crack propagation simulation results obtained with the finite element program πCRACK are presented. The propagation starts in one of the crack tips of a straight impermeable crack of length $2a = 0.02\,\mathrm{m}$ located in a square plate depicted in Fig. 3. The plate is loaded with the stresses σ_{22}^{∞} and σ_{12}^{∞} as well as the electric displacement D_2^{∞}. The parameters of the considered piezoelectric material PZT4 are presented in Table 1. Thereby $\{c_{11}, c_{22}, c_{13}, c_{12}, c_{44}\}$, $\{e_{16}, e_{21}, e_{22}\}$ and $\{\kappa_{11}, \kappa_{22}\}$ are the elastic, piezoelectric and dielectric material parameters, respectively. In the simulation, one assumes that the condition (5) is always fulfilled. Two cases are investigated: the isotropic with $K_c^{\perp} = K_c^{||}$ and anisotropic with $2K_c^{\perp} = K_c^{||}$. The length of the crack propagation step is set constant and equals 5×10^{-4} m. Adaptive refinement steps are performed between the crack propagation steps. The chosen number of adaptive steps guarantees stabilization of the computed intensity factors. In Fig. 4, the initial finite element mesh and finite element meshes just after each of the nine propagation steps are exemplarily presented. The meshes correspond to the case with the isotropic fracture toughness. After the first propagation step in which a sharp change of the crack orientation can be observed, the propagation direction stabilizes. In Fig. 5, mechanical and dielectric intensity factors are plotted for the isotropic case as a function of both the refinement and propagation steps. The starting eleven steps correspond to the finite element mesh refinement which is carried out to obtain stable intensity factors for the straight initial crack. Afterwards, the first propagation step is performed. This results in an abrupt drop of the intensity factor K_{II}. In the next eight refinement

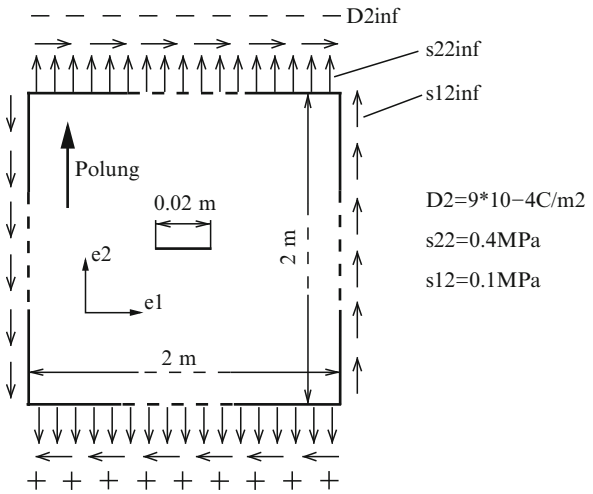

Fig. 3 Griffith's problem model

Table 1 PZT4 material parameters

c_{11} (N/m^2)	c_{22} (N/m^2)	c_{13} (N/m^2)	c_{12} (N/m^2)	c_{44} (N/m^2)
1.402×10^{11}	1.158×10^{11}	7.892×10^{10}	7.565×10^{10}	2.527×10^{10}
e_{16} (C/m^2)	e_{21} (C/m^2)	e_{22} (C/m^2)	κ_{11} (C^2/N m^2)	κ_{22} (C^2/N m^2)
13.00	-5.268	15.44	6.368×10^{-9}	5.523×10^{-9}

steps, stable values of the three intensity factors K_I, K_{II} and K_{IV} are reached. In the twenty first step, the second propagation is realized. The next four steps are once again refinement steps resulting in the convergence of the intensity factor K_{II} to zero. This value of the intensity factor under consideration is approximately kept constant till the end of the computation. In this way, the fracture criterion assuming crack propagation in the direction of $K_{II} = 0$ is indirectly recovered. Numerical tests show that the non-zero value of K_{II} after the first propagation step converges to zero with the decrease of the length of the crack propagation step. Apart from certain crack propagation steps, the intensity factors K_I and K_{IV} increase slowly but monotonically in the whole computation.

In Fig. 6, the modified hoop stress intensity factor $K^*(\theta)$ is presented around the crack tip. The diagram corresponds to the situation immediately before the first propagation step. The modified hoop stress intensity factor in the diagram under consideration is multiplied by the fracture toughness $K_c^{\perp}$ defined in direction perpendicular to the poling direction. The two already mentioned cases: isotropic and anisotropic toughness, the maximum value of $K^*(\theta)$ is reached for $\theta = -26°$, whereas in the case of the anisotropic fracture toughness, for $\theta = -7°$. The first of the two propagation directions is corrected in the second propagation step and

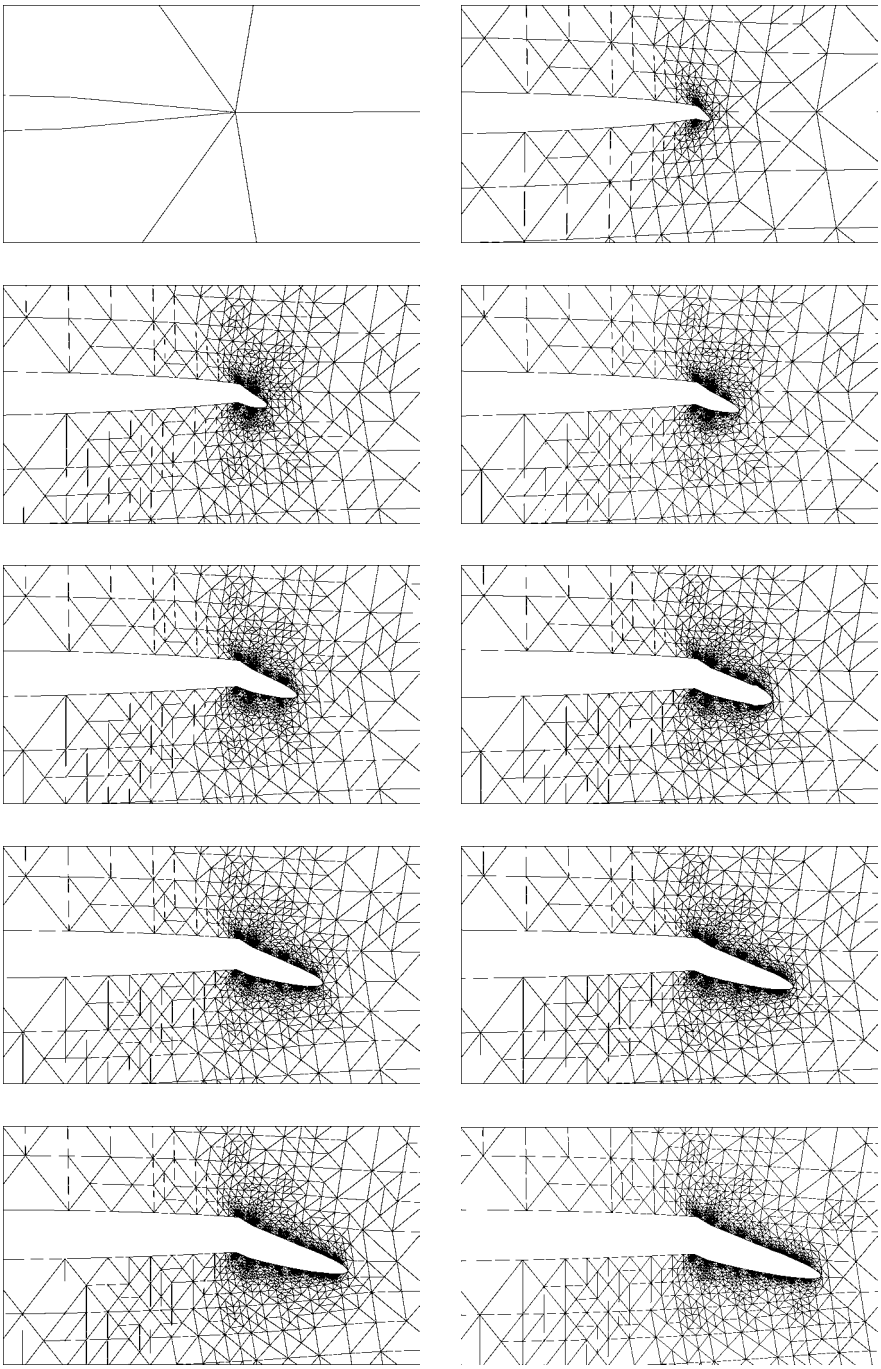

Fig. 4 Finite element meshes after each of the nine crack propagation steps

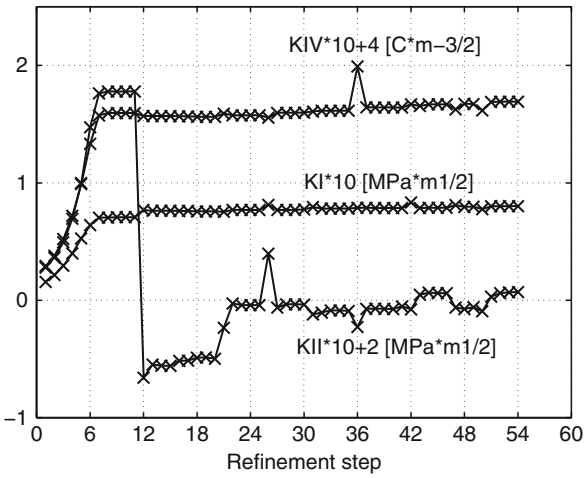

Fig. 5 Dependence of intensity factors on the mesh refinement or propagation step

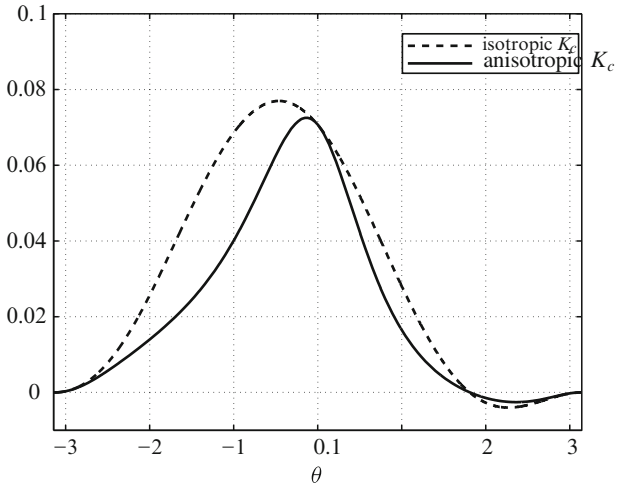

Fig. 6 Modified hoop stress intensity factor around the crack tip

remains approximately constant to the end of the simulation. This correction, which gives the value $\theta = -17°$, is associated with the finite length of the crack propagation step. The second of the two propagation directions remains approximately constant already after the first propagation step. Since the length of the crack propagation step is the same for the isotropic and anisotropic fracture toughness, it is the value of the propagation direction angle which is also important considering the precision of the propagation direction prediction. In Fig. 7, mechanical and dielectric intensity factors are plotted for the anisotropic case as a function of both the refinement and propagation steps. Contrary to the diagram in Fig. 5, the intensity factor

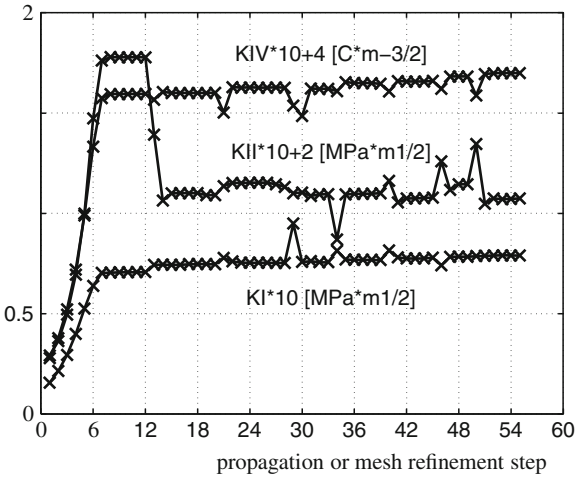

Fig. 7 Dependence of intensity factors on the mesh refinement or propagation step

K_{II} in Fig. 7 does not converge to zero, which is due to the anisotropic toughness behaviour. Apart from certain crack propagation steps, the two intensity factors K_I and K_{IV} increase slowly but monotonically with increasing computation step.

Acknowledgements The support of this work by the German Research Foundation under grants KU929/12-2 and ME1224/5-2 is gratefully acknowledged.

References

1. Alshoaibi AM, Hadi MSA, Ariffin AK (2007) An adaptive finite element procedure for crack propagation analysis. J Zhejiang Univ Sci A 8:228–236
2. Belytschko T, Black T (1999) Elastic crack growth in finite elements with minimal remeshing. Int J Numer Method Eng 45:601–620
3. Bordas S, Duflot M (2007) Derivative recovery and a posteriori error estimate for extended finite elements. Comput Method Appl Mech Eng 196:3381–3399
4. Haertling GH (1999) Ferroelectric ceramics: History and technology. J Am Ceramic Soc 82:797–818
5. Janski L, Scherzer M, Steinhorst P, Kuna M (2010) Adaptive finite element computation of dielectric and mechanical intensity factors in piezoelectrics with impermeable cracks. Int J Numer Method Eng 81:1492–1513
6. Kuna M (2006) Finite element analyses of cracks in piezoelectric structures: A survey. Arch Appl Mech 76:725–745
7. Park SB, Sun CT (1995) Effect of electric field on fracture of piezoelectric ceramics. Int J Fract 70:203–216

8. Pisarenko GG, Chushko VM, Kovalev SP (1985) Anisotropy of fracture toughness of piezoelectric ceramics. J Am Ceramic Soc 68:259–265
9. Rabold F, Meyer A, Scherzer M (2006) Efficient finite element simulation of crack propagation using adaptive iterative solvers. Commun Numer Method Eng 22:93–108
10. Xu X-L, Rajapakse RKND (2000) A theoretical study of branched cracks in piezoelectrics. Acta Mater 48:1865–1882

This page intentionally left blank

Periodic Set of the Interface Cracks with Limited Electric Permeability

V.V. Loboda and S.V. Kozinov

Abstract Plane problem for an infinite space which consists of two different piezoelectric materials with periodic set of the limited electrically permeable interface cracks is considered. Uniformly distributed electromechanical loading is applied. The solution of the problem is obtained in close form by use of complex function theory. Formulae for stresses, electric displacement vector, elastic displacements and electric potential jump at the interface as well as the intensity factors at the crack tips are given. The main attention is paid to the influence of electric permeability of the cracks on electromechanical fields in the composite. As a particular case the periodic set of limited permeable cracks in a homogeneous piezoelectric material is studied.

1 Introduction

Due to their intrinsic coupled electromechanical behavior, piezoelectric ceramics are widely used in engineering as sensors, transducers and actuators. However, these materials are very brittle and predisposed to fracture. Their premature failure can be caused by high mechanical stresses or electrical fields. Therefore, it is very important to study the fracture behavior of piezoelectric ceramics under combined action of mechanical stresses and electrical fields. But the problems related to the fracture mechanics of piezoelectric ceramics are rather complex and they are far from their complete solutions.

Much difficulty calls the problem of correct formulation of electrical conditions at the crack faces. Because a crack is usually filled by some media (air, water and so on) the properties of this media should be taken into consideration. But it was not easy and therefore the simplified limiting cases of electrically permeable crack was

V.V. Loboda (✉) and S.V. Kozinov
Department of Theoretical and Applied Mechanics, Dniepropetrovsk National University, Gagarina 72, Dniepropetrovsk 49010, Ukraine
e-mail: loboda@mail.dsu.dp.ua

M. Kuna and A. Ricoeur (eds.), *IUTAM Symposium on Multiscale Modelling of Fatigue, Damage and Fracture in Smart Materials*, IUTAM Bookseries 24,
DOI 10.1007/978-90-481-9887-0_17,

suggested by Parton [14] and opposite case of electrically impermeable crack was suggested and essentially developed by Deeg [1], Pak [13] and Suo et al. [17]. Many investigations have been performed in the framework of these models, however Parton and Kudryavtsev [15] and Hao and Shen [6] suggested the crack face conditions which take into account the property of the crack medium. This conditions has attract grate attention in the literature [5,12,18] among many others. Govorukha et al. [4] and Li and Chen [10] applied this conditions to the interface crack investigation. Energetically consistent boundary conditions were suggested by Landis [9] and developed by Li et al. [11], Ricoeur and Kuna [16].

Investigation of a periodic set of electrically permeable cracks between a piezoelectric and a conductor was performed by Kudryavtsev and Rakitin [8] and a periodic set of electrically insulated cracks in a magnetoelectroelastic solid was considered by Gao et al. [3]. However, to the authors' knowledge a periodic set of cracks with limited electrical permeability has been considered yet neither for interface cracks nor for cracks in a homogeneous piezoelectric media. Such a problem for a periodic set of limited permeable interface cracks is considered in a present paper and the results for a crack in a homogeneous media are presented as a particular case of the obtained solution as well.

2 General Solution of Basic Equations

The constitutive relations for a linear piezoelectric material in the absence of body forces and free charges can be presented in the form [13]:

$$\Pi_{iJ} = \mathrm{E}_{iJKl}\mathrm{V}_{K,l}, \tag{1}$$

$$\Pi_{iJ,i} = 0, \tag{2}$$

where

$$\mathrm{V}_K = \begin{cases} u_k, & K = 1,2,3, \\ \varphi, & K = 4, \end{cases} \tag{3}$$

$$\Pi_{iJ} = \begin{cases} \sigma_{iJ}, & i,J = 1,2,3, \\ D_i, & i = 1,2,3; \quad J = 4, \end{cases} \tag{4}$$

$$\mathrm{E}_{iJKl} = \begin{cases} C_{ijkl}, & J,K = 1,2,3, \\ e_{lij}, & J = 1,2,3; \quad K = 4, \\ e_{ikl}, & K = 1,2,3; \quad J = 4, \\ -\varepsilon_{il}, & J = K = 4. \end{cases} \tag{5}$$

$u_k, \varphi, \sigma_{ij}, D_i$ are elastic displacements, electric potential, stresses and electric displacements, respectively. Small subscripts in (1)–(5) and afterwards are ranging from 1 to 3, capital subscripts are ranging from 1 to 4.

Conducting some transformations, similar to Herrmann and Loboda [7] the following expressions for the elastic displacements and electric potential jump, stress tensor components and electric displacement vector are obtained at the interface:

$$\left[\left[\mathbf{V}'(x_1,0)\right]\right] = \mathbf{W}^{+}(x_1) - \mathbf{W}^{-}(x_1), \tag{6}$$

$$\mathbf{t}^{(1)}(x_1,0) = \mathbf{G}\mathbf{W}^{+}(x_1) - \bar{\mathbf{G}}\mathbf{W}^{-}(x_1) \tag{7}$$

where

$$\left[\left[\mathbf{V}'(x_1,0)\right]\right] = \mathbf{V}'^{(1)}(x_1) - \mathbf{V}'^{(2)}(x_1), \tag{8}$$

and $\mathbf{G} = \mathbf{B}^{(1)}\mathbf{D}^{-1}, \mathbf{D} = \mathbf{A}^{(1)} - \bar{\mathbf{A}}^{(2)}\left(\bar{\mathbf{B}}^{(2)}\right)^{-1}\mathbf{B}^{(1)}, \mathbf{W}^{+}(x_1) = \mathbf{W}(x_1 + i0)$, $\mathbf{W}^{-}(x_1) = \mathbf{W}(x_1 - i0); \mathbf{A}^{(m)}, \mathbf{B}^{(m)}$ are known matrices [17], where m = 1 is related to the "upper" material and m = 2 to the "lower" one; $\mathbf{V} = \{u_1, u_2, u_3, \varphi\}^{\mathrm{T}}$ and $\mathbf{t} = \{\sigma_{13}, \sigma_{23}, \sigma_{33}, D_3\}^{\mathrm{T}}$. $\mathbf{W}(z)$ is analytic vector-function in the whole plane except the cracks region.

3 Statement of the Problem

Consider an infinite piezoelectric bimaterial containing periodic set of interface cracks, as shown in Fig. 1. The materials are specified by the elastic moduli $C_{ijkl}^{(m)}$, piezoelectric constants $e_{ikl}^{(m)}$ and dielectric constants $\varepsilon_{il}^{(m)}$, where $m = 1$ is related to the "upper" material and $m = 2$ to the "lower" one.

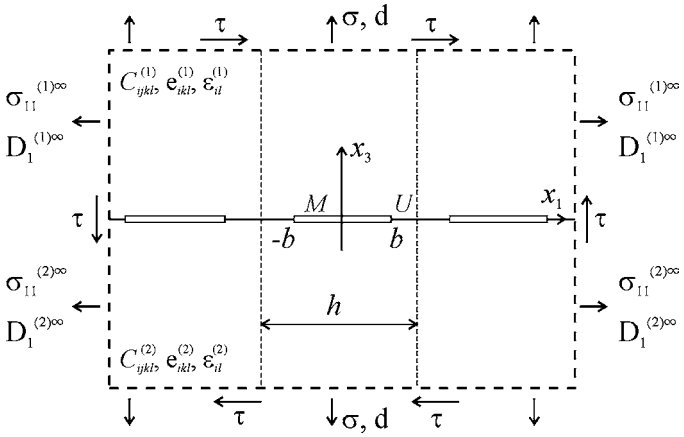

Fig. 1 Periodic set of the interface cracks in the piezoelectric bimaterial

Assume that uniformly distributed tensile σ and shear τ stressed and electric displecement d are applied at infinity. Under such loading cracks are opened. The crack tips in the fundamental strip [2] are denoted as $-b$ and b, the period length is h. Additionally, the union of the open crack faces is denoted as M and the bonded parts of the interface as U (see Fig. 1).

We assume that the electric field inside the cracks can be found as $E_a = -(\varphi^+ - \varphi^-)/(u^+ - u^-)$ and taking into account that $D_3 = \varepsilon_a E_a$, one arrive to the electric condition $D_3 = -\varepsilon_a(\varphi^+ - \varphi^-)/(u^+ - u^-)$ along the cracks region. Here $\varepsilon_a = \varepsilon_0 \varepsilon_r$ is the permittivity of the material inside the crack, $\varepsilon_0 = 8{,}85 \cdot 10^{-12}\mathrm{C}/(\mathrm{V} \cdot \mathrm{m})$. The obtained conditions are the same as in Hao and Shen [6]. Thus, sssuming that the open crack faces are unloaded, the continuity and boundary conditions can be written

$$[[\mathbf{V}(x_1, 0)]] = 0, \quad [[\mathbf{t}(x_1, 0)]] = 0, \quad x_1 \in U, \tag{9}$$

$$\begin{gathered} \sigma_{13}^{\pm}(x_1, 0) = 0, \quad \sigma_{33}^{\pm}(x_1, 0) = 0, \\ D_3 \left[[u_3(x_1, 0)]\right] = -\varepsilon_a \left[[\varphi(x_1, 0)]\right], \quad [[D_3(x_1, 0)]] = 0, \quad x_1 \in M, \end{gathered} \tag{10}$$

where [[ ]] stands for the jump of the function while crossing the interface.

4 Solution of the Boundary Value Problem

Suppose that the piezoelectric materials are of the symmetry class 6 mm [15] poled in the direction x_3. In this case for of the loading under consideration the plane strain state takes place and the matrix $\mathbf{G}$ has the following structure (without the second row and column):

$$\mathbf{G} = \begin{bmatrix} ig_{11} & g_{13} & g_{14} \\ g_{31} & ig_{33} & ig_{34} \\ g_{41} & ig_{43} & ig_{44} \end{bmatrix},$$

where all g_{ij} $(i, j = 1, 3, 4)$ are real and are defined by the electromechanical constants of the piezoelectric composite material.

Combination of the Eqs. (6) and (7) leads to the following formula:

$$\sigma_{33}^{(1)}(x_1, 0) + m_{j4} D_3^{(1)}(x_1, 0) + i m_{j1} \sigma_{13}^{(1)}(x_1, 0) = F_j^+(x_1) + \gamma_j F_j^-(x_1), \tag{11}$$

where

$$F_j(z) = n_{j1} W_1(z) + i\left[n_{j3} W_3(z) + n_{j4} W_4(z)\right], \tag{12}$$

The coefficients m_{jl}, n_{jl}, γ_j $(j, l = 1, 3, 4)$ depends on the electromechanical properties of the composite and for the ceramic of class 6 mm are real.

Assume that the electric flux is constant along the crack faces:

$$D_3^+(x_1,0) = D_3^-(x_1,0) = D, \quad x_1 \in M. \tag{13}$$

Using Eqs. (11) and (13) together with conditions (10) at the crack faces, one gets the following periodic Riemann boundary value problem:

$$F_j^+(x_1) + \gamma_j F_j^-(x_1) = m_{j4} D \quad (j = 1,3,4), \quad x_1 \in M. \tag{14}$$

Introducing new function:

$$\Phi_j(z) = F_j(z) - m_{j4} D/(1+\gamma_j), \tag{15}$$

the Eq. (14) attains the following form:

$$\Phi_j^+(x_1) + \gamma_j \Phi_j^-(x_1) = 0 \quad (j = 1,3,4) \quad x_1 \in M, \tag{16}$$

$$\Phi_j(z)\big|_{\to \pm i\infty} = \sigma_j^* - i\tau_j^*, \tag{17}$$

where $\sigma_j^* = [\sigma + m_{j4}(d-D)]/(1+\gamma_j)$, $\quad \tau_j^* = -m_{j1}\tau/(1+\gamma_j)$. A solution to (16) one presents in the following form [2]:

$$\Phi_j(z) = \frac{C_{1j}\cos(\pi z/h) + C_{2j}\sin(\pi z/h)}{\sqrt{\sin(\pi(z-b)/h)\sin(\pi(z+b)/h)}} \left[\frac{\sin(\pi(z+b)/h)}{\sin(\pi(z-b)/h)}\right]^{i\varepsilon_j}. \tag{18}$$

Here $\varepsilon_j = \ln\gamma_j/(2\pi)$. The function $\Phi_j(z)$ has the following behavior at infinity:

$$\Phi_j(z)\big|_{z\to+i\infty} = (C_{2j} - iC_{1j})e^{2\pi b\varepsilon_j/h}, \quad \Phi_j(z)\big|_{z\to-i\infty} = (C_{2j} + iC_{1j})e^{-2\pi b\varepsilon_j/h}. \tag{19}$$

Making use of Eqs. (17) and (19) one can derive the system of equations for the arbitrary constants C_{1j} and C_{2j} determination. The solution of this system is the following:

$$C_{1j} = -\sin(2\pi i\varepsilon_j b/h)\left(\sigma_j^* - i\tau_j^*\right), \quad C_{2j} = \cos(2\pi i\varepsilon_j b/h)\left(\sigma_j^* - i\tau_j^*\right).$$

Substituting previous formulae into Eq. (18) and conducting some transformations the solution of the homogeneous Riemann boundary problem (16) can be written as

$$\Phi_j(z) = \left(\sigma_j^* - i\tau_j^*\right)\frac{\Xi(z-2i\varepsilon_j b)}{\sqrt{\Xi(z-b)\Xi(z+b)}}\left[\frac{\Xi(z+b)}{\Xi(z-b)}\right]^{i\varepsilon_j}. \tag{20}$$

where $\Xi(\vartheta) = \sin(\pi\vartheta/h)$.

Using (12), the following relations yield:

$$n_{j1}\left[\left[u_1'(x_1,0)\right]\right]+i\left(n_{j3}\left[\left[u_3'(x_1,0)\right]\right]+n_{j4}\left[\left[\varphi'(x_1,0)\right]\right]\right)=F_j^+(x_1)-F_j^-(x_1).$$

Since $\Phi_j^-(x_1)=-\Phi_j^-(x_1)/\gamma_j,\ x_1\in M$, then $F_j^+(x_1)-F_j^-(x_1)=(\gamma_j+1)/\gamma_j\Phi_j^+(x_1)$ the formula for the displacement jump derivatives takes the form:

$$\begin{aligned}&n_{j1}\left[\left[u_1'(x_1,0)\right]\right]+i\left(n_{j3}\left[\left[u_3'(x_1,0)\right]\right]+n_{j4}\left[\left[\varphi'(x_1,0)\right]\right]\right)\\&=-i\frac{\gamma_j+1}{\sqrt{\gamma_j}}\left(\sigma_j^*-i\tau_j^*\right)\frac{\Xi(x_1-2i\varepsilon_j b)}{\sqrt{\Xi(b-x_1)\Xi(b+x_1)}}\left[\frac{\Xi(b+x_1)}{\Xi(b-x_1)}\right]^{i\varepsilon_j},x_1\in M,\end{aligned}\tag{21}$$

Further, conducting some transformations for the last expression taking into account smallness of the ε_1 value and the fact that $\varepsilon_4=0$, and using (10), one obtains the equation for the electric displacement D inside the crack determination:

$$D=\varepsilon_a\frac{n_{43}\sigma_1^*(D)-n_{13}\sigma_4^*(D)}{n_{44}\sigma_1^*(D)-n_{14}\sigma_4^*(D)},\tag{22}$$

It can be rewritten in the form

$$\eta_1^*D^2+\eta_2^*D+\eta_3^*=0,\tag{23}$$

where

$$\begin{aligned}\eta_1^*&=\sqrt{\gamma_1}m_{44}n_{14}-m_{14}n_{44},\\\eta_2^*&=(s_1n_{44}+\varepsilon_a m_{14}n_{43})-\sqrt{\gamma_1}(s_4n_{14}+\varepsilon_a m_{44}n_{13}),\\\eta_3^*&=\varepsilon_a(\sqrt{\gamma_1}n_{13}s_4-n_{43}s_1).\end{aligned}$$

Use of the Eqs. (11), (15) and (20) for $j=1$ and their real part for $j=4$ leads to the set of equations for the stresses and electric displacement determination for $x_1\in U$:

$$\begin{aligned}&\sigma_{33}^{(1)}(x_1,0)+m_{14}D_3^{(1)}(x_1,0)+im_{11}\sigma_{13}^{(1)}(x_1,0)=\\&=(\sigma+m_{14}(d-D)+im_{11}\tau)\frac{\Xi(x_1-2i\varepsilon_1 b)}{\sqrt{\Xi(x_1-b)\Xi(x_1+b)}}\left[\frac{\Xi(x_1+b)}{\Xi(x_1-b)}\right]^{i\varepsilon_1}+m_{14}D,\end{aligned}\tag{24}$$

$$\sigma_{33}^{(1)}(x_1,0)+m_{44}D_3^{(1)}(x_1,0)=(\sigma+m_{44}(d-D))\frac{\Xi(x_1)}{\sqrt{\Xi(x_1-b)\Xi(x_1+b)}}+m_{44}D.\tag{25}$$

Intensity factors (IF) can be introduced similar to Govorukha et al. [4]:

$$K_1 + m_{14}K_4 + im_{11}K_2 = \lim_{x_1 \to b+0} \sqrt{2\pi(x_1 - b)}(x_1 - b)^{i\varepsilon_1} \left[\sigma_{33}^{(1)}(x_1, 0) + m_{14}D_3^{(1)}(x_1, 0) + im_{11}\sigma_{13}^{(1)}(x_1, 0)\right], \quad (26)$$

$$K_1 + m_{44}K_4 = \lim_{x_1 \to b+0} \sqrt{2\pi(x_1 - b)}\left[\sigma_{33}^{(1)}(x_1, 0) + m_{44}D_3^{(1)}(x_1, 0)\right]. \quad (27)$$

Using formulae (24), (25) at $x_1 \to b + 0$, one obtains the following system for the IFs determination:

$$K_1 + m_{14}K_4 + im_{11}K_2 = \sqrt{2\pi}\,(\sigma + m_{14}(d - D) + im_{11}\tau)\,\frac{\Xi\,(b - 2i\varepsilon_1 b)}{\sqrt{\frac{\pi}{h}\,\Xi(2b)}}\left[\frac{h}{\pi}\,\Xi(2b)\right]^{i\varepsilon_1},$$

$$K_1 + m_{44}K_4 = \sqrt{\pi}\sqrt{\frac{h}{\pi}\tan\frac{\pi b}{h}}\,(\sigma + m_{44}(d - D))\,.$$

5 Numerical Results for the Piezoelectric Bimaterial

Examine the influence of the external mechanical and electrical loading on the electric displacement inside the crack and the IFs for some electric permeability values. Piezoelectric bimaterial PZT-4/PZT-5 is under consideration, the period is taken π, the length of the crack is the tenth part of the period. It should be noticed that the relative electric permeability ε_r value for air is 1, for the silicon oil is 2.5, for water 81. Values of ε_r equal to 10^{-6} and 4,000 can be considered as for completely impermeable and fully permeable cracks, correspondingly.

In the Table 1 some results for the case of strong mechanical and weak electric loading are presented. Mechanical IF K_1 for the different crack permeability changes insignificantly. At the same time variation of K_2 is more sensible. Electric IF K_4 depends essentially on the permeability of the crack.

Table 1 Electric displacement and IFs variation under strong mechanical ($\sigma = 10$ MPa) and weak electric ($d = 0.001\,\mathrm{C/m^2}$) loading

ε_r	D (C/m^2)	K_1 (MPa/m$^{1/2}$)	K_2 (MPa/m$^{1/2}$)	$K_4 \times 10^4$ (C/m$^{3/2}$)
10^{-6}	-5.72×10^{-9}	7.05319	0.131331	7.05494
1	−0.00130	7.05303	0.159217	16.2392
2.5	−0.00154	7.05300	0.164234	17.8916
81	−0.00175	7.05298	0.168734	19.3734
4,000	−0.00175	7.05298	0.168897	19.4272

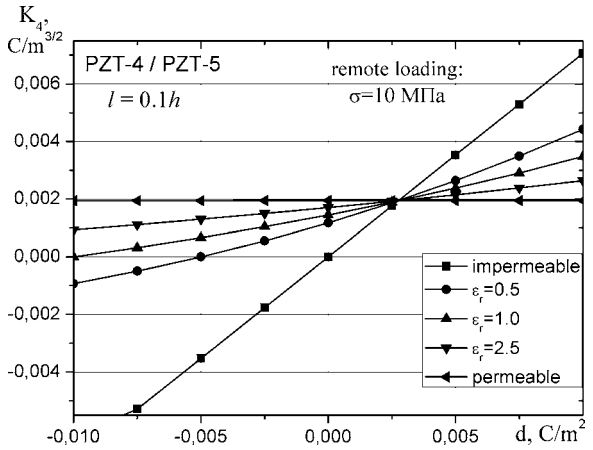

Fig. 2 Dependence of the electric IF K_4 from the external electric loading for the different crack permeability values

Table 2 Electric displacement and IFs variation under weak mechanical ($\sigma = 1{,}000\,\text{Pa}$) and strong electric ($d = 0.01\,\text{C/m}^2$) loading

ε_r	D (C/m^2)	K_1 (kPa/m$^{1/2}$)	K_2 (kPa/m$^{1/2}$)	$K_4 \times 10^4$ (C/m$^{3/2}$)
10^{-6}	3.21×10^{-8}	−0.5039	214.2	70.5407
1	0.00999	0.7052	0.0281	0.00564
2.5	0.00999	0.7053	0.0204	0.00311
81	0.00999	0.7053	0.0170	0.00197
4,000	0.00999	0.7053	0.0169	0.00194

In Fig. 2 the relationship between electric IF K_4 and external electric loading which changes continuously from -0.01 to $0.01\,\text{C/m}^2$ for different crack permeability ε_r values is shown. For the completely permeable crack K_4 value is almost constant, but with the ε_r reduction the influence of the eclectic loading becomes more significant, because smaller electric conductivity leads to greater electric singularity at the vicinity of the crack tips due to electric shielding. For zero electric loading only completely permeable crack has zero K_4 value. In other cases mechanical loading has an influence on the electric singularity because electric displacement perpendicular to the crack faces in nonzero. At point $d = 0.0025\,\text{C/m}^2$ all curves intersect in the same point which means that for such loading K_4 value coincide for impermeable and completely permeable cracks as well as for cracks with arbitrary electric permeability.

Results for weak mechanical and strong electric loading are presented in Table 2. Significant increase the IFs magnitude when ε_r tends to zero can be noticed. It is connected with the singularity of the stress fields at the crack tips and strong electric loading.

6 Periodic Set of the Interface Cracks with Limited Electric Permeability in Homogeneous Material

Consider as a particular case a periodic set of the cracks in a homogeneous piezoelectric material. Equation (22) is now exact without any assumptions and formulae for the stresses and electric displacement at the crack line have the following form:

$$\sigma_{33}^{(1)}(x_1,0)=\sigma\frac{\Xi(x_1)}{\sqrt{\Xi(x_1-b)\Xi(x_1+b)}},\quad x_1\in U, \tag{28}$$

$$\sigma_{13}^{(1)}(x_1,0)=\tau\frac{\Xi(x_1)}{\sqrt{\Xi(x_1-b)\Xi(x_1+b)}},\quad x_1\in U, \tag{29}$$

$$D_3^{(1)}(x_1,0)=(d-D)\frac{\Xi(x_1)}{\sqrt{\Xi(x_1-b)\Xi(x_1+b)}}+D,\quad x_1\in U. \tag{30}$$

Introduction of the IFs by the formulae

$$K_1=\lim_{x_1\to b+0}\sqrt{2\pi(x_1-b)}\sigma_{33}^{(1)}(x_1,0), \tag{31}$$

$$K_2=\lim_{x_1\to b+0}\sqrt{2\pi(x_1-b)}\sigma_{13}^{(1)}(x_1,0),$$

$$K_4=\lim_{x_1\to b+0}\sqrt{2\pi(x_1-b)}D_3^{(1)}(x_1,0), \tag{32}$$

leads to their following expressions:

$$K_1=\sqrt{\pi}\sqrt{\frac{h}{\pi}\tan\frac{\pi b}{h}}\sigma,\ K_2=\sqrt{\pi}\sqrt{\frac{h}{\pi}\tan\frac{\pi b}{h}}\sigma\tau,$$

$$K_4=\sqrt{\pi}\sqrt{\frac{h}{\pi}\tan\frac{\pi b}{h}}\sigma(d-D). \tag{33}$$

It should be mentioned that for $\varepsilon_1=0$ Eqs. (26) and (27) coincide with the formulae (32) and (32) and the IFs presented for the bimaterial are simplified to the expressions (33).

Elastic displacements and electric potential jump are expressed by the following formulae:

$$[[u_3(x_1,0)]]=\{\vartheta_{11}\sigma+\vartheta_{12}(d-D)\}H(x_1),\quad x_1\in U, \tag{34}$$

$$[[u_1(x_1,0)]]=-m_{11}n_{11}^{-1}\tau H(x_1),\quad x_1\in U, \tag{35}$$

$$[[\varphi(x_1,0)]]=\{\vartheta_{21}\sigma+\vartheta_{22}(d-D)\}H(x_1),\quad x_1\in U. \tag{36}$$

where

$$H(x_1)=\frac{h}{\pi}\ln\frac{\cos(\pi x_1/h)+\sqrt{\sin(\pi(b-x_1)/h)\sin(\pi(b+x_1)/h)}}{\cos(\pi b/h)},$$

$$\Delta = n_{13}n_{44} - n_{14}n_{43},$$
$$\vartheta_{11} = \frac{n_{44} - n_{14}}{\Delta}; \quad \vartheta_{12} = \frac{m_{14}n_{44} - m_{44}n_{14}}{\Delta}; \quad \vartheta_{21} = \frac{n_{13} - n_{43}}{\Delta};$$
$$\vartheta_{22} = \frac{m_{44}n_{13} - m_{14}n_{43}}{\Delta}.$$

According to Eqs. (28)–(30) stresses and electrical displacement asymptotic behavior at $x_1 \to b + 0$ has the form:

$$\sigma_{33}^{(1)}(x_1, 0) = \sigma\sqrt{\frac{h}{2\pi(x_1 - b)}\tan\frac{\pi b}{h}}, \quad \sigma_{13}^{(1)}(x_1, 0) = \tau\sqrt{\frac{h}{2\pi(x_1 - b)}\tan\frac{\pi b}{h}},$$
$$D_3^{(1)}(x_1, 0) = (d - D)\sqrt{\frac{h}{2\pi(x_1 - b)}\tan\frac{\pi b}{h}}. \tag{37}$$

Energy release rate ERR at point $x_1 = b$ is introduced according to Suo et al. [17].

$$G = \lim_{\Delta l \to 0} \frac{1}{2\Delta l} \int_b^{b+\Delta l} \left\{ \begin{array}{l} \sigma_{33}^{(1)}(x_1, 0)\,[[u_3(x_1 - \Delta l, 0)]] + \\ +\sigma_{13}^{(1)}(x_1, 0)\,[[u_1(x_1 - \Delta l, 0)]] + D_3^{(1)}(x_1, 0)\,[[\varphi(x_1 - \Delta l, 0)]] \end{array} \right\} dx_1.$$

Substituting the Eqs. (37)–(40) into the previous formula, one obtains:

$$G = \frac{\pi}{4} \cdot \frac{h}{\pi} \tan\frac{\pi b}{h} \left[\vartheta_{11}\sigma^2 + (\vartheta_{12} + \vartheta_{21})\sigma(d - D) + \vartheta_{22}(d - D)^2 - \frac{m_{11}}{n_{11}}\tau^2 \right].$$

7 Numerical Results

Consider the influence of the external mechanical and electrical loading on the electric displacement inside the crack and the IFs for some electric permeability values. Piezoelectric material PZT-4 is chosen. The period is taken π, the length of the crack is tenth part from the period.

In the Tables 3 and 4 results for the electric displacement inside the crack, electric IF K_4 and ERR G for the case of strong mechanical and weak electric loading acting in both directions are presented.

In Table 5 the variation of the electromechanical state of the crack in the case of very strong electric and moderate mechanical loading is analyzed. The strongest influence is observed for permeability values less than 1, i.e. when the crack is filled with substance possessing low electric permeability.

The influence of the external applied loading on the ERR is presented in Fig. 3a. It can be easily seen that for the limited permeable cracks the ERR does not vary proportionally with proportional electromechanical loading increase. Areas of the proportional variation start with approaching of the electrical permeability coefficient to its limited values.

Table 3 Electric displacement, electric IF and ERR variation under strong mechanical ($\sigma = 10$ MPa) and weak electric ($d = 0.001\,C/m^2$) loading

ε_r	D (C/m^2)	$K_4 \times 10^4$ (C/m$^{3/2}$)	G (N/m)
10^{-6}	-6.00×10^{-9}	7.05	524.191
1	−0.00119	15.4	572.478
2.5	−0.00137	16.7	574.462
81	−0.00152	17.8	575.022
4,000	−0.00153	17.8	575.023

Table 4 Electric displacement, electric IF and ERR variation under strong mechanical ($\sigma = 10$ MPa) and weak electric ($d = -0.001\,C/m^2$) loading

ε_r	D (C/m^2)	$K_4 \times 10^4$ (C/m$^{3/2}$)	G (N/m)
10^{-6}	-1.7879×10^{-8}	−7.0538	303.787
1	−0.00276356	12.4401	562.321
2.5	−0.00316293	15.2572	572.136
81	−0.00351383	17.7324	575.019
4,000	−0.00352648	17.8216	575.023

Table 5 Electric displacement, electric IF and ERR variation under moderate mechanical ($\sigma =$ 1MPa) and very strong electric ($d = 0,03\,C/m^2$) loading

ε_r	D (C/m^2)	$K_4 \cdot 10^4$ (C/m$^{3/2}$)	G (N/m)
10^{-6}	3.38×10^{-8}	211.6	−19291.7
1	0.0265	24.67	−223.879
2.5	0.0292	5.47	−0.2095
81	0.0297	1.86	5.7476
4,000	0.0297	1.78	5.7502

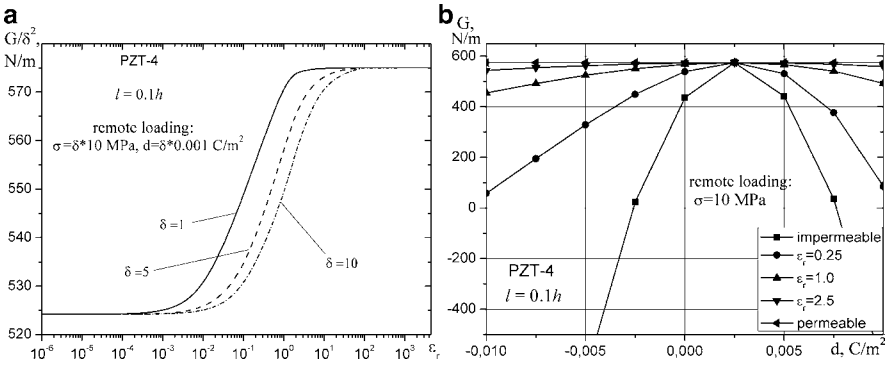

Fig. 3 ERR G with proportional electromechanical loading increase (**a**) and relation between ERR G and external applied electric loading (**b**) for the different electrical permeability coefficient values

In Fig. 3b the values of the ERR G with respect to the external electric loading at constant mechanical loading are shown. The strongest variation is observed for the cracks with low permeability coefficient. For the impermeable cracks the ERR in negative because of strong singularity. For the crack filled with air ($\varepsilon_r = 1$) singularity of the electric field is essentially lower and ERR acquires positive values. It should be noted that one of the methods which is based on the assumption that filled with air crack can be considered as electrically impermeable one results in contradiction when ERR is used as fracture criterion. According to this criterion the fracture will not take place because more energy is accumulated than released. On the contrary the energy release takes place with crack growth when permeability ($\varepsilon_r = 1$) is taken into account. With electric loading growth the ERR decreases which points on its restrictive impact on materials fracture.

8 Conclusions

The problem for the periodic set of the interface cracks with taking into account permeability of the crack medium is studied. The problem is solved analytically both for piezoelectric bimaterial and for homogeneous piezoelectric material. Analytical formulae for the stresses and electric displacement, stress intensity factors K_1, K_2, electrical intensity factor K_4 and the ERR G are derived. Numerical results are given for the bimaterial pair PZT-4 and PZT-5 and in a homogeneous case the piezoelectric PZT-4 is chosen. It is found that under weak external electric loading results are close to that obtained in the framework of fully permeable cracks. The fact of nonlinear variation of the electric displacement, IFs and the ERR under proportional increase of the external electromechanical loading is demonstrated.

References

1. Deeg W (1980) The analysis of dislocation, crack and inclusion problems in piezoelectric solids. Ph.D. Thesis, Stanford University
2. Gakhov F (1966) Boundary value problems. Pergamon Press, Oxford
3. Gao C-F, Kessler H, Balke H (2003) Crack problem in magnetoelectroelastic solids. Part II: general solution of collinear cracks. Int J Eng Sci 41:983–994
4. Govorukha V, Loboda V, Kamlah M (2006) On the influence of the electric permeability on an interface crack in a piezoelectric bimaterial compound. Int J Solids Struct 43:1979–1990
5. Gruebner O, Kamlah M, Munz D (2003) Finite element analysis of cracks in piezoelectric materials taking into account the permittivity of the crack medium. Eng Fract Mech. 70:1399–1413
6. Hao T, Shen Z (1994) A new electric boundary condition of electric fracture mechanics and its applications. Eng Fract Mech 47:793–802
7. Herrmann K, Loboda V (2000) Fracture-mechanical assessment of electrically permeable interface cracks in piezoelectric bimaterials by consideration of various contact zone models. Arch Appl Mech 70:127–143

8. Kudryavtsev B, Rakitin V (1976) Periodic set of cracks in the boundary of a piezoelectric and a rigid conductor. Isv. AN SSSR. Mechanika Tvordogo Tela 2:121–129 [in Russian]
9. Landis C (2004) Electrically consistent boundary conditions for electromechanical fracture. Int J Solids Struct 41:6291–6315
10. Li Q, Chen Y (2008) Solution for a semi-permeable interface crack in elastic dielectric/piezoelectric bimaterials. ASME J Appl Mech 75:011010-1-13
11. Li W, McMeeking R, Landis (2008) On the crack face boundary conditions in electromechanical fracture and an experimental protocol for determining energy release rates. Eur J Mech A/Solids 27:285–301
12. McMeeking R (1999) Crack tip energy release rate for a piezoelectric compact tension specimen. Eng Fract Mech 64:217–244
13. Pak Y (1992) Linear electro-elastic fracture mechanics of piezoelectric materials. Int J Fract 54:79–100
14. Parton V (1976) Fracture mechanics of piezoelectric materials. Acta Astronaut 3:671–683
15. Parton V, Kudryavtsev B (1988) Electromagnetoelasticity. Gordon and Breach Science Publishers, New York
16. Ricoeur A, Kuna M (2009) Electrostatic traction at dielectric interfaces and their implication for crack boundary conditions. Mech Res Commun 36:330–335
17. Suo Z, Kuo C, Barnett D, Willis J (1992) Fracture mechanics for piezoelectric ceramics. J Mech Phys Solids 40:739–765
18. Wang B, May Y (2003) On the electrical boundary conditions on the crack surfaces in piezoelectric ceramics. Int J Eng Sci 41:633–652

This page intentionally left blank

Interfacial Delamination of PZT Thin Films

Fulin Shang, Yabin Yan, and Takayuki Kitamura

Abstract The interface strength of $Pb(Zr, Ti)O_3$ (PZT) thin films on a silicon substrate is studied experimentally and numerically in this work. First, a sandwiched cantilever specimen is proposed to perform the delamination tests. The experimental results show that the multilayered Cr/PZT/PLT/Pt/Ti thin films deposited on single-crystal silicon substrates are delaminated along the interface between Cr and PZT layers in a brittle manner. Second, based on cohesive zone models (CZMs), numerical simulations are carried out to extract the fracture toughness of the interface Cr/PZT. Three types, exponential, bilinear and trapezoidal, of CZMs are adopted. Characteristic CZM parameters are obtained through comparisons with experimental results. The simulation results indicate that (i) cohesive strength and work of separation are the dominating parameters in the CZMs; (ii) the bilinear CZM is more suitable in describing this brittle interfacial delamination; and (iii) compared with typical film/coating materials of several millimetre thicknesses, the fracture energy of this weak interface Cr/PZT is quite low. Our study demonstrates a methodology of how to measure and determine the interface bonding strength parameter of PZT thin films, which will be useful for assessing the structural integrity and reliability of PZT devices.

1 Introduction

Many functional devices using piezoelectric thin films are made from multi-layered thin films of different materials with many interfaces; however, these bi-material interfaces frequently delaminate during processing. Delamination occurs especially

F. Shang (✉)
Department of Engineering Mechanics, Xi'an Jiaotong University,
Xi'an 710049, China
e-mail: shangfl@mail.xjtu.edu.cn

Y. Yan and T. Kitamura
Department of Mechanical Engineering and Science, Kyoto University,
Kyoto 606-8501, Japan

M. Kuna and A. Ricoeur (eds.), *IUTAM Symposium on Multiscale Modelling of Fatigue, Damage and Fracture in Smart Materials*, IUTAM Bookseries 24,
DOI 10.1007/978-90-481-9887-0_18,

at the free edge of thin films because of stress concentration due to the mismatch of deformation, leading to failure of these devices. Therefore, it is very important to evaluate the interface strength between thin film layers on a substrate.

The present paper studies the delamination at the free edge of the interface between a piezoelectric lead zirconate titanate (PZT) thin film layer and a metallic chromium (Cr) film layer deposited on silicon substrate. We begin by describing an experimental specimen to clearly measure the mechanical strength of the interface in thin films structures. This specimen is sandwiched cantilever type and is able to avoid plastic deformation and fracture of thin films during the delamination test. In addition, this experimental technique is suited to characterizing delamination crack initiation at the free edge of the interface. Next, towards understanding the relationship between experimental data and the interfacial fracture resistance of the interface Cr/PZT, we adopt cohesive zone model to simualte the fracture process. Finally, we discuss the interfacial toughness of the Cr/PZT/PLT/Pt/Ti thin films tested.

2 Experimental Materials, Method and Results

The thin film stacks studied in our experimental tests were fabricated on single crystal silicon substrates using radio-frequency magnetron sputtering deposition process. Thin Ti layer, to enhance the adhesion of the subsequent layers, was deposited at first. Pt layer was deposited next as a bottom electrode. After sputtering a seed layer PLT at 750 °C, the PZT layer was sputtered at 700 °C with 180 W rf power, which is the main functional layer in this multilayer stack. The PZT film thicknesses were nominally 2.5 μm. A thin layer of chromium (Cr) was lastly deposited onto the top surface of the PZT layer. X-ray diffraction (XRD) patterns show that the PZT thin films were perfectly oriented along c-axis, and SEM images reveal that the PZT layers possess very homogenous structures in the absence of grain boundaries.

To carry out delamination tests, a sandwiched cantilever type specimen [1] as shown in Fig. 1 was utilized in the present study. A square section was cut from the thin films/substrate wafers and bonded onto the lower surface of the cantilever with standard epoxy followed by curing at 60 °C for 4 h. A micro-material testing system (MCTE-500, Shimadzu) with a maximum load capacity of 5 N was used to load the samples under constant loading rate of 0.004 N/s. The load, P, was applied near one edge end of the cantilever made of stainless steel. The relatively stiff cantilever and the silicon substrate are expected to constrain plastic deformation of the thin films during the tests. Loads were measured to a resolution of 0.001 N by an electromagnetic actuator and recorded as a function of the loading point displacement, u. Tests were conducted in a laboratory air environment at 25 °C.

Figure 2 shows the load–displacement curves of the specimens up to the delamination. Linear relationships between the load P and the displacement u are seen for all the specimens. It is clear from the experimental observations that the delamination initiated at the left edge of the specimens. And immediately after the initiation of the delamination, the specimens fractured abruptly into two parts;

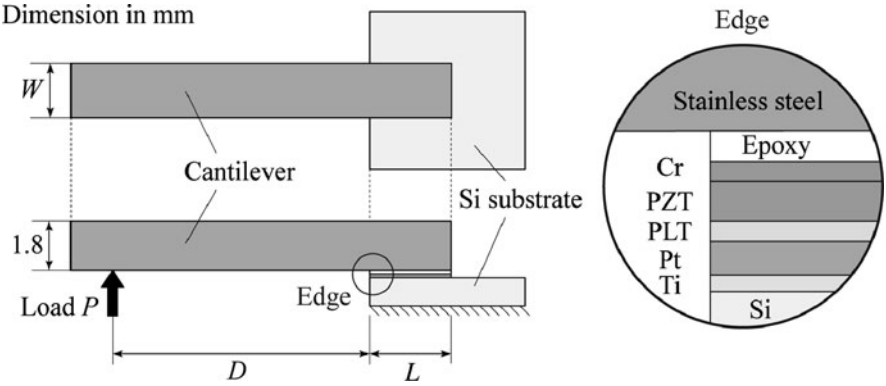

Fig. 1 Schematics of the sandwiched cantilever specimen and loading system

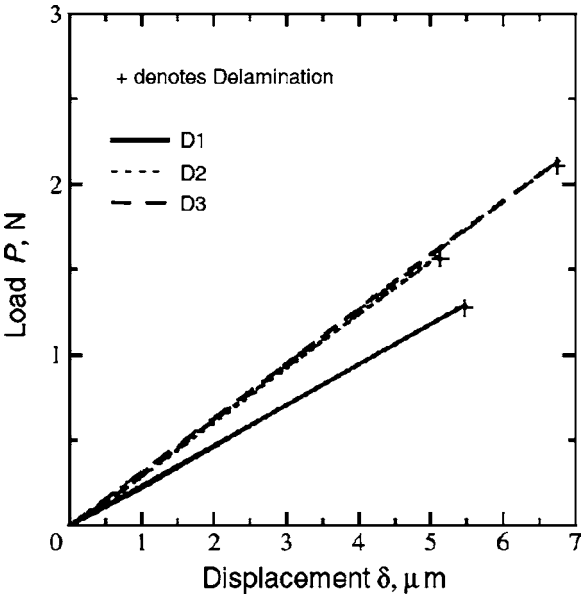

Fig. 2 Load–displacement curves of the sandwiched cantilever specimens

there is no evidence of slow, stable growth of delamination crack in all the tests. Following the delamination tests, the fracture surfaces of the samples were examined by means of an optical microscope and Auger electron spectroscopy (AES). The microscope observations show that the fracture surfaces are smooth and flat on both of the cantilever and substrate sides, and the two sides clearly show different glosses. AES further determines precisely the positions of delamination initiation and cracking in the thin films stacks. It is found that the fracture surfaces of the cantilever sides are covered by Cr elements, and the PZT layer remains on the surfaces

of the substrate sides of the specimens. Hence, it is known that the delamination initiated at the free edge of the interface between the thin Cr layer and the PZT layer, and the cracking took place just along the interface Cr/PZT. From the experimental facts, we can conclude that this interfacial delamination is of a brittle nature.

3 Numerical Simulation Based on Cohesive Zone Models

It is common to use the stress intensity parameter K_{d} in fracture mechanics theory to formulate the delamination criterion [1–3]. However, we found that the regions of K_{d}-dominance near the interface edge are very limited, about same order of magnitude of the film thicknesses. Accordingly, for these situations, the utility of linear elastic fracture mechanics based analysis to measure the fracture resistance of the bi-material interfaces could become a challenging problem [1]. Furthermore, the characteristic parameter of fracture resistance of the interface K_{dc} is related to the combinations of the joint geometry and the bi-material properties. That is to say, K_{dc} is not independent of specimen geometry; therefore, it cannot be employed to model the delamination behavior of the same bi-material interface in otherwise geometries [2, 3]. Also, it cannot be applied to model the subsequent growth of the delamination crack, since the stress singularity changes after the generation of the delamination crack.

To surmount the above-mentioned drawbacks, we make use of cohesibe zone model (CZM) to investigate the delamination process of the Cr/PZT interface. In our study, three types of CZMs are adopted, including the exponential, bilinear, and trapezoidal models. A cohesive zone model is featured by the relationship between the cohesive-zone tractions in equilibrium with the stress fields of the surrounding body and the cohesive-zone separations compatible with the deformation fields of the surrounding body [4]. The primary parameters are the work of interface separation per unit area Γ_0 required for separation of the adjacent planes of the bi-material and the maximum cohesive traction $\sigma_{\max}$ that arises in the fracture process, see Fig. 3 for these features. If the separation of the adjacent planes is denoted by δ, then the work of interface separation is the work done in overcoming the cohesive tractions or

$$\Gamma_0 = \int_0^{\delta_c} \sigma(\delta)\mathrm{d}\delta, \tag{1}$$

where δ_c is a critical separation displacement. When the energy dissipation due to plastic deformation is not negligible, then the total amount of work per unit area of interface Γ will be the sum of the work absorbed in the process zone Γ_0 plus the energy dissipated through plastic deformation Γ_{p}. Concerning the case of our delamination tests, the interfaces are relatively weak and almost no plasticity is observed. Consequently, the effect of plastic deformation on the resistance to crack initiation at the interface edge and crack growth along the interface is negligible. Hence, the driving force necessary to effect the interface separation needs only overcome Γ_0,

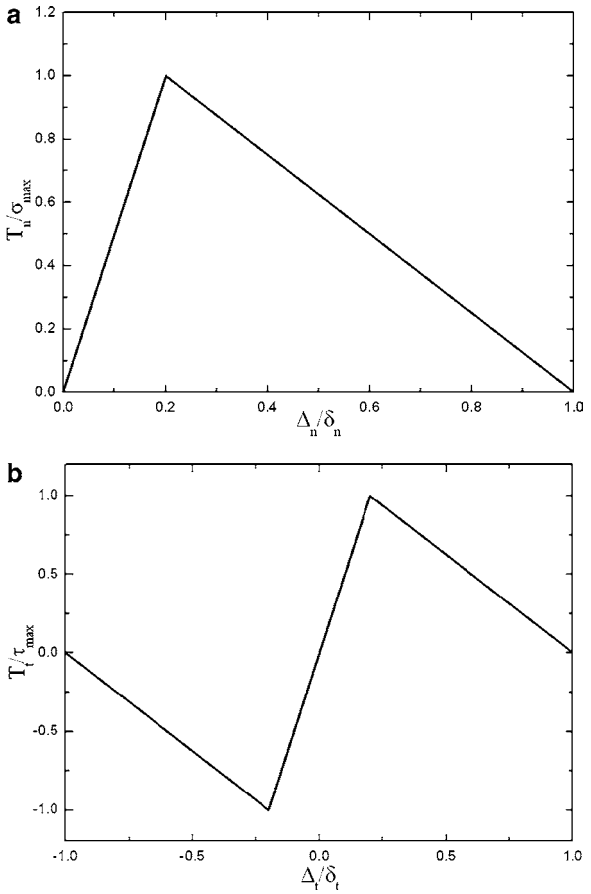

Fig. 3 (**a**) Normal and (**b**) tangential traction–separation curves for the bilinear CZM

which is a material parameter of the interface and independent of the experimental samples.

Figure 4 collects the results of the load–displacement curves obtained from all of the above CZM simulations. For the three types of CZMs, the same tendency appears in that the calculated curves better match the experimental curve when increasing the cohesive strength. For the exponential and bilinear CZMs, setting the cohesive strength to 28 MPa gives the best predictions. For the trapezoidal CZM, the proper choice is $\sigma_{max} = 25$ MPa. It is seen that the calculated curves from the bilinear CZM agree comparatively well with the experimental curve for the entire cracking process, from initiation to propagation along the interface. Further more, the calculated displacements at the loading point are compared with the experimental value, and that of the bilinear CZM are smallest among the three CZMs. Therefore, the bilinear CZM is arguably more suitable in characterizing this interfacial delamination [5].

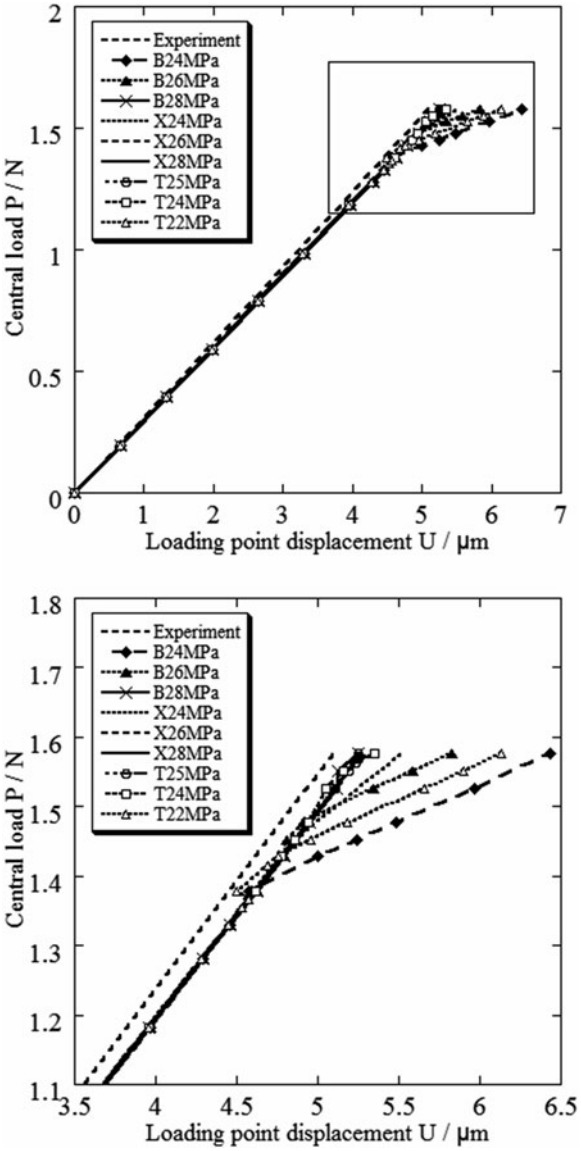

Fig. 4 Comparisons of the load–displacement curves from the three CZMs to the experimental curve

From the above simulations, the values of the characteristic parameters of the Cr/PZT interface are determined to be as follows: Cohesive strength, $\sigma_{max} = 28\,\text{MPa}$; work of normal separation, $0.14\,\text{J/m}^2$; and work of tangential separation, $0.28\,\text{J/m}^2$. It is well known that the rupture strength of bulk Cr material is about 80 MPa, and the bending strengths of typical ceramics are around several hundreds

of MPa. By comparing the cohesive strength of 28 MPa of the Cr/PZT interface with these values, it can be stated that this interface is not strongly bonded. According to Freund and Suresh [4], the interface fracture toughness of thin films or coatings of millimeter thickness can be as low as $0.5\,J/m^2$ and higher than $300\,J/m^2$, and typically weak interfaces have low fracture energies in the range of $1–10\,J/m^2$. After a comprehensive review of some results of interfacial toughness measurements for about 25 film/substrate multilayered systems, Volinsky et al. [6] showed that film systems, such as those with carbon as a contaminant between Al, Al_2O_3, and SiO_2 film layers, can have a very low adhesion toughness, e.g., $0.25–0.33\,J/m^2$. They also observed that, when increasing the film thickness from 200 to 2,000 nm, there is a remarkable increase in fracture resistance from about 4 to $12\,J/m^2$ for strong interfaces like Al/innerlayer/SiO_2 or Al/innerlayer/Al_2O_3, as long as the inner layer is reasonably thin. From our results (0.14, $0.28\,J/m^2$), we remark that the Cr/PZT interface in the Cr/PZT/PLT/Pt/Ti/Si film system investigated in this work has a relatively low bonding strength, and is a weak interface. In this multilayered thin film, the Cr layer is only $0.2\,\mu m$ thick while the PZT layer is about $2.5\,\mu m$ thick. The other three film layers are all thinner than the PZT layer, e.g., the PLT and Ti layers are about 20 nm thick. Therefore, it might be reasonable that the Cr/PZT interface here does have such a low fracture energy.

4 Conclusions

This paper studies the interfacial delamination resistance for weak interface between piezoelectric PZT and metallic Cr thin films layers deposited on silicon substrate. An experimental technique using sandwiched cantilever type specimen was developed to clearly measure the mechanical strength of the interface in thin films structures. This technique is currently suited to characterizing delamination crack initiation at the free edge of a weak interface. To understand better the experimental data obtained from the delamination tests, we considered cohesive zone models to extract the fracture toughness of the Cr/PZT interface. Through calibration with the experimental results, the bilinear CZM was found to be more suitable in describing Cr/PZT interfacial delamination. The characteristic values of its cohesive strength and work of separation were found to be 28 MPa and $0.14\,J/m^2$, respectively. These results show that the fracture toughness of this Cr/PZT interface is also quite low. It is thus confirmed that the examined Cr/PZT interface is weakly bonded and its fracture process is characterized as brittle.

References

1. Shang F, Kitamura T, Hirakata H, et al (2005) Experimental and theoretical investigations of delamination at free edge of interface between piezoelectric thin films on a substrate. Int J Solids Struct 42:1729–1741
2. Akisanya AR, Meng CS (2003) Initiation of fracture at the interface corner of bi-material joints. J Mech Phys Solids 51:27–46
3. Reedy ED, Guess TR (1993) Comparison of butt tensile strength data with interface corner stress intensity factor prediction. Int J Solids Struct 30:2929–2936
4. Freund LB, Suresh S (2003) Thin film materials. Cambridge University Press, Cambridge
5. Yan Y, Shang F (2009) Cohesive zone modeling of interfacial delamination in PZT thin films. Int J Solids Struct 46:2739–2749
6. Volinsky AA, Moody NR, Gerberich WW (2002) Interfacial toughness measurements for thin films on substrates. Acta Materialia 50:441–466

Mechanical Behavior of Thin Film Comprised of Sculptured Nano-elements

Takayuki Kitamura, Takashi Sumigawa, and Taisuke Sueda

Abstract The focus in this project is put on the mechanical property of nano-components (nano-elements). The deformation property of a thin film consisting discretely arrayed nano-elements on a substrate is evaluated by means of an atomic force microscope (AFM) with a loading apparatus. The fact that the thin film eliminates stress singular field at the interface edge between dissimilar materials is numerically and experimentally elucidated.

1 Introduction

New deposition techniques enable us to fabricate nano-sized structures. In particular, a thin film consisting of nano-elements is formed on a substrate by means of the dynamic oblique deposition (DOD) [1, 2]. It has the potential to play a key role in mechanical electronic devices because the thin films would exhibit significantly characteristic mechanical properties in comparison with solid films. The geometrical anisotropy of constituent nano-elements would cause the mechanical anisotropy of film, and insertion of the thin film between dissimilar materials as an interface layer may break down a continuum approximation of the stress field near the interface owing to discrete structure of the film. However, the investigation of the mechanical properties of nano-elements has not been enough yet. On the basis of noble experimental methods for nano- or micro-components [3–6], we have been clarified the properties.

In this paper, we review our experimental and analytical works on the mechanical properties of a thin film consisting of nano-elements.

T. Kitamura (✉), T. Sumigawa, and T. Sueda
Department of Mechanical Engineering and Science, Kyoto University,
Kyoto 606-8501, Japan
e-mail: takasan@mbox.kyoto-inet.or.jp

M. Kuna and A. Ricoeur (eds.), *IUTAM Symposium on Multiscale Modelling of Fatigue, Damage and Fracture in Smart Materials*, IUTAM Bookseries 24,
DOI 10.1007/978-90-481-9887-0_19,

2 Mechanical Property of Thin Film Consisting of Nanosprings [7]

2.1 Experimental Procedure

As a base layer, a Ta_2O_5 solid film is deposited on a silicon (100) substrate by electron beam (EB) evaporation. Then, nanosprings (helical nano-elements) of Ta_2O_5 are grown by the dynamic oblique deposition (DOD). A Ta_2O_5 cap layer with a thickness of 280 nm is deposited on the nanosprings. Figure 1a shows a scanning electron micrograph of the multi-layered thin films. The height of the nanosprings, h_s, is 560 nm. The areal number density of springs is 65 per μm^2. The number of turns, the outside radius, and diameter of wire of the nanospring are 3.5, 75 nm, and 60 ± 10 nm, respectively.

Figure 1b shows the specimen configuration. Specimens for the loading tests are cut from the multi-layered thin films by a focused ion beam (FIB).

Several specimens with different areas ($S = 1.9$–$13.2\,\mu m^2$) are prepared.

The tests are conducted using an atomic force microscope with a loading apparatus (Hysitron: Triboscope). Figure 1c and d schematize the loading test. The vertical and lateral forces, F_v and F_l, are applied to the cap layer by the diamond tip. In the vertical loading tests, the vertical force is applied to the cap layer at

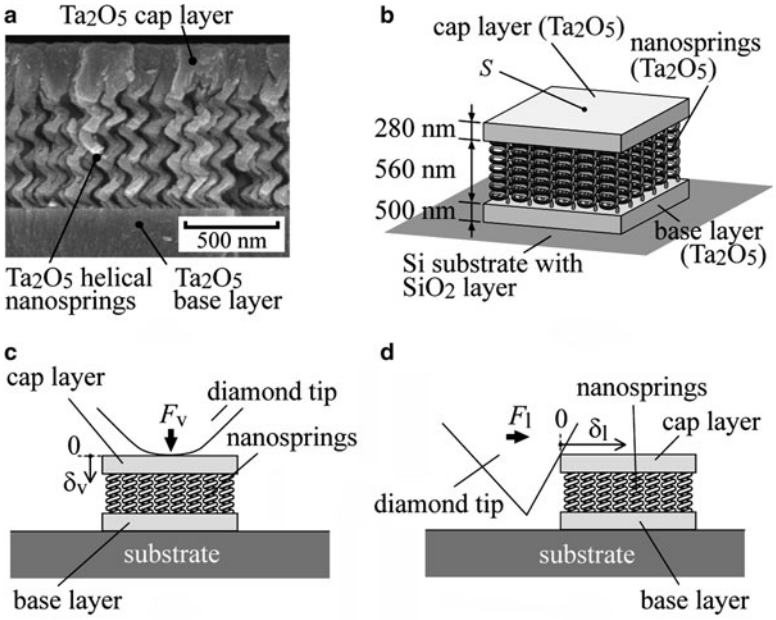

Fig. 1 (**a**) SEM micrograph of multi-layered thin films, (**b**) configuration of specimen, (**c**) vertical loading method, and (**d**) Lateral loading method

a constant loading velocity of 10 μN/s (see Fig. 1c). In the lateral loading tests, the lateral force is applied to the side edge of the cap layer (see Fig. 1d). The loading tip is moved along the substrate surface toward the specimen at a constant velocity of 5 nm/s.

2.2 Results

Figure 2a plots the F_v against the vertical displacement, δ_v, for a specimen with $S = 3.3\,\mu m^2$. The fact that the relation between F_v and δ_v is almost linear indicates that the specimen deforms elastically. The vertical stiffness of the thin film, K_v ($= F_v/\delta_v$), is evaluated by the least-squares approximation. The relationship between K_v and S is shown by solid circles in Fig. 2c. K_v has an almost linear relationship with S. The apparent Young's modulus, E', and stiffness constant, k_v, of a spring are defined as $E' = K_v(h_s/S)$ and $k_v = K_v/m$, respectively. The mean values of E' and k_v obtained from the vertical loading tests are 0.375 GPa and 10.29 N/m, respectively.

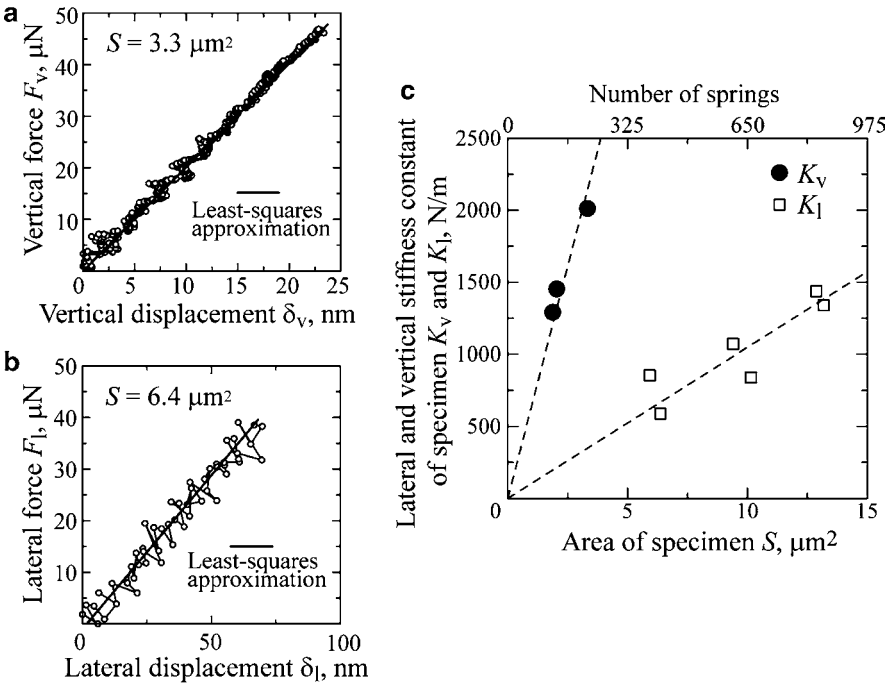

Fig. 2 Relationship between force and displacement: (**a**) vertical loading method, (**b**) lateral loading method, and (**c**) relationship between stiffness and area of specimen

Figure 2b shows the F_l plotted against the lateral displacement, δ_l, in the lateral loading test of a specimen with $S = 6.4\,\mu m^2$. F_l increases almost linearly with δ_l. The lateral stiffness of the thin film, K_l ($= F_l/\delta_l$), is evaluated. The open squares in Fig. 2c show the relationship between K_l and S. K_l increases almost linearly with increasing S. The apparent shear modulus of the thin film, G', and the lateral stiffness measurement, k_l, of a spring are defined as $G' = K_l(h_s/S)$ and $k_l = K_l/m$, respectively. The mean values of G' and k_l obtained from the lateral loading tests are 0.060 GPa and 1.66 N/m, respectively.

The E' and G' of the thin film consisting of Ta_2O_5 nanosprings are 2–3 orders of magnitude lower than those of the solid Ta_2O_5 film ($E \approx 117$ GPa and $G \approx 47$ GPa). The ratio of E' to G' is 6.2, while that of isotropic solid materials given as $2(1 + \nu)$ must be at most 3.0 because the maximum value of ν is 0.5. This means that the thin film composed of Ta_2O_5 helical nanosprings has a strong anisotropy.

3 Effect of Thin Film Consisting of Nanosprings on Stress Fields at Interface Edge and Crack Tip [8]

3.1 Analytical Procedure

Stress analysis is conducted under plane strain condition through FEM using ABAQUS 6.5. Each nanospring is replaced by the equivalent cylindrical beam with a height of $h_b = 560$ nm, a diameter of $D_b = 259$ nm, and a Young's modulus of $E_b = 0.11$ GPa. The D_b and E_b can be derived from the vertical and lateral stiffness measurements of a single spring, k_v and k_l.

Figure 3 shows the model used for analyzing the stress distribution near the interface edges between the thin film and a solid body. The thin film consisting of Ta_2O_5 nanosprings with a thickness of 560 nm is sandwiched between an elastic solid body and a substrate. Figure 3c shows the mesh division for the models. Two types of models with different interface edges between the thin film and the solid body are prepared. One has a free edge where the surface-interface angle is 90°–90° (see Fig. 3a), and the other has an interface crack with a length of 4 μm (see Fig. 3b). The Young's modulus and Poisson's ratio of the Ta_2O_5 solid body are 117 GPa and 0.23, respectively. The distance between springs is 125 nm, which is derived from the areal number density of springs. In addition, models without nanosprings are prepared for comparison (Fig. 3d–f). The models with and without the thin film consisting of nanosprings are designed as "spring model" and "non-spring model", respectively. The uniform displacement Δu_z is applied to the top of the model.

3.2 Results

The stresses in the elements of the elastic solid body along the interface are extracted. Figure 4a and b show the distributions of the normal stresses, σ_x and

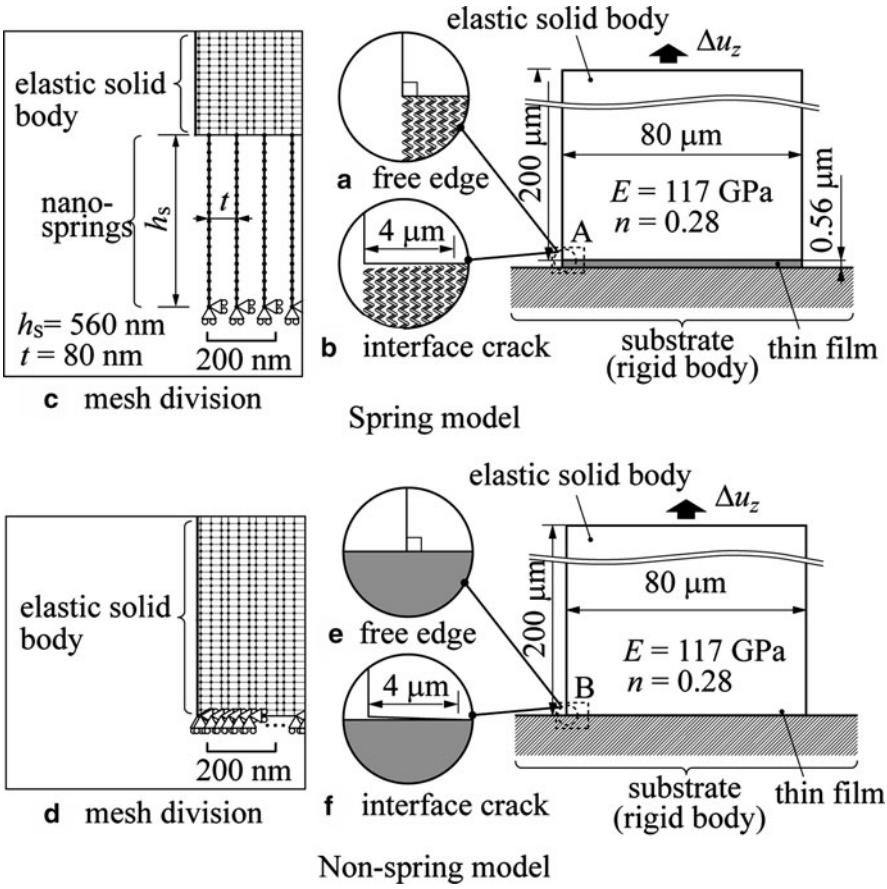

Fig. 3 Analytical models for FEM

σ_z, and the shear stress, τ_{zx}, along the interface in the models with a free edge. The stresses are normalized by the z-directional normal stress at the center of the interface, σ_0, in each model. In the no-spring model (Fig. 4a), the stresses increase near the free edge. A stress singularity represented by $\sigma_{ij}/\sigma_0 = K/r^{\lambda}$ $(i,\ j = z,\ x)$ [9] is observed near the free edge in each distribution curve. Here, K is the stress intensity factor, r is the distance from the free edge, and λ is a parameter that depends on the materials and the edge geometry. In the spring model (Fig. 4b), there is no stress singularity near the free edge.

Figure 4c and d show the distributions of the normalized stresses along the interface in the models containing an interface crack. In the non-spring model (Fig. 4c), the stresses are concentrated in the region near the crack tip. Stress singularity is observed near the crack tip. In the spring model (Fig. 4d), σ_z and τ_{zx} are almost constant over the interface as in the case of the model with the free edge. No singular stress field occurs in any of the distributions.

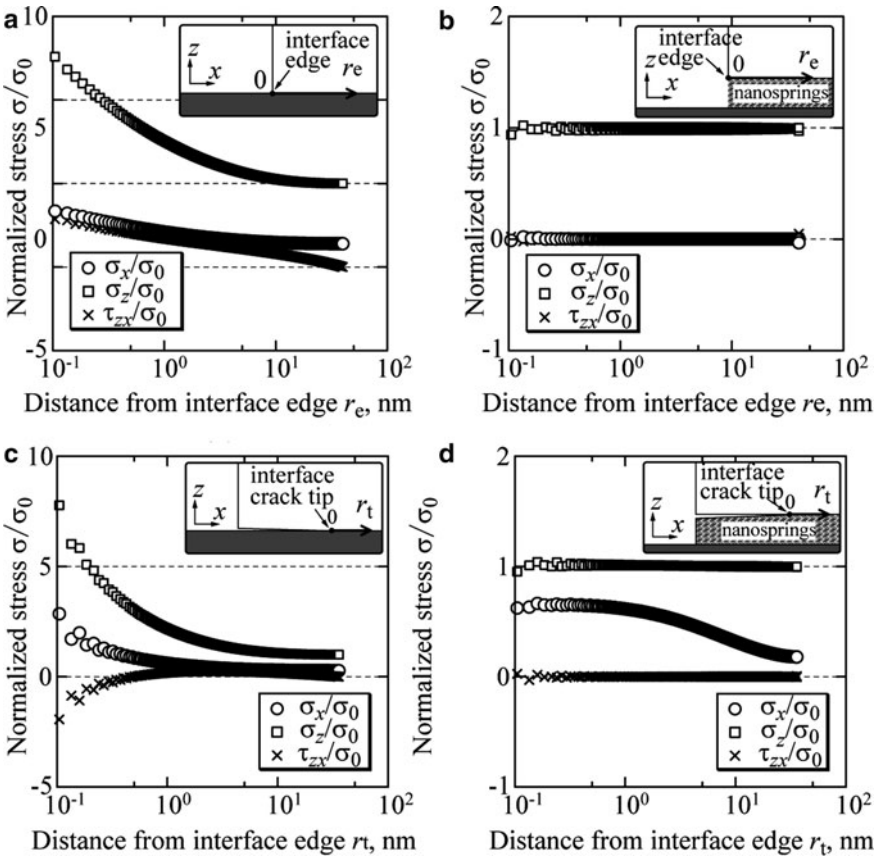

Fig. 4 Distribution of normal stresses, σ_z and σ_x, and shear stress, τ_{zx}, along the interface: (**a**) near the interface edge in non-spring model, (**b**) near the interface edge in spring model, (**c**) near the interface crack tip in non-spring model, (**d**) near the interface crack tip in spring model

The stress concentration at the free edge of an interface is induced by the mismatch of deformation on the interface. The mismatch is mainly due to the difference in Poisson's contractions between the different components. Since nanosprings are oriented vertically on the substrate and are separated from each other, the in-plane deformation of the thin film follows that of the adjoining component on the interface. In short, the difference of Poisson's contractions for the vertical deformation is zero. The stress concentration at the interface crack tip is induced by not only the mismatch of deformation on the interface but also the traction force from above and below the crack. However, no traction force is exerted on the crack tip in the spring model because the under part of the crack is constitutively separated from the crack tip.

4 Effect of Thin Film Consisting of Nanosprings on Crack Initiation at Interface Edge [10]

4.1 Experimental Procedure

A thin film consisting of Ta_2O_5 nanosprings is formed on a Si substrate by means of the DOD. A Ta_2O_5 solid film with a height of 1,700 nm is then deposited on the thin film by the EB evaporation (see Fig. 5a). The number of turns, the outside radius, and diameter of wire of the nanospring are 3.5, 90 nm, and 40 ± 10 nm, respectively.

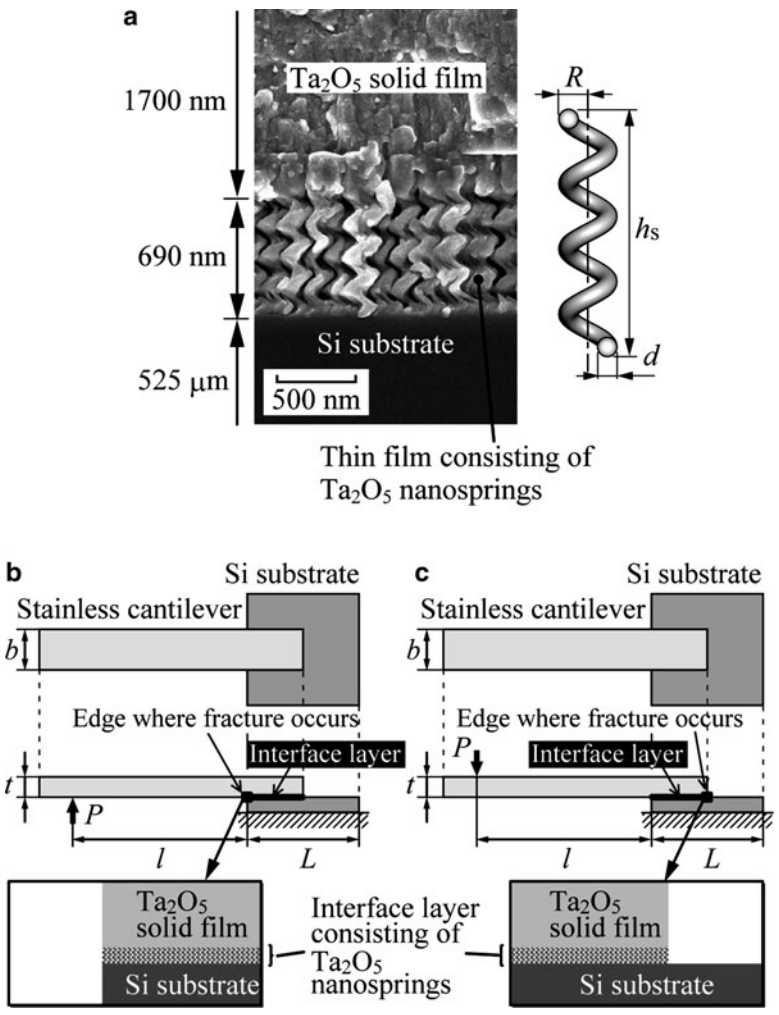

Fig. 5 (**a**) SEM micrograph of dissimilar material including a thin film comprising of Ta_2O_5 nanosprings, (**b**) and (**c**) Illustrations of specimen and loading method

Table 1 Dimensions of specimens used for the crack initiation experiment. Dimensions are in mm

	L	*b*	*t*	*l*
A-1	2.27	1.58	1.92	17.5
A-2	2.17	2.09	1.87	11.0
A-3	1.37	1.77	1.90	15.5
B-1	1.74	1.68	1.90	15.5
B-2	1.85	1.95	1.89	16.0

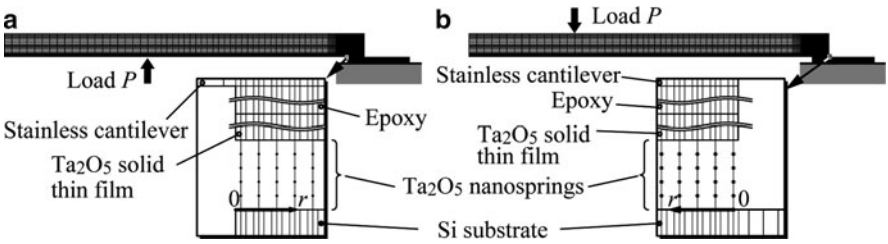

Fig. 6 Mesh division for FEM analysis: (**a**) Type A test, and (**b**) Type B test

The material is cut to a square coupon with a size of 5 mm × 5 mm. A stainless cantilever is bonded to the thin film of the coupon using an epoxy adhesive. The thin film except the bonded region is mechanically removed.

Figure 5b and c illustrates the specimen configuration and the loading method. We carry out two types of experiments, which are designated as "Type A test" and "Type B test", respectively. Table 1 lists the sizes of the specimens. A vertical load applied to the lower face of the stainless steel cantilever (Fig. 5b) initiates a crack at the left edge of the thin film. On the other hand, a vertical load applied to the upper face of the cantilever (Fig. 5b) initiates a crack at the right edge of the thin film.

The experiments are conducted at a room temperature in an air by means of a loading machine with an electromagnetic actuator. The vertical load is applied to the stainless cantilever at the point of l from the edge of the thin film with a constant displacement rate of 50 μm/s.

4.2 Analytical Procedure

Figure 6 illustrates mesh divisions for analytical models. The nanosprings are translated to equivalent beam elements. The Young's modulus and Poisson's ratio of the Ta_2O_5 solid body are 117 GPa and 0.23, respectively. In addition, models where the Ta_2O_5 solid film is directly laminated on the Si substrate without the thin film are analyzed for comparison. Hereafter, the analytical models with and without the thin film are designated as "thin film model" and "non-thin film model", respectively.

4.3 Results

In the experiments, the displacement at the loading point, u_y, increases linearly with increasing the applied load, P. The sharpen drop of the load at the maximum value points out that the interface crack is initiated.

Figure 7a shows the typical relationship between the normal stress, σ_y, and the distance from the interface edge, x, at the crack initiation in the non-thin film model. σ_y is extracted from the elements adjoining the interface in the Si substrate. No stress singularity takes place at the left edge of the interface with the 90°–90° interface edge shape of the Ta_2O_5 solid film and the Si substrate (Type A). On the other hand, the right edge of the interface where the interface edge shape is 90°–180° generates a stress singularity due to the edge shape (Type B).

Figure 7b shows the typical relationship between the apparent normal stress of the nanospring, σ', and the distance from the interface edge, x, at the crack initiation in the thin film model. Using the longitudinal displacement of the nanospring, λ, the height, h_s, the Young's modulus, E_b, the diameter, D_b of the beam element, and the outer diameter of the nanospring, d, the apparent normal stress, σ', in the longitudinal direction of the nanospring is represented as follow:

$$\sigma' = (E_b \lambda / h_s)\left({D_b}^2/d^2\right). \tag{1}$$

In Fig. 7b, the stresses near the edge are nearly constant. The no strong stress concentration points out that the thin film consisting of nanosprings eliminates the stress singularity. Moreover, the stress distribution curves of all specimens show a good agreement near the interface edge. This signifies that the stress near the edge dominates the crack initiation. The magnitude of critical stress is evaluated as $78.5 \pm 4.0\,\mathrm{MPa}$ $\left(\varepsilon_C{}' = 5.1 \pm 0.2 \times 10^{-2}\right)$.

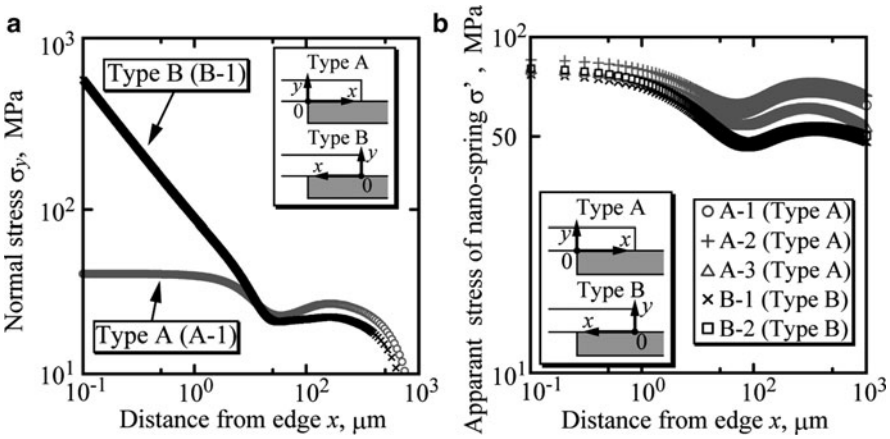

Fig. 7 Relationship between normal stress, σ, and distance from the edge of thin film, r: (**a**) Non-thin film model, and (**b**) thin film model

5 Summary

The mechanical properties of nano-elements have been investigated in this project. Novel experiments and stress analyses for the nano-elements elucidate the specific behavior of deformation and fracture. Furthermore, first-principles calculations reveal the fundamental mechanism of domain switching from the atomistic point of view. The main results obtained are summarized as follows.

1. Apparent Young's modulus, E′, and shear modulus of a thin film consisting of Ta_2O_5 nanosprings are evaluated as 0.375 and 0.060, respectively. These values are 2–3 orders of magnitude smaller than those of a conventional Ta_2O_5 solid thin film. Moreover, the thin film has a strong deformation anisotropy which solid materials cannot attain.
2. Vertical stiffness k_v and lateral stiffness, k_l, of the single Ta_2O_5 nanospring are evaluated as 10.29 and 1.66 N/m, respectively.
3. No stress singularity is found near the free edge of an interface and near the interface crack tip between the thin film consisting of nanosprings and an elastic solid body. The marked stress relaxation is due to the discrete structure of the thin film.
4. Elimination of the stress singularity owing to the thin film consisting of nanosprings is experimentally demonstrated. The crack initiation at the interface edge is dominated by the apparent stress of the nanospring.

References

1. Suzuki M, Taga Y (2001) Integrated sculptured thin films. Jap J Appl Phys 40:L358–L359
2. Robbie K, Brett MJ, Lakhtakia A (1995) First thin film realization of a helicoidal bianisotropic medium. J Vacuum Sci Technol A1:2991–2993
3. Hirakata H, Hirako T, Takahash Y et al (2008) Creep crack initiation at a free edge of an interface between submicron thick elements. Eng Fract Mech 75:2907–2920
4. Takahashi Y, Hirakata H, Kitamura T (2008) Quantitative evaluation of plasticity of a ductile nano-component. Thin Solid Films 516:1925–1930
5. Hirakata H, Kitamura T, Yamamoto Y (2004) Evaluation of interface strength of micro-dot on substrate by means of AFM. Int J Solids Struct 41:3243–3253
6. Hirakata H, Kitazawa M, Kitamura T, (2006) Fatigue crack growth along interface between metal and ceramics submicron-thick films in inert environment. Acta Materualia 54:89–97
7. Hirakata H, Matsumoto S, Takemura M et al (2007) Anisotropic deformation of thin films comprised of helical nanosprings. Int J Solids Struct 44:4030–4038
8. Sumigawa T, Hirakata T, Takemura T et al (2008) Disappearance of stress singularity at interface edge due to nanostructured thin film. Eng Fract Mech 75:3073–3083
9. Bogy DB (1968) Edge-bonded dissimilar orthogonal elastic wedges under normal and shear loading. J Appl Mech 35:460–466
10. Sumigawa T, Sueda T, Futamura Y et al (2009) Effect of interface layer consisting of nanosprings on stress field near interface edge. Eng Fract Mech 76:1336–1344

Propagation of SAW and PSAW in a Smart AlN/Diamond/γ-TiAl Structure

L.M. Gao, Ch. Zhang, Z. Zhong, C.-P. Fritzen, X. Jiang, H.-J. Christ, and U. Pietsch

Abstract For online monitoring and prediction of surface or near-surface changes such as corrosion, cracks and crack-like defects, propagation of surface acoustic waves (SAW) and pseudo surface acoustic waves (PSAW) in a layered AlN/Diamond/γ-TiAl structure is investigated. Depending on the layer thicknesses and the frequency, both SAW and PSAW may exist in the AlN/Diamond/γ-TiAl structure. True SAW or Rayleigh waves exist only in the range of small normalized waver numbers kh_p and kh_d. Beyond this range, PSAW exist. Low-loss PSAW with high velocities have certain advantages compared to SAW. Since surface or near-surface changes and defects are closely related to the propagation characteristics of SAW and PSAW, both SAW and PSAW can be used to detect and characterize the location and the size of such surface or near-surface changes and flaws. Special attention of the paper is devoted to the analysis of the propagation of SAW and PSAW, and the computation of the electro-mechanical coupling coefficient in a layered AlN/Diamond/γ-TiAl structure.

1 Introduction

Since Lord Rayleigh discovered surface acoustic waves (SAW) in 1885 [1], Tiersten studied SAW propagation in a piezoelectric plate [2], and White invented the interdigital transducers (IDTs) utilized for transmitting and receiving SAW signals in

L.M. Gao and Ch. Zhang (✉)
Department of Civil Engineering, University of Siegen, 57068 Siegen, Germany
e-mail: c.zhang@uni-siegen.de

Z. Zhong
School of Aerospace Engineering and Applied Mechanics, Tongji University, Shanghai 200092, PR China

C.-P. Fritzen, X. Jiang, and H.-J. Christ
Department of Mechanical Engineering, University of Siegen, 57068 Siegen, Germany

U. Pietsch
Department of Physics, University of Siegen, 57068 Siegen, Germany

M. Kuna and A. Ricoeur (eds.), *IUTAM Symposium on Multiscale Modelling of Fatigue, Damage and Fracture in Smart Materials*, IUTAM Bookseries 24,
DOI 10.1007/978-90-481-9887-0_20,

1965 [3], SAW are adopted successfully in electronics such as filters, delay lines, resonators, and oscillators for signal processing applications. Along with the rapid development of information and communication technology high-performance surface acoustic wave devices operating in the GHz range of frequencies are demanded. In order to operate at higher frequencies, smart layered structures consisting of diamond and thin piezoelectric film were fabricated by Yamanouchi [4], and investigated by Adler et al. [5] and Nakahata et al. [6] due to the fact that diamond has the highest acoustic wave velocity among all solid materials. Besides choosing materials with higher wave velocity, another measure utilizing leaky SAW or pseudo SAW (PSAW) instead of SAW can be taken. Leaky surface acoustic waves without including piezoelectric effects were investigated by Engan et al. [7] and Lim et al. [8], and detected by Engan [7] in quartz crystals. Leaky surface acoustic waves consist of coupled modes involve terms decaying into the substrate beneath the free surface and a term representing a bulk wave radiating into the solid. Piezoelectric leaky SAW including piezoelectric effects were analyzed and detected by Yamanouchi et al. [9, 10] for the first time. Leaky wave propagation in layered structures was investigated by Naumenko et al. [11] at first. Leaky wave propagation in three layered AlN/Diamond/Si structures was studied by Benetti et al. [12].

γ-TiAl offer advantages for use in the working temperature range between 500°C and 850°C and lead to weight reductions of up to 40% because of their low density, advanced mechanical properties and high oxidation and creep resistances. For this reason, they are widely used in automotive and aerospace industries. For online monitoring and prediction of defects in γ-TiAl, smart layered AlN/Diamond/γ-TiAl structures are promising, because AlN has the highest acoustic velocities among all piezoelectric materials and excellent electrical and mechanical properties, and diamond has the highest acoustic velocities among non-piezoelectric solid materials. Although three layered structures like AlN/Diamond/Si have been studied previously, they have been simplified as two layered AlN/Diamond structures, because the acoustic behavior of two layered structures tends to that of three layered structures when the thickness of diamond is large enough. However, if the thickness of diamond is not sufficiently large, the two layered structures cannot replace the original three layered ones. In addition, SAW and leaky PSAW in layered structures, in which the transverse wave velocity of the substrate is smaller than that of the surface layer, are not investigated until now to the author's knowledge.

2 Theoretical Analysis

A layered AlN/Diamond/γ-TiAl structure as shown in Fig. 1 is concerned. Here, x_1 is the direction of wave propagation. The general equations describing the SAW and the PSAW propagation in a piezoelectric medium are governed by the following relations

$$c_{ijkl}\frac{\partial^2 u_l}{\partial x_j \partial x_k} + e_{kij}\frac{\partial^2 \phi}{\partial x_j \partial x_k} = \rho\frac{\partial^2 u_l}{\partial t^2},$$

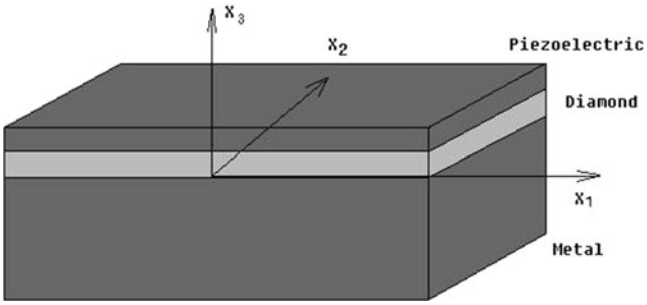

Fig. 1 Schematic sketch of a layered Piezoelectric/Diamond/Metal structure

Table 1 Material parameters

	c_{11} (GPa)	c_{13} (GPa)	c_{33} (GPa)	c_{44} (GPa)	e_{15} (cm^{-2})	e_{31} (cm^{-2})	e_{33} (cm^{-2})	ϵ_{11} (pFm^{-1})	ϵ_{33} (pFm^{-1})	ρ (kgm^{-3})
AlN	345	120	395	118	−0.48	−0.58	1.55	80	95	3260
Diamond	115.3			533				55	55	3512
γ–TiAl	222.1			63.5						3900

$$e_{jkl}\frac{\partial^2 u_l}{\partial x_j \partial x_k} - \varepsilon_{jk}\frac{\partial^2 \phi}{\partial x_j \partial x_k} = 0, \tag{1}$$

where $\rho, t, c_{ijkl}, e_{ijk}$ and ε_{jk} are respectively the mass density, time, elastic, piezoelectric and dielectric tensors of the considered material, u_i represent the particle displacements and ϕ denotes the electric potential. The material parameters are given in Table 1.

Since AlN is transversally isotropic while diamond and γ-TiAl are isotropic materials, all components in the x_2-direction can be neglected. The displacements and the potential in each medium are assumed to be a linear combination of partial waves expressed as

$$\begin{aligned} u_1 &= A_1 \exp(bx_3)\sin[k(x_1 - ct)], \\ u_3 &= A_3 \exp(bx_3)\cos[k(x_1 - ct)], \\ \phi &= A_2 \exp(bx_3)\cos[k(x_1 - ct)], \end{aligned} \tag{2}$$

where k, c and b represent the wave number, the phase velocity and the decay coefficient in the x_3-direction, respectively.

Substitution of Eq. (2) into Eq. (1) leads to a six-order eigenvalue equation for the eigenvalue b for AlN. Thus, the general solution for the displacements and the potential in AlN can be written as

$$u_1^{(\mathrm{P})} = \sin[k(x_1 - ct)]\sum_{i=1}^{6} A^{(\mathrm{P}i)}\beta_1^{(\mathrm{P}i)}\exp\left(b^{(\mathrm{P}i)}x_3\right),$$

$$u_3^{(\mathrm{P})} = \cos\left[k\left(x_1 - ct\right)\right] \sum_{i=1}^{6} A^{(\mathrm{P}i)} \beta_3^{(\mathrm{P}i)} \exp\left(b^{(\mathrm{P}i)} x_3\right),$$

$$\phi^{(\mathrm{P})} = \cos\left[k\left(x_1 - ct\right)\right] \sum_{i=1}^{6} A^{(\mathrm{P}i)} \beta_2^{(\mathrm{P}i)} \exp\left(b^{(\mathrm{P}i)} x_3\right), \tag{3}$$

where $\beta_j^{(Pi)}$ $(i = 1 \sim 6, j = 1 \sim 3)$ are the amplitude factors and $A^{(Pi)}$ $(i = 1 \sim 6)$ have to be determined.

For diamond the mechanical displacements and the electric potential are uncoupled, which results in two independent eigenvalue equations. One is a four-order equation for the mechanical displacements and another is a second-order equation for the electric potential. From these equations, the decay coefficients are obtained as $b^{(\mathrm{D1})} = k\sqrt{1 - \left(\frac{c}{c_{\mathrm{L}}^{(\mathrm{D})}}\right)^2}, b^{(\mathrm{D2})} = -k\sqrt{1 - \left(\frac{c}{c_{\mathrm{L}}^{(\mathrm{D})}}\right)^2}, b^{(\mathrm{D3})} = k\sqrt{1 - \left(\frac{c}{c_{\mathrm{T}}^{(\mathrm{D})}}\right)^2}, b^{(\mathrm{D4})} = -k\sqrt{1 - \left(\frac{c}{c_{\mathrm{T}}^{(\mathrm{D})}}\right)^2}$ for the displacements, and $b^{(\mathrm{D5})} = 1$, $b^{(\mathrm{D6})} = -1$ for the electric potential, where $c_{\mathrm{L}}^{(\mathrm{D})} = \sqrt{c_{11}/\rho}$ and $c_{\mathrm{T}}^{(\mathrm{D})} = \sqrt{c_{44}/\rho}$ are the velocities of the longitudinal and the transverse waves of diamond. The general solution for the displacements and the potential in diamond is given by

$$u_1^{(\mathrm{D})} = \sin\left[k\left(x_1 - ct\right)\right] \sum_{i=1}^{4} A^{(\mathrm{D}i)} \beta_1^{(\mathrm{D}i)} \exp\left(b^{(\mathrm{D}i)} x_3\right),$$

$$u_3^{(\mathrm{D})} = \cos\left[k\left(x_1 - ct\right)\right] \sum_{i=1}^{4} A^{(\mathrm{D}i)} \beta_3^{(\mathrm{D}i)} \exp\left(b^{(\mathrm{D}i)} x_3\right),$$

$$\varphi^{(\mathrm{D})} = \cos\left[k\left(x_1 - ct\right)\right] \sum_{i=5}^{6} A^{(\mathrm{D}i)} \exp\left(b^{(\mathrm{D}i)} x_3\right). \tag{4}$$

Since the displacements and the potential in γ-TiAl must exponentially decay in the thickness direction, only positive decay coefficients should be retained. Thus, the general solution for γ-TiAl is given as

$$u_1^{(\mathrm{M})} = \sin\left[k\left(x_1 - ct\right)\right] \sum_{i=1}^{2} A^{(\mathrm{M}i)} \beta_1^{(\mathrm{M}i)} \exp\left(b^{(\mathrm{M}i)} x_3\right),$$

$$u_3^{(\mathrm{M})} = \cos\left[k\left(x_1 - ct\right)\right] \sum_{i=1}^{2} A^{(\mathrm{M}i)} \beta_3^{(\mathrm{M}i)} \exp\left(b^{(\mathrm{M}i)} x_3\right),$$

$$\varphi^{(\mathrm{M})} = \cos\left[k\left(x_1 - ct\right)\right] A^{(\mathrm{M3})} \exp\left(b^{(\mathrm{M3})} x_3\right). \tag{5}$$

By substituting Eqs. (3)–(5) into the following boundary and continuity conditions for a short-circuited surface

$$\begin{aligned} &T_{3j}^{(\mathrm{P})} = \varphi^{(\mathrm{P})} = 0, \quad \text{at } x_3 = h^{(\mathrm{D})} + h^{(\mathrm{P})}, \\ &u_i^{(\mathrm{D})} = u_i^{(\mathrm{P})}, T_{3i}^{(\mathrm{D})} = T_{3i}^{(\mathrm{P})}, \varphi^{(\mathrm{D})} = \varphi^{(\mathrm{P})}, D_3^{(\mathrm{D})} = D_3^{(\mathrm{P})}, \quad \text{at } x_3 = h^{(\mathrm{D})}, \\ &u_i^{(\mathrm{M})} = u_i^{(\mathrm{D})}, T_{3i}^{(\mathrm{M})} = T_{3i}^{(\mathrm{D})}, \varphi^{(\mathrm{M})} = \varphi^{(\mathrm{D})}, D_3^{(\mathrm{M})} = D_3^{(\mathrm{D})}, \quad \text{at } x_3 = 0, \end{aligned} \tag{6}$$

we can obtain the following system of linear algebraic equations

$$\mathbf{K} \cdot \mathbf{A} = \mathbf{0}, \tag{7}$$

where $\mathbf{K}$ is a 15×15 matrix, and

$$\mathbf{A} = \left[A^{(\mathrm{P1})}, \cdots A^{(\mathrm{P6})}, A^{(\mathrm{D1})}, \cdots A^{(\mathrm{D6})}, A^{(\mathrm{M1})}, A^{(\mathrm{M2})}, A^{(\mathrm{M3})} \right].$$

The condition that $\mathbf{A}$ has a nontrivial solution gives the following eigenvalue equation

$$\mathrm{Det}\,(\mathbf{K}) = 0 \tag{8}$$

for computing the phase velocity c.

The boundary and continuity conditions for an open-circuited surface are the same as Eq. (6) for the short-circuited surface with the exception that $\varphi^{(\mathrm{P})} = 0$ in Eq. (6) should be replaced by $D_3^{(\mathrm{P})} = -\varepsilon_0 k \phi^{(\mathrm{P})}$ on the surface of AlN. The electromechanical coupling coefficient K^2 can be determined from the relation

$$K^2 = 2\frac{c_{\mathrm{O}} - c_{\mathrm{S}}}{c_{\mathrm{O}}}, \tag{9}$$

where c_{O} and c_{S} are the phase velocities of open-circuited and short-circuited cases.

3 Results and Discussions

The influence of the substrate in three layered structures on the SAW propagation is often neglected by assuming that the thickness of the layer (diamond) beneath the surface is large enough. Then, the three layered structure can be replaced by a two layered structure, and diamond can be assumed to be semi-infinite [12, 13]. Figure 2 presents the corresponding results for a two layered AlN/Diamond structure, which shows that the velocity of the first wave (Rayleigh wave) mode starts from the Rayleigh wave velocity of diamond and tends to the Rayleigh wave velocity of AlN. The velocities of other wave modes tend to the transverse wave velocity of AlN.

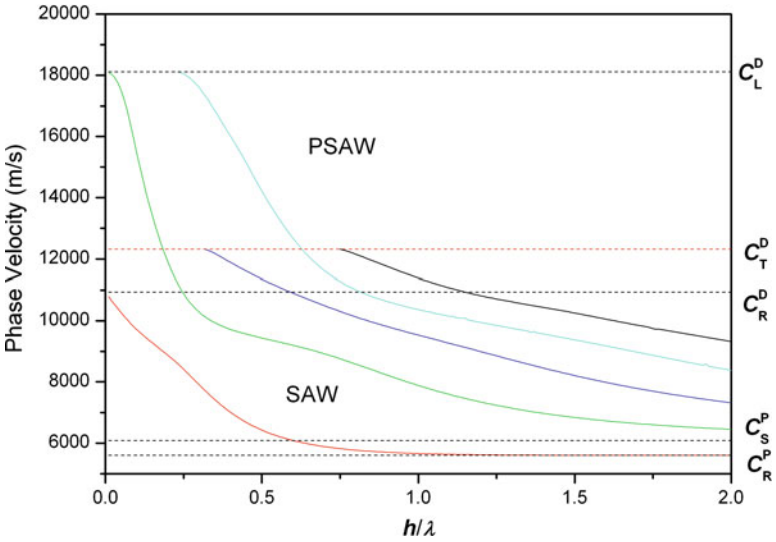

Fig. 2 Phase velocities in an AlN/Diamond structure

All SAW velocities in a two layered AlN/Diamond structure are higher than the Rayleigh wave velocity in a semi-infinite AlN solid due to the presence of the diamond. Beside SAW there exist PSAW in this structure above the transverse wave velocity of diamond.

Subsequently, a two layered AlN/γ-TiAl structure, in which the transverse wave velocity of the substrate is smaller than that of the surface layer, is considered. The dispersion curves of the Rayleigh wave and the first mode PSAW are shown in Fig. 3.

From this figure, it can be seen that the dispersion curve of Rayleigh mode is interrupted by the transverse wave velocity of the substrate. In other words, SAW exists only in a small range of h^P/λ in this layered structure. Since the velocity of SAW should be smaller than the transverse wave velocity of the substrate and larger than the transverse wave velocity of the surface layer, there is no other SAW mode except the Rayleigh mode in the AlN/γ-TiAl structure due to the fact that the transverse wave velocity of γ-TiAl is smaller than that of AlN. In addition, there are leaky SAW or PSAW in this structure. The first mode of the PSAW is shown in Fig. 3 and its velocity tends to the Rayleigh wave velocity of AlN with increasing thickness of the AlN layer.

Figure 4 gives the SAW velocity in a three layered AlN/Diamond/γ-TiAl structure. SAW exists only if the thicknesses of AlN and diamond belong to the area beneath the bonding curve. In contrast to the two layered AlN/Diamond structure, SAW disappear in a three layered AlN/Diamond/γ-TiAl structure with increasing thickness of AlN and diamond. Thus, for this kind of structure, in which the transverse wave velocity of the substrate is smaller than that of the surface layer, the

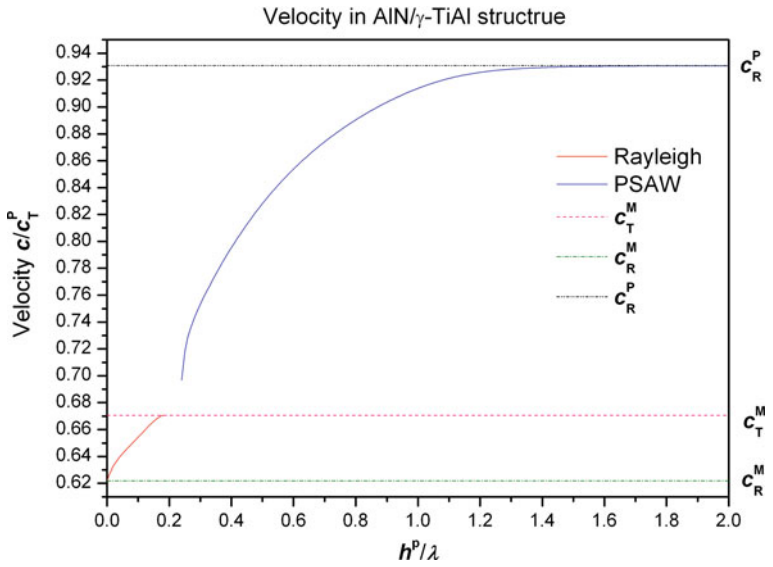

Fig. 3 Phase velocity in an AlN/γ-TiAl structure

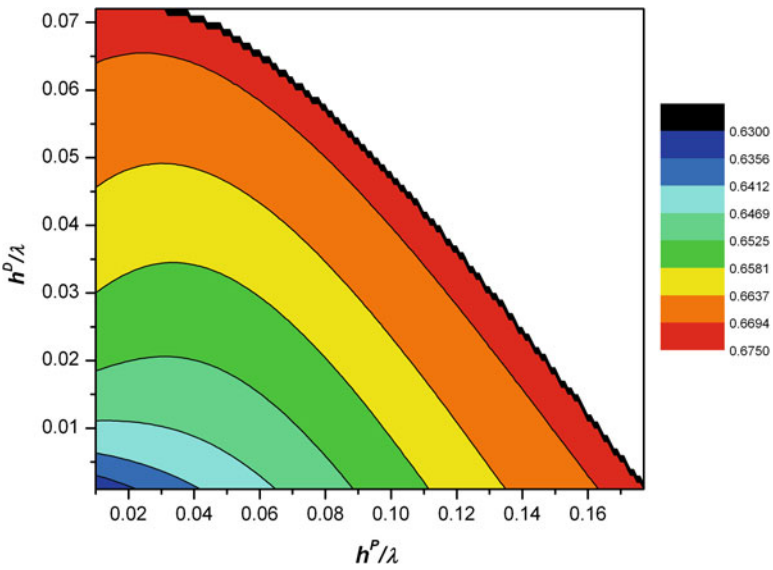

Fig. 4 SAW velocity in an AlN/Diamond/γ-TiAl structure

influence of the substrate on SAW cannot be neglected. That is to say, the two layered AlN/Diamond structure cannot replace the three layered AlN/Diamond/γ-TiAl structure. The intersection of the bounding curve and the horizontal axis is the same as the cut-off of SAW in the two layered AlN/γ-TiAl structure. This implies

that the three layered AlN/Diamond/γ-TiAl structure will degenerate into the two layered AlN/γ-TiAl structure with the decrease of the diamond thickness.

Figures 5–8 show the dispersion surfaces and the electromechanical coupling coefficient K^2 of the first and the second mode of PSAW in a three layered AlN/Diamond/γ-TiAl structure respectively.

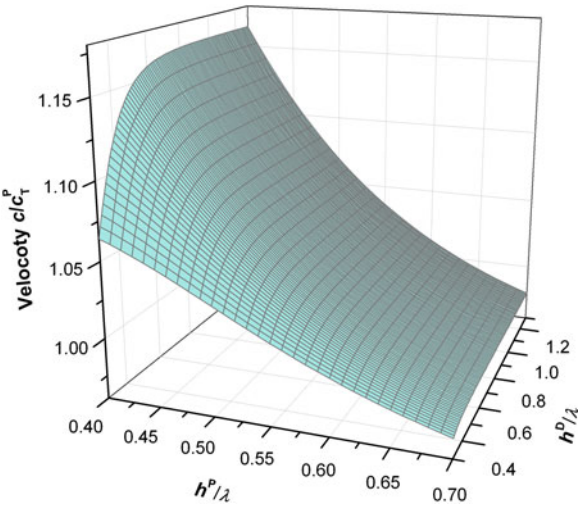

Fig. 5 Dispersion of the first PSAW mode in an AlN/Diamond/γ-TiAl structure

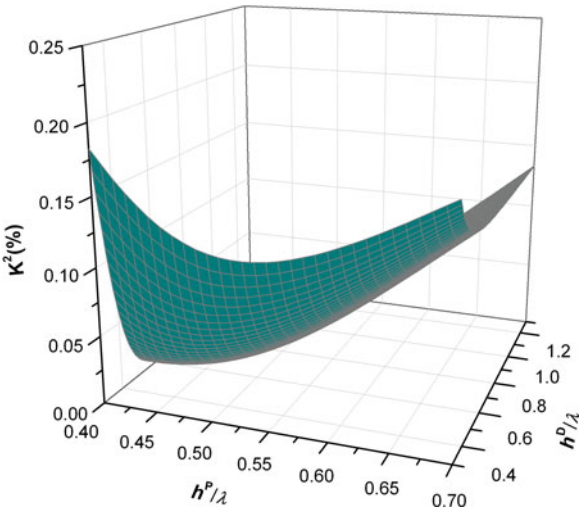

Fig. 6 Electromechanical coupling coefficient K^2 of the first PSAW mode in an AlN/Diamond/γ-TiAl structure

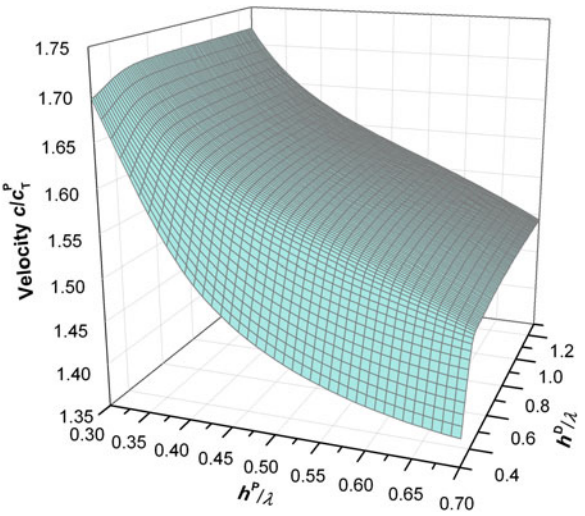

Fig. 7 Dispersion of the second PSAW mode in an AlN/Diamond/γ-TiAl structure

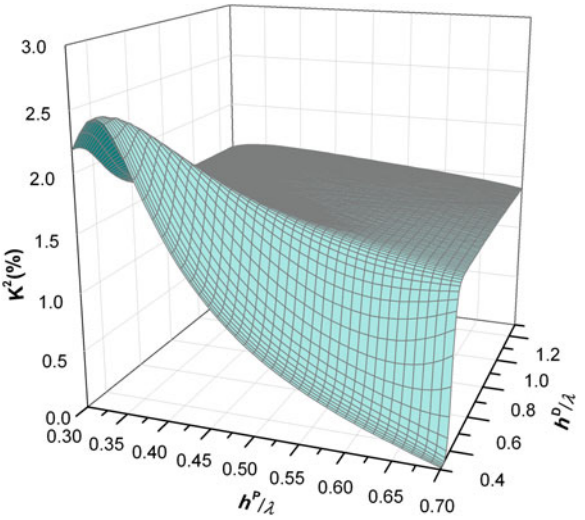

Fig. 8 Electromechanical coupling coefficient K^2 of the second PSAW mode in an AlN/Diamond/γ-TiAl structure

From Figs. 5 and 7 it can be seen that the velocities of the first and the second mode of PSAW increase with the increase of the diamond thickness and decrease with the increase of the AlN thickness. Thus, the diamond layer has a remarkable amplification effect on the velocities of SAW and PSAW in the three layered AlN/Diamond/γ-TiAl structure. By comparing Figs. 6 and 8 it can be concluded

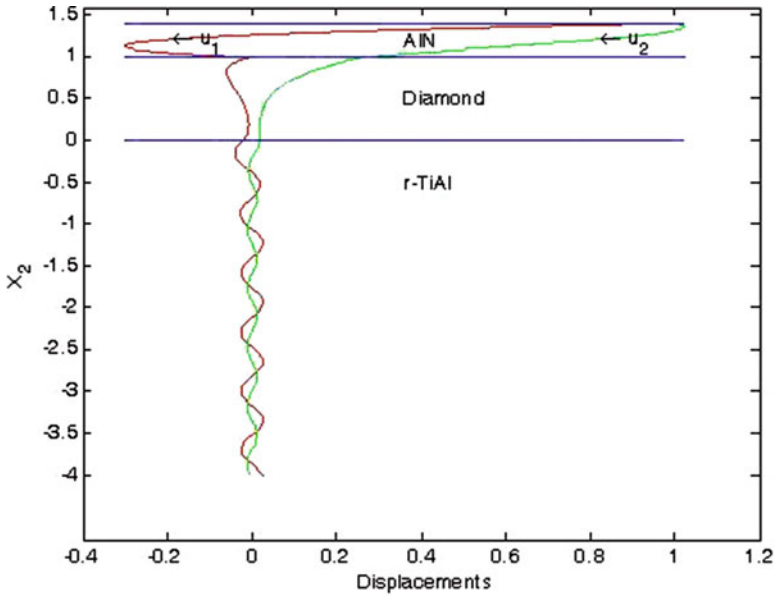

Fig. 9 Displacements in an AlN/Diamond/γ-TiAl structure with $h^P = 0.4\lambda$, $h^D = \lambda$ and $c = (1.16457 - 0.000082i) \times c_T^P$

that the electromechanical coupling coefficient of the second leaky wave mode is distinctly larger than that of the first leaky wave mode.

For the purpose of comparing the penetrability of SAW and PSAW, the displacements in the three layered AlN/Diamond/γ-TiAl structure with $h^P = 0.4\lambda$ and $h^D = \lambda$ are shown in Fig. 9. It is clear that the displacements never disappear even at a deep position from the free surface, because leaky waves consist of coupled modes involving terms decaying into the substrate beneath the free surface and a term representing a bulk wave radiating into the solid. PSAW possess a high sensitivity to defects on or near the interfaces of AlN/Diamond and Diamond/γ-TiAl due to their good penetrability in the thickness direction.

4 Conclusions

From this analysis, the following conclusions can be drawn:

- SAW exist only in a small thickness range of AlN and diamond in a three layered AlN/Diamond/γ-TiAl structure.
- The two layered AlN/Diamond structure cannot replace the three layered AlN/Diamond/γ-TiAl structure in general, in which the transverse wave velocity of substrate is smaller than that of the surface layer.
- Diamond can increase the SAW and PSAW velocities apparently.

- The electromechanical coupling coefficient K^2 of the second PSAW mode is larger than that of the first PSAW mode in a three layered AlN/Diamond/γ-TiAl structure.
- PSAW possess a high sensitivity to defects on or near interfaces due to their good penetrability in the thickness direction.

References

1. Rayleigh L (1885) On waves propagated along the plane surface of an elastic solid. Proc Lond Math Soc S1–17(1):4–11
2. Tiersten HF (1963) Thickness vibrations of piezoelectric plates. J Acoust Soc Am 35(1):53–58
3. White RM (1965) Direct piezoelectric coupling to surface elastic waves. Appl Phys Lett 7:314–316
4. Yamanoukhi K (1989) SAW propagation characteristics and fabrication technology of piezoelectric thin film/diamond structures. Proceedings of the IEEE Ultrasonic Symposium, Montreal, Quebec, Canada, pp 351–354
5. Adler EL (1995) ZnO on diamond: SAWs and PSEUDO-SAWs. Proceedings of the IEEE Ultrasonic Symposium, Seattle, WA, pp 341–344
6. Nakahata H (1995) SAW devices on diamond. Proceeedings of the IEEE Ultrasonic Symposium,Seattle, WA, pp 361–370
7. Engan H (1967) Elastic surface wave in a-quartz: observation of leaky surface waves. Appl Phys Lett 10:311–313
8. Lim TC (1969) Character of pseudo surface waves on anisotropic crystals. J Acoust Soc Am 45:845–851
9. Yamanouchi K (1972) Propagation and amplification of Rayleigh waves and piezoelectric surface waves in LiNbO. J Appl Phys 43(3):856–862
10. Takayanagi A (1970) Piezoelectric leaky surface waves in $LiNbO_3$. Appl Phys Lett 17(5): 225–227
11. Naumenko NF (1998) Leaky wave propagation in layered structures. Proceedings of the IEEE Ultrasonic Symposium, Sendai, Japan, pp 149–154
12. Benetti M (2005) Gigahertz-range electro-acoustic devices based on pseudosurface-acoustic waves in AlN/diamond/Si structures. Appl Phys Lett 87(3)
13. Benetti M (2004) SAW sensors on AlN/Diamond/Si structures. Proceedings of the IEEE Ultrasonic Symposium, pp 753–756

This page intentionally left blank

Experimental Investigation and Theoretical Modeling of Piezoelectric Actuators Used in Fuel Injectors

M.S. Senousy, R.K.N.D. Rajapakse, and M. Gadala

Abstract Piezoelectric actuators are increasingly used in fuel injectors. Experimental results for soft Lead Zirconate Titanate (PZT) actuators have shown that a significant amount of heat is generated when they are driven under high frequency and/or high electric-field magnitudes, both of which occur in fuel injectors. They also exhibit hysteretic nonlinear behavior when driven under high electric-field magnitudes. A mathematical model for self-heating that accounts for different controlling parameters relevant to fuel injection is developed in this paper, as well as a domain-switching model for PZT materials. The switching model is based on changes in potential energy, and accounts for full thermo-electro-mechanical coupling and the effect of temperature on domain switching. It is assumed that 180° switching is a two-step process caused by two 90° domain switching occurrences. The model shows good agreement with experimental results at different temperatures.

1 Introduction

Piezoelectric actuators are used in micropositioning applications due to their precise accuracy and quick response [1–3]. Automotive fuel injectors incorporating piezoelectric actuators have been recently developed [4, 5]. In injector applications, the design of the actuator should be adapted to the operational requirements of fuel injection, which necessitates operating under high dynamical excitations at elevated temperatures. Understanding the thermo-electro-mechanical performance of these actuators under such operating conditions is therefore important.

M.S. Senousy and M. Gadala
The University of British Columbia, Department of Mechanical Engineering,
Vancouver, BC, Canada V6T 1Z4
e-mail: msenousy@interchange.ubc.ca

R.K.N.D. Rajapakse (✉)
The University of British Columbia, Department of Mechanical Engineering,
Vancouver, BC, Canada V6T 1Z4
and
Faculty of Applied Sciences, Simon Fraser University, Burnaby, Canada V5A 1S6
e-mail: rajapakse@sfu.ca

M. Kuna and A. Ricoeur (eds.), *IUTAM Symposium on Multiscale Modelling of Fatigue, Damage and Fracture in Smart Materials*, IUTAM Bookseries 24,
DOI 10.1007/978-90-481-9887-0_21,

The dynamic performance of PZT actuators custom-made by *Kinetic Ceramics Inc*. has been experimentally investigated by the authors over a temperature range of −30 °C to 80 °C [6]. The results showed that the actuators generate heat when they are driven under high electric-field magnitudes and/or high frequency; they also exhibit nonlinear behavior. This heat generated may affect the piezoelectric properties and positioning accuracy of the actuators. Selfheating and nonlinearities in PZT actuators are major challenges in utilizing them in dynamically loaded systems such as fuel injectors.

In this paper, actuator self-heating and its effect on actuator response are experimentally and theoretically studied. A mathematical model for self-heating is presented and assessed against selected experimental results. A domain-switching model developed by the authors that extends the concepts of Hwang et al. [7] and accounts for electromechanical coupling, temperature, and different energy barriers for 180 °C and 90 °C switching is then summarized. A comparison of the present switching model with Hwang et al.'s model [7] and with experimental results is provided. Details of the new switching model and additional numerical results are presented in [8].

2 Piezoelectric Properties and Self-heating in PZT Actuators

PZT actuators custom made by *Kinetic Ceramics Inc*. were used in this work. Table 1 shows their geometry and material properties.

An analytical model for self-heating in PZT actuators based on the first law of thermodynamics was recently developed by the authors [9]. The model provides a closed-form solution for temperature increase that shows the classical exponential variation with respect to time, and accounts for the effects of geometry, electric field, frequency, and duty-cycle percentage. It is assumed in the model that the temperature distribution is uniform along the actuator length. The law of energy conservation can then be expressed as

$$d_t D_f \left(n\varepsilon_{33}\varepsilon_0 AE\right) f - hA_1 \left(\theta - \theta_0\right) = m C_p {}^{d\theta}/_{dt} \tag{1}$$

where D_f is the loss of the sample per electric charge per driving cycle; f is the driving-field frequency; E is the electric-field magnitude; d_t is the duty-cycle

Table 1 Geometry and material properties of actuators

Property	Value	Property	Value
Actuator diameter (mm)	5	Max. operating voltage (V)	1,000
Actuator length (mm)	30	Max. operating electric field (kV/mm)	2
Layer thickness (mm)	0.5	Piezoelectric coefficient d_{33} (pC/N)	370
Number of layers	54	Young's Modulus Y_{33} (GPa)	48
Capacitance (nF)	69	Heat capacity c (J/kg°C)	420

percentage; n is the number of layers; ε_0 is the free-space permittivity; ε_{33} is the dielectric constant in the poling direction; m is the mass of the actuator; C_p is the specific heat capacity of the actuator; A is the cross-sectional area of the actuator; A_1 represents the actuator's surface area; h is the convective heat coefficient of the surrounding air; θ is the surface temperature of the actuator; and θ_0 is the surrounding temperature.

The experimental results presented in [9] showed that, at a specified electric-field level, the displacement hysteresis D_f is linearly dependent on temperature and can be fitted in the form $D_f = a_1 + a_2\theta$. By solving Eq. (1), the temperature increase $\delta\theta$ is obtained as follows:

$$\delta\theta = \delta\theta_\infty \left(1 - e^{-t/\tau}\right) \tag{2}$$

where $\tau = \beta m C_p/(hA_1 - c_1 a_2)$ is a time constant, the steady state temperature $\delta\theta_\infty = c_1(a_1 + a_2\theta_0)/(hA_1 - c_1 a_2)$, and $c_1 = d_t n \varepsilon_{33}\varepsilon_0 AEf$.

For the purpose of testing, a 10-min loading cycle was used. $\delta\theta$ under a sinusoidal driving field is shown in Fig. 1 for $E = 1.4\,\text{kV/mm}$, $f = 100\,\text{Hz}$, and different duty cycles. It can be seen from Fig. 1 that $\delta\theta$ showed an initially increasing trend and then reached a steady state temperature. Moreover, decreasing the duty cycle percentage decreased the heat generated in the actuators. It can also be seen that the proposed self-heating model (Eq. (2)) provides a good agreement with experimental results.

Self-heating affects the piezoelectric properties of PZT actuators. Assuming that the thermal-expansion coefficient α does not change with electric-field magnitude, the longitudinal piezoelectric constant d_{33} can be calculated by dividing the measured longitudinal strain by the applied electric field. d_{33} was calculated over a temperature range of $-30\,°\text{C}$ to $80\,°\text{C}$ under electric-field magnitudes of up to $2.8\,\text{kV/mm}$. Under low electric-field magnitudes ($\leq 0.6\,\text{kV/mm}$), the material

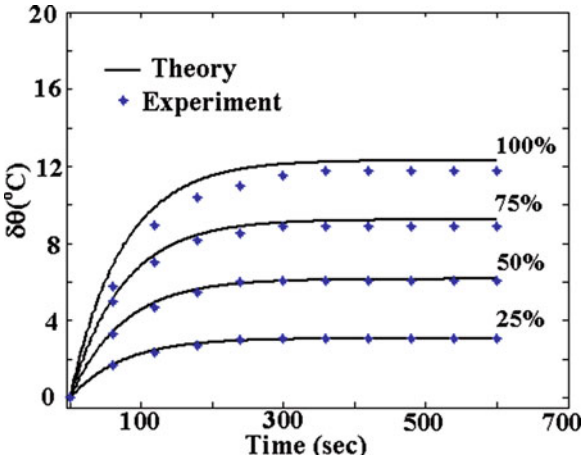

Fig. 1 Variation of $\delta\theta$ with time for different duty cycles ($E = 1.4\,\text{kV/mm}$ and $f = 100\,\text{Hz}$)

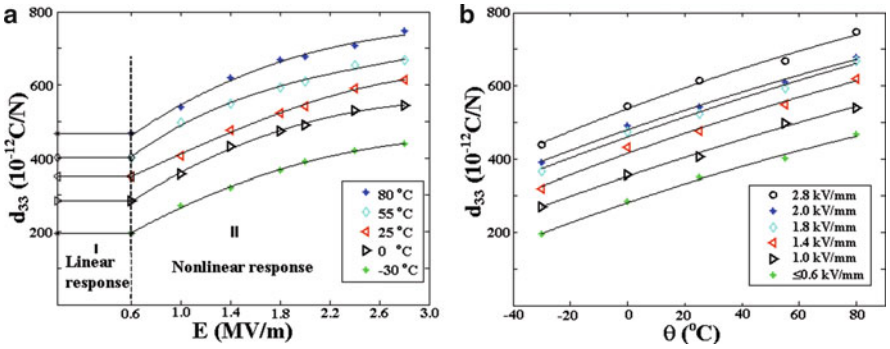

Fig. 2 Variation of d_{33} with (**a**) electric field, and (**b**) ambient temperature ($f = 100$ Hz and 10% duty cycle)

behavior was approximately linear and d_{33} was almost constant, as shown in Fig. 2a. When the applied electric field increased, d_{33} increased nonlinearly with E. Fig. 2(b) is a re-plotting of Fig. 2a to delineate the variation of d_{33} with ambient temperature. It shows that d_{33} is linearly dependent on temperature.

A polynomial representing the curves shown in Fig. 2 is obtained by using the multiple regression analysis technique such that

$$d_{33}(E, \theta) = b_0 + b_1 E + b_2 E^2 + b_3 \theta \tag{3}$$

where E is the electric-field magnitude, θ is the ambient temperature, and b_0, b_1, b_2, and b_3 are experimental-fitting constants.

3 Domain-Switching Model

In this section, a temperature-dependent two-step domain-switching model for PZT materials that accounts for the influence of piezothermoelastic coupling and material anisotropy is summarized. The details of the model can be found in [8]. The switching criterion is based on the fundamental concepts of Hwang et al. [7].

3.1 Governing Equations

The constitutive relations describing the behavior of a piezothermoelastic continuum can be expressed as follows:

$$\begin{aligned} \varepsilon_{ij} &= s_{ijkl}^{(E,\theta)} \sigma_{kl} + d_{ijk} E_k + \alpha_{ij} \theta + \varepsilon_{ij}^r \\ D_i &= d_{ijk} \sigma_{jk} + \kappa_{ij}^{(\sigma,\theta)} E_j + p_i \theta + P_i^r \\ I &= \alpha_{ij} \sigma_{ij} + p_i E_i + \alpha_v^{(\sigma,E)} \theta \end{aligned} \tag{4}$$

where ε_{ij}^{r} is the remnant strain tensor; P_i^r is the remnant polarization vector; $c_{ijkl}^{(E,\theta)}$ is the elastic constants measured at constant electric field and constant temperature; d_{ijk} are the piezoelectric-strain constants; $\kappa_{ij}^{(\sigma,\theta)}$ are the dielectric coefficients measured under constant stress and constant temperature; α_{ij} are the thermal-strain coefficients; p_i are the pyroelectric constants; $\alpha_v^{(\varepsilon,E)}$ is a material constant $\left(\alpha_v^{(\varepsilon,E)} = \rho c_v^{(\varepsilon,E)} \theta_r^{-1}\right)$, where ρ is the mass density; and $c_v^{(\varepsilon,E)}$ is the specific heat at a constant volume and a constant electric field.

The equilibrium equations for the continuum can be expressed as

$$\sigma_{ij,j} = 0, \quad D_{i,i} = 0, \quad q_{i,i} - \dot{I}\theta_r = 0 \tag{5}$$

where σ_{ij} is the stress tensor; D_i is the electric displacement vector; θ_r is a reference temperature; and I is the entropy density.

The relevant boundary conditions are

$$\begin{aligned} u_i &= u_i^0 \ \text{ on } s_u, \text{ or } \sigma_{ij} n_j = t_i \quad \text{on } s_t \\ \varphi &= \varphi^0 \ \text{ on } s_\varphi, \text{ or } D_i n_i = -Q \quad \text{on } s_Q \\ \theta &= \theta^0 \ \text{ on } s_\theta, \text{ or } -K_{ij}\theta_{,j} n_i = q_s + h_v\left(\theta_f - \theta\right) \quad \text{on } s_q \end{aligned} \tag{6}$$

where u_i^0, t_i, φ^0, Q and n_i are the specified mechanical displacement, surface traction, electric potential, electric-surface charge, and the outward unit normal vector components, respectively; θ^0 is a prescribed temperature; q_s is the rate of heat flow per unit area; θ_f is the surrounding temperature; K_{ij} are the heat conduction coefficients; h_v is the convection heat transfer coefficient; s_u and s_t are the surfaces where mechanical displacements and tractions, respectively, are specified; s_φ and s_Q are the surfaces where electric potential and electric charges, respectively, are specified; and s_θ and s_q are the surfaces with specified temperature and heat flow, respectively.

3.2 Domain-Switching Criterion

It is assumed that when a domain switches, the total potential energy is reduced [7]. The change in potential energy can be expressed as

$$\Delta \prod = \int_v \Delta F \, dv - \int_{s_t} t_i \Delta u_i^0 \, ds_t - \int_{s_Q} \varphi^0 \Delta Q \, ds_Q - \int_{s_\theta} \theta^0 \Delta q_s \, s_\theta \tag{7}$$

where F is the free-energy density (energy per unit volume).

Making use of the governing equations in Sect. 3.1, and assuming that the switching process is instantaneous, the following domain-switching criterion is developed:

$$E_i \Delta P_i^r + \sigma_{ij} \Delta \varepsilon_{ij}^r + E_i \Delta d_{ijk} \sigma_{jk} + E_i \Delta p_i \theta + \sigma_{ij} \Delta \alpha_{ij} \theta + \frac{E_i \Delta \kappa_{ij}^{(\sigma,\theta)} E_j}{2} + \frac{\sigma_{ij} \Delta s_{ijkl}^{(E,\theta)} \sigma_{kl}}{2} + \frac{\theta \, \Delta \alpha_v^{(\sigma,E)} \theta}{2} \geq \psi_b(\theta) \quad (8)$$

where Δ represents the change between the state before switching and the state after switching. The first two terms in Eq. (8) represent the contribution due to the changes in the remnant polarization and the remnant strain, respectively, and they are identical to the corresponding terms in Hwang et al.'s model [7].

It is assumed in this model that 180° domain switching is composed of two successive 90° domain-switching occurrences; the critical energy barrier for 180° domain switching $\psi_b(\theta)|_{180^\circ}$ is therefore the summation of two critical energy barriers $\psi_b(\theta)|_{90^\circ}^1$ and $\psi_b(\theta)|_{90^\circ}^2$. The energy barriers for the first 90° and 180° ferroelectric domain switching can be expressed as

$$\psi_b(\theta)|_{90^\circ}^1 = E_c(\theta) P^s(\theta) + d_{33} E_c(\theta) \sigma_c(\theta) \quad (9.a)$$

$$\psi_b(\theta)|_{180^\circ} = 2 E_c(\theta) P^s(\theta) \quad (9.b)$$

where the coercive electric field $E_c(\theta)$, the coercive stress $\sigma_c(\theta)$, and the spontaneous polarization $P^s(\theta)$ are assumed to be temperature dependent.

3.3 Model Results

PZT discs custom-made by *Kinetic Ceramics Inc*. (Table 2) were used in the simulation. A single disc with two surface electrodes was studied to represent an actuator. The experimental results were provided by *aixACCT* (*www.aixacct.com*).

The switching model was implemented in a finite element scheme [8]. The discs were modeled as axisymmetric domains using 800 four-node isoparametric

Table 2 Properties of the soft *KCI-PZT* ceramics at room temperature

Property	Supplied value	Measured value
Disc diameter (mm)	10	10
Disc thickness (mm)	0.5	0.5
Young's modulus c_{33} (GPa)	48	66
Piezoelectric coefficient d_{33} (pC/N)	370	250
Dielectric permittivity κ_{33}	3,400	2,082
Coercive electric field E_c (MV/m)		1.08
Saturated remnant polarization P_{sat} (C/m^2)		0.45
Remnant polarization P^r (C/m^2)		0.40

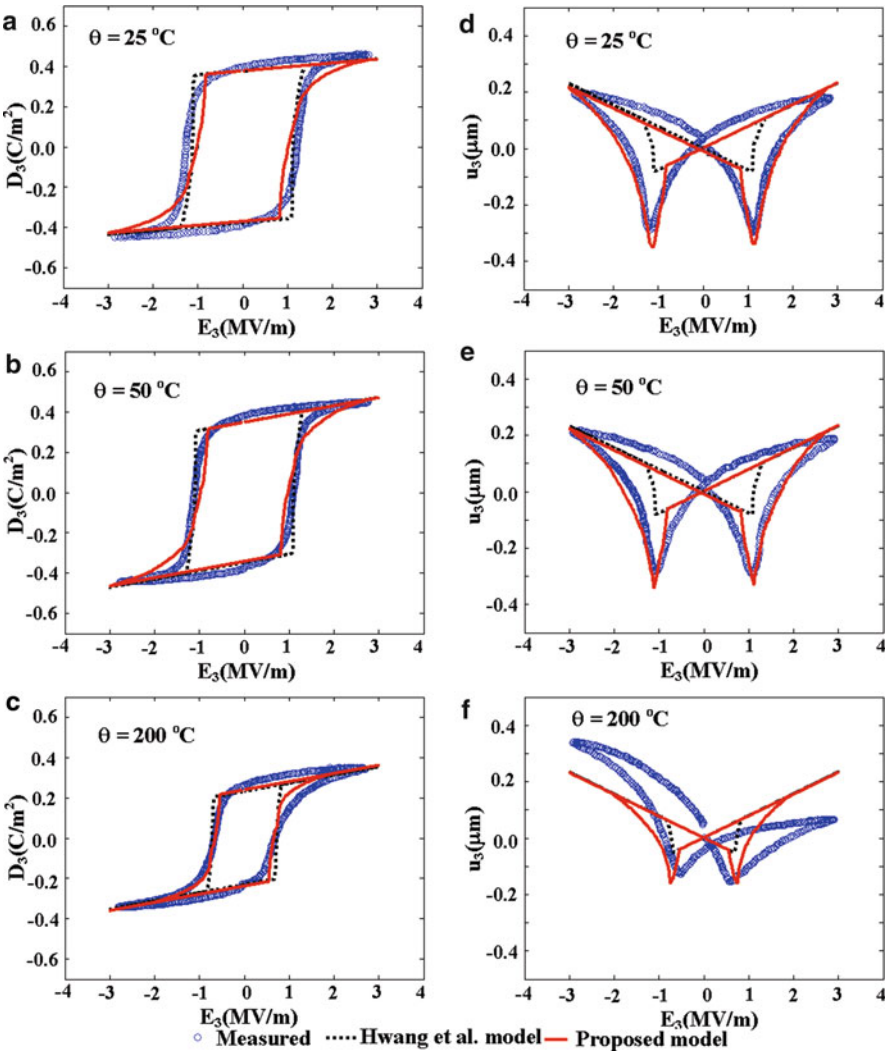

Fig. 3 Simulated and measured D–E (a–c), and S–E (d–f) hysteresis loops under pure electric loading at three different temperatures

elements. The polarization direction of each element was randomly assigned. The boundary conditions were imposed such that at the bottom surface both the vertical displacement and the electric potential were fixed. At the central line of the disc, the radial displacement was fixed. The electric potential was prescribed at the top surface. The right edge was stress and charge free.

During solution, the electric-potential at the upper surface was incrementally applied, and the temperature distribution, considered to be constant and uniform,

was input into the model. The temperature dependence of the domain-switching behavior was accounted for by considering the dependency of the piezoelectric coefficient, the remnant polarization, and the coercive field on temperature.

The $D_3 - E_3$ and $S_3 - E_3$ hysteresis loops were computed. Figure 3 shows a comparison of the results from the present model with the results based on the model developed by Hwang et al. [7], and the experimental results under an electric loading of $E = 3.0\,\mathrm{MV/m}$ at three different temperatures (25 °C; 50 °C, and 200 °C). All experimental results were obtained from tests done at the laboratories of *aixACCT*. It can be seen from Fig. 3(a–c) that the present model successfully predicts the experimental $D_3 - E_3$ hysteresis loops at the three different temperatures. It is noted that the experimental domain-switching starting points (for example, points B and G in Fig. 3a) show rounded edges in the $D_3 - E_3$ hysteresis loops, whereas the current model shows slightly sharper edges. The sharp edges of the simulation could possibly be due to the assumption that domain switching is an instantaneous process. It can also be seen from Fig. 3(a–c) that temperature has a significant effect on the $D_3 - E_3$ curves; the remnant polarization, saturation polarization, and coercive electric field steadily decrease with increasing temperature.

4 Conclusion

Self-heating in PZT actuators was experimentally studied at operating conditions relevant to the fuel injection process. A mathematical model that represents a closed-form solution for temperature increase and shows the classical exponential variation with respect to time, in the form $\delta\theta = \delta\theta_\infty(1-e^{-t/\tau})$, was developed. Additionally, a temperature-dependent domain-switching model that accounts for the influence of piezothermoelastic coupling and material anisotropy was developed. The switching criterion is based on the fundamental concepts of Hwang et al. [7]. The two-step switching process suggests different energy barriers for 90 ° and 180 ° electric-field driven switching. This model successfully predicted the experimentally obtained hysteresis loops at different electric-field magnitudes and temperatures. It also provided a better prediction of the butterfly loops than the previous models.

Acknowledgements This research was supported by a grant from the Natural Sciences and Engineering Research Council (NSERC) of Canada, with substantial in-kind support provided by Westport Power Inc.

References

1. Ardelean EV, Cole DG, Clark RL (2004) High performance "V-stack" piezoelectric actuator. J Int Mater Syst Struct 15:879
2. Chen Q, Yao DJ, Kim CJ, Carman GP (1998) Frequency response of an inchworm motor fabricated with micromachined interlocking surface mesoscale actuator device (MAD). In: Smart materials and integrated systems, vol 3329. pp 768

3. Jäker P (1997) Electro-mechanical characterization of high-performance piezoactuators. In: Smart materials and integrated systems, vol 3039. pp 670
4. Fujii A, Toyao T (2006) Piezoelectric actuators with high reliability for diesel injection valve. 10th international conference on new actuators, p 177
5. Schuh C, Steinkopff T, Wolff A, Lubitz K (2003) Piezoceramic multilayer actuators for fuel injection systems in automotive area. In: Proceedings of SPIE, vol 3992. pp 165
6. Senousy MS, Li F, Mumford D, Gadala MS, Rajapakse RKND. (2009) Thermo-electro-mechanical performance of piezoelectric stack actuators for fuel injector applications. J Int Mater Syst Struct 20:387
7. Hwang SC, Lynch CS, McMeeking RM (2073) Ferroelectric/ferroelastic interactions and a polarization switching model. Acta Materialia 1995:43
8. Senousy MS, Rajapakse RKND, Gadala MS (2009) A temperature-dependent two-step domain switching model for ferroelectric materials. Acta Materialia 57:6735–6745
9. Senousy MS, Rajapakse RKND, Mumford D, Gadala MS (2009) Self-heat generation in piezoelectric stack actuators used in fuel injectors. J Smart Mater Struct 18:045008

This page intentionally left blank

Analytical Homogenizations of Piezoceramic d_{15} Shear Macro-fibre Composites

Ayech Benjeddou and Mohammed Al-Ajmi

Abstract Closed-form expressions of effective electromechanical constants are derived for the new d_{15} *shear* macro-fibre composite (MFC) using two different *analytical homogenization* approaches: the *uniform fields method* (UFM), and the *asymptotic homogenization method* (AHM). The former is used with both *e-form* and *h-form* piezoelectric constitutive equations, while the latter is used with the *e-form* ones only. Then, the usual *unidirectional electric field* (UDEF) and *plane stress* (PS) electromechanical assumptions are considered in order to derive *simplified* sets of the homogenized electromechanical constants. *Parametric analyses* are conducted in term of the piezoelectric *fibre volume fraction* (FVF) in order to choose its optimum value for this new smart material. It is found that: (i) the effective electromechanical coefficients values from both methods are exactly identical; (ii) the simplifying UDEF and PS assumptions have no influence on the shear response homogenized electromechanical constants; (iii) on the basis of the effective *electromechanical coupling coefficient* (EMCC) as a *design criterion*, the optimum FVF lies in the range of 0.9–0.95, which is higher than that (0.86) of commercial MFC; (iv) the new d_{15} shear MFC has a *unidirectional* piezoelectric shear coupling and *high* effective material shear EMCC; thesenice features allow the application of this new MFC for active *torsion/twist* vibration and shape control, *shear* strains actuation/sensing and *shear* waves-based health monitoring.

1 Introduction

Smart composite materials with piezoceramic fibres find growing interests of the smart materials and structures researchers and practitioners due to their main advantages of conformability and unidirectional or anisotropic actuation. Several types

A. Benjeddou (✉)
Institut Supérieur de Mécanique de Paris, LISMMA – Structures, 3 rue Fernand Hainault, 93407 SAINT OUEN CEDEX, France
e-mail: Benjeddou@supmeca.fr

M. Al-Ajmi
Kuwait University, Mechanical Engineering Department, P.O. Box 5969, Safat 13060, Kuwait

M. Kuna and A. Ricoeur (eds.), *IUTAM Symposium on Multiscale Modelling of Fatigue, Damage and Fracture in Smart Materials*, IUTAM Bookseries 24,
DOI 10.1007/978-90-481-9887-0_22,

of piezoceramic fibre composites are currently commercially available or under development (see [1] for a recent review). They differ mainly by the fibres section size (micro or macro) and form (square, circular, tubular, rectangular). In particular, the so-called *macro-fibre composites* (MFC), that use rectangular piezoceramic macro-fibres [2], are becoming relatively widely used as sensors and actuators. However their direct (experimental, analytical) or/and inverse (numerical) characterizations are still confusing. In fact, mainly two-dimensional (2D) mechanics-based characterization of d_{33}-*type* (*longitudinal*) MFC is available [3]; piezoelectric charge (strain) constants are either referred to the initial values in [2] or to a supplier website [4]; while, except the transverse component that can be calculated from the measured capacitance [4], the dielectric properties are rarely provided. Besides, three-dimensional (3D) mechanical and piezoelectric data sets are sometimes provided using monolithic piezoceramics symmetry properties without justification [5] or by completing above 2D analytical properties of the prototype MFC [3] with commercial MFC constants that are homogenized using the finite element (FE) method and the representative volume element technique [6] although the original (prototype) [2,3] and commercial [4] MFC do not have the same constituents. Hence, it is not reasonable to use the prototype MFC data for the commercial one. To overcome these inconsistent published MFC electromechanical properties, recently 3D and 2D FE and uniform field method (UFM)-based analytical homogenizations of d_{31}-*type* (*transverse*) [7,8] and d_{33}-*type* (longitudinal) MFC [8] have been conducted for the commercial MFC.

As can be noticed from above literature review, only d_{31}-*type* and d_{33}-*type* MFC are available commercially. Nevertheless, d_{15} *shear* actuated fibre composite (SAFC) theoretical concept has been proposed recently [9]. Its modelling has been conducted in two steps: first its *active layer* 3D homogenization has been conducted using the UFM under the classical *unidirectional electric field* (UDEF) assumption; then, its 7-layers laminate has been homogenized using the classical *equivalent single layer* (ESL) modelling approach under the usual *plane stress* (PS) assumption that assumes *no stress through the thickness*. The presented results include a parametric analysis of the shear piezoelectric (stress/strain) coupling, thickness dielectric, and transverse shear modulus constants in term of the *fibre volume fraction* (FVF), and a parametric analysis of the piezoelectric coupling constants in terms of the piezoceramic and electrode fibre orientation.

The above SAFC concept [9] manufacturing aspects are here *revisited* so that they can be feasible and can be seen simply as a d_{15}-*type* (*shear*) MFC. The active layer of the latter is characterized by deriving its effective electromechanical properties using two different *analytical homogenization* approaches: the UFM [10], and the *asymptotic homogenization method* (AHM) [11]. The former is used with the piezoelectric constitutive equations in both *e-form* [9] and *h-form*, that is first proposed here and found more suitable for the shear MFC; while, the AHM is used with the *e-form* only. Then, UDEF and PS electromechanical assumptions are considered for deriving suitable 3D and 2D data sets for piezoelectric-thermal analogy FE [5,12] analysis for example. Parametric analyses are then conducted in term of the piezoelectric FVF in order to choose its optimum value for this new smart material.

For this purpose, the effective *electromechanical coupling coefficient* (EMCC) is here proposed for the first time as a *design criterion* for the MFC. Due to the lengthy equations of UFM and AHM, and to space limitation, focus is here made on the description of the used techniques and significant results of the effective electromechanical properties parametric analyses.

2 Shear MFC Concepts

The macro-fibre composite (MFC) is a 7-layer laminate which has an *active layer* consisting of several piezoceramic fibres, of *rectangular cross-section*, that are diced from monolithic piezoceramic patches and assembled in parallel with an epoxy filling material. This active layer (piezoceramic fibres + epoxy matrix) is sandwiched between *continuous* or *interdigitated* electrodes (IDE), made of copper and polyimide film, and encapsulating layers made of acrylic and kapton [2–4]. The initial MFC concept [2] uses the d_{33} (longitudinal) piezoelectric mode response since the polarization (by convention along the material 3-axis) and *dominant* electric field are made in parallel along the piezoceramic fibre length, and the electrically induced strain is also along this direction. The IDE was here used to force the electric field to lie along the fibres length. However, the resulting electric field is *non uniform* and this configuration requires a *high* actuation voltage [8]. To overcome these shortcomings, an alternative MFC design has been commercialized later [4]; it uses the d_{31} (transverse) piezoelectric mode response resulting from parallel polarization and electric field that are both along the fibres thickness. In this configuration, the induced strain remains along the fibres length but the electric field is now *uniform* and the actuation voltage is much *lower* [8]. The shear actuated fibre composite (SAFC) proposed recently [9] adapts the MFC concept by using *width-polarized* fibres and 90°-rotated *IDE electrodes*; the latter are supposed to force a *uniform* electric field along the fibres *thickness*. The macro-fibres are put together for their single step width polarization. Here, it is believed that the fabrication aspects feasibility, as in Fig. 1 of [9], is doubtful; in particular, the 90°-rotated IDE electrodes cannot enforce a *uniform* electric field along the fibres *thickness*. Rather than an alternative [9], *permanent continuous* electrodes should replace the 90°-rotated IDE ones to get uniform electric field along the fibres thickness. Also, the proposed [9] width polarization procedure can be avoided or enhanced by using *temporal* IDE electrodes or simply dicing the macro-fibres from a piezoceramic cube or parallelepiped that is polarized along the material 2-axis. With these concept enhancements, it is believed that "d_{15}*-type* (*shear*) MFC" prototyping is feasible.

3 Piezoelectric Shear-mode Response

It is well known that the piezoelectric shear mode response can be reached only for *perpendicular* polarization and electric field [13], and that the presence of electrodes imposes a *dominant* electric field in the direction perpendicular to them. Hence,

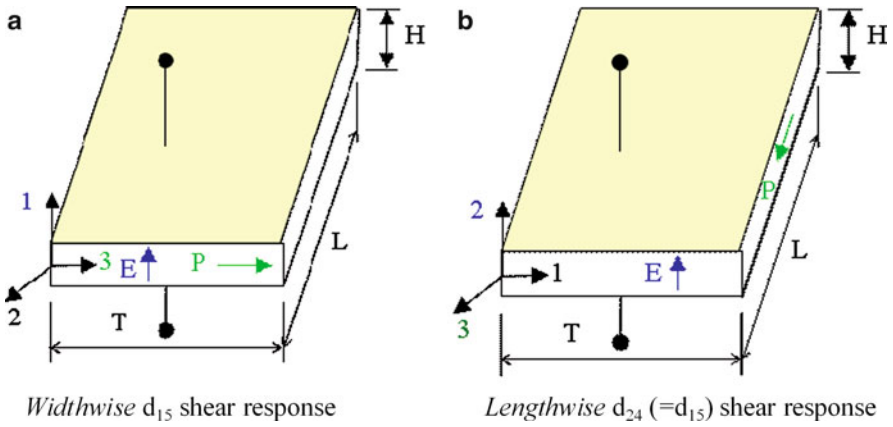

Fig. 1 Possible transverse shear mode responses of a patch with electroded major surfaces. (**a**) *Widthwise* d_{15} shear response and (**b**) *lengthwise* d_{24} $(= d_{15})$ shear response

considering a piezoelectric patch that is electroded on its major surfaces, results in a dominant electric field along its thickness. The patch will then respond in its *lengthwise* transverse shear response (Fig. 1a) when poled along its length and in its *widthwise* one (Fig. 1b) when poled along its width. The latter is the basis of the d_{15} shear MFC concept because it shall require lower poling voltage. The piezoceramic patch dimensions allow thin structures 2D kinematics; hence, it can be reasonably assumed that the through-the-thickness stress is negligible compared to the other components of the stress tensor. Besides, the presence of the electrodes, imposing a dominant electric field, justifies the UDEF assumption. The combination of the nil thickness stress and UDEF assumption defines here the PS one that will be used later to derive simplified 2D electromechanical data sets. Hence, in the frame system shown in Fig. 1a, the UDEF only and PS (here plane L-T = plane 2–3) assumptions are, respectively

$$E_2 = E_3 = 0 \tag{1}$$

$$E_2 = E_3 = T_1 = 0 \tag{2}$$

Where, E_α $(\alpha = 2, 3)$, T_1 are in-plane electric field and thickness stress components. The frame system shown in Fig. 1a is retained later for the *results interpretation* since the *polarization* is along the 3-*axis* as for the commercial MFC notations; However, for the *theoretical formulations*, it is more convenient to consider that the *polarization* is along the composite x_1-*axis* and that the *electric field* is along its x_3-*axis* (see Fig. 2a); above UDEF and PS (here plane L-T = plane 1–2) assumptions read as is usually considered in literature and commercial FE codes

$$E_1 = E_2 = 0 \tag{3}$$

$$E_1 = E_2 = T_3 = 0 \tag{4}$$

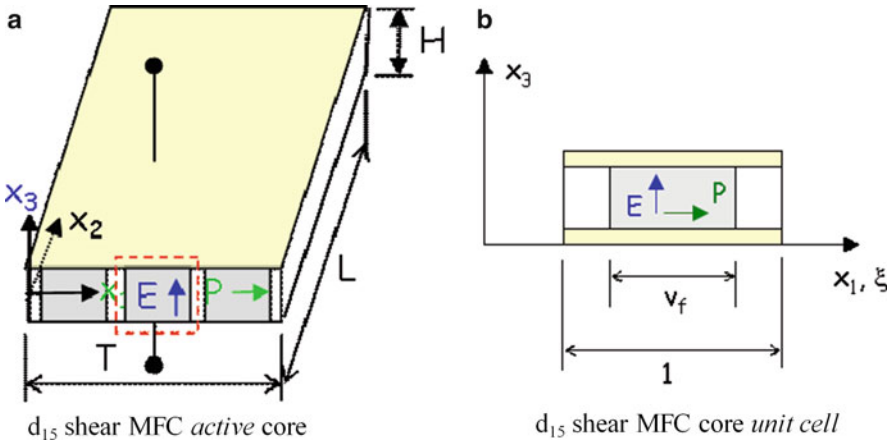

Fig. 2 d_{15} shear MFC active core and its unit cell to be used for the analytical homogenizations. (**a**) d_{15} shear MFC *active* core and (**b**) d_{15} shear MFC core *unit cell*

4 Analytical Homogenizations of Shear MFC

In contrary to commercial d_{33} or d_{31} MFC, which is a laminate that can be modelled macroscopically as an ESL, the new d_{15} shear MFC has to be considered as a *sandwich* construction with a piezoelectric macro-fibre reinforced composite core and *laminated* faces. The former should be shear resistant and is composed of the piezoceramic macro-fibres and epoxy matrix, but could include the electrodes through their effects that impose an UDEF, while the latter could be modelled as an ESL using the classical plate laminate theory; the faces are mainly constituted of the encapsulating layers but could include also the electrodes if they are not included in the core model. Here, the focus is made on the active core homogenization using the *unit cell* concept, as in Fig. 2b, for which an "*average*" quantity 'a' per unit length of the unit cell is defined in terms of its fibre (f) and matrix (m) constituents' properties and their respective volume (v) fractions as

$$\langle a \rangle = \int_0^1 a(x)dx = a^f v_f + a^m v_m;\ v_{\mathrm{m}} = 1 - v_{\mathrm{f}} \tag{5}$$

The objective here is to replace the active composite core by a homogenous layer which effective electromechanical properties are evaluated using the UFM and AHM; the latter is *considered here for the first time for the MFC* analytical homogenization. Both techniques use the e-form piezoelectric constitutive equations, which is the only one used in *commercial* FE packages. The UFM is a classical analytical tool for composites homogenization that is used here for the validation of the AHM results. Since both AHM and UFM do not provide friendly closed-form

explicit expressions of the full 3D constants, it is worthy to mention here that the use of the piezoelectric constitutive equations in their *h-form* within the UFM provides simpler expressions. The obtained 3D effective constants sets are then simplified using the UDEF assumption in order to compare with the available literature [9]. Here, it is also considered that the UDEF assumption can approximate *crudely* the presence of the electrodes on the major surfaces of the piezoelectric shear MFC core (see shaded areas in Fig. 2). Since the latter should be shear resistant, only the nil thickness stress can be considered, in combination with the UDEF, to represent the electromechanical PS assumptions.

4.1 Asymptotic Homogenization Method

The AHM relies on the concept of *periodic* microstructure by considering that the MFC active core is made of identical unit cells, of local axis $\xi = x_1/\lambda$, which are distributed in the x_1 direction to represent the whole structure (Fig. 2); λ is the ratio of the unit cell length to the MFC core one in the direction of periodicity x_1. The existence of the local axis ξ requires the derivative (denoted by the subscript comma), with respect to x_1, to be transformed using the chain rule such that

$$(.)_{,x_1} \rightarrow (.)_{,x_1} + \lambda^{-1}(.)_{,\xi} \tag{6}$$

Substituting the strains-displacements and electric fields-potential relations in the *e-form* constitutive equations of an x_1-polarized piezoelectric material gives

$$\begin{aligned} &T_1 = C_{33}^E u_{1,1} + C_{23}^E u_{2,2} + C_{13}^E u_{3,3} + e_{33}\varphi_{,1},\ T_4 = C_{66}^E(u_{2,3} + u_{3,2}) \\ &T_2 = C_{23}^E u_{1,1} + C_{22}^E u_{2,2} + C_{12}^E u_{3,3} + e_{32}\varphi_{,1},\ T_5 = C_{55}^E(u_{1,3} + u_{3,1}) + e_{15}\varphi_{,3} \\ &T_3 = C_{13}^E u_{1,1} + C_{12}^E u_{2,2} + C_{11}^E u_{3,3} + e_{31}\varphi_{,1},\ T_6 = C_{44}^E(u_{1,2} + u_{2,1}) + e_{24}\varphi_{,2} \end{aligned} \tag{7a}$$

$$\begin{aligned} &D_1 = e_{33}u_{1,1} + e_{32}u_{2,2} + e_{31}u_{3,3} - \in_{33}^S \varphi_{,1},\ D_2 = e_{24}(u_{1,2} + u_{2,1}) - \in_{22}^S \varphi_{,2} \\ &D_3 = e_{15}(u_{1,3} + u_{3,1}) - \in_{11}^S \varphi_{,3} \end{aligned} \tag{7b}$$

With T_p, u_i, D_i, φ, C_{pq}^E, e_ip, $\in_{ii}^S$ (i = 1, 2, 3, p = 1, ..., 6) the stresses, displacements, electric displacement, electric potential, elastic constants at constant electric field, piezoelectric stress constants, and dielectric constants at constant strains.

The first step of the AHM is to expand *asymptotically* the mechanical displacements and electric potential as [11]

$$\begin{aligned} u_i &= u_i^0(\underline{x},\xi,t) + \lambda u_i^1(\underline{x},\xi,t) + \cdots + \lambda^k u_i^k(\underline{x},\xi,t) + \cdots \\ &\qquad\qquad ; \underline{x} = (x_1, x_2, x_3) \\ \varphi &= \varphi^0(\underline{x},\xi,t) + \lambda \varphi^1(\underline{x},\xi,t) + \cdots + \lambda^k \varphi^k(\underline{x},\xi,t) + \cdots \end{aligned} \tag{8}$$

Then, using (6, 8) in (7) expands also the stresses and electric displacements as

$$\begin{aligned} T_p &= T_p^0(\underline{x},\xi,t) + \lambda T_p^1(\underline{x},\xi,t) + \cdots + \lambda^k T_p^k(\underline{x},\xi,t) + \cdots \\ D_i &= D_i^0(\underline{x},\xi,t) + \lambda D_i^1(\underline{x},\xi,t) + \cdots + \lambda^k D_i^k(\underline{x},\xi,t) + \cdots \end{aligned} \tag{9}$$

The second step of the AHM is to make the following separation of variables

$$u_i^1(\underline{x},\xi) = N_{irs}(\xi) u_{r,s}^0 + \Phi_{is}(\xi)\varphi_{,s}^0, \varphi^1(\underline{x},\xi) = M_{rs}(\xi) u_{r,s}^0 + \Psi_s(\xi)\varphi_{,s}^0 \tag{10}$$

Where, M, N, Φ and Ψ are *local periodic functions* in ξ to be determined. For this purpose, substituting (10) in the constitutive equations resulting with (9) for the order k=0, and comparing the "average" of the resulting expressions with the constitutive equations, provide the homogenized coefficients in terms of the periodic functions. To solve for the former explicitly, (9) is substituted in the *unloaded* electromechanical equilibrium equations and terms with similar powers of λ^{-1} are equated in order to get the following conditions, that can be interpreted as *homogeneities* in ξ or *continuities* if wrote at the interfaces

$$T_{1,\xi}^0 = T_{5,\xi}^0 = T_{6,\xi}^0 = 0, D_{1,\xi}^0 = 0 \tag{11}$$

Substituting again (10) in the constitutive equations resulting with (9) for the order $k = 0$, and applying (11), provide a set of *local* problems on the unit cell which solution for the periodic functions provides *closed-form* expressions of the effective electromechanical constants under the following *uniqueness* conditions

$$< N_{irs,\xi} > = < M_{rs,\xi} > = < \Phi_{is,\xi} > = < \Psi_{s,\xi} > = 0 \tag{12}$$

Due to space limitation, the obtained lengthy 3D AHM expressions of the effective electromechanical constants of the shear MFC are not provided; however, considering the UDEF assumptions (3) in (7) and applying the above outlined AHM procedure, provide the following *friendly* explicit expressions where both fibre and matrix materials are let piezoelectric for completeness

$$C^H_{\alpha\beta} = C^f_{\alpha\beta} v_f + C^m_{\alpha\beta}(1-v_f) - v_f(1-v_f) \frac{\left(C^f_{\alpha 3} - C^m_{\alpha 3}\right)\left(C^f_{\beta 3} - C^m_{\beta 3}\right)}{C^m_{33} v_f + C^f_{33}(1-v_f)},\ \alpha,\beta = 1,2 \tag{13a}$$

$$C^H_{rr} = \frac{C^f_{rr} C^m_{rr}}{C^m_{rr} v_f + C^f_{rr}(1-v_f)},\ \mathrm{r} = 3,4,5; C^H_{66} = C^f_{66} v_f + C^m_{66}(1-v_f) \tag{13b}$$

$$C^H_{\alpha 3} = \frac{C^f_{\alpha 3} C^m_{33} v_f + C^m_{\alpha 3} C^f_{33}(1-v_f)}{C^m_{33} v_f + C^f_{33}(1-v_f)},\ \alpha = 1,2;$$

$$e^H_{15} = \frac{e^f_{15} C^m_{55} v_f + e^m_{15} C^f_{55}(1-v_f)}{C^m_{55} v_f + C^f_{55}(1-v_f)}, \tag{13c}$$

$$\in^H_{11} = \in^f_{11} v_f + \in^m_{11} (1-v_f) + v(1-v) \frac{\left(e^f_{15} - e^m_{15}\right)^2}{C^m_{55} v_f + C^f_{55}(1-v_f)} \tag{13d}$$

It is worthy to mention that it is found that the *UDEF assumption has no influence* on the shear behaviour constants: $C^H_{44},\ C^H_{55},\ C^H_{66},\ e^H_{15},\ \in^H_{11}$. Also, a proved (checked analytically) nice feature is that 3D UDEF expressions (13) can be implemented simply by vanishing $e_{3\mathrm{i}}$ ($\mathrm{i} = 1,\ 2,\ 3$) in the closed-form full 3D ones.

Under 2D PS assumptions, 3D UDEF expressions (13) simplify further into

$$Q^H_{33} = \frac{Q^f_{33} Q^m_{33}}{Q^m_{33} v_f + Q^f_{33}(1-v_f)},\ Q^H_{23} = \frac{Q^f_{23} Q^m_{33} v_f + Q^m_{23} Q^f_{33}(1-v_f)}{Q^m_{33} v_f + Q^f_{33}(1-v_f)} \tag{14a}$$

$$Q^H_{22} = Q^f_{22} v_f + Q^m_{22}(1-v_f) - v_f(1-v_f) \frac{\left(Q^m_{23} - Q^f_{23}\right)^2}{Q^m_{33} v_f + Q^f_{33}(1-v_f)} \tag{14b}$$

where, $Q^k_{\alpha\beta} = C^k_{\alpha\beta} - \frac{C^k_{\alpha 3} C^k_{\beta 3}}{C^k_{11}};\ k = f,\ m;\ \alpha,\ \beta = 2,\ 3.$

Again, it is found that the *PS assumptions have no influence* on the shear response constants: $C^H_{44},\ C^H_{55},\ C^H_{66},\ e^H_{15},\ \in^H_{11}$. Hence, they are as in (13).

4.2 Unified Fields Method

This approach is based on the iso-fields assumption such that stresses, strains, electric field, and electric displacements are *uniform* throughout the structure at the *macroscopic* level without consideration of the *micro-structural* details [10]. That is, the unit cell (Fig. 2b) is analyzed and its *average* response represents

the response of the MFC active core (Fig. 2a) at-large. The approach begins by applying stress and strain mechanics to the unit cell in Fig. 2b. Hence, the average normal strains in the x_2 and x_3 directions and their corresponding shear strain in the 2–3 plane must be equal to those strains in each of the fibre and matrix, while other remaining strains are the average of those in the two phases. On the other hand, average normal stresses in the x_1 direction, as well as its shear stress components are equal in both phases while remaining stress components are mixed between the two phases. Similar analogy can be used for the electric field and displacement, respectively. With $\underline{\boldsymbol{\varepsilon}} = \{T_1, S_2, S_3, S_4, T_5, T_6, D_1, E_2, E_3\}^T$ and $\underline{\boldsymbol{\sigma}} = \{S_1, T_2, T_3, T_4, S_5, S_6, E_1, D_2, D_3\}^T$, the electromechanical conditions become

$$\underline{\boldsymbol{\sigma}} = <\underline{\boldsymbol{\sigma}}>, \ \underline{\boldsymbol{\varepsilon}} = \underline{\boldsymbol{\varepsilon}}^f = \underline{\boldsymbol{\varepsilon}}^m \tag{15a,b}$$

The piezoelectric constitutive equations are then manipulated and rewritten as

$$\underline{\boldsymbol{\sigma}} = \underline{\underline{\mathbf{A}}}\,\underline{\boldsymbol{\varepsilon}} \tag{16}$$

Where $\underline{\underline{\mathbf{A}}}$ is a 9×9 matrix operator which terms depend on the used e- or h-form. Hence, to get the latter matrix from the *e-form* constitutive equations (7), the electric field E_1 is first *condensed* between D_1 and T_1; then, the strain S_1 should be extracted from the expression of T_1 after its updating with the expression of E_1 obtained in the previous step. Finally, S_1 and E_1, updated with S_1, expressions are substituted back in T_2 and T_3. The *complexity* of the e-form UFM comes mainly from the condensation of E_1 and *updating* of E_1 and S_1. However, to get the matrix of (16) from the *h-form*, the previous tasks are avoided since S_1 is extracted from T_1 then substituted back in T_2, T_3 and E_1. After these, D_2 is *condensed* from T_6 and E_2, while D_3 is *condensed* from T_5 and E_3.

Now, writing (16) separately for the fibre and matrix materials, then substituting the resulting relations in (15a) and taking advantage of (15b) lead to

$$\underline{\boldsymbol{\sigma}} = \underline{\underline{\mathbf{A}}}^{\mathrm{H}}\underline{\boldsymbol{\varepsilon}}, \ \underline{\underline{\mathbf{A}}}^{\mathrm{H}} = <\underline{\underline{\mathbf{A}}}> \tag{17}$$

Where $\underline{\underline{\mathbf{A}}}^{\mathrm{H}}$ is the matrix of *homogenized* electromechanical coefficients, which explicit expressions depend on the used e- or h-form. The e-form use leads to lengthy expressions for most of the constants except the shear ones, while the reverse happens for the h-form use.

5 Results and Discussion

Using the commercial MFC fibre and matrix material data [7,8], parametric analyses in terms of the FVF were conducted for the 3D, UDEF and PS AHM and e-/h-UFM resulting effective engineering constants at constant electric field (generally under short-circuit electric conditions denoted SC). They showed that:

- 3D AHM and e-/h-form UFM provide the *same* engineering constants.
- The fibre piezoceramic material isotropy transverse *symmetry is preserved*.
- Transverse and longitudinal piezoelectric couplings are *negligible* for FVF $<$ 0.9, while the shear coupling is *dominant* and *close* to that of the fibre for FVF $>$ 0.9.
- UDEF and PS assumptions affect only Young's moduli and Poisson's ratios (Fig. 3) and *do not affect the shear response* as shown in Fig. 4, which indicates that a good shear MFC *design parameter* is its effective material *EMCC*. The latter shows that, the shear MFC *optimum* FVF should be chosen in the range of 0.9–0.95; this is *higher* than that calculated (0.86) for the commercial MFC. In this range, the MFC effective shear properties are *very close* to those of the fibres (Fig. 4) while keeping the MFC flexibility; this nice feature is a good motivation for the shear MFC *prototyping* which is still open.

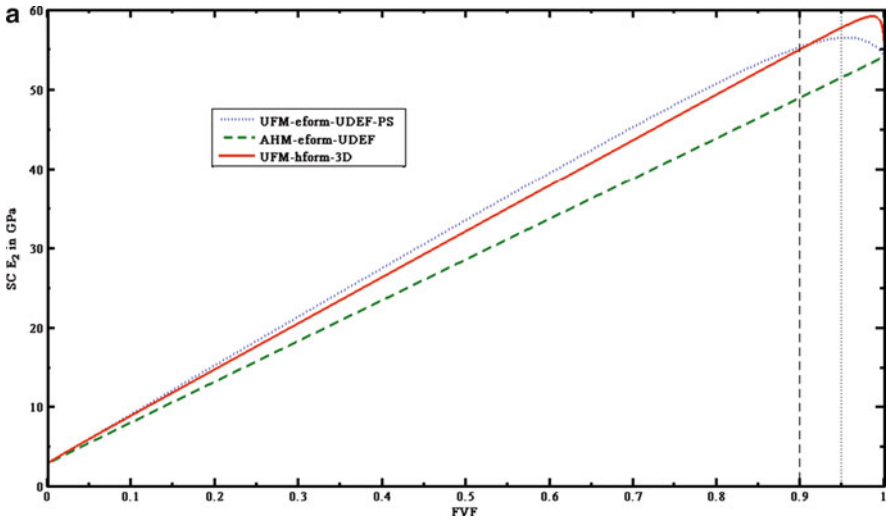

Fig. 3 d_{15} shear MFC active core 3D vs 3D-UDEF vs 2D PS effective elastic constants. (**a**) Length Young's modulus, (**b**) transverse Young's modulus, (**c**) major Poisson's ratio, and (**d**) Minor Poisson's ratio

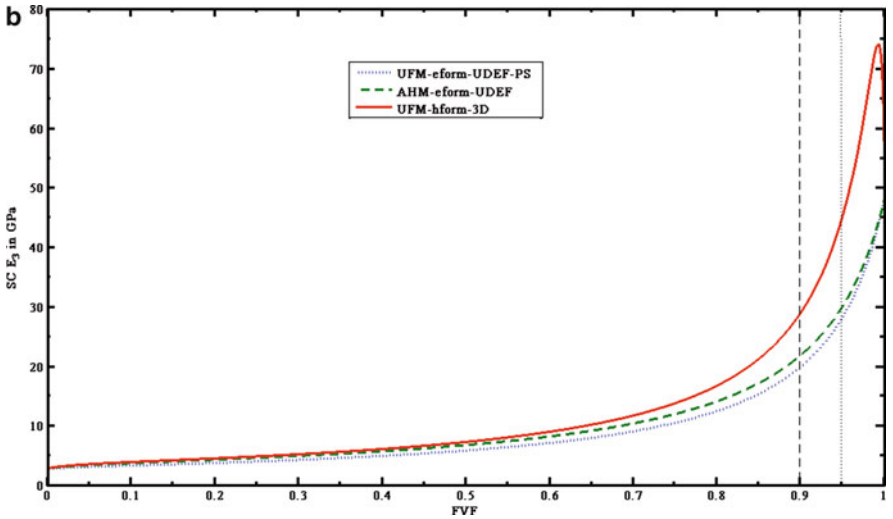

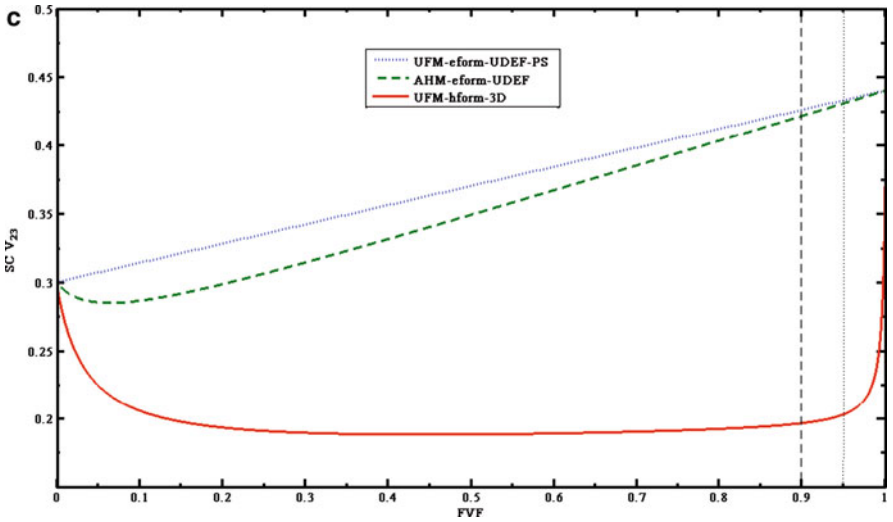

Fig. 3 (continued)

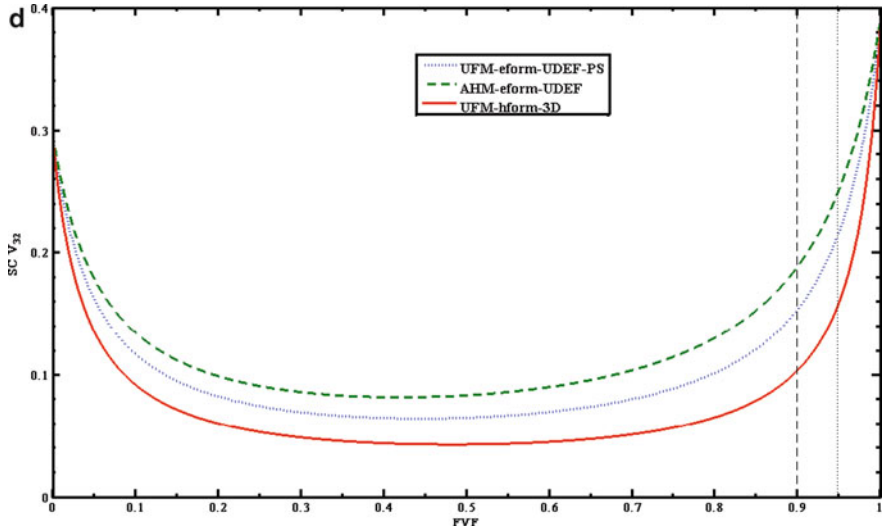

Fig. 3 (continued)

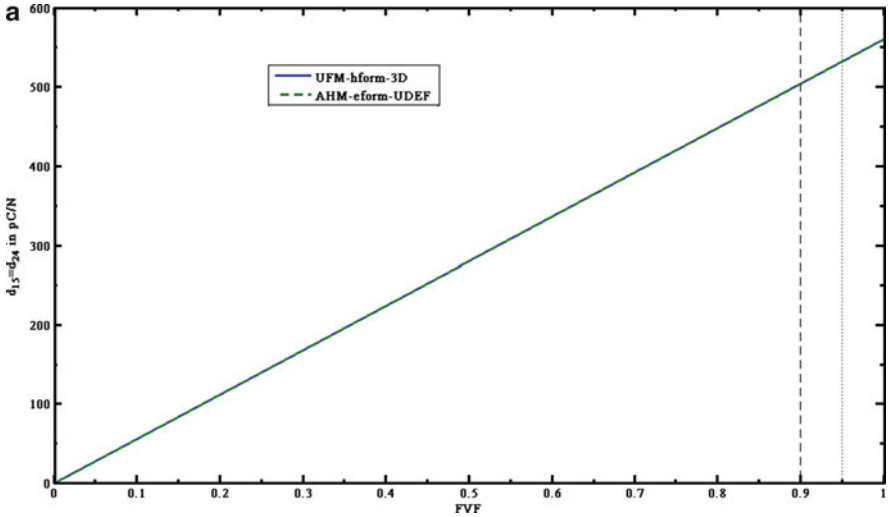

Fig. 4 d_{15} shear MFC active core effective piezoelectric, dielectric and EMCC constants. (**a**) Shear strain piezoelectric coupling constants, (**b**) relative free dielectric constant and (**c**) shear electromechanical coupling constant

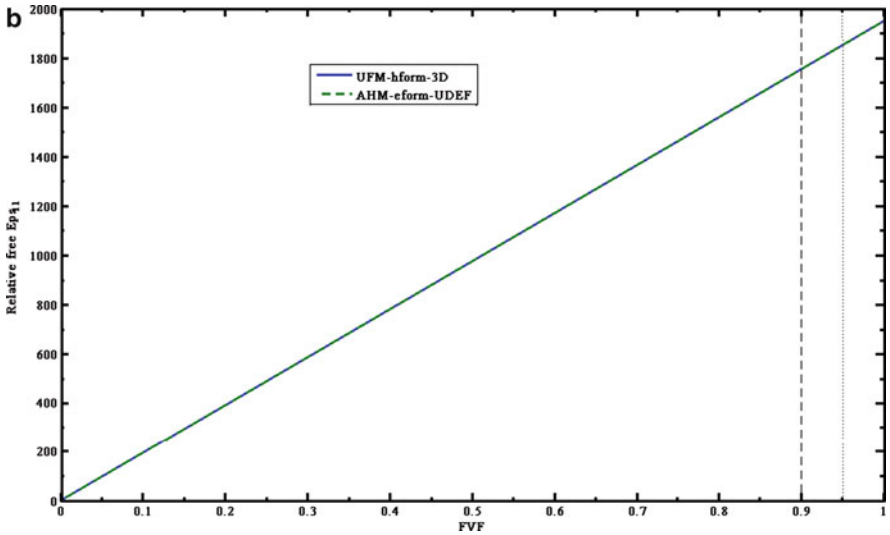

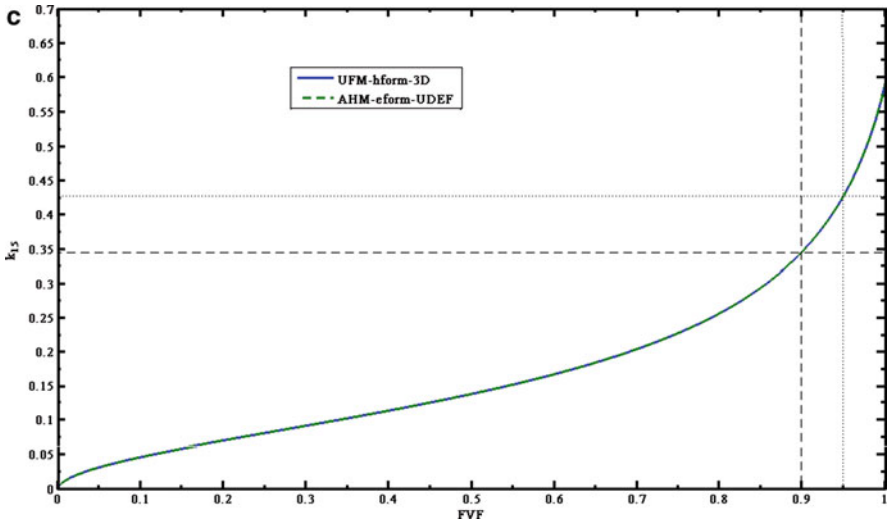

Fig. 4 (continued)

References

1. Lin Y, Sodano HA (2009) Electromechanical characterization of a active structural fiber lamina for multifunctional composites. Compos Sci Techol 69:1825–1830
2. Wilkie WK et al (2000) Low-cost piezocomosite actuator for structural control applications. In: Proceedings of the SPIE 7th annual international symposium on smart structure and materials, Newport Beach (CA), 5–9 Mar
3. Williams RB (2004) Nonlinear mechanical and actuation characterization of piezoceramic fiber composites. Ph.D. Dissertation, Blacksburg (VA)
4. http://www.smart-material.com
5. Barkanov E, Gluhih S, Kovalov A (2008) Optimal design of the active twist for helicopter rotor blades with c-spar. Mech Adv Mater Struct 15:325–334
6. Dano ML, Gakwaya M, Jullière B (2008) Compensation of thermally induced distortion in composite structures using macro-fiber composites. J Intel Mater Sys Struct 19:225–233
7. Deraemaeker A, Preumont A, Benjeddou A, Ben Elechi, S (2007) Analytical and numerical computation of homogenized properties of MFCS: application to a composite boom with MFC actuators and sensors. In: Ostachowicz W, Holnicki-Szulc J, Mota Soares CA (eds) III thematic ECCOMAS conference on smart structure and materials, Gdansk, Poland, 9–11 July
8. Deraemaeker A, Nasser H, Benjeddou A, Preumont A (2009) Mixing rules for the piezoelectric properties of macro fiber composites. J Intel Mater Sys Struct 20:1475–1482
9. Raja S, Ikeda T (2008) Concept and electro-elastic of shear actuated fiber composite using micro-mechanics approach. J Intel Mater Sys Struct 19:1173–1183
10. Tan P, Tong L (2001) Micro-electromechanics models for piezoelectric-fiber-reinforced composite materials. Compos Sc Tech 61:759–769
11. Otero JA et al (2005) Dynamic behavior of a layered piezocomposite using the asymptotic homogenization method. Mech Mater 37:33–44
12. Kim DK, Kim HI, Han JH, Kwon KJ (2008) Experimental investigation on the aerodynamic characteristics of a bio-mimetic flapping wing with macro-fiber composites. J Intel Mater Sys Struct 19:423–431
13. Benjeddou A (2007) Shear-mode piezoceramic advanced materials and structures: a state of the art. Mech Adv Mater Struct 14:263–275

Influence of the Load Dependent Material Properties on the Performance of Multilayer Piezoelectric Actuators

Hannes Grünbichler, Josef Kreith, Raúl Bermejo, Clemens Krautgasser, and Peter Supancic

Abstract Multilayer piezoelectric actuators are commonly used to control injection valves in modern combustion-engines. Their structural and functional integrity is associated with the loading conditions as well as with the actuator-design. In service mechanical stresses are an inherent loading scenario of such electro-mechanical converter components. Internal inhomogeneous mechanical and electrical fields may harm their integrity and accelerate phenomena such as degradation, fatigue and subcritical crack growth. A way to delay these phenomena is to reduce the tensile field-amplitudes by operating these piezoelectric components under a low compressive bias-stress. However, this also may influence the component's performance. Interestingly, this bias-stress enhances its strain characteristics.

In this work the electro-mechanical behaviour of a multilayer actuator has been characterised under different loading conditions using an adapted universal materials testing machine (UTM). The stiffness of the UTM has also been adjusted to simulate realistic conditions. This adaption enables the measurement of mechanical properties – such as mechanical stress and the corresponding strain – and electrical quantities, i.e. the electrical charge (or electric displacement) and the applied voltage (or electrical field) to the actuator. As a result, the stiffness, hysteresis-loops, such as the dielectric and butterfly curves and the stress-strain loop, as well as the actuator's performance, can be measured.

H. Grünbichler (✉), R. Bermejo, and P. Supancic
Institut für Struktur- und Funktionskeramik, Montanuniversität Leoben Peter Tunner-Straße 5, 8700 Leoben, Austria

H. Grünbichler, J. Kreith, C. Krautgasser, and P. Supancic
Materials Center Leoben Forschung GmbH, Roseggerstraße 12, 8700 Leoben, Austria
e-mail: hannes.gruenbichler@unileoben.ac.at

M. Kuna and A. Ricoeur (eds.), *IUTAM Symposium on Multiscale Modelling of Fatigue, Damage and Fracture in Smart Materials*, IUTAM Bookseries 24,
DOI 10.1007/978-90-481-9887-0_23,

1 Introduction

Lead-zirconate-titanate- (PZT-) based piezo-ceramics are commonly used for technological applications such as low-voltage multilayer piezoelectric actuators employed in fuel injection systems, for instance [1, 2]. Their rapid operation (opening and closing of the injection-valve takes only few milliseconds) results in lower fuel consumption, high precision control and less noise compared to common electromagnetic actuators [2].

Usually such adaptive devices are designed as laminates of thin piezo-ceramic layers separated by metallic electrodes [3, 4]. The piezo-ceramic material itself is poly-crystalline. The crystals show cubic centro-symmetry at sinter-temperature, *i.e.* typically $1,100\,°\mathrm{C}$ [4]. When cooling down below the Curie point – *circa* $350\,°\mathrm{C}$ for PZT for instance – a phase transition takes place from the paraelectric (cubic phase) into the ferroelectric (tetragonal or rhombohedral phase) state [5]. The lattice structure becomes then deformed and less symmetric. As a result, the ferroelectric phase exhibits spontaneous polarisation and strain. Due to the misfit of the distinct variants of the unit cells, the microstructure becomes mechanically stressed and electrically charged and hence twinned in order to reduce mechanical constraints and electric depolarisation fields [5, 6].

In poly-crystalline piezoelectrics, the domains of uniform spontaneous polarisation and strain are oriented randomly at the as-sintered state. Viz., no macroscopic piezoelectric behaviour is observable. Because of the ferroic nature of the material, it is possible to force permanent alignment of the different domains using a strong electrical field ($>1\,\mathrm{MV/m}$), the so-called poling process. In such case, the ceramic behaves now as a piezoelectric, and the material is remanently polarised and remanently strained. (In general the deflection caused by the poling process is a multiple of the stroke during application.) The "poled state" of the material can be modified by exceeding its electrical, mechanical and thermal limits [5–7]. Please consider that this is also true for real piezoelectric devices [2, 8].

Commercial low-voltage multilayer piezoelectric actuators are designed as stacks of thin PZT-ceramic layers with interdigitated Ag/Pd- or Cu-electrodes in between. The typical thicknesses of such ceramic layers are slightly below $100\,\mu\mathrm{m}$, whereas those of the electrodes are only one fortieth in average (i.e. $\sim 2\,\mu\mathrm{m}$) [4]. Akin to multilayer capacitors, the inner structure of multilayer actuators is divided into an active zone, with inner electrodes of mutual polarities, and into an inactive zone around the outer electrodes, the so-called isozone (Fig. 1).

These layered structures (so-called stacks) enable the achievement of high electrical field strengths causing large material displacements with relative low voltages [3]. For example, the electrical field strength for multilayer actuators with layer thicknesses of approximately $80\,\mu\mathrm{m}$ and an external applied voltage of $160\,\mathrm{V}$ is $2\,\mathrm{MV/m}$. Characteristic corresponding strains are in the order of 0.1%. Viz., the elongation for typical multilayer actuators length of $40\,\mathrm{mm}$ is about $40\,\mu\mathrm{m}$. The resulting stroke, which is important for their technical application, is associated with the nonlinear ferroic effects, such as ferroelectricity and ferroelasticity.

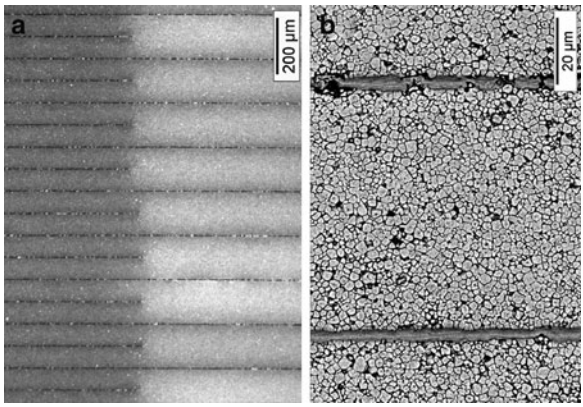

Fig. 1 A section of a multilayer actuator with vertical poling axis. The design of the inner electrodes is shown in (**a**) as well as in the very fine microstructure and the Ag/Pd-electrode. A detail of (**a**) is shown in (**b**)

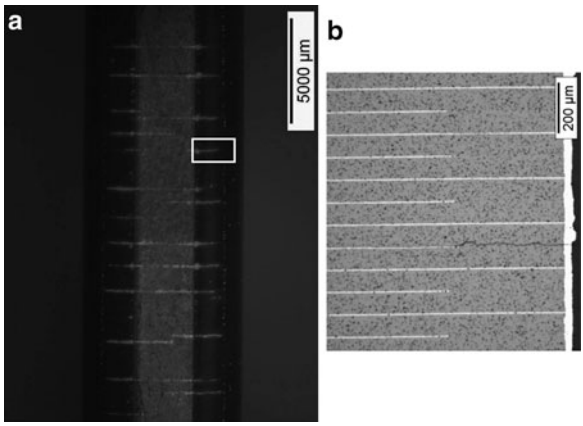

Fig. 2 Due to the poling process plenty of cracks are induced within the multilayer actuator. A fluorescent colour penetrates the cracks and becomes visible under an UV-lamp (**a**). The cracks are prone to concentrate around very sharp electrode tips; a detail of (**a**) is captured in (**b**)

In summary, the key feature of such piezoelectric components is the use of the inverse piezoelectric effect [9]; namely the low voltage is transformed into a relative large mechanical strain. Due to their specific design (a layered structure with interdigitated metallic electrodes in between, cf. Fig. 1) a strain misfit results between the field-free isozone and the inner active zone during poling and also in service. The hindered strains locally yield relative high mechanical stresses [6, 10, 11]. In order to relief these mechanical stresses cracks may appear, which are prone to concentrate at the infinitely sharp electrode tips because of very local field enhancements [12, 13] (Fig. 2).

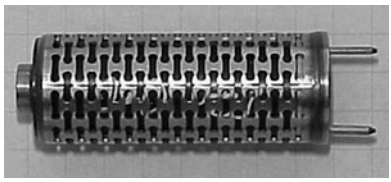

Fig. 3 The multilayer actuator is mounted into a well defined clamp spring and pre-stressed in order to delay such time dependent phenomena like degradation, fatigue and subcritical crack growth

In service, the actuating-process is soever a result of the periodic reorientation of the piezoelectric crystals (domain switching). During this process, cyclic inelastic deformation and weak self heating occur. These effects may lead to periodic tensile stresses concentrated around the electrode-tips or pores. Such cyclic loading can favour degradation [14], fatigue and subcritical crack growth [15–17] in the very brittle piezo-ceramic [18, 19], thus affecting the structural and functional integrity of the multilayer actuator.

In order to decrease the harmful influence of electrical field enhancements and tensile stresses on the component's lifetime, the multilayer actuator is mounted into a very well designed clamp spring and slightly pre-stressed (in compression) [9]. Due to this mechanical clamping when mounting the actuator into the spring (Fig. 3), the reservoir of switchable domains – the resulting switching strain – is also affected [20].

During the actuating process, on the one hand the component's behaviour is dominated by the nonlinear ferroelectric effect. The multilayer actuator is subjected to strong electrical field strength as driving force for domain-switching processes. On the other hand, when no external electrical field is applied, its behaviour is dominated by ferroelastic effects (the relaxation of domains) [21].

For application purposes a detailed knowledge of the coupled phenomena among the field-type quantities mechanical stress and electrical field is absolutely necessary to boost the actuator performance (i.e. the achievement of high switching strains under the presence of compressive stresses) [2, 9]. Their functionality is associated with the loading conditions as well as with the actuator design and in-service electro-mechanical reliability. Thus, it is of great importance to find an optimum between the applied bias-stress (mechanical clamping) and the achievable switching strain during the unipolar electrical loading.

2 Experimental Procedures

2.1 Material of Study

Commercially available PZT-based multilayer actuators with dimensions of approximately $7.5 \times 7.5 \times 40\,\text{mm}^3$ have been used in the experiments. The device

itself consists of a stack of *circa* 450 piezo-ceramic layers (∼80 μm thick) with interdigitated electrodes in between (∼2 μm). The width of the isozone is one tenth (i.e. around 800 μm) of the lateral length.

The piezo-ceramic material is an Nd_2O_3-$PbTiO_3$-$PbZrO_3$ ternary phase system incorporating approximately 2–3% of the rare-earth oxide [4] on the tetragonal side of the morphotropic phase boundary of PZT. The rare earth Neodymium in the composition acts as a donor to make the material "soft" [7] and stabilises the piezoelectric properties in the automotive temperature range, i.e. from −50 °C up to +150 °C [21]. The electrode material is a silver/palladium alloy, incorporating 70% Ag and 30% Pd.

2.2 Setup of the Smart Materials Testing Machine

The electro-mechanical characterisation has been performed using a universal testing machine (UTM), MIDI 25–5 $7 \times 13,''$ from Messphysik, Austria. An adaptation of this UTM enables the measurement of both mechanical quantities such as mechanical stresses and the corresponding strains, as well as electrical quantities such as charge flux (or polarisation) and the applied voltage (or electrical field strength) to the multilayer actuator [22].

The use of a controller (type Doli EDC 580) in the UTM facilitates the processing of additional data feed via extra input lines. Additional measurement equipment is connected to the EDC. A computer equipped with a data acquisition board and a material testing software, also provided by Messphysik, is used to control the UTM. Simultaneously the high-voltage power supply provides a monitor signal which corresponds to its output voltage. All equipment output signals are first passed through insulated dc input/output signal-conditioning modules and then digitally recorded.

The electric displacement – the charge flux – can be measured by a modified Sawyer–Tower circuit. A high input resistance electrometer (type Keithley 6514) is employed to monitor voltage fluctuations across 600 μF reference capacitors connected in series with the specimen. The charge is calculated by means of the known capacity and the measured voltage drop of the capacitors. A detailed description can be found in [7].

For the strain measurements, the multilayer actuator is mounted at the centre of circular ceramic plates, cf. Fig. 4. Three versatile strain transducers (type HBM DD1) are used to measure the induced actuator stroke, by tracking the position of three different points of the circular plate located 120° apart. The outcome of the average value of the transducers indicates the total displacement of the multilayer actuator.

The accuracy of the charge- and strain-measurement corresponds to a relative error less than 1%.

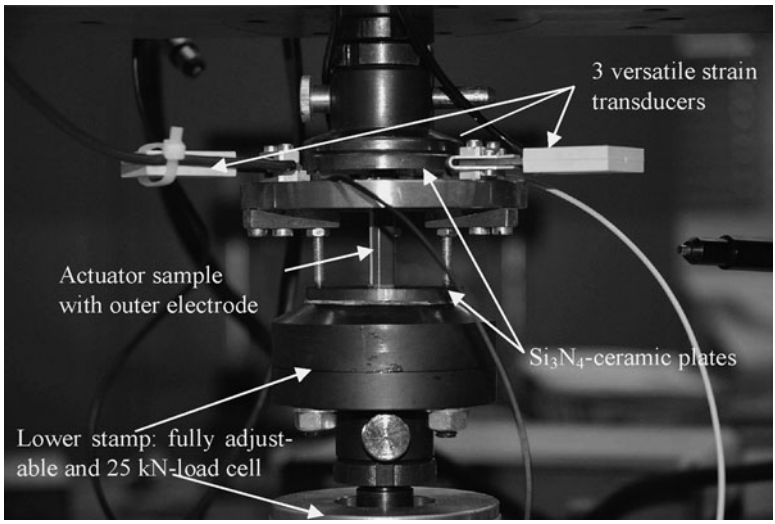

Fig. 4 Sample fixture during the measurement. Three versatile strain transducers are used to assess the actuator stroke, by tracking the position of three different points of the upper circular plate located 120 degree apart. For the simulation of real loading conditions a spring system (with the same 120°-arrangement of the springs and spring constants of 1 N/μm) has been assembled onto the lower stamp to modify the stiffness of the smart materials testing machine

2.3 Sample Fixture

The multilayer piezo-actuator is mounted into a uniaxial compression test configuration. The pressure plate at the bottom is fixed; the upper plate enables a spherical alignment relative to the fixed one. Both plates are made of a Si_3N_4-ceramic. This setup is used to measure the stiffness of the actuators. In order to measure the piezoelectric (voltage) coefficients, a unique spring system (with a 120°-arrangement of the springs and spring constants of 1 N/μm) has been used to modify the stiffness of the smart materials testing machine to realistic (combustion engine) conditions.

2.4 Measurements

The experiments were performed on initially non-poled (i.e. virgin piezo-ceramic material) and poled specimens, respectively; full cycles of ramp-shaped electric field strengths (up to 2 MV/m in magnitude or higher) were applied to the sample under different axial compressive preloads. Two properties of the multilayer actuator were measured: the effective piezoelectric voltage constants in actuation direction at distinct electrical loadings and pre-stresses, and the stroke at different electromechanical loading scenarios.

3 Results and Discussion

The actuator performance can be assessed by either a "step by step" – or a continuous approach. The first is conducted as follows: The multilayer stack is mechanically pre-loaded (pre-stressed) and subsequently electrically loaded (three times unipolar cycled up to 200 V, i.e. 2.5 MV/m), while the mechanical load is held constant. As result the deflection and effective piezoelectric voltage constant, d_{33}, of the multilayer actuator – the slope of the stroke-voltage-hysteresis, Fig. 5a – can be assessed for each mechanical pre-load. The plot of the (mean value of the) effective piezoelectric voltage constant versus the mechanical clamping stress in Fig. 5b

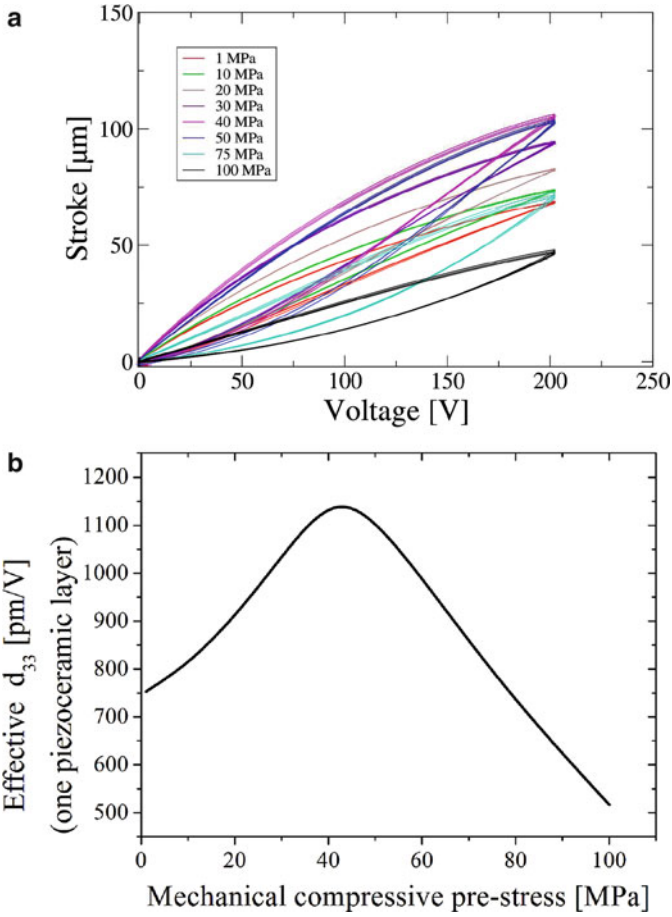

Fig. 5 The stroke of the pre-stressed actuator; assessed from quasistatic measurement with an electrical loading frequency of 0.1 Hz (**a**). The effective piezoelectric voltage constant is the slope between 0–200 V. The measurements in (**b**) show that there is a maximum performance at a slightly pre-stressing of about 40 MPa (high $d_{33,eff}$ and moderate hysteretic losses)

shows a significant increase in the magnitude from 750 up to 1,150 pm/V (for only one piezo-ceramic layer). An increase of approximately 50% in the performance is achievable, when pre-stressing the piezo-actuators. The maximum performance appears at the pre-stress range of around 30–40 MPa (with relative low hysteretic losses).
At excessive pre-stresses the performance decreases dramatically, because the mechanical load hinders the domains to align into the electrical field direction.

Furthermore their lifetime may also increase because of lowering the amplitudes of the field enhancements around the electrode tips, for instance. This procedure is very time-consuming.

The second – the continuous approach – is more time efficient. Therefore, the multilayer piezoelectric actuator employed for this measurement was first poled with unipolar electrical field strength in the order of approximately 2 MV/m at room temperature. The initially non-preferentially orientated domains are forced to align into the direction of the external applied electrical field strengths, so that the piezo-actuator is remanently polarised and strained. The device now behaves macroscopically as piezoelectric.

After this poling process, the multilayer actuator was then continuously driven by a unipolar sinusoidal voltage and simultaneously mechanically stressed. The clamping force, at the beginning −200 N, is steadily increased up to −4000 N with a constant loading rate of 1 N/s. Compared to the frequency of the superposed sinusoidal voltage, i.e. 1 Hz – this is very slow. Figure 6 shows the experimental relation between the stroke, i.e. the switching strain, of a multilayer actuator and the clamping force (the so-called "actuator-performance").

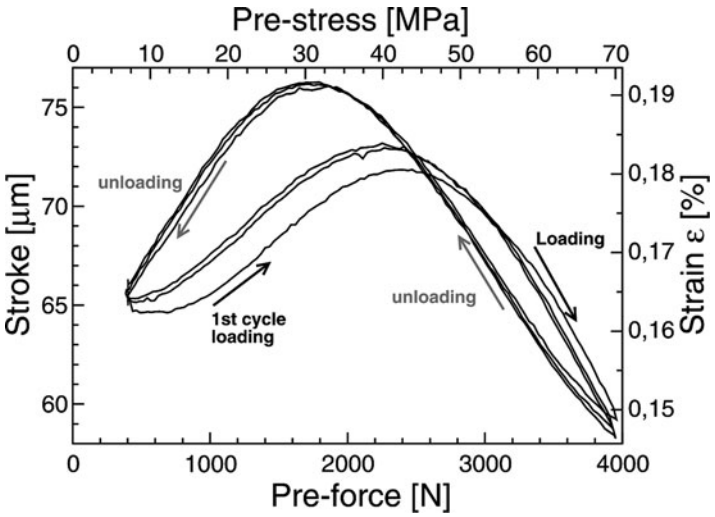

Fig. 6 The so-called continuous approach to measure the performance of a multilayer actuator

After the maximum force is reached, the clamping force is again reduced down to −200 N (see Fig. 6 "unloading"). This procedure is repeated three times to ensure reproducibility. It can be deduced from the referred figure that the first loading process always differs from the subsequent loading steps, due to the transient behaviour of such adaptive materials [cf. 7, 20]. Within this loading range, the piezoelectric effect on the one hand and the ferroelectric and ferroelastic effect on the other hand, contribute together to the total stroke of the stack in distinct quantities. This characteristic yields strokes from a minimum up to nearly 80 μm in magnitude (i.e. a strain of about 0.2%). The maximum performance (loading branch) also appears at a pre-stress of circa 40 MPa. This agrees with the findings of the so-called "step by step"-approach.

Furthermore, two maximum stroke values corresponding to the loading and unloading process can be observed, respectively. Due to a moderate pre-stressing of the actuator, the reservoir of switchable domains increases because of their alignment perpendicular to the external applied mechanical load, yielding higher strokes and a better actuator-performance. In this regard, relative large compressive forces lead to a partial de-poling of the PZT-material because the unfavourably orientated domains are prone to switch perpendicular to the sufficiently strong externally applied mechanical load in order to reduce the mechanical stresses [23]. When these mechanical stresses are lowered, the increased reservoir of switchable domains can be used during the actuating process [cf. 20]. At excessive mechanical stresses, however, the ferroelastic effect dominates the ferroelectric effects and the values of the stroke diminish significantly.

Therefore, the performance of multilayer actuators is strongly dependent on both nonlinear ferroic effects such as ferroelectricity and ferroelasticity.

4 Conclusions

The adaptation of the universal testing machine has enabled the measurement of mechanical stress, the corresponding strain, electrical charge (or polarisation) and the applied voltage within a multilayer piezoelectric actuator. The stiffness, dielectric hysteresis, "butterfly loop" and the "performance" have been determined. The measured data is very useful for multilayer actuator manufacturers, because it helps them to assess (and boost) the performance of their products.

In future investigations the impact of the third influencing quantity, the temperature, on the actuator's performance will be assessed by an integration of a temperature chamber into the test facility to characterise these components under fully coupled thermo-electrical-mechanical loading scenarios.

Acknowledgments Financial support by the Austrian Federal Government (in particular from the Bundesministerium für Verkehr, Innovation und Technologie and the Bundesministerium für Wirtschaft und Arbeit) and the Styrian Provincial Government, represented by Österreichische Forschungsförderungsgesellschaft mbH and by Steirische Wirtschaftsförderungsgesellschaft mbH, within the research activities of the K2 Competence Centre on "Integrated Research in Materials,

Processing and Product Engineering," operated by the Materials Center Leoben Forschung GmbH in the framework of the Austrian COMET Competence Centre Programme, is gratefully acknowledged.

The authors thank furthermore Mr. Athenstaedt W, Mr. Auer C and Mr. Hoffmann C for critical discussions and the company EPCOS OHG, Deutschlandsberg, Austria, for providing the material for this investigation.

References

1. Uchino K (1997) Piezoelectric actuators and ultrasonic motors. In: Tuller HL (ed) Electronic materials: science and technology, Kluwer Academic Publishers
2. Mock R, Lubitz K (2009) Piezoelectric injection systems. In: Heywang W, Lubitz K, Wersing W (eds) Piezoelectricity. Evolution and future of a technology, vol 114. Springer Series in Materials Science
3. Setter N (2002) Piezoelectric materials in devices. Ceramics Laboratory, EPFL Swiss Federal Institute of Technology, Ljubljana
4. Helke G, Lubitz K (2009) Piezoelectric PZT ceramics. In: Heywang W, Lubitz K, Wersing W (eds) Piezoelectricity. Evolution and future of a technology, vol 114. Springer Series in Materials Science
5. Bhattacharya K, Ravichandran G (2003) Ferroelectric perovskites for electromechanical actuation. Acta Mat 51:5941–5960
6. Kamlah M (2001) Review article – ferroelectric and ferroelastic piezoceramics – modelling of electromechanical hysteresis phenomena. Continuum Mech Thermodyn 13:219–268
7. Zhou DY (2003) Experimental investigation of non-linear constitutive behavior of PZT piezoceramics. Ph.D.-thesis, University of Karlsruhe
8. Mitrovic M, Carman GP, Straub FK (2001) Response of piezoelectric stack actuators under combined electro-mechanical loading. Int J Solids Struct 38:4357–4374
9. Arnold S, Pertsch P, Spanner K (2009) Piezoelectric Positioning. In: Heywang W, Lubitz K, Wersing W (eds) Piezoelectricity. Evolution and Future of a Technology, vol 114. Springer Series in Materials Science
10. dos Santos e Lucato SL, Lupascu DC, Kamlah M, et al (2001) Constraint-induced crack initiation at electrode edges in piezoelectric ceramics. Acta Mat 49:2751–2759
11. Elhadrouz M, Ben Zineb T, Patoor E (2006) Finite element analysis of a multilayer piezoelectric actuator taking into account the ferroelectric and ferroelastic behaviors. I J Eng Sci 44(15–16):996–1006
12. Aburatani H, Harada S, Uchino K, et al (1994) Destruction mechanisms in ceramic multilayer actuators. Jpn J Appl Phys 33:3091–3094
13. Furuta A, Uchino K (1993) Dynamic observation of crack propagation in piezoelectric multilayer actuators. J Am Ceram Soc 76:1615–1617
14. He M-Y, Suo Z, McMeeking RM, et al (1994) The mechanics of some degradation mechanisms in ferroelectric ceramic actuators. Proc. SPIE 2189:344–355
15. Ru CQ, Mao X, Epstein M (1998) Electric-field induced interfacial cracking in multilayer electrostrictive actuators. J Mech Phys Solids 46(8):1301–1318
16. Mao GZ, Fang DN (2004) Fatigue crack growth induced by domain switching under electromechanical load in ferroelectrics. Theor Appl Fract Mech 41:115–123
17. Salz CRJ, Hoffmann M, Westram I, Rödel J (2005) Cyclic fatigue crack growth in PZT under mechanical loading. J Am Ceram Soc 88:1331–1333
18. Bermejo R, Grünbichler H, Kreith J, Auer C (2009) Fracture resistance of a doped PZT ceramic for multilayer piezoelectric actuators: Effect of mechanical load and temperature. J Eur Ceram Soc. doi:10.1016/j.jeurceramsoc.2009.08.013

19. Bermejo R, Grünbichler H, Kreith J, Danzer R (2008) Evaluation of toughness anisotropy of doped PZT ceramics as a function of load and temperature. In: Pokluda J, Lukáš P, Šandera P, Dlouhý I (eds) Proceedings of the 17th european conference on fracture, VUTIUM Brno, pp 1701–1708
20. Kerkamm I, Hiller P, Granzow T, Rödel J (2009) Correlation of small- and large-signal properties of lead zirconate titanate multilayer actuators. Acta Mat 57:77–86
21. Grünbichler H, Kreith J, Bermejo R, et al (2009) Modelling of the ferroic material behaviour of piezoelectrics: characterisation of temperature-sensitive functional properties. J Eur Ceram Soc. doi:10.1016/j.jeurceramsoc.2009.04.033
22. Kreith J, Grünbichler H, Bermejo R, et al (2008) Adaptation of a materials testing machine to characterise piezoelectric actuators. In: Freer R (ed) Proceedings of electroceramics XI, Manchester
23. Wersing W, Heywang W, Beige H, Thomann H (2009) The role of ferroelectricity for piezoelectric materials. In: Heywang W, Lubitz K, and Wersing W (eds) Piezoelectricity. Evolution and future of a technology, vol 114. Springer Series in Materials Science

This page intentionally left blank

Roles of Micro-cracking and Phase Transition on Electric Fatigue for [001]-Oriented $Pb(Mg_{1/3}Nb_{2/3})O_3$-$PbTiO_3$ Single Crystals

F. Fang, W. Yang, and X. Luo

Abstract In-situ observations of microstructure and polarization degradation under cyclic electric loadings are carried out for [001]-oriented $Pb(Mg_{1/3}Nb_{2/3})O_3$-$PbTiO_3$ ferroelectric single crystals. Direct evidences of the effects of micro-cracking and phase transition on the polarization degradation are revealed. Upon cyclic electric loading with a comparatively low field magnitude, there is no phase transition while the propagation of micro-cracks significantly reduces the polarization. When electric loading is cycled under a high field magnitude, the single crystal transforms from a rhombohedral phase to a monoclinic phase. Both micro-cracking and phase transition inhibit ferroelectric domain switching and reduces the number of electric dipoles that can efficiently switch their orientation under cyclic electric field. The phase transition degrades the polarization to a greater degree than do the micro-cracks. The findings are of importance concerning the long-term reliability of the high performance PMN-PT single crystals.

1 Introduction

Ferroelectrics are widely used in current technologies, such as actuators, sensors, and memory devices. Recently, PMN-PT Single crystals have been extensively studied because of their outstanding piezoelectric and ferroelectric properties. It was reported that ultrahigh strain ($>1.0\%$), along with high electromechanical coupling ($k_{33}>90\%$) and low hysteresis could be achieved for $<001>$ oriented rhombohedral crystals close to the morphotropic phase boundary (MPB) [1, 2]. The application

F. Fang (✉) and X. Luo
AML, School of Aerospace, Tsinghua University, Beijing 100084, China
e-mail: fangf@mail.tsinghua.edu.cn

W. Yang
AML, School of Aerospace, Tsinghua University, Beijing 100084, China
Zhejiang University, Hangzhou 310058, China

M. Kuna and A. Ricoeur (eds.), *IUTAM Symposium on Multiscale Modelling of Fatigue, Damage and Fracture in Smart Materials*, IUTAM Bookseries 24,
DOI 10.1007/978-90-481-9887-0_24,

of the single crystals caused breakthrough in ultrasonic transducer materials and devices [3]. The mechanisms underlying the ultrahigh performance of the single crystals are mainly attributed to the rotation of polarization vectors and coexistence of multi-phases [4–10].

Ferroelectrics are typically subjected to electric, mechanical, or combined electro-mechanical loads. Under cyclic electric loadings, ferroelectrics are susceptible to electric fatigue, which reflects the polarization degradation with electric cycles. Electric fatigue not only causes the loss of memory function, but also reduces the piezoelectric effect, and causes the actuators to function improperly [11]. Various mechanisms have been proposed to interpret the fatigue behavior, such as micro-cracking [12–16], domain wall pinning by point-defect agglomeration [17–21], and non-switchable interfacial layer [12, 15, 20].

Due to the intrinsic brittleness of ferroelectrics, the fracture toughness is in the order of 1 MPa$\sqrt{m}$ and micro-cracks are prone to nucleate and to propagate under both static and cyclic electric loadings [22]. Early studies demonstrated that cracks were found to initiate near the internal electrode edges and propagate toward the interior of the ferroelectric material for multi-layer actuators [23]. For ferroelectric ceramics, cracks were found predominantly to grow in a direction normal to the applied electric field, or along the grain boundaries [24–27]. For ferroelectric single crystals, apart from the applied electric field direction, the material aspects, such as crystallographic fracture anisotropy and non-180° domain boundary structure, play an important role in the crack propagation path [28]. Recently, we reported that in PMN-PT single crystal, the crack propagation deviated from its original path after the occurrence of phase transition from rhombohedral (R) to tetragonal (T) phase [29].

Compared with the normal ferroelectrics, PMN-PT single crystals near MPB exhibit more complex domain boundary structures due to multi-phase phase coexistence under the applied electric loading [7,8,30,31]. Besides, micro-cracks are more prone to occur in single crystals because of the high value of electric-field-induced strain. Though many studies were carried out on fatigue crack growth [28,29,32–34] and phase transition under the applied electric loadings [7,8,11,30,31] for PMN-PT single crystals, in-situ studies on the interaction between the microstructure evolution, such as micro-cracking or phase transition, and the polarization degradation behavior are rare. This paper intends to provide direct evidence of the close relationship between the microstructure evolution and the polarization degradation behavior. The results are of significance in understanding the long-term performance of the PMN-PT single crystals.

2 Experimental Procedures

PMN-PT single crystals were grown directly from the melt by a modified Bridgman technique [35]. Nominal composition of $0.74Pb(Mg_{1/3}Nb_{2/3})O_3$-$0.26PbTiO_3$ (PMN-26PT) were used. The samples were edge oriented parallel to <001> by

using an x-ray diffractometer. The orientation in this paper is based on the axis of prototype cubic phase of perovskite structure.

The samples were cut and polished into a size of approximately $0.2 \times 5 \times 5\,\text{mm}^3$. Semi-transparent gold electrodes were sputtered on the top and the bottom surfaces ($5 \times 5\,\text{mm}^2$) of the samples, and silver leads were attached to the electrodes with air-dry silver paste. That allows the application of out-of-plane electric fields to the single crystal samples. A high voltage power supply consisting of a function generator (TTI-TG1010, by Thurlby Thandar Instruments Ltd., UK) and a voltage amplifier (Trek-610E-K-CE, by Trek Inc., USA) were used to apply both static and alternating electric fields to the single crystal specimens. The ac field has a sinusoidal wave form, with a fixed frequency of 5 Hz.

For the samples with the nominal composition of PMN-26PT, both x-ray diffraction and optical microscope observations revealed the *R* phase nature of the sample. Thus, PMN-26PT sample was directly subjected to cyclic electric field without previous poling. It was first subjected to the cyclic electric loading with a field magnitude of 2.5 kV/cm. After 200,000 electric cycles, it was further subjected to the cyclic electric loading with a much higher field magnitude, 5 kV/cm.

In order to prevent electric breakdown, the specimens were immersed in a silicon oil tank made of transparent and insulating Plexiglas during electric loading. An Olympus optical microscope with a video imaging system was used to observe and to record changes in the domain configuration, as well as the initiation and propagation of micro-cracks. All the micrographs were taken under the cross-polarized light where the polarizer (designated as "*P*") was set at 90° with respect to the analyser (designated as "*A*"). At the same time, the polarization hysteresis loops ($P - E$ curves) at different number of cycles were measured using the Sawyer–Tower technique. All the tests were performed at room temperature.

3 Results and Discussions

3.1 Effects of Micro-cracking on Polarization Degradation

The single crystal sample of PMN-26PT was directly subjected to cyclic electric loadings without previous poling. The initial sample belongs to *R* phase because it exhibits optical extinction along <110> directions. Figure 1a shows the initial morphology of the PMN-26PT single crystal sample when the polarizer is set at an angle of 0° with respect to the [010] direction. It was first subjected to cyclic electric loading with the field magnitude of 2.5 kV/cm for 200,000 electric cycles. The sample was then further subjected to cyclic electric field with the magnitude of 5 kV/cm, again for 200,000 cycles.

Under a field magnitude of 2.5 kV/cm, in-situ observations demonstrated apparent micro-cracking at the very beginning Shown in Fig. 1(b) is the crack morphology

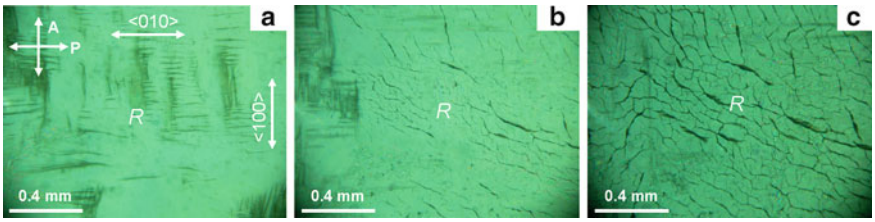

Fig. 1 Formation of micro-cracks for PMN-26PT single crystal under cyclic electric loading at a field magnitude of 2.5 kV/cm: (**a**) 0, (**b**) 2,500, and (**c**) 200,000 electric cycles. The applied electric field direction is normal to the plane

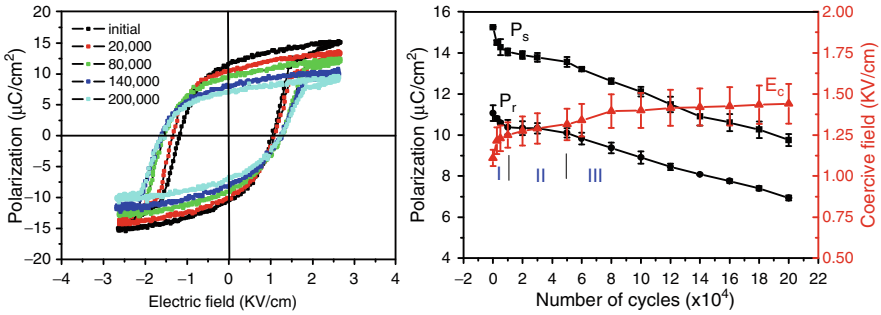

Fig. 2 (**a**) Polarization hysteresis loops under different number of cycles, and (**b**) P_r, P_s, and E_c *vs* number of cycles (N) for PMN-26PT single crystal at a field magnitude of 2.5 kV/cm

after 2,500 cycles. As the number of cycles increases, the micro-cracks increase in quantity and become broader and deeper. After about 10^4 cycles, no distinct change is found in crack morphology. Shown in Fig. 1c is the crack morphology for the PMN-26PT single crystal electrically cycled at a field magnitude of 2.5 kV/cm for 2×10^5 cycles. There is no phase transition during this electric cycling process.

Shown in Fig. 2a are the polarization loops under different number of cycles for PMN-26PT single crystal. At a field magnitude of 2.5 kV/cm, the polarization loops are already quite squared. The values of E_c, P_r and P_s for the initial sample are 1.1 kV/cm, 11.1 $\mu C/cm^2$ and 15.2 $\mu C/cm^2$. As the number of cycles increases, P_r and P_s decrease, while E_c increases, as shown in Fig. 2b. The P_r (or P_s) versus N curve can also be divided into three stages: stage *I* from 0 to 10^4 cycles with a rather steep slope; stage *II* from 10^4 to 5×10^4 cycles with a smooth one; and stage *III* from 5×10^4 to 2×10^5 cycles, again with a comparatively steep slope. The degradation rate of P_r per 10^4 cycles of these three stages can be estimated as follows:

$$k_{P_r}^{0-10,000} = 0.8\ \mu C/cm^2 \cdot 10^4 \text{ cycles}$$
$$k_{P_r}^{10,000-50,000} = 0.08\ \mu C/cm^2 \cdot 10^4 \text{ cycles}$$
$$k_{P_r}^{50,000-200,000} = 0.21\ \mu C/cm^2 \cdot 10^4 \text{ cycles}$$

Combining the in-situ optical microscope observation and the polarization degradation, one concludes that the polarization deteriorates rapidly during the period of crack initiation and propagation (stage *I* in Fig. 2b). The polarization degrades at comparatively low rates when there is no distinct crack morphology change (stage *II* in Fig. 2b).

The mechanism of micro-cracks on the electric fatigue was previously reported by Arias et al. [12], Nuffer et al. [14], and Lupascu et al. [15]. The mechanical displacement and electric-potential discontinuity [12], as well as concentration of defects at the micro-cracks [14,15] could pin the movement of domain walls. Therefore, micro-cracks act as the trapping sites that pin the electric dipoles. Accordingly, with the nucleation and propagation of micro-cracks, the number of dipoles that can switch orientation repeatedly under an applied electric field will decrease, resulting in a corresponding decrease of the polarization. Due to the effective locking of domains around the micro-cracks, E_c increases during crack emanation process, which is evidenced in both Fig. 2b. Apart from the polarization degradation caused by micro-cracking, other electric fatigue mechanisms may act at certain degrees. For example, the occurrence of the stage *III* in Fig. 2b should be related to other electric fatigue mechanism, such as non-switchable interfacial layer close to the electrodes [12,15,20].

Three competing mechanisms dictate the crack propagation path: they are (1) concentrated electric field depending on the external electric field direction, (2) the fracture anisotropy, and (3) the incompatible strain caused by non-180° domain boundaries [28]. In our experimental setup, however, the applied electric field is normal to the sample plane. Accordingly, the main plane is isotropic and the direction of the applied electric field would have no effect on the crack propagation path. For PMN-26PT single crystal, it starts with the *R* phase. Accordingly, there are eight equivalent polarization variants along <111> crystallographic directions prior to electric cycling. Under the cyclic electric field, the domain variants are reduced to the four aligned with the applied field direction, i.e, they are in the engineered domain state. Either two adjacent domains of the four can form domain walls in [100] or [010] directions. Previous transmission electron microscopies revealed polar nanodomains of several hundred angstroms in size for PMN-xPT when $x < 0.3$ [36]. Therefore, the domain boundary bears less effect on the crack propagation behavior than that in PMN-32PT where apparent domain boundaries can be observed under optical microscope (Fig. 1). Besides, Vicker's indentations have revealed that the cleavage planes for rhombohedral PMN-PT single crystals are {110} [28]. As a result, the competition between domain boundary effect and fracture anisotropy dictates the observed crack patterns for PMN-26PT as shown in Fig. 1b, c.

3.2 Effects of Phase Transition on Polarization Degradation

The PMN-26PT single crystal was later subjected to additional cycling at a much higher field magnitude: 5 kV/cm. Figure 3a shows the initial crack morphology and

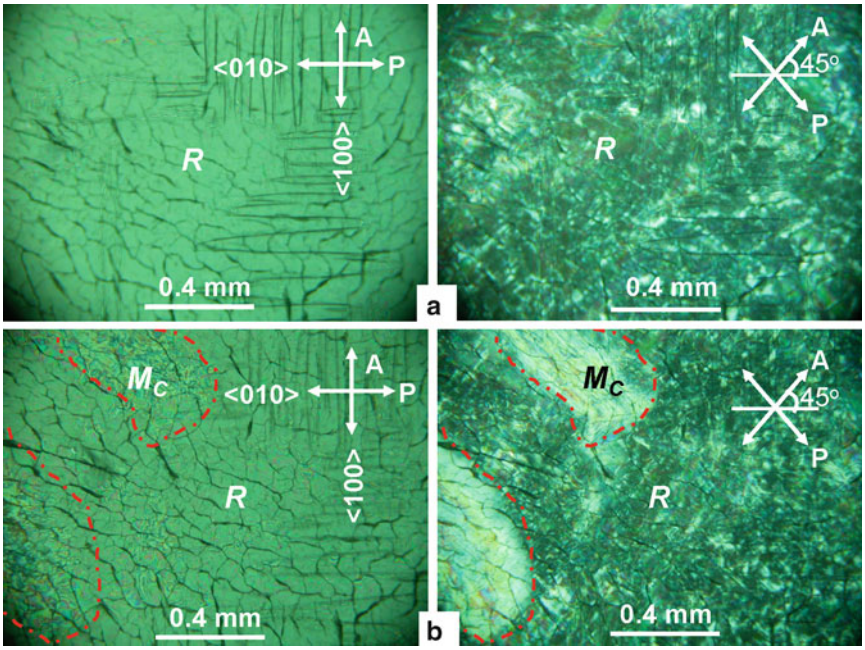

Fig. 3 Crack morphology and domain patterns (**a**) prior to and (**b**) after cyclic electric loading at a field magnitude of 5 kV/cm for 5,000 cycles. The micrographs in the left- and right-hand side are taken when the polarizer is set parallel to [010] and [110] directions, respectively

domain patterns prior to the electric cycling at 5 kV/cm. The single crystal sample is still of *R* phase but with apparent domain boundaries, indicating the growth of domains during the initial electric cycling at a field magnitude of 2.5 kV/cm. In-situ observation demonstrates that phase transition from *R* to *M* takes place after 5,000 cycles, as shown in Fig. 3b. Since the contoured regions show no optical extinction along either <010>, or <110> direction, they should belong to a monoclinic (*M*) phase. The contoured regions can be designated as *M*c phase since they have exactly the same morphology as that we previously reported in Ref. [37] as the field cycles further, the morphology remains unchanged till 200,000 cycles.

Shown in Fig. 4a are the polarization loops under different number of cycles for PMN-26PT single crystal at a field magnitude of 5 kV/cm. The P_r, P_s and E_c versus N curves are shown in Fig. 4b. The same trend that P_r and P_s decrease while E_c increases with the cycles can be found. The P_r (or P_s) versus N curve can be roughly divided into two stages: stage *I* from 0 to 5,000, and stage *II* from 5,000 to 200,000 cycles. The degradation rate of P_r per 10^4 cycles of these two stages can be estimated as follows:

$$k_{P_r}^{0-5,000} = 4.4\mu C/cm^2 \cdot 10^4 \text{cycles}$$
$$k_{P_r}^{5,000-200,000} = 0.1\mu C/cm^2 \cdot 10^4 \text{cycles}$$

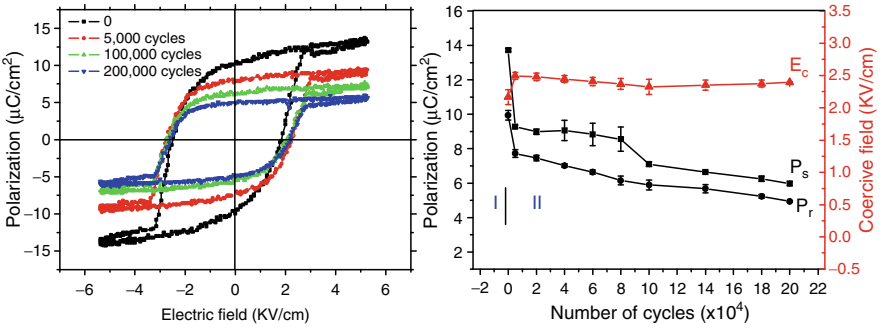

Fig. 4 (**a**) Polarization hysteresis under different number of cycles, and (**b**) P_r, P_s, and E_c *vs* the number of cycles for PMN-26PT single crystal at a field magnitude of 5 kV/cm

Since neither the temperature nor the composition of the sample has changed, the phase transition might be caused by a significant accumulation of residual strain. The phase transition would cause abrupt decrease of the polarization, in a much larger extent than that of micro-cracking. If the mixture law is adopted, one has

$$P_r = (1 - f)P_r^R + fP_r^M \tag{1}$$

where f denotes volume fraction of M_C phase, P_r is total polarization of the single crystal sample, with the superscripts R and M labeling the rhombohedral and monoclinic phases. Dipoles in domains of R phase can easily reorient and their domain walls are of higher mobility due to the engineered domain state under cyclic electric field. The observation that [001]-oriented rhombohedral $Pb(Zn_{1/3}Nb_{2/3})O_3$-$PbTiO_3$ (PZN-PT) single crystal has a high domain mobility was previously reported by Takemura et al. [21]. Therefore, phase transition from R to M_C limits the domain wall mobility, reduces the number of effective dipoles that can reorient upon reversals of cyclic electric field, and leads to dramatic increase of the coercive field while decrease of the polarization.

4 Conclusions

In-situ observations of microstructure evolution and polarization degradation under cyclic electric loading are carried out for PMN-PT single crystals. The results demonstrate that in the absence of phase transition, initiation and propagation of micro-cracks play an important role in the polarization degradation. Emanation and propagation of micro-cracks are the result of the competition between the incompatible strain around the non-180° domain boundaries and the fracture anisotropy under electric field. When the phase shifts from R to M_C, the polarization shows a dramatical decrease, in a much larger drop than that of micro-cracking. Both

micro-cracks and phase transition limit the domain wall mobility, and reduce the number of effective dipoles that can switch their orientation under cyclic electric field. Consequently, the polarization decreases while the coercive field increases dramatically during the process of micro-cracking and phase transition.

Acknowledgements The authors would like to thank the supports from the National Natural Science Foundation through the Grant Number 10772090 and from the National Key Projects for Basic Researches (973). The authors express sincere thanks to Prof. H. S. Luo in Shanghai Institute of Ceramics, Chinese Academy of Sciences, for providing us the single crystal samples.

References

1. Park SE, Shrout TR (1997) Ultrahigh strain and piezoelectric behavior in relaxor based ferroelectric single crystals. J Appl Phys 82:1804–1811
2. Liu S, Park SE, Shrout TR, Cross LE (1999) Electric field dependence of piezoelectric properties for rhombohedral $0.955Pb(Zn_{1/3}Nb_{2/3})O_3$-$0.045PbTiO_3$ single crystals. J Appl Phys 85:2810–2814
3. Chen J, Panda R (2005) Commercialization of piezoelectric single crystals for medical imaging applications. IEEE international ultrasounics symposium proceedings, Rotterdam, The Netherlands, 18–21 Sept, pp. 235
4. Fu H, Cohen RE (2000) Polarization rotation mechanism for ultrahigh electromechanical response in single-crystal piezoelectrics. Nature 403:281–283
5. Vanderbilt D, Cohen MH (2001) Monoclinic and triclinic phases in higher-order Devonshire theory. Phy Rev B 63:094108
6. Ye ZG, Noheda B, Dong M, Cox D, Shirane G (2001) Monoclinic phase in the relaxor-based piezoelectric/ferroelectric $Pb(Mg_{1/3}Nb_{2/3})O_3$–$PbTiO_3$ system. Phy Rev B 64:184114
7. Noheda B, Cox DE, Shirane G, Gao J, Ye ZG (2002) Phase diagram of the relaxor (1-x) $Pb(Mg_{1/3}Nb_{2/3})O_3$–$xPbTiO_3$. Phys Rev B 66:054104
8. Noheda B, Cox DE, Shirane G, Park SE, Cross LE, Zhong Z (2001) Polarization rotation via a monoclinic phase in the piezoelectric $92\%PbZn_{1/3}Nb_{2/3}O_3$_$8\%PbTiO_3$. Phy Rev Lett 86:3891–3894
9. Viehland D, Powers J, Cross LE, Li JF (2001) Importance of random fields on the properties and ferroelectric phase stability of 001 oriented $0.7\,Pb(Mg_{1/3}Nb_{2/3})O_3$–$0.3\,PbTiO_3$ crystals. Appl Phys Lett 78:3508–3510
10. Viehland D (2000) Symmetry-adaptive ferroelectric mesostates in oriented $Pb(BI_{1/3}BII_{2/3})O_3$–$PbTiO_3$ crystals. J Appl Phys 88:4794–4806
11. Liu M, Hsia KJ (2003) Locking of electric-field-induced non-180° domain switching and phase transition in ferroelectric materials upon cyclic electric fatigue. Appl Phys Lett 83:3978–3980
12. Arias S, Serebrinsky, M. Ortiz (2006) A phenomenological cohesive model of ferroelectric fatigue. Acta Materialia 54:975–984
13. Jiang QY, Cao WW, Cross LE (1994) Electric fatigue in lead ziconate titanate ceramics. J Am Ceram Soc 77:211–215
14. J Nuffer, Lupascu DC, Rodel J (2001) Microcrack clouds in fatigued electrostrictive 9.5/65/35 PLZT. J Eur Ceram Soc 21:1421–1423
15. Lupascu DC, Rodel J (2005) Fatigue in bulk lead zirconate titanate actuator materials. Adv Eng Mater 7:882–898
16. Zhou LJ, Rixecker G, Zimmermann A, Aldinger F, Zhao Z, Nygren M (2005) Electric fatigue in antiferroelectric lead zirconate stannate titanate ceramics prepared by spark plasma sintering. J Am Ceram Soc 88:2952–2954

17. Shvartsman VV, Kholkin AL, Verdier C, Lupascu DC (2005) Fatigue-induced evolution of domain structure in ferroelectric lead zirconate titanate ceramics investigated by piezoresponse force microscopy. J Appl Phys 98:094109
18. Chou CC, Hou CS, Yeh TH (2005) Domain pinning behavior of ferroelectric $Pb_{1-x}Sr_xTiO_3$ ceramics. J Eur Ceram Soc 25:2505–2508
19. Le JK, Yi JY, Hon K S (2004) Physical mechanism for orientation dependence of ferroelectric fatigue in $Pb(Zn_{1/3}Nb_{2/3})O_3$-5% $PbTiO_3$ crystals. J Appl Phys 96:7471–7475
20. Stolichnov I, Tagantsev A, Setter N, Cross JS, Tsukada M (1999) Top-interface-controlled switching and fatigue endurance of (Pb, La)(Zr, Ti)O_3 ferroelectric capacitors. Appl Phys Lett 74:3352–3354
21. Takemula K, Ozgul M, Bornand V, McKinstry ST (2000) Fatigue anisotropy in single crystal $Pb(Zn_{1/3}Nb_{2/3})O_3$-$PbTiO_3$. J Appl Phys 88:7272–7277
22. W. Yang (2002) Mechatronic Reliability. 1st edn. THU-Springer-Verlag, Berlin
23. Furuta A, Uchino K (1993) Dynamic observation of crack propagation in piezoelectric multilayer actuators. J Am Ceram Soc 76:1615–1617
24. Cao H C, Evans AG (1994) Electric-field-induced crack growth in piezoelectrics. J Am Ceram Soc 77:1783–1786
25. Fang F, Yang W, Zhu T (1999) Crack tip 90° domain switching in tetragonal lanthanum modified lead zirconate titanate under an electric field. J Mater Res 14:2940–2944
26. Fang DN, Liu B, Sun CT (2004) Fatigue crack growth in ferroelectric ceramics driven by alternating electric fields. J Am Ceram Soc 87:840–846
27. Shieh J, Huber JE, Fleck NA (2006) Fatigue crack growth in ferroelectrics under electrical loading. J Eur Ceram Soc 26:95–109
28. Fang F, Yang W, Zhang FC, H Qing (2008) Electric field-induced crack growth and domain structure evolution for [100]- and [101]-oriented 72%Pb(Mg1/3Nb2/3)O3-28%PbTiO3 ferroelectric single crystals. J Mater Res 23:3387–3395
29. Fang F, Yang W, Zhang FC, Qing H (2007) Domain structure evolution and fatigue cracking of <001>-oriented (Pb(Mg1/3Nb2/3)O3)0.67(PbTiO3)0.33 ferroelectric single crystals under cyclic electric loading. Appl Phys Lett 91:081903
30. Davis M, Damjanovic D, Setter N (2006) Electric-field-, temperature-, and stress-induced phase transitions in relaxor ferroelectric single crystals. Phys Rev B 73:014115
31. Bai F, Wang N, Li JF, Viehland D, Gehring PM (2004) X-ray and neutron diffraction investigations of the structural phase transformation sequence under electric field in $0.7Pb(Mg_{1/3}Nb_{2/3})$-$0.3PbTiO_3$ crystal. J Appl Phys 96:620–1627
32. Tan X, Xu Z, Shang JK (2000) Direct observations of electric field-induced domain boundary cracking in <001> oriented piezoelectric $Pb(Mg_{1/3}Nb_{2/3})O_3$–$PbTiO_3$ single crystal. Appl Phys Lett 77:1529–1531
33. Xu Z (2003) In situ TEM study of electric field-induced microcracking in piezoelectric single crystals. Mater Sci Eng B 99:106–111
34. Jiang YJ, Fang D N (2007) In-situ observation of electric-field-induced domain switching and crack propagation in poled PMNT 62/38 single crystals. Mater Lett 61:5047–5049
35. Xu GS, Luo HS, Guo YP, Gao YQ, Xu HQ, Qi ZY, Zhong WZ, Yin ZW (2001) Growth and piezoelectric properties of $Pb(Mg_{1/3}Nb_{2/3})O_3$–$PbTiO_3$ crystals by the modified Bridgman technique. Solid State Commun 120:321–324
36. Viehland D, Li JF (2004) Domain structure changes in (1-x) with composition, dc bias, and ac field. J Appl Phys 96:3379–3381
37. Fang F, Luo X, Yang W (2009) Polarization rotation and multiphase coexistence for $Pb((Mg_{1/3}Nb_{2/3})O_3$–$PbTiO_3$ single crystals at the morphotropc phase boundary under electric loading. Phys Rev B 79:174118

This page intentionally left blank

Multiscale Modeling of Electro-mechanically Coupled Materials: Homogenization Procedure and Computation of Overall Moduli

Jörg Schröder and Marc-André Keip

Abstract In this contribution, a meso-macro transition procedure for electro-mechanically coupled materials is presented. The utilized mesoscopic material model will be introduced and implemented into an FE^2-homogenization approach. The resulting two-scale formulation is capable to compute macroscopic boundary value problems under consideration of attached heterogeneous representative volume elements at each macroscopic point. The presented direct homogenization procedure also allows for the efficient computation of effective electro-mechanical material parameters.

1 Introduction

The effective properties of a material play an essential role for the macroscopic modeling of micro-heterogeneous and polycrystalline materials. In this regard, the derivation of upper and lower bounds and the computation of estimates for the overall properties have to be distinguished. The estimates of such bounds are based on the fundamental works [3], and later [5, 20, 21], and more recently [2]. These methods have been applied for the prediction of mechanical as well as non-mechanical properties. In [1], exact results for the overall properties of piezoelectric composites have been established. Utilizing a unit-cell method, Li et al. [6] investigated the relation between effective properties and different geometries of microvoids based on a 3-D finite element analysis. An algorithm for the description of micro-heterogeneous coupled thermo-electro-magnetic continua has been presented in [24]. In the following a general direct homogenization procedure is presented which couples the macroscopic to the mesoscopic scale, see also [7–10, 13, 18, 19, 22, 25].

J. Schröder (✉) and M.-A. Keip
Institute for Mechanics, Faculty of Engineering Sciences, Department of Civil Engineering, University of Duisburg-Essen, Universitätsstraße 15, 45141 Essen, Germany
e-mail: j.schroeder@uni-due.de; marc-andre.keip@uni-due.de

M. Kuna and A. Ricoeur (eds.), *IUTAM Symposium on Multiscale Modelling of Fatigue, Damage and Fracture in Smart Materials*, IUTAM Bookseries 24,
DOI 10.1007/978-90-481-9887-0_25,

2 Boundary Value Problems on the Macro- and the Mesoscale

In the following the electro-mechanically coupled boundary value problems (BVP) on both scales are described. The material behavior for the individual constituents on the mesoscale are modeled within a coordinate invariant formulation. Here we restrict ourselves to transversely isotropic material behavior as presented in [11, 12, 15].

2.1 Macroscopic Electro-mechanically Coupled BVP

The body of interest $\mathscr{B} \subset \mathbf{R}^3$ on the macroscopic scale is parameterized in $\overline{\mathbf{x}}$. $\overline{\mathbf{u}}$ and $\overline{\phi}$ denote the macroscopic displacement field and the macroscopic electric potential, respectively. The basic kinematic and electric variables are the linear strain tensor $\overline{\boldsymbol{\varepsilon}}(\overline{\mathbf{x}}) := \text{sym}[\overline{\nabla}\overline{\mathbf{u}}(\overline{\mathbf{x}})]$ and the electric field vector $\overline{\mathbf{E}}(\overline{\mathbf{x}}) := -\overline{\nabla}\,\overline{\phi}(\overline{\mathbf{x}})$, where $\overline{\nabla}$ denotes the gradient operator w.r.t. $\overline{\mathbf{x}}$.

The governing field equations for the quasi-static case are the balance of linear momentum and Gauss' law $\text{div}_{\overline{\mathbf{x}}}[\overline{\boldsymbol{\sigma}}] + \overline{\mathbf{f}} = \mathbf{0}$ and $\text{div}_{\overline{\mathbf{x}}}[\overline{\mathbf{D}}] = \overline{q} \quad \forall\ \overline{\mathbf{x}} \in \mathscr{B}$, where $\text{div}_{\overline{\mathbf{x}}}$ denotes the divergence operator with respect to $\overline{\mathbf{x}}$. $\overline{\boldsymbol{\sigma}}$ represents the symmetric Cauchy stress tensor, $\overline{\mathbf{f}}$ is the given body force, $\overline{\mathbf{D}}$ denotes the vector of electric displacements and $\overline{q}$ is the given density of free charge carriers. The boundary conditions are listed in Table 1, where $\overline{\mathbf{n}}$ is a unit normal vector pointing outwards from the surface of the body. Instead of postulating the existence of a thermodynamical potential on the macroscale, we attach a representative volume element ($\mathscr{RVE}$) at each macroscopic point $\overline{\mathbf{x}}$ (see Table 1 and figures on top).

In order to link the macroscopic variables $\{\overline{\boldsymbol{\varepsilon}}, \overline{\boldsymbol{\sigma}}, \overline{\mathbf{E}}, \overline{\mathbf{D}}\}$ with their microscopic counterparts $\{\boldsymbol{\varepsilon}, \boldsymbol{\sigma}, \mathbf{E}, \mathbf{D}\}$, we define in this two-scale approach the macroscopic variables in terms of some suitable surface integrals over the boundary of the $\mathscr{RVE}$ with volume V. It should be remarked, that a definition of macroscopic quantities in terms of surface integrals is necessary in general. Respective definitions of macroscopic values by means of simple volume averages could lead to physically unreasonable results and would not allow for reliable interpretations of simple experiments, see e.g. [13]. The macroscopic strains and stresses are given by

$$\overline{\boldsymbol{\varepsilon}} := \frac{1}{V} \int\limits_{\partial\mathscr{RVE}} \text{sym}[\mathbf{u} \otimes \mathbf{n}]\, da \quad \text{and} \quad \overline{\boldsymbol{\sigma}} := \frac{1}{V} \int\limits_{\partial\mathscr{RVE}} \text{sym}[\mathbf{t} \otimes \mathbf{x}]\, da, \tag{1}$$

where $\mathbf{u}$ and $\mathbf{t}$ are the displacement and traction vectors on the boundary of the $\mathscr{RVE}$, respectively. Furthermore, the macroscopic electric field and electric displacements are defined by the surface integrals

$$\overline{\mathbf{E}} := \frac{1}{V} \int\limits_{\partial\mathscr{RVE}} -\phi\, \mathbf{n}\, da \quad \text{and} \quad \overline{\mathbf{D}} := \frac{1}{V} \int\limits_{\partial\mathscr{RVE}} -Q\, \mathbf{x}\, da, \tag{2}$$

with the electric potential ϕ and the electric charge density Q on $\partial\mathscr{RVE}$.

Table 1 Basic equations of the two-scale homogenization procedure

Coupling between macro- and mesoscale

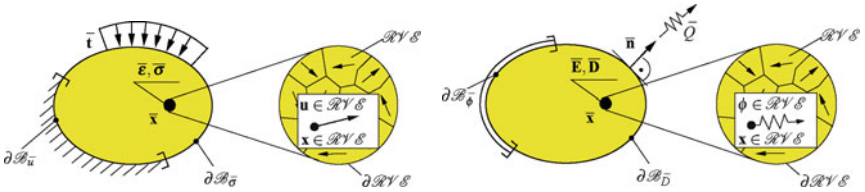

Macroscale: Electro-mechanically coupled boundary value problem

Mechanical field equations & bc's		Electrical field equations & bc's	
$\bar{\boldsymbol{\varepsilon}} = \text{sym}[\overline{\nabla}\bar{\mathbf{u}}]$		$\bar{\mathbf{E}} = -\overline{\nabla}\,\bar{\phi}$	
$\text{div}_{\bar{\mathbf{x}}}\bar{\boldsymbol{\sigma}} + \bar{\mathbf{f}} = \mathbf{0}$	in $\mathscr{B}$	$\text{div}_{\bar{\mathbf{x}}}\bar{\mathbf{D}} = \bar{q}$	in $\mathscr{B}$
$\bar{\mathbf{u}} = \bar{\mathbf{u}}_b$	on $\partial\mathscr{B}_u$	$\bar{\phi} = \bar{\phi}_b$	on $\partial\mathscr{B}_\phi$
$\bar{\mathbf{t}} = \bar{\boldsymbol{\sigma}} \cdot \bar{\mathbf{n}}$	on $\partial\mathscr{B}_\sigma$	$-\bar{Q} = \bar{\mathbf{D}} \cdot \bar{\mathbf{n}}$	on $\partial\mathscr{B}_D$

Definition of macroscopic field variables ($V = vol(\mathscr{RVE})$)

$$\bar{\boldsymbol{\sigma}} = \frac{1}{V}\int_{\partial\mathscr{RVE}} \text{sym}[\mathbf{t} \otimes \mathbf{x}]\, da \qquad \bar{\mathbf{D}} = \frac{1}{V}\int_{\partial\mathscr{RVE}} -Q\,\mathbf{x}\, da$$

$$\bar{\boldsymbol{\varepsilon}} = \frac{1}{V}\int_{\partial\mathscr{RVE}} \text{sym}[\mathbf{u} \otimes \mathbf{n}]\, da \qquad \bar{\phi} = \frac{1}{V}\int_{\partial\mathscr{RVE}} -\phi\,\mathbf{n}\, da$$

Mesoscale: Electro-mechanically coupled boundary value problem

Mechanical field equations		Electrical field equations	
$\boldsymbol{\varepsilon} = \text{sym}[\nabla\mathbf{u}]$		$\mathbf{E} = -\nabla\phi$	
$\text{div}\boldsymbol{\sigma} = \mathbf{0}$	in $\mathscr{RVE}$	$\text{div}\mathbf{D} = 0$	in $\mathscr{RVE}$

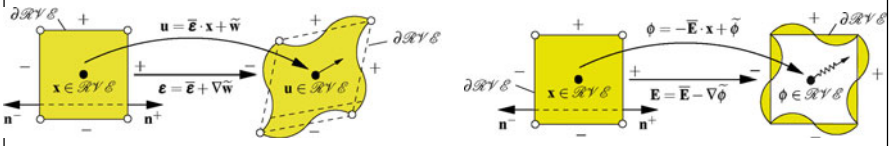

Mechanical bc's		Electrical bc's
$\mathbf{t} = \bar{\boldsymbol{\sigma}} \cdot \mathbf{n}$	Neumann bc's	$Q = -\bar{\mathbf{D}} \cdot \mathbf{n}$
$\mathbf{u} = \bar{\boldsymbol{\varepsilon}} \cdot \mathbf{x}$	Dirichlet bc's	$\phi = -\bar{\mathbf{E}} \cdot \mathbf{x}$
$\mathbf{u} = \bar{\boldsymbol{\varepsilon}} \cdot \mathbf{x} + \widetilde{\mathbf{w}}$, $\widetilde{\mathbf{w}}^+ = \widetilde{\mathbf{w}}^-$, $\mathbf{t}^+ = -\mathbf{t}^-$	periodic bc's	$\phi = -\bar{\mathbf{E}} \cdot \mathbf{x} + \widetilde{\phi}$, $\widetilde{\phi}^+ = \widetilde{\phi}^-$, $Q^+ = -Q^-$

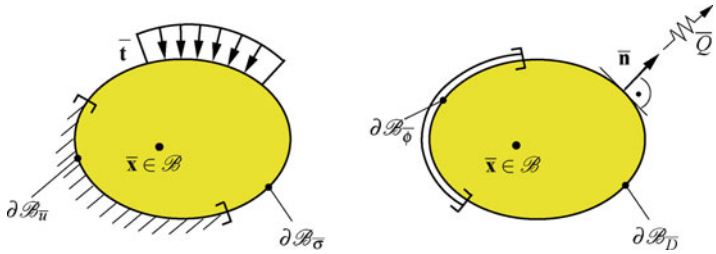

Fig. 1 Boundary decomposition of $\partial\mathscr{B}$ into mechanical, i.e. $\partial\mathscr{B}_u \cup \partial\mathscr{B}_\sigma = \partial\mathscr{B}$ with $\partial\mathscr{B}_u \cap \partial\mathscr{B}_\sigma = \emptyset$, and electrical parts: $\partial\mathscr{B}_\phi \cup \partial\mathscr{B}_D = \partial\mathscr{B}$ with $\partial\mathscr{B}_\phi \cap \partial\mathscr{B}_D = \emptyset$

2.2 Mesoscopic Electro-mechanically Coupled BVP

On the mesoscopic scale we consider a BVP defined on $\mathscr{RVE} \subset \mathbf{R}^3$, which is parameterized in the mesoscopic cartesian coordinates $\mathbf{x}$. The governing balance equations are the balance of linear momentum neglecting body forces, and the Gauss' law neglecting the density of free charge carriers $\operatorname{div}[\boldsymbol{\sigma}] = \mathbf{0}$ and $\operatorname{div}[\mathbf{D}] = 0 \quad \forall\ \mathbf{x} \in \mathscr{RVE}$. The mesoscopic strains and electric field vector are given by $\boldsymbol{\varepsilon} := \operatorname{sym}[\nabla\mathbf{u}(\mathbf{x})]$ and $\mathbf{E} := -\nabla\phi(\mathbf{x})$, where ∇ denotes the gradient operator and div the divergence operator with respect to $\mathbf{x}$. In order to complete the description of the mesoscopic BVP we define some appropriate boundary conditions on $\partial\mathscr{RVE}$ or some constraint conditions in the whole $\mathscr{RVE}$. Therefore, we apply a generalized macro-homogeneity condition

$$\overline{\boldsymbol{\sigma}} : \dot{\overline{\boldsymbol{\varepsilon}}} + \overline{\mathbf{D}} \cdot \dot{\overline{\mathbf{E}}} = \frac{1}{V} \int_{\mathscr{RVE}} \boldsymbol{\sigma} : \dot{\boldsymbol{\varepsilon}}\, dv + \frac{1}{V} \int_{\mathscr{RVE}} \mathbf{D} \cdot \dot{\mathbf{E}}\, dv\,, \tag{3}$$

in this context see [4]. This condition yields the boundary conditions on $\partial\mathscr{RVE}$ which are listed in Table 1. A detailed derivation of the respective boundary conditions is given in [14]. For convenience, the set of equations of the two-scale homogenization including illustrations is listed in Table 1.

3 Effective Properties of Piezoelectric Materials

The aim of this two-scale approach is to achieve quadratic convergence within the Newton–Raphson iteration scheme for the discretized boundary value problem on the macroscale. For this we have to perform the consistent linearization of the macroscopic stresses and electric displacements with respect to the macroscopic strains and electric field. In detail we need the macroscopic (overall) mechanical

moduli $\overline{\mathbb{C}}$, piezoelectric moduli $\overline{\mathbf{e}}$, and dielectric moduli $\overline{\boldsymbol{\epsilon}}$, which enter the incremental constitutive relations

$$\begin{aligned} \Delta\overline{\boldsymbol{\sigma}} &= \quad \overline{\mathbb{C}} : \Delta\overline{\boldsymbol{\varepsilon}} - \overline{\mathbf{e}}^T \Delta\overline{\mathbf{E}}, \\ -\Delta\overline{\mathbf{D}} &= -\overline{\mathbf{e}} : \Delta\overline{\boldsymbol{\varepsilon}} - \overline{\boldsymbol{\epsilon}} \ \Delta\overline{\mathbf{E}}. \end{aligned} \tag{4}$$

Formally, we obtain the overall moduli by partial differentiation of the volume averages of the mesoscopic stresses and electric displacements with respect to the macroscopic strains and electric field, i.e.

$$\begin{bmatrix} \Delta\overline{\boldsymbol{\sigma}} \\ -\Delta\overline{\mathbf{D}} \end{bmatrix} = \frac{1}{V} \begin{bmatrix} \partial_{\overline{\boldsymbol{\varepsilon}}} \left\{ \int\limits_{\mathscr{RVE}} \boldsymbol{\sigma} \, dv \right\} & \partial_{\overline{\mathbf{E}}} \left\{ \int\limits_{\mathscr{RVE}} \boldsymbol{\sigma} \, dv \right\} \\ -\partial_{\overline{\boldsymbol{\varepsilon}}} \left\{ \int\limits_{\mathscr{RVE}} \mathbf{D} \, dv \right\} & -\partial_{\overline{\mathbf{E}}} \left\{ \int\limits_{\mathscr{RVE}} \mathbf{D} \, dv \right\} \end{bmatrix} \begin{bmatrix} \Delta\overline{\boldsymbol{\varepsilon}} \\ \Delta\overline{\mathbf{E}} \end{bmatrix}. \tag{5}$$

For the analysis of the mesoscopic BVP we conduct an additive decomposition of the mesoscopic strains and electric field into a constant part and a fluctuating part, i.e. $\boldsymbol{\varepsilon} = \mathrm{sym}[\nabla\mathbf{u}(\mathbf{x})] = \overline{\boldsymbol{\varepsilon}} + \widetilde{\boldsymbol{\varepsilon}}$ and $\mathbf{E} = -\nabla\phi = \overline{\mathbf{E}} + \widetilde{\mathbf{E}}$. Exploiting these relations in Eq. 5 leads after application of the chain rule to

$$\begin{bmatrix} \Delta\overline{\boldsymbol{\sigma}} \\ -\Delta\overline{\mathbf{D}} \end{bmatrix} = \frac{1}{V} \left(\int\limits_{\mathscr{RVE}} \begin{bmatrix} \mathbb{C} & -\mathbf{e}^T \\ -\mathbf{e} & -\boldsymbol{\epsilon} \end{bmatrix} dv + \int\limits_{\mathscr{RVE}} \begin{bmatrix} \mathbb{C} : \partial_{\overline{\boldsymbol{\varepsilon}}}\widetilde{\boldsymbol{\varepsilon}} & -\mathbf{e}^T \cdot \partial_{\overline{\mathbf{E}}}\widetilde{\mathbf{E}} \\ -\mathbf{e} : \partial_{\overline{\boldsymbol{\varepsilon}}}\widetilde{\boldsymbol{\varepsilon}} & -\boldsymbol{\epsilon} \cdot \partial_{\overline{\mathbf{E}}}\widetilde{\mathbf{E}} \end{bmatrix} dv \right) \begin{bmatrix} \Delta\overline{\boldsymbol{\varepsilon}} \\ \Delta\overline{\mathbf{E}} \end{bmatrix}. \tag{6}$$

Let us now consider the weak forms of the balance of linear momentum and Gauss' law:

$$G_u = -\int\limits_{\mathscr{RVE}} \mathrm{div}\boldsymbol{\sigma} \cdot \delta\widetilde{\mathbf{w}} \, dv = \underbrace{\int\limits_{\mathscr{RVE}} \delta\widetilde{\boldsymbol{\varepsilon}} : \boldsymbol{\sigma} \, dv}_{G_u^{int}} - \underbrace{\int\limits_{\partial\mathscr{RVE}} \delta\widetilde{\mathbf{w}} \cdot (\boldsymbol{\sigma} \cdot \mathbf{n}) \, da}_{G_u^{ext}} \tag{7}$$

and

$$G_\phi = -\int\limits_{\mathscr{RVE}} \mathrm{div}\mathbf{D} \, \delta\widetilde{\phi} \, dv = \underbrace{\int\limits_{\mathscr{RVE}} \delta\widetilde{\mathbf{E}} \cdot \mathbf{D} \, dv}_{G_\phi^{int}} - \underbrace{\int\limits_{\partial\mathscr{RVE}} \delta\widetilde{\phi}(\mathbf{D} \cdot \mathbf{n}) \, da}_{G_\phi^{ext}}, \tag{8}$$

respectively. Now we compute the sensitivities of the mesoscopic fluctuation fields w.r.t. their incremental macroscopic counterparts. Therefore we linearize the weak forms at an equilibrium state:

$$\begin{aligned} \int\limits_{\mathscr{RVE}} \delta\widetilde{\boldsymbol{\varepsilon}} : \mathbb{C} : (\Delta\overline{\boldsymbol{\varepsilon}} + \Delta\widetilde{\boldsymbol{\varepsilon}}) \; dv - \int\limits_{\mathscr{RVE}} \delta\widetilde{\boldsymbol{\varepsilon}} : \mathbf{e}^T \cdot \left(\Delta\overline{\mathbf{E}} + \Delta\widetilde{\mathbf{E}}\right) \; dv = 0, \\ \int\limits_{\mathscr{RVE}} \delta\widetilde{\mathbf{E}} \cdot \mathbf{e} : (\Delta\overline{\boldsymbol{\varepsilon}} + \Delta\widetilde{\boldsymbol{\varepsilon}}) \; dv + \int\limits_{\mathscr{RVE}} \delta\widetilde{\mathbf{E}} \cdot \boldsymbol{\epsilon} \cdot \left(\Delta\overline{\mathbf{E}} + \Delta\widetilde{\mathbf{E}}\right) \; dv = 0, \end{aligned} \tag{9}$$

where we have used the abbreviations

$$\mathbb{C} := \partial_{\boldsymbol{\varepsilon}}\boldsymbol{\sigma}, \quad \mathbf{e} = -\{\partial_{\mathbf{E}}\boldsymbol{\sigma}\}^T = \partial_{\boldsymbol{\varepsilon}}\mathbf{D}, \quad \boldsymbol{\epsilon} = \partial_{\mathbf{E}}\mathbf{D}. \tag{10}$$

For the discretization of the latter equations we only have to account for the fluctuation fields of the displacements and electric potential. Thus, the finite element approximation of the fluctuation fields, virtual fluctuation fields and incremental fluctuation fields appear as

$$\widetilde{\mathbf{w}} = \sum_{I=1}^{n_{node}} N_u^I \; \widetilde{\mathbf{d}}_I^u, \quad \delta\widetilde{\mathbf{w}} = \sum_{I=1}^{n_{node}} N_u^I \; \delta\widetilde{\mathbf{d}}_I^u, \quad \Delta\widetilde{\mathbf{w}} = \sum_{I=1}^{n_{node}} N_u^I \; \Delta\widetilde{\mathbf{d}}_I^u \tag{11}$$

and

$$\widetilde{\phi} = \sum_{I=1}^{n_{node}} N_\phi^I \; \widetilde{d}_I^\phi, \quad \delta\widetilde{\phi} = \sum_{I=1}^{n_{node}} N_\phi^I \; \delta\widetilde{d}_I^\phi, \quad \Delta\widetilde{\phi} = \sum_{I=1}^{n_{node}} N_\phi^I \; \Delta\widetilde{d}_I^\phi, \tag{12}$$

where $N_{u,\phi}$ denote the ansatz functions, $\widetilde{\mathbf{d}}^{u,\phi}$ the nodal degrees of freedom and n_{node} the number of nodes per element. Let $\mathbf{B}_u^e$ and $\mathbf{B}_\phi^e$ characterize the B-Matrices associated to fluctuation strains and electric field. The finite element approximations of the actual, virtual and incremental strains are

$$\widetilde{\boldsymbol{\varepsilon}} = \mathbf{B}_u^e \; \widetilde{\mathbf{d}}^u, \quad \delta\widetilde{\boldsymbol{\varepsilon}} = \mathbf{B}_u^e \; \delta\widetilde{\mathbf{d}}^u, \quad \Delta\widetilde{\boldsymbol{\varepsilon}} = \mathbf{B}_u^e \; \Delta\widetilde{\mathbf{d}}^u.$$

Analogously, the fields associated to the electric potential appear as

$$\widetilde{\mathbf{E}} = -\mathbf{B}_\phi^e \; \widetilde{\mathbf{d}}^\phi, \quad \delta\widetilde{\mathbf{E}} = \mathbf{B}_\phi^e \; \delta\widetilde{\mathbf{d}}^\phi, \quad \Delta\widetilde{\mathbf{E}} = -\mathbf{B}_\phi^e \; \Delta\widetilde{\mathbf{d}}^\phi.$$

After inserting the approximations in Eq. 9 we obtain

$$\begin{aligned} \sum_{e=1}^{n_{ele}} \left\{ \delta\widetilde{\mathbf{d}}^{uT} \left(\mathbf{l}_{uu}^e \; \Delta\overline{\boldsymbol{\varepsilon}} + \mathbf{k}_{uu}^e \; \Delta\widetilde{\mathbf{d}}^u + \mathbf{l}_{u\phi}^e \; \Delta\overline{\mathbf{E}} + \mathbf{k}_{u\phi}^e \; \Delta\widetilde{\mathbf{d}}^\phi \right) \right\} = 0 \\ \sum_{e=1}^{n_{ele}} \left\{ \delta\widetilde{\mathbf{d}}^{\phi T} \left(\mathbf{l}_{\phi u}^e \; \Delta\overline{\boldsymbol{\varepsilon}} + \mathbf{k}_{\phi u}^e \; \Delta\widetilde{\mathbf{d}}^u + \mathbf{l}_{\phi\phi}^e \; \Delta\overline{\mathbf{E}} + \mathbf{k}_{\phi\phi}^e \; \Delta\widetilde{\mathbf{d}}^\phi \right) \right\} = 0, \end{aligned} \tag{13}$$

with the matrices

$$\begin{aligned}
\mathbf{l}^e_{uu} &= \int_{\mathscr{B}^e} \mathbf{B}^{eT}_u \mathbb{C}\, dv, \quad \mathbf{k}^e_{uu} = \int_{\mathscr{B}^e} \mathbf{B}^{eT}_u \mathbb{C}\mathbf{B}^e\, dv, \quad \mathbf{l}^e_{u\phi} = -\int_{\mathscr{B}^e} \mathbf{B}^{eT}_u \mathbf{e}^T\, dv, \\
\mathbf{k}^e_{u\phi} &= \int_{\mathscr{B}^e} \mathbf{B}^{eT}_u \mathbf{e}^T \mathbf{B}^e_\phi\, dv, \quad \mathbf{l}^e_{\phi u} = \int_{\mathscr{B}^e} \mathbf{B}^{eT}_\phi \cdot \mathbf{e}\, dv, \quad \mathbf{k}^e_{\phi u} = \int_{\mathscr{B}^e} \mathbf{B}^{eT}_\phi \mathbf{e}\mathbf{B}^e_u\, dv, \\
\mathbf{l}^e_{\phi\phi} &= \int_{\mathscr{B}^e} \mathbf{B}^{eT}_\phi \boldsymbol{\epsilon}\, dv, \quad \mathbf{k}^e_{\phi\phi} = -\int_{\mathscr{B}^e} \mathbf{B}^{eT}_\phi \boldsymbol{\epsilon}\mathbf{B}^e\, dv.
\end{aligned} \tag{14}$$

After the standard assembling procedure we obtain

$$\begin{bmatrix} \delta\widetilde{\mathbf{D}}^u \\ \delta\widetilde{\mathbf{D}}^\phi \end{bmatrix}^T \left(\begin{bmatrix} \mathbf{K}_{uu} & \mathbf{K}_{u\phi} \\ \mathbf{K}_{\phi u} & \mathbf{K}_{\phi\phi} \end{bmatrix} \begin{bmatrix} \Delta\widetilde{\mathbf{D}}^u \\ \Delta\widetilde{\mathbf{D}}^\phi \end{bmatrix} + \begin{bmatrix} \mathbf{L}_{uu}\, \Delta\overline{\boldsymbol{\varepsilon}} + \mathbf{L}_{u\phi}\, \Delta\overline{\mathbf{E}} \\ \mathbf{L}_{\phi u}\, \Delta\overline{\boldsymbol{\varepsilon}} + \mathbf{L}_{\phi\phi}\, \Delta\overline{\mathbf{E}} \end{bmatrix} \right) = 0 \tag{15}$$

with the abbreviations

$$\begin{aligned}
\mathbf{K}_{uu} &= \mathop{\mathbf{A}}_{e=1}^{n_{ele}} \mathbf{k}^e_{uu}, \mathbf{K}_{u\phi} = \mathop{\mathbf{A}}_{e=1}^{n_{ele}} \mathbf{k}^e_{u\phi}, \mathbf{K}_{\phi u} = \mathop{\mathbf{A}}_{e=1}^{n_{ele}} \mathbf{k}^e_{\phi u}, \mathbf{K}_{\phi\phi} = \mathop{\mathbf{A}}_{e=1}^{n_{ele}} \mathbf{k}^e_{\phi\phi}, \\
\mathbf{L}_{uu} &= \mathop{\mathbf{A}}_{e=1}^{n_{ele}} \mathbf{l}^e_{uu}, \ \mathbf{L}_{u\phi} = \mathop{\mathbf{A}}_{e=1}^{n_{ele}} \mathbf{l}^e_{u\phi}, \ \mathbf{L}_{\phi u} = \mathop{\mathbf{A}}_{e=1}^{n_{ele}} \mathbf{l}^e_{\phi u}, \ \mathbf{L}_{\phi\phi} = \mathop{\mathbf{A}}_{e=1}^{n_{ele}} \mathbf{l}^e_{\phi\phi}.
\end{aligned} \tag{16}$$

The solution, i.e. the incremental nodal fluctuations due to the incremental macroscopic strains and electric field, is formally given by

$$\begin{bmatrix} \Delta\widetilde{\mathbf{D}}^u \\ \Delta\widetilde{\mathbf{D}}^\phi \end{bmatrix} = -\begin{bmatrix} \mathbf{K}_{uu} & \mathbf{K}_{u\phi} \\ \mathbf{K}_{\phi u} & \mathbf{K}_{\phi\phi} \end{bmatrix}^{-1} \begin{bmatrix} \mathbf{L}_{uu}\, \Delta\overline{\boldsymbol{\varepsilon}} + \mathbf{L}_{u\phi}\, \Delta\overline{\mathbf{E}} \\ \mathbf{L}_{\phi u}\, \Delta\overline{\boldsymbol{\varepsilon}} + \mathbf{L}_{\phi\phi}\, \Delta\overline{\mathbf{E}} \end{bmatrix}. \tag{17}$$

Inserting the finite element approximations in Eq. 6 and exploiting the definitions of the L-Matrices (16) leads to

$$\begin{bmatrix} \overline{\mathbb{C}} & -\overline{\mathbf{e}}^T \\ -\overline{\mathbf{e}} & -\overline{\boldsymbol{\epsilon}} \end{bmatrix} = \frac{1}{V} \int_{\mathscr{RVE}} \begin{bmatrix} \mathbb{C} & -\mathbf{e}^T \\ -\mathbf{e} & -\boldsymbol{\epsilon} \end{bmatrix} dv + \frac{1}{V} \begin{bmatrix} \mathbf{L}^T_{uu} & \mathbf{L}^T_{\phi u} \\ \mathbf{L}^T_{u\phi} & \mathbf{L}^T_{\phi\phi} \end{bmatrix} \begin{bmatrix} \partial_{\overline{\boldsymbol{\varepsilon}}} \Delta\widetilde{\mathbf{D}}^u \\ \partial_{\overline{\mathbf{E}}} \Delta\widetilde{\mathbf{D}}^\phi \end{bmatrix}. \tag{18}$$

Obviously, we have to compute the sensitivities of the nodal fluctuations w.r.t. the macroscopic strains and electric field. Utilizing Eq. 17, we obtain the derivatives of the incremental solutions

$$\begin{bmatrix} \partial_{\overline{\boldsymbol{\varepsilon}}} \Delta \widetilde{\mathbf{D}}^{u} \\ \\ \partial_{\overline{\mathbf{E}}} \Delta \widetilde{\mathbf{D}}^{\phi} \end{bmatrix} = - \begin{bmatrix} \mathbf{K}_{uu} & \mathbf{K}_{u\phi} \\ \\ \mathbf{K}_{\phi u} & \mathbf{K}_{\phi\phi} \end{bmatrix}^{-1} \begin{bmatrix} \mathbf{L}_{uu} & \mathbf{L}_{u\phi} \\ \\ \mathbf{L}_{\phi u} & \mathbf{L}_{\phi\phi} \end{bmatrix},$$

which leads to the final algorithmic expression for the macroscopic (overall) electro-mechanical tangent moduli

$$\begin{bmatrix} \overline{\mathbb{C}} & -\overline{\mathbf{e}}^{T} \\ \\ -\overline{\mathbf{e}} & -\overline{\boldsymbol{\epsilon}} \end{bmatrix} = \frac{1}{V} \int_{\mathscr{RVE}} \begin{bmatrix} \mathbb{C} & -\mathbf{e}^{T} \\ \\ -\mathbf{e} & -\boldsymbol{\epsilon} \end{bmatrix} dv$$
$$- \frac{1}{V} \begin{bmatrix} \mathbf{L}_{uu}^{T} & \mathbf{L}_{\phi u}^{T} \\ \\ \mathbf{L}_{u\phi}^{T} & \mathbf{L}_{\phi\phi}^{T} \end{bmatrix} \begin{bmatrix} \mathbf{K}_{uu} & \mathbf{K}_{u\phi} \\ \\ \mathbf{K}_{\phi u} & \mathbf{K}_{\phi\phi} \end{bmatrix}^{-1} \begin{bmatrix} \mathbf{L}_{uu} & \mathbf{L}_{u\phi} \\ \\ \mathbf{L}_{\phi u} & \mathbf{L}_{\phi\phi} \end{bmatrix}.$$

The authors would like to emphasize that the presented solution procedure is general in the sense that it can be applied to linear as well as to nonlinear problems. However, in this context it should be noted that quadratic convergence behavior on the macroscale can only be achieved, if an algorithmic consistent linearization of the nonlinear weak forms on the mesoscale has been carried out. For a more detailed derivation of the expressions for the electro-mechanical moduli the reader is referred to [16] and [17].

4 Computation of Effective Electro-mechanical Moduli of a Three-Dimensional Voided Mesostructure

In the following we analyze a three-dimensional heterogeneous representative volume element in order to determine the effective material parameters of a voided piezoelectric material.

The material parameters which are applied in this contribution are taken from [23] and fitted to the underlying transversely isotropic material model by means of a least-squares approximation. The expressions of the stresses and electric displacements are derived from a quadratic electric enthalpy function. In the present case of linear piezoelectric material behavior we obtain the general representation

$$\left.\begin{aligned} \boldsymbol{\sigma} &= \mathbb{C} : \boldsymbol{\varepsilon} - \mathbf{e}^{T} \cdot \mathbf{E} \\ \mathbf{D} &= \mathbf{e} : \boldsymbol{\varepsilon} + \boldsymbol{\epsilon} \cdot \mathbf{E} \end{aligned}\right\} \quad \text{and} \quad \left\{\begin{aligned} \sigma_{ij} &= \mathbb{C}_{ijkl} \varepsilon_{kl} - e_{kij} E_{k} \\ D_{i} &= e_{ikl} \varepsilon_{kl} + \epsilon_{ik} E_{k} \end{aligned}\right. \tag{19}$$

in direct and tensorial notation, respectively. Here $\mathbb{C}$ denotes the fourth-order elasticity tensor, $\mathbf{e}$ the third-order tensor of piezoelectric moduli and $\boldsymbol{\epsilon}$ the second-order tensor of dielectric moduli.

Following [15] we use a coordiante-invariant representation and focus on transversely isotropic solids, where $\mathbf{a}$ (with $||\mathbf{a}|| = 1$) is the preferred direction of the transversely isotropic material. We obtain

$$\mathbb{C} = \lambda \mathbf{1} \otimes \mathbf{1} + 2\mu \mathbb{I} + \alpha_3 [\mathbf{1} \otimes \mathbf{m} + \mathbf{m} \otimes \mathbf{1}] + 2\alpha_2 \mathbf{m} \otimes \mathbf{m} + \alpha_1 \Xi, \tag{20}$$

where $\mathbf{m} = \mathbf{a} \otimes \mathbf{a}$ denotes the second-order structural tensor, $\mathbf{1}$ the second-order unity tensor, $\mathbb{I}$ the fourth-order unity tensor and $\Xi_{ijkl} := [a_i \delta_{jk} a_l + a_k \delta_{il} a_j]$. The second-order tensor of dielectric moduli is given by

$$\boldsymbol{\epsilon} = -2\gamma_1 \mathbf{1} - 2\gamma_2 \mathbf{m} \tag{21}$$

and the third-order tensor of the piezoelectric moduli appears in the form

$$\mathbf{e} := -\beta_1 \mathbf{a} \otimes \mathbf{1} - \beta_2 \mathbf{a} \otimes \mathbf{m} - \beta_3 \bar{\mathbf{e}} \tag{22}$$

with the abbreviation $\{\bar{\mathbf{e}}\}_{kij} := \frac{1}{2}[a_i \delta_{kj} + a_j \delta_{ki}]$. The mechanical moduli in the coordinate-invariant setting appear as

$$\lambda = 108, \quad \mu = 57, \quad \alpha_1 = -53, \quad \alpha_2 = 14.5, \quad \alpha_3 = 3, \tag{23}$$

in units of GPa, the components of the dielectric tensor $\boldsymbol{\epsilon}$ are

$$\gamma_1 = -9.5, \quad \gamma_2 = 9.252083,$$

in units of 10^{-9} C/Vm, and the piezoelectric components are

$$\beta_1 = 0.7, \quad \beta_2 = 61, \quad \beta_3 = -68.4,$$

in units of C/m^2.

Three-dimensional discretizations of the periodic piezoelectric mesostructure with ellipsoidal microvoids are depicted in Fig. 2. The void ratio of the $\mathscr{RVE}$ is 2.83%. In order to assess the needed mesh density of the discretization of the heterogeneous mesostructure, a convergence study is conducted.

The results of the convergence study are depicted in Fig. 3. As can be seen, the effective macroscopic moduli converge with increasing number of elements on the mesolevel.

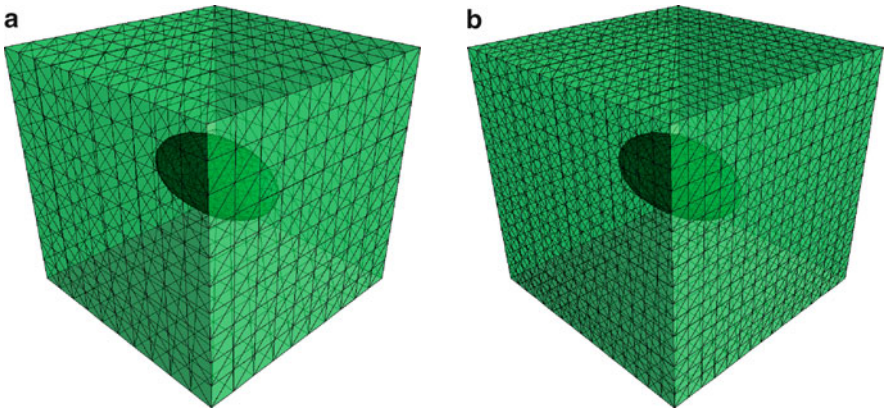

Fig. 2 Discretizations of the mesostructure: (**a**) 21287 and (**b**) 43395 linear tetrahedral elements

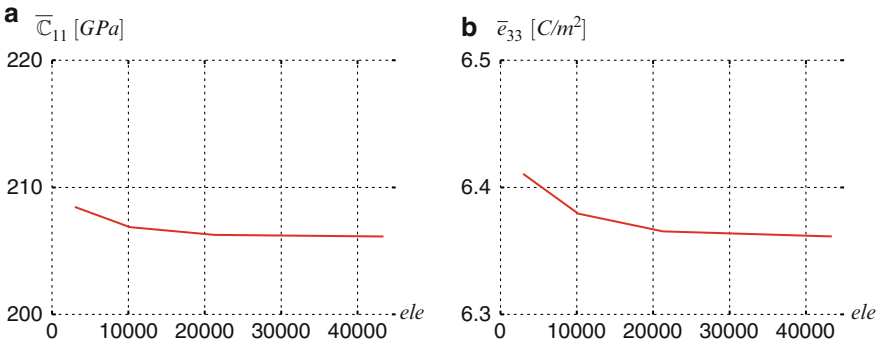

Fig. 3 Effective (**a**) mechanical modul $\overline{\mathbb{C}}_{11}$ and (**b**) piezoelectric modul $\overline{e}_{33}$ vs. number of elements

5 Conclusion

In this contribution, a framework for a general two-scale homogenization procedure for the analysis of electro-mechanically coupled boundary value problems was presented. In this regard, a meso-macro transition procedure for electro-mechanically coupled materials in two and three dimensions was derived. The meso-macro transition procedure was implemented into an FE^2-homogenization environment, which allows for the computation of macroscopic boundary value problems under consideration of attached mesoscopic representative volume elements. The presented homogenization formulation is also capable for the efficient and accurate determination of effective electro-mechanical moduli.

References

1. Chen T (1994) Micromechanical estimates of the overall thermoelectroelastic moduli of multiphase fibrous composites. Int J Solid Struct 31(22):3099–3111
2. Francfort GA, Murat F (1986) Homogenization and optimal bounds in linear elasticity. Arch Ration Mech Anal 94:307–334
3. Hashin Z, Shtrikman S (1962) On some variational principles in anisotropic and nonhomogeneous elasticity. J Mech Phys Solid 10:335–342
4. Hill R (1963) Elastic properties of reinforced solids: Some theoretical principles. J Mech Phys Solid 11:357–372
5. Kröner E (1977) Bounds for effective elastic moduli of disordered materials. J Mech Phys Solid 25:137–155
6. Li Z, Wang C, Chen C (2003) Effective electromechanical properties of transversely isotropic piezoelectric ceramics with microvoids. Comput Mater Sci 27(3):381–392
7. Markovic D, Niekamp R, Ibrahimbegovic A, Matthies HG, Taylor RL (2005) Multi-scale modeling of heterogeneous structures with inelastic constitutive behavior. Int J Comput Aid Eng Software 22(5/6):664–683
8. Miehe C, Koch A (2002) Computational micro-to-macro transitions of discretized microstructures undergoing small strains. Arch Appl Mech 72(4):300–317
9. Miehe C, Schotte J, Schröder J (1999) Computational micro-macro transitions and overall moduli in the analysis of polycrystals at large strains. Comput Mater Sci 16(1–4):372–382
10. Miehe C, Schröder J, Schotte J (1999) Computational homogenization analysis in finite plasticity simulation of texture development in polycrystalline materials. Comput Method Appl Mech Eng 171(3–4):387–418
11. Romanowski H (2006) Kontinuumsmechanische Modellierung ferroelektrischer Materialien im Rahmen der Invariantentheorie. PhD thesis, Institut für Mechanik, Fakultät Ingenieurwissenschaften, Abteilung Bauwissenschaften, Universität Duisburg-Essen
12. Romanowski H, Schröder J (2005) Coordinate invariant modelling of the ferroelectric hysteresis within a thermodynamically consistent framework. A mesoscopic approach. In: Wang Y, Hutter K (eds) Trends in applications of mathematics and mechanics. Shaker Verlag, Aachen, pp 419–428
13. Schröder J (2000) Homogenisierungsmethoden der nichtlinearen Kontinuumsmechanik unter Beachtung von Instabilitäten. Bericht aus der Forschungsreihe des Instituts für Mechanik (Bauwesen), Lehrstuhl I, Universität Stuttgart
14. Schröder J (2009) Derivation of the localization and homogenization conditions for electromechanically coupled problems. Comput Mater Sci 46:595–599
15. Schröder J, Gross D (2004) Invariant formulation of the electromechanical enthalpy function of transversely isotropic piezoelectric materials. Arch Appl Mech 73:533–552
16. Schröder J, Keip M-A (2009) Computation of the overall properties of microheterogeneous piezoelectric materials. (in preparation)
17. Schröder J, Keip M-A (2010) Computer methods in mechanics – Lectures on the CMM 2009, chapter A framework for the two-scale homogenization of electro-mechanically coupled boundary value problems. Springer, vol. 1, III:311–329
18. Smit RJM, Brekelmans WAM, Meijer HEH (1998) Prediction of the mechanical behavior of nonlinear heterogeneous systems by multi-level finite element modeling. Comput Method Appl Mech Eng 155:181–192
19. Terada K, Kikuchi N (2001) A class of general algorithms for multi-scale analyses of heterogeneous media. Comput Method Appl Mech Eng 190(40–41):5427–5464
20. Walpole LJ (1966) On bounds for the overall elastic moduli of inhomogeneous system. J Mech Phys Solid 14:151–162
21. Willis JR (1966) Bounds and self-consistent estimates for the overall properties of anisotropic composites. J Mech Phys Solid 25:185–202
22. Xia Z, Zhang Y, Ellyin F (2003) A unified periodical boundary conditions for represantative colume elements of composites and applications. Int J Solid Struct 40:1907–1921

23. Zgonik M, Bernasconi P, Duelli M, Schlesser R, Günter P, Garrett MH, Rytz D, Zhu Y, Wu X (1994) Dielectric, elastic, piezoelectric, electro-optic, and elasto-optic tensors of $BaTiO_3$ crystals. Phys Rev B 50(9):5941–5949
24. Zohdi TI (2008) On the computation of the coupled thermo-electromagnetic response of continua with particulate microstructure. Int J Numer Method Eng 76(8):1250–1279
25. Zohdi TI, Wriggers P (2005) Introduction to computational micromechanics. In: Pfeiffer F, Wriggers P (eds) Lecture notes in applied and computational mechanics, vol 20. Springer, Berlin

A Boundary Element Method Coupled to Phase Field to Compute Ferroelectric Domains in Complex Geometries

Kaushik Dayal and Kaushik Bhattacharya

Abstract Ferroelectrics display couplings between mechanics, electromagnetism and optics. Hence they are in use and have been proposed as elements of MEMS and nanotechnological devices. In these applications, ferroelectrics are machined to have complex geometries and electrode arrangements, and are subjected to microstructural rearrangements.

Current mesoscale calculations of ferroelectric microstructure with the phase-field method are typically limited to completely periodic geometries or other special boundary conditions. This is due to the infeasible computational expense in accurately accounting for the stray electric fields caused by charges and electrodes; it requires solution of the electrostatic equations over all of space.

We present a computational technique to predict ferroelectric microstructure in complex geometries. The key issue is to resolve both the internal electric fields in the ferroelectric, as well as the stray electric fields that exist outside the material. In particular, we apply a Boundary Element Method (BEM) or Dirichlet-to-Neumann map to calculate the stray electrostatic fields that are generated by a ferroelectric specimen with no a priori restrictions on geometry. This allows us to move beyond periodic boundary conditions, yet retain accuracy and numerical efficiency in computing the stray electric fields. We couple this implementation to a real-space phase-field method and elasticity solver to obtain domain patterns under electromechanical loads. We apply this to calculate the microstructural rearrangements at the tip of a notch.

K. Dayal (✉)
Carnegie Mellon University, Pittsburgh
e-mail: kaushik@cmu.edu

K. Bhattacharya
California Institute of Technology, Pasadena
e-mail: bhatta@caltech.edu

M. Kuna and A. Ricoeur (eds.), *IUTAM Symposium on Multiscale Modelling of Fatigue, Damage and Fracture in Smart Materials*, IUTAM Bookseries 24,
DOI 10.1007/978-90-481-9887-0_26,

1 Introduction

Ferroelectric materials are used for actuation, in high-speed memories, as elements of microwave circuits [3], and as photonic switches [2] at small lengthscales. Fracture processes in ferroelectrics are strongly coupled to domain evolution. Design and manufacture of new devices and predicting failure requires an understanding of the detailed microstructure in realistic geometries.

Understanding domain patterns in ferroelectrics and their evolution in response to applied loads has motivated much recent research. The time-dependent Devonshire-Landau-Ginzburg (TDGL) framework using phase-field has led to important insights into the overall behavior, examples include microstructure in barium titanate [6] and lead titanate [10]. The ability of TDGL phase-field methods to model these microstructural phenomena makes them good candidates for further efforts in this direction.

However, electrostatic fields generated by devices are *nonlocal*. Stray fields extend not only within the material but over all of space. Current numerical methods to evaluate electrostatic contributions to the free energy rely on the FFT technique for efficient computation. This restricts analysis to periodic domains. Other approaches focus on completely shielded systems that are completely covered by electrodes and hence do not allow stray fields outside the body. As devices of interest grow smaller and are micromachined to have complex features, there is a need to extend the framework to deal with the complex geometries that can not be adequately understood with current techniques.

We present here our implementation of a *boundary element* technique that allows for the accurate and efficient resolution of electrostatic fields over all space, without the assumptions of periodicity or shielding, and allows us to deal with complex geometries. Boundary element techniques have been developed and are standard techniques in the context of electromagnetism, acoustics and other areas that require the resolution of fields over finite regions but with the boundary conditions specified over an infinite domain. Examples of can be found in [18] and references therein.

We couple our boundary element implementation to a phase-field model [1, 14] for the evolution of domain patterns in ferroelectrics, and present examples of computations and geometries that are possible with this technique. This phase field model has been used to characterize domain patterns that are formed in barium titanate under different electromechanical loadings and captures the essential features. In this model, the electric field is formulated explicitly in real-space rather than in a periodic geometry, as is typical in previous work involving phase-field models. We exploit the real-space formulation to implement the boundary element technique.

We begin by presenting the phase-field equations and the associated gradient flow evolution equations in Section 2. In Section 3, we present the techniques we use to solve the evolution equations, emphasizing the details of the boundary element technique. We present an example in Section 4.

2 The Phase-Field Formulation

From [14], the potential energy E of a ferroelectric body Ω can be written:

$$E(\boldsymbol{\varepsilon}, \mathbf{p}) = \int_{\Omega} \left[U(\nabla \mathbf{p}) + W(\boldsymbol{\varepsilon}, \mathbf{p}) \right] d\Omega + \frac{\varepsilon_0}{2} \int_{\mathbb{R}^3} |\nabla \phi|^2 dV \tag{1}$$

and is a function of the strain field $\boldsymbol{\varepsilon}$ and the polarization field $\mathbf{p}$. The contributions are a surface energy U that penalizes gradients in $\mathbf{p}$ and models the energy contributions from domain walls, an anisotropy energy W that penalizes $\mathbf{p}$ not being aligned with the prefered directions, and the electrostatic energy in the electric fields $\mathbf{E} = -\nabla\phi$, where ϕ is obtained from Maxwells equation:

$$\nabla \cdot (\mathbf{p} - \varepsilon_0 \nabla \phi) = 0 \quad \text{over} \quad \mathbb{R}^3 \tag{2}$$

The first two terms are local to the body being considered, while the electrostatic contribution is over all space.

We model the evolution of the system through gradient flow of the potential energy. Taking the first variation:

$$\mu \frac{dp_i}{dt} = \left(\frac{\partial U}{\partial p_{i,j}} \right)_{,j} - \frac{\partial W}{\partial p_i} - \phi_{,i} \quad \text{over} \quad \Omega \tag{3a}$$

$$\left(\frac{\partial W}{\partial \varepsilon_{ij}} \right)_{,j} = 0 \quad \text{over} \quad \Omega \tag{3b}$$

$$p_{i,i} - \varepsilon_0 \phi_{,ii} = 0 \quad \text{over} \quad \mathbb{R}^3 \tag{3c}$$

The boundary conditions from the variation are $\nabla \mathbf{p} \cdot \mathbf{n} = 0$ associated with the evolution of $\mathbf{p}$, conventional elasticity boundary conditions for the elasticity, and voltage specified on the electrodes and decaying at infinity for the electrostatics.

We work with barium titanate, and specialize the constitutive models for this material. Further, we restrict ourselves to a two-dimensional plane strain system for the computational implementation, but our formulation is general.

We use the same material model as [19]:

$$U(\nabla \mathbf{p}) = \frac{a_0}{2} \left(p_{1,1}^2 + p_{1,2}^2 + p_{2,1}^2 + p_{2,2}^2 \right) \tag{4}$$

$$\begin{aligned} W(\boldsymbol{\varepsilon}, \mathbf{p}) = {} & \frac{a_1}{2} \left(p_1^2 + p_2^2 \right) + \frac{a_2}{4} \left(p_1^4 + p_2^4 \right) + \frac{a_3}{2} p_1^2 p_2^2 + \frac{a_4}{6} \left(p_1^6 + p_2^6 \right) \\ & + \frac{a_5}{4} p_1^4 p_2^4 + (\boldsymbol{\varepsilon} - \boldsymbol{\varepsilon}_T(\mathbf{p})) \cdot \mathbb{C} \cdot (\boldsymbol{\varepsilon} - \boldsymbol{\varepsilon}_T(\mathbf{p})) \end{aligned} \tag{5}$$

where we have assumed that the energy due to misfit strain is linear elastic, and the stress-free strain is coupled to the local polarization.

We use the material constants $a_0, a_1, a_2, a_3, a_4, a_5, \mathbb{C}$ and the expression for $\boldsymbol{\varepsilon}_T(\mathbf{p})$ chosen by [19], as these have been shown to adequately reproduce the response of barium titanate.

3 Solving the Phase-Field Evolution Equations

In this section, we detail the numerical method that we will use. Our strategy is to use an initial guess for the strain and polarization fields in the interior of the ferroelectric, and evolve in the direction of the gradient flow until we reach an equilibrium state. At each time step of the gradient flow, as we update the polarization, we solve the electrostatic and elastostatic equations to find the strain and electric potential caused by the updated polarization field. These new fields are then used to again update the polarization, and the process is repeated.

The polarization update is achieved using a simple explicit time marching scheme. The elasticity equations are solved by using a standard displacement-based FEM.

The electrostatic potential is obtained from the solution of Maxwell's equation over all space. However, we have from the equation for the polarization update that we only require the potential field within the body. This leads to boundary elements to transform the nonlocal problem of obtaining the electrostatic potential by solving over all space, to a local problem that provides the solution only over the region of interest. This transformation is an efficient method to solve the electrostatic equations, without any loss of accuracy.

The key idea behind the boundary element method is the Dirichlet to Neumann map, i.e., we transform our boundary conditions from being partially specified on the boundary (through a given voltage at the electrodes) and partially specified at infinity (through the requirement that the field decays far away) to simpler boundary conditions: that the surface charge is specified *everywhere* on the boundary, *including* at the electrodes.

In the following, we note that we are solving the electrostatics problem at a given instant in time. Hence, the polarization is a fixed quantity that is specified for the purposes of solving for the electric field.

Writing out the electrostatics equation and its boundary conditions:

$$\varepsilon_0 \nabla \cdot \nabla \phi(\mathbf{x}) = \nabla \cdot \mathbf{p}(\mathbf{x}) =: \rho(\mathbf{x}) \quad \text{over} \quad \mathbb{R}^3 \tag{6a}$$

$$\phi(\mathbf{x}) = V_0(\mathbf{x}) \quad \text{on} \quad \partial\Omega_\phi \tag{6b}$$

$$\varepsilon_0 [\![\nabla \phi(\mathbf{x})]\!] \cdot \hat{\mathbf{n}} = \mathbf{p}(\mathbf{x}) \cdot \hat{\mathbf{n}} =: \sigma(\mathbf{x}) \quad \text{on} \quad \partial\Omega_\sigma \tag{6c}$$

$$\nabla \phi(\mathbf{x}) \to 0 \quad \text{as} \quad (\mathbf{x}) \to \infty \tag{6d}$$

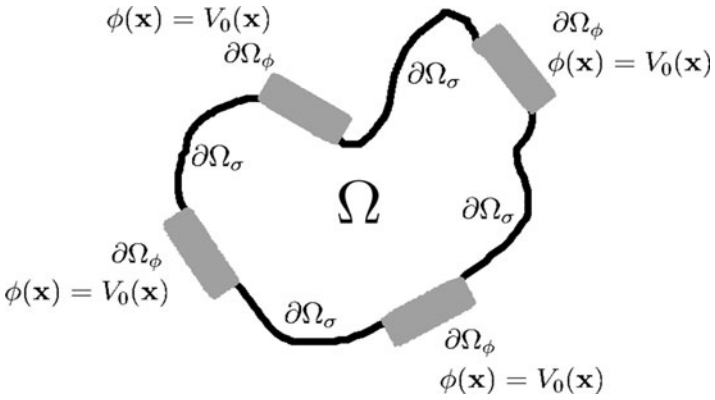

Fig. 1 Boundary conditions for the electrostatics problem

The notation: $\partial\Omega_\phi, \partial\Omega_\sigma$ are the portions of the boundary with electrodes, free surfaces respectively. Electrode boundaries have voltage specified and free surfaces have surface charge density (from discontinuous polarization) specified (Fig. 1). We do not consider any other electrical boundary conditions in this work, and hence $\partial\Omega_\phi \cup \partial\Omega_\sigma = \partial\Omega$ covers the entire ferroelectric Ω.[1]

We replace the voltage boundary conditions over $\partial\Omega_\phi$ by unknown surface charges σ^*:

$$\varepsilon_0 \nabla \cdot \nabla\phi(\mathbf{x}) = \rho(\mathbf{x}) \quad \text{over} \quad \mathbb{R}^3 \tag{7a}$$

$$\varepsilon_0 [\![\nabla\phi(\mathbf{x})]\!] \cdot \hat{\mathbf{n}} = \begin{cases} \sigma(\mathbf{x}) & \text{on} \quad \partial\Omega_\sigma \\ \sigma^*(\mathbf{x}) & \text{on} \quad \partial\Omega_\phi \end{cases} \tag{7b}$$

$$\nabla\phi(\mathbf{x}) \to 0 \quad \text{as} \quad (\mathbf{x}) \to \infty \tag{7c}$$

If $G(\mathbf{x}, \mathbf{x}')$ is the fundamental (Greens) solution to this equation:

$$\phi(\mathbf{x}) = \int_\Omega G(\mathbf{x}, \mathbf{x}')\rho(\mathbf{x}')d\mathbf{x}' + \int_{\partial\Omega_\sigma} G(\mathbf{x}, \mathbf{x}')\sigma(\mathbf{x}')d\mathbf{x}' + \int_{\partial\Omega_\phi} G(\mathbf{x}, \mathbf{x}')\sigma^*(\mathbf{x}')d\mathbf{x}' \tag{8}$$

Applying this to $\partial\Omega_\phi$ where $\phi(\mathbf{x}) = V_0(\mathbf{x})$:

$$V_0(\mathbf{x}) = \int_\Omega G(\mathbf{x}, \mathbf{x}')\rho(\mathbf{x}')d\mathbf{x}' + \int_{\partial\Omega_\sigma} G(\mathbf{x}, \mathbf{x}')\sigma(\mathbf{x}')d\mathbf{x}' + \int_{\partial\Omega_\phi} G(\mathbf{x}, \mathbf{x}')\sigma^*(\mathbf{x}')d\mathbf{x}' \tag{9}$$

[1] The surface charge balance is not a boundary condition for the electrostatic equation, but comes from the weak form of the electrostatics equation at a discontinuity, i.e. the body surface.

Now, we have the surface charge density on the entire boundary as well as the charge density in the interior. This enables us to find ϕ at any point in space by using the fundamental solution (8), and in particular, we evaluate ϕ over $\partial\Omega$, and we denote this $\phi^*(\mathbf{x})$. The problem has now been reduced to finding the potential within a finite domain, given the charge density in the interior and the potential on the entire boundary. We have thus decoupled the electrical field problem in the interior from the exterior:

$$\varepsilon_0 \nabla \cdot \nabla \phi(\mathbf{x}) = \rho(\mathbf{x}) \quad \text{in} \quad \Omega \tag{10a}$$

$$\phi(\mathbf{x}) = \phi^*(\mathbf{x}) \quad \text{on} \quad \partial\Omega \tag{10b}$$

and this can be solved using conventional and efficient techniques.

4 Microstructure at a Notch

Crack formation and growth due to combined electrical and mechanical loading is an important failure mechanism in ferroelectrics. The fracture process is more complex than in a purely mechanical setting due to the interaction between electrical and mechanical processes. Crack growth in ferroelectrics under both cyclic and constant loading has been studied experimentally, with PZT/PLZT receiving much attention (see, for example,[8, 9, 11, 12]). Experimental work in tetragonal ferroelectrics examining the 90° switching at the crack tip has been studied by [4,5,16]. Theoretical understanding of the crack growth phenomenon is difficult due to the need to incorporate local domain switching and formation of microstructure caused by the air gap. Efforts at understanding this process by making simplifying assumptions on the nature of the electrostatics, microstructure and surface structure are described, e.g., in [7, 13, 15, 17].

We use a simplified geometry as a first approximation: a rectangular computational domain with a thin rectangular notch removed. We ground the entire bottom face, and apply electrodes on either side of the notch. We use traction free boundary conditions over the entire boundary. We begin our computations with the polarization oriented along the horizontal direction to the right, with no applied loads or voltages. The large electric fields caused by the polarization ending on the notch faces with this domain pattern lead to the formation of closure domains as we evolve the polarization. Figure 2 shows the equilibrated domain pattern that is obtained. The domain pattern that we see is not compatible in a stress-free state. Thus, the notch causes stresses to develop even when no mechanical loads are applied. The polarization closely approximates a divergence-free field and the electrodes on the surface assist in the closure microstructure.

Once the field has settled into an equilibrium state, we apply a DC bias on the left electrode and AC forcing on the right electrode as in Fig. 3a. After an initial transient, the domain patterns settle into a cyclic evolution pattern. Figure 4 shows some snapshots in the cycle.

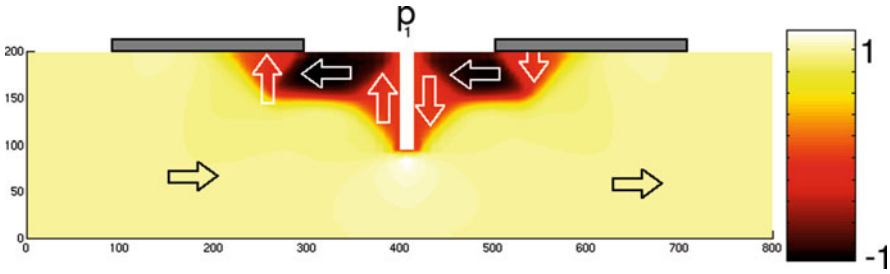

Fig. 2 Equilibrium domain pattern that develops from an initially *a*-axis crystal. The gray blocks mark the electrodes that are grounded during equilibration

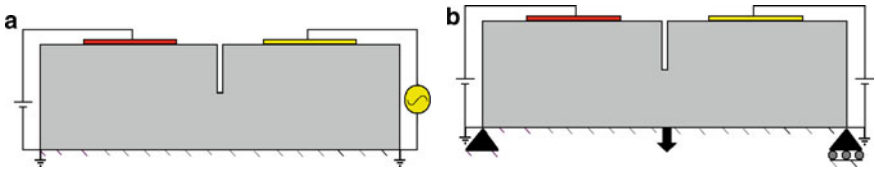

Electrical boundary conditions during AC cycling

Electromechanical boundary conditions during bending

Fig. 3 Schematic of the different load cases on the notched specimen

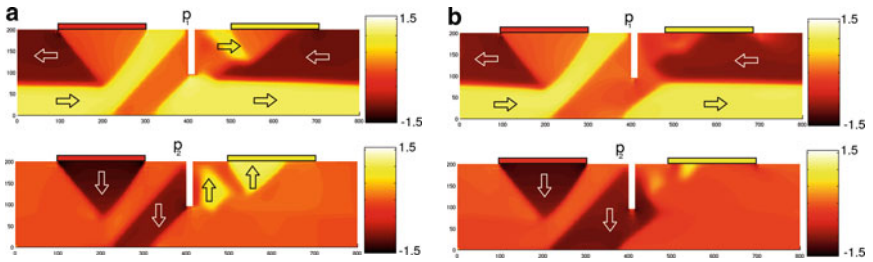

Domain patterns at time *t*

Domain patterns at quarter cycle beyond *t*

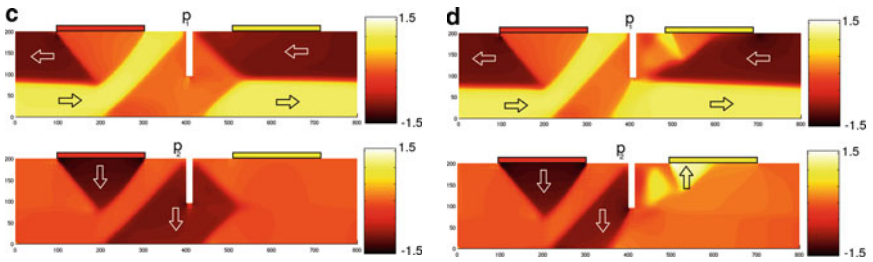

Domain patterns at half cycle beyond *t*

Domain patterns at three quarter cycle beyond *t*

Fig. 4 Snapshots of the polarization field. In each subfigure, the upper plot represents the horizontal component of **p** and the lower plot represents the vertical component of **p**. The arrows are only to guide the reader. The entire movie is available from the authors

The DC bias at the left electrode causes a c^- domain to form beneath it. As we can see from snapshots of the entire cycle, this domain hardly changes over the cycle. We also see that the presence of the notch has caused the entire upper half of the crystal to switch to a-axis oriented to the left. While this domain changes shape slightly in the vicinity of the AC electrode, it retains its structure over the rest of the crystal over the entire cycle. In fact, the domain pattern in the entire crystal to the left of the notch does not change much at all under cycling and seems decoupled from the changes that occur due to the AC electrode. The domain pattern in the crystal to the right of the notch also does not change much except for some switching near the edge of the electrode close to the notch and the rearrangement of adjacent domains to maintain electrical compatibility.

The region between the notch and the right (AC) electrode is the only portion of the crystal that has large response to the AC forcing. In Fig. 4a, with zero AC voltage and climbing, the domain between the notch and the right electrode is c^+ from the previous cycle. As the voltage is increased, the domain switches to a-axis and the snapshot at the positive peak AC voltage, Fig. 4b, shows that the c^+ domain has almost completely switched to a-axis. In Fig. 4c, at zero AC voltage and dropping, the switching is complete and there is no c^+ remaining. Figure 4d at the lowest point of the AC cycle shows that the negative voltage has caused switching and the c^+ domain has reappeared.

We now consider a calculation with a combination of mechanical and electrical loads that may provide insight into local domain switching of at crack tips. We begin with a notched crystal that is equilibrated from an a-axis poling as described above in Fig. 2. We now apply a point mechanical load as shown in Fig. 3b. While applying this mechanical load, we ground both the electrodes at the surface and also keep the the entire bottom surface grounded as in the previous calculations. We apply sufficient load to cause domain switching at the tip. Once the specimen has been equilibrated, we superpose DC voltages applied at the electrodes on the surface and examine the domain switching at the notch tip.

Figure 5a shows the domain patterns that form when the mechanical load is applied without electrical loading. By comparing the domain patterns just below the tip of the notch in Figs. 2 and 5a, we see that local switching has occurred. The domain patterns elsewhere in the specimen have shifted slightly, but no major rearrangements have occurred at this magnitude of loading. For larger loads, we find changes in the domain pattern over much of the specimen. Smaller loads do not unambiguously cause switching.

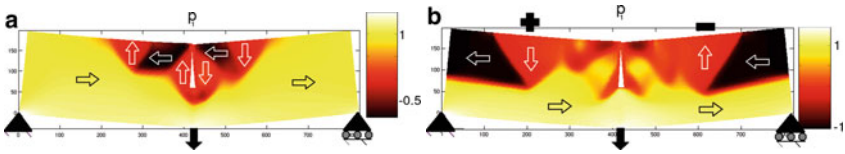

Fig. 5 (**a**) Domain pattern after back-switching the domain at the notch tip using DC bias at both electrodes. (**b**) Domain pattern that develops when a point mechanical load is applied while keeping the electrodes grounded

It would seem that the mechanics in this simple case can be understood through ideas from beam theory. When we apply the load, it causes the specimen to bend. The region of the specimen above the middle, i.e., above the tip of the notch, cannot bear much load, and the load is mostly taken by the lower half. The lower portion of the specimen below the notch acts as a beam, and the region near the bottom has $\sigma_{11} > 0$ and the region just below the notch has $\sigma_{11} < 0$. This stress below the notch tip favors c-axis strains and causes some of the a-axis domain to switch.

This idea is confirmed by applying the a load of opposite sense at the same point to cause the notch to open. We find switching from a-axis to c-axis in the lowermost region of the specimen and the strain just below the notch tip goes further away from c-axis.

By examining the distorted specimen in Fig. 5a, we see that the crystal has undergone large bending. As ferroelectric materials are quite brittle, we do not expect such large distortions to occur and it is likely that the specimen will mechanically fail before we see domain switching at the notch tip.

We now superpose different DC bias voltages to both of the electrodes in an attempt to reverse the switching. It is unlikely that it is possible to reverse the domain patterns to the mechanically unloaded state in the entire specimen by applying the voltages at the specific positions that we have chosen for the electrodes in this example. Instead, we examine the switching at the notch tip only.

For moderate voltage (compared to the applied voltage in the cycling) applied at the electrodes, we are able to reverse the mechanically induced switching at the notch tip. Figure 5b shows the complex domain patterns that develop elsewhere in the specimen as a result of applied voltages superposed over the large mechanical load. The distortion of the specimen induced by the mechanical loading does not show any significant reversal due to the application of voltage.

Acknowledgments This work draws from the doctoral dissertation of Kaushik Dayal at the California Institute of Technology. We acknowledge the partial financial support of the US Army Research Office through MURI Grant # DAAD 19-01-1-0517.

References

1. Dayal K, Bhattacharya K (2007) A real-space non-local phase-field model of ferroelectric domain patterns in complex geometries. Acta Mater 55(6):1907–1917
2. Dayal K, Bhattacharya K (2007) Active tuning of photonic device characteristics during operation by ferroelectric domain switching. J Appl Phys 102:064102
3. El-Naggar MY, Dayal K, Goodwin DG, Bhattacharya K, Graded ferroelectric capacitors with robust temperature characteristics. J Appl Phys 100:114115
4. Fang F, Yang W, Zhu T (1999) Crack tip 90° domain switching in tetragonal lanthanum-modified lead zirconate titanate under an electric field. J Mater Res 14(7):2940–2944
5. Fang F, Yang W, Zhang FC, Luo HS (2005) Fatigue crack growth for $BaTiO_3$ ferroelectric single crystals under cyclic electric loading. J Am Ceram Soc 88(9):2491–2497
6. Hu HL, Chen LQ (1998) Three-dimensional computer simulation of ferroelectric domain formation J Am Ceram Soc 81(3):492–500

7. Hao TH, Gong X, Suo Z (1996) Fracture mechanics for the design of ceramic multilayer actuators. J Mech Phys Solids 44(1):23–48
8. Lupascu DC, Aulbach E, Rodel J (2003) Mixed electromechanical fatigue in lead zirconate titanate. J Appl Phys 93(9):5551–5556
9. Lynch CS, Chen L, Suo Z, McMeeking RM, Yang W (1995) Crack growth in ferroelectric ceramics driven by cyclic polarization switching. J Intel Mat Syst Str 6(2):191–198
10. Li YL, Hu SY, Liu ZK, Chen LQ (2002) Effect of substrate constraint on the stability and evolution of ferroelectric domain structures in thin films. Acta Mater 50(2):395–411
11. Lynch CS (1998) Fracture of ferroelectric and relaxor electro-ceramics: Influence of electric field. Acta Mater 46(2):599–608
12. Oates WS, Lynch CS, Kounga Njiwa AB, Lupascu DC (2005) Anisotropic fracture behavior in ferroelectric relaxor PZN-4.5%PT single crystals. J Am Ceram Soc 88(7):1838–1844
13. Park S, Sun C-T (1995) Fracture criteria for piezoelectric ceramics. J Am Ceram Soc 78(6):1475–1480
14. Shu YC, Bhattacharya K (2001) Domain patterns and macroscopic behavior of ferroelectric materials. Philos Mag B 81(12):2021–2054
15. Suo Z, Kuo C-M, Barnett DM, Willis JR (1992) Fracture mechanics for piezoelectric ceramics. J Mech Phys Solids 40(4):739–765
16. Tan X, Xu Z, Shang JK, Han P (2000) Direct observations of electric field-induced domain boundary cracking in oriented piezoelectric single crystal. Appl Phys Lett 77(10):1529–1531
17. Wang J, Landis CM (2004) Fracture of ferroelectric and relaxor electro-ceramics: Influence of electric field Acta Mater 52:3435–3446
18. Wrobel LC (2002) The boundary element method: Applications in thermo-fluids and acoustics, vol 1. Wiley, Sussex, UK
19. Zhang W, Bhattacharya K (2005) A computational model for ferroelectric domains. Acta Mater 53:185–198

Low Energy Periodic Microstructure in Ferroelectric Single Crystals

Nien-Ti Tsou, Ingo Münch, and John E. Huber

Abstract Two distinct modelling approaches are used to find minimum energy (equilibrium) microstructural states in tetragonal ferroelectric single crystals. The first approach treats domain walls as sharp interfaces and uses analytical solutions of the compatibility conditions at domain walls to identify multi-rank laminate microstructures that are free of residual stress and electric field. The second method treats domain walls as diffuse interfaces, using a phase-field model in 3-dimensions. This is computationally intensive, but takes the full field equations into account and allows a more general class of periodic microstructure to be explored. By searching for minimum energy configurations of a cube of tetragonal material, candidate unit cells of a periodic microstructure are identified. Adding periodic boundary conditions allows the assembly of the unit cells into a macro-structure of low energy. A noteworthy structure identified in this way is a "hexadomain" vortex consisting of six tetragonal domains meeting along the major diagonal of a cube. Several of the structures identified by the phase-field model are found to be special cases of multi-rank laminate structure. Thus the analytical approach offers a fast method for finding equilibrium microstructures, while the phase-field model provides a validation of these solutions.

N.-T. Tsou
Department of Engineering Science, University of Oxford, Parks Road, Oxford, OX1 3PJ, UK
e-mail: Nien-Ti.Tsou@eng.ox.ac.uk

I. Münch
Karlsruhe Institute of Technology, Universität Karlsruhe, Kaiserstraße 12,
D-76131 Karlsruhe, Germany
e-mail: ingo.muench@kit.edu

J.E. Huber (✉)
Department of Engineering Science, University of Oxford, Parks Road, Oxford, OX1 3PJ, UK
e-mail: john.huber@eng.ox.ac.uk

M. Kuna and A. Ricoeur (eds.), *IUTAM Symposium on Multiscale Modelling of Fatigue, Damage and Fracture in Smart Materials*, IUTAM Bookseries 24,
DOI 10.1007/978-90-481-9887-0_27,

1 Introduction

The design of devices employing ferroelectric crystals relies on an understanding of the microstructure that forms within the crystals. Early studies of ferroelectric microstructure [8, 9] identified domains as regions of locally uniform electrical polarization, whose polar direction is dictated by the crystal lattice. When appropriately organized, the domains allow ferroelectric crystals to exhibit, at a macroscopic scale, a net polarization and other effects such as piezoelectricity and pyroelectricity. Thus the domain structure at the micro- or nano-scale, plays a key role in determining the properties and performance of ferroelectric devices. Theory and observation of ferroelectric microstructure have established that domains naturally organize into patterns, such as laminae [2, 8] or herringbone structure [2]. More recently, nano-scale polarization vortices and related structures have been predicted [6, 12, 13].

The aim of the present work is to explore the range of possible domain patterns, with particular focus on periodic microstructures of low energy. Low energy states of a ferroelectric crystal typically correspond to conditions of compatibility at the junctions of domains, so that domain walls are free of charge and dislocations. The compatibility conditions give rise to equations that relate the polarization and strain states of the domains, with the orientation of the domain wall separating them [3, 15]. This defines the set of possible domain walls. Two methods for finding low energy microstructural states can readily be developed: (1) Treat the domain wall as a sharp interface. Solve the equations of compatibility directly to find the compatible periodic structures, such as laminations, that are possible within a given crystal structure [4, 11]. (2) Treat the domain wall as a diffuse interface in a continuum. Use an appropriate continuum model such as a phase-field method [5] to study the equilibrium states of domains in a small region of material subject to periodic boundary conditions. In this work, each of these two methods is used to identify periodic microstructures. Naturally arising microstructure in ferroelectrics is typically non-periodic, though it may contain small regions of nearly periodic regularity. The emphasis here is on finding periodic arrangements that meet the requirements of stability/compatibility, rather than on determining the structures that form naturally. Thus the aim is not prediction or analysis of naturally occurring microstructure, so much as exploration of the inherent possibilities of the microstructure. If such exploration yields microstructures with properties of interest or value then this would motivate the further study necessary to find how they could be engineered in practice.

In the following sections, the theory of compatibility is briefly presented and then illustrated by generating all the examples of rank-1 and rank-2 laminated microstructure that exist in the tetragonal crystal system of barium titanate. Next, the diffuse interface (phase-field) approach is introduced and used to find equilibrium states of a cubic region of tetragonal material. These are then arranged into a variety of periodic assemblies and it is shown that some of these arrangements (though not all) are special cases of solutions arising from the theory of multi-rank laminates.

2 Sharp Interface Model: Theory of Compatible Domains

The theory of compatible microstructures has been given in previous works [3, 11, 15, 18]. A brief summary is given here, in the context of the example studied in this paper, namely the polar tetragonal crystal structure of ferroelectrics such as barium titanate and lead titanate. The unit cell of the crystal structure is tetragonal, with volume $V = a^2c$ where a and c are lattice parameters and $c > a$. The crystal is polar, with polarization $\mathbf{P}$ in one of the three orthogonal directions parallel to the edges of the unit cell, and with magnitude P_0 ($\mathbf{P} = \pm[100]P_0$, $\pm[010]P_0$, or $\pm[001]P_0$). Associated with each of the six polarization states is a spontaneous strain, relative to a reference cube of volume V, given by $\varepsilon_{ij} = \varepsilon_0(\hat{p}_i\hat{p}_j - \delta_{ij}/3)$ where $\varepsilon_0 = (c-a)/a$ is a measure of the distortion of the unit cell away from cubic, $\hat{\mathbf{p}}$ is the unit vector in the polarization direction, and $\boldsymbol{\delta}$ is the Kronecker delta. Let the six crystal variants be numbered $i = 1 \cdots 6$. Then a compatible domain wall between adjacent domains of type i and j can form if:

$$(\mathbf{P}_i - \mathbf{P}_j).\mathbf{n} = 0 \tag{1}$$

$$\boldsymbol{\varepsilon}_i - \boldsymbol{\varepsilon}_j = (\mathbf{a} \otimes \mathbf{n} + \mathbf{n} \otimes \mathbf{a})/2 \tag{2}$$

Here $\mathbf{a}$ is any vector and $\mathbf{n}$ is the unit normal vector at the domain wall. Equations 1 and 2 give only two types of solution in the tetragonal crystal system, corresponding to the well known 180° and 90° domain walls.

In the present work, we consider the application of Eqs. 1 and 2 to periodic, multi-rank laminates. A rank-1 laminate consists of alternating layers of two distinct crystal variants. Only two distinct forms of rank-1 laminate are possible (see Fig. 1), corresponding to the two types of domain wall. A rank-2 laminate consists of alternating layers, each of which is a rank-1 laminate; the arrangement of the crystal variants that are present can be represented by a tree-diagram as shown in Fig. 2. This tree diagram represents a laminate in which crystal variants 1 and 2 are first laminated together to form a rank-1 laminate. Similarly, variants 3 and 4 are laminated together. Then, the resulting pair of rank-1 laminates are joined to form a rank-2 laminate. We can describe this structure using the designation "1234" representing the crystal variants found in the bottom level of the tree-diagram. The final lamination is carried out in such a way that variant 1 meets with variant 3 across the highest

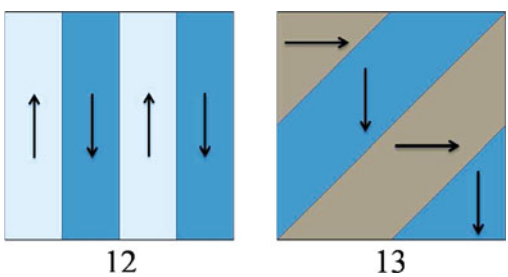

Fig. 1 The two possible rank-1 periodic structures in the polar tetragonal crystal system. A 180° domain laminate formed by laminating variants 1 and 2, and a 90° domain laminate formed by laminating variants 1 and 3

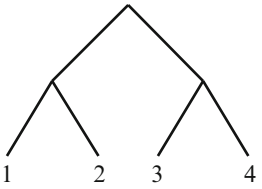

Fig. 2 An example of a rank-2 tree diagram. Crystal variants 1 and 2 are laminated together and crystal variants 3 and 4 are laminated together. The resulting pair of rank-1 laminates are then joined

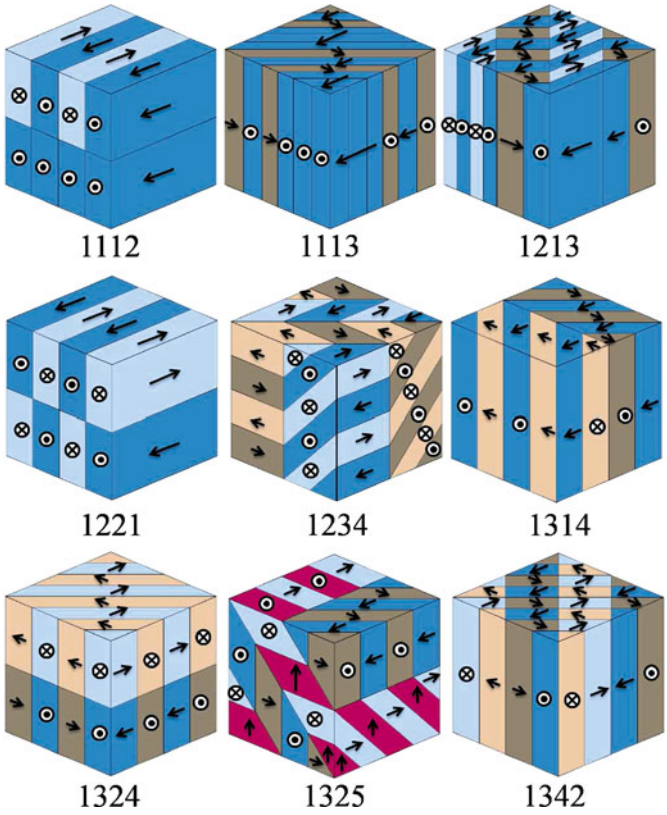

Fig. 3 The nine possible rank-2 periodic laminate structures in the polar tetragonal crystal system, and the designations of their tree-diagrams

level domain wall, while variant 2 meets with variant 4 at the same domain wall. At first sight it appears that there may be as many as 6^4 ways of combining the 6 crystal variants of the tetragonal system to form rank-2 laminates. However, many of these structures are simply rotations or reflections of other structures; eliminating these leaves only 19 distinct topologies. Some of these, such as "1212" simplify into rank-1 structures, further reducing the possibilities. Finally, taking account of Eqs. 1 and 2 leaves only 9 distinct topologies that satisfy the compatibility equations exactly at all domain walls. These nine structures and their designations are shown in Fig 3.

Each structure shown in Fig. 3 is a cube shaped region of material illustrated with the six crystal variants shown in different shades. Arrows are used to indicate local polarization directions. The cubes shown in this diagram represent unit-cells of microstructure that can be assembled into exactly compatible periodic structures. Structures of this type have been discussed previously by several authors. For example, the rank-2 laminate designated "1325" in Fig. 3 was described by Arlt and Sasko [2] and is shown in reflection in figure 4 of their paper; the same structure was also predicted by Shu and Bhattacharya [15] and appears in their Fig.8(c). Higher rank periodic laminates that satisfy exact compatibility requirements are also possible. These are not enumerated in the present work, though some special cases are discussed below.

3 Diffuse Interface Model: Phase-Field Method

An alternative method for finding low energy microstructural states is to model the evolution of domain walls into a stable pattern with periodic boundary conditions. The phase-field method provides a useful framework for such modelling. Again, since the application of the phase-field method to ferroelectric crystals has been described elsewhere [7, 17, 20], only a brief summary is given here. Each material point is associated with an order parameter, here taken to be the local polarization field **P**, that defines which crystal variant is present. At a typical material point, the order parameter will adopt one of the six states of polarization of the tetragonal system, as defined in Section 6. However, near the domain walls, the order parameter deviates from these states over a region of finite width, producing diffuse interfaces between domains. The model is derived from a free-energy function ψ dependent on the strain and polarization of the unit cell, with sufficient richness to provide energy wells at each of the six stable states of polarization and remanent strain. The local linear properties such as piezoelectricity, elastic and dielectric behaviour depend on the curvature of these energy wells [10, 17]:

$$\begin{aligned}\psi = {} & \frac{1}{2}a_{ijkl}P_{i,j}P_{k,l} + \frac{1}{2}a'_{ij}P_iP_j + \frac{1}{4}a''_{ijkl}P_iP_jP_kP_l \\ & + \frac{1}{6}a'''_{ijklmn}P_iP_jP_kP_lP_mP_n + \frac{1}{8}a''''_{ijklmnrs}P_iP_jP_kP_lP_mP_nP_rP_s \\ & - b_{ijkl}\varepsilon_{ij}P_kP_l + \frac{1}{2}c_{ijkl}\varepsilon_{ij}\varepsilon_{kl} + f_{ijklmn}\varepsilon_{ij}\varepsilon_{kl}P_mP_n \\ & + g_{ijklmn}\varepsilon_{ij}P_kP_lP_mP_n + \frac{1}{2\kappa_0}(D_i - P_i)^2. \end{aligned} \tag{3}$$

Here, P_i is the order parameter (local polarization vector), while ε_{ij} is the local strain; D_i is the electric displacement, and all other quantities are material dependent parameters. Following Su and Landis [17], a generalized form of the Ginzburg-

Landau equation can be derived, allowing the evolution of polarization with time to be modelled:

$$\left(\frac{\partial \psi}{\partial P_{i,j}}\right)_{,j} - \frac{\partial \psi}{\partial P_i} = \beta \dot{P}_i \tag{4}$$

where β is an inverse mobility parameter that determines the speed of moving domain walls. Writing Eq. 4 along with the standard mechanical and electrical equilibrium equations in weak form allows boundary value problems to be solved for regions of material of arbitrary shape using the finite element method. Phase-field models in 2-dimensions have been used to predict a variety of microstructures, including multi-rank laminates. For example, the rank-1 laminate designated "13" in Fig. 1 was found as a periodic solution by several authors [1,19]. Similarly, Shu [16] found rank-1 and rank-2 laminate structures as stable periodic solutions in a rhombohedral ferroelectric. Note that because certain rank-1 and rank-2 structures (for example "1314") are prismatic in form, they can be found by 2-dimensional models, while non-prismatic structures (for example "1325") could not.

By running the phase-field model in 3-dimensions, several forms of periodic structure can be identified. Two equilibrium states for a cubic region of material that have the particular property of forming flux closures (the normal component of polarization is zero at all surfaces) are shown in Fig. 4. These structures also have zero displacement boundary conditions at all surfaces. In Fig. 4a, a square polarization

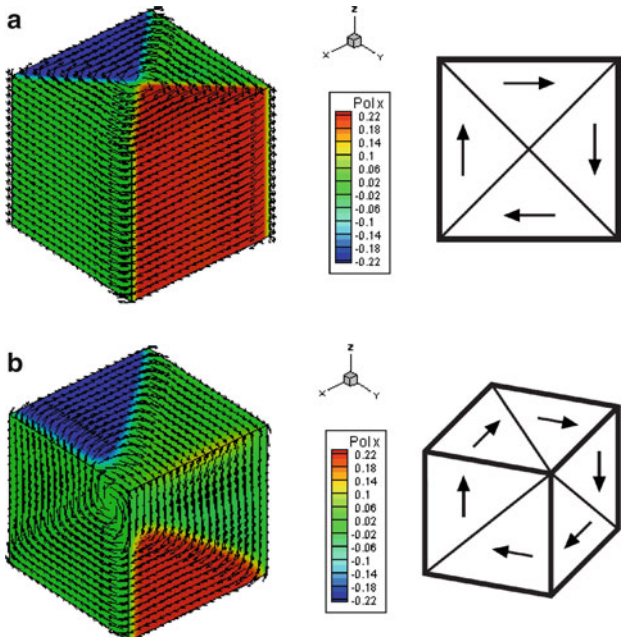

Fig. 4 Two solutions of the phase-field model for a cube of tetragonal ferroelectric material which form flux closures; (**a**) the tetradomain vortex, and (**b**) the hexadomain vortex

vortex has formed, consisting of four domains with polarization arranged head-to tail. The phase-field solution is shown using arrows to represent local polarization directions, and colour to indicate the magnitude of polarization in the x-direction. This arrangement is prismatic and a sketch of the domain arrangement in 2-dimensions is also shown. Figure 4b shows another phase-field solution, with a 3-dimensional form consisting of six domains arranged in a polarization vortex around the major diagonal of the cube. An idealised sketch of this arrangement is also shown. In each case the simulation was started with the order parameter close to zero throughout, and stable domains evolved to minimise the total energy. The initial values of the order parameter were set using a small random field to break symmetry. The two solutions shown have very similar values of free energy and were obtained by starting the simulation with different random fields. In previous work [12] the vortex shown in Fig. 4a was named a "tetradomain vortex", and that in Fig. 4b was named a "hexadomain vortex".

The two vortices shown in Fig. 4 are capable of assembly into low-energy periodic structures. Consider first the tetradomain vortex of Fig. 4a. Taking this cube as a unit cell, a periodic structure can be assembled which is prismatic in form (see Fig. 5a, b), by imposing 180° domain walls on four faces of the cube. Note that

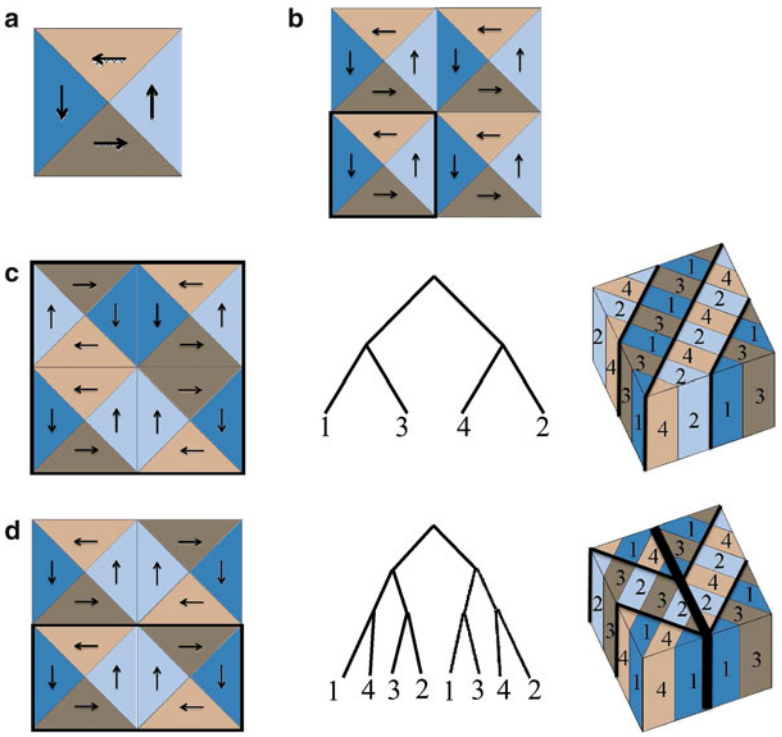

Fig. 5 The tetradomain vortex and various periodic assemblies, showing the corresponding laminate structures and their tree-diagrams

each unit cell in this assembly has a net toroid moment **G** [13], which is the total moment of polarization, calculated by

$$\mathbf{G} = \int_V \mathbf{r} \times \mathbf{P} \, \mathrm{d}v \tag{5}$$

where **P** is the local polarization and **r** is the position vector. Neglecting domain walls, the toroid moment per unit volume, **g**, of this assembly is $wP_0/3$ where w is the width of the unit cell. Alternative periodic assemblies can be produced by enlarging the unit cell by reflection to include four vortices such that the domains of each vortex are continuous with the next vortex (no 180° domain walls). The resulting structure is shown in Fig. 5c and has zero net toroid moment. It is interesting to note that this structure formed by periodic assembly of vortices is in fact a special case of the rank-2 laminate structure designated "1342" that appeared in Fig. 3. The laminate is redrawn in Fig. 5c; to make it match exactly with the periodic assembly of tetradomains, all domain wall spacings must be equal. A similar structure, described as an antiferrotoroidic supercell was found by Prosandeev et al. [14] using Monte Carlo and molecular dynamics methods. Figure 5d shows a periodic assembly of the tetradomain vortex in which the unit cell comprises a pair of vortices related by reflection. The resulting assembly has zero toroid moment and is also a special case of a rank-3 laminate, with designation "14321342". The spacing of the highest level domain walls (shown by a heavy line in Fig. 5d) must be exactly $\sqrt{2}$ times the spacing of all the other domain walls in order to match the tetradomain assembly. Returning to the assembly in Fig. 5b, careful examination reveals that this is also a special case of a laminate structure: it is a rank-4 laminate with designation "1324423114233241".

The hexadomain vortex shown in Fig. 4b can be assembled into periodic structures with either 180° domain walls or continuous domains (no domain wall) at the junctions of adjacent vortices. Combining eight vortices with 180° domain walls at their junctions gives the unit cell of microstructure shown in Fig. 6a. Alternatively, combining eight vortices with continuous domains at their junctions gives the unit cell shown in Fig. 6b. Other combinations are possible. Like the individual hexadomain, the resulting periodic structures have the properties of zero average polarization and remanent strain. However, while a single hexadomain vortex has toroid moment of magnitude $wP_0/2\sqrt{3}$ per unit volume, the assemblies shown in Fig. 6 have zero toroid moment. It is interesting to consider whether such topologies as are shown in Fig. 6 can be represented as special cases of multi-rank laminate structure. Like laminates, the structures built from these unit cells are permeated by continuous planar domain walls. However, examination of these topologies shows that they do not satisfy the conditions of exactly compatible laminate structure as described by Tsou and Huber [18]. Thus the hexadomain assemblies are not special cases of multi-rank laminate structure.

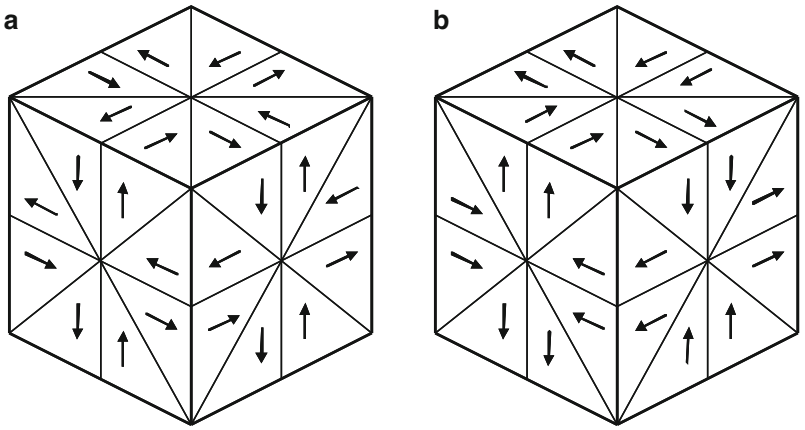

Fig. 6 Two examples of unit cells for periodic assembly, each made from eight hexadomain vortices, (**a**) with 180° domain walls, and (**b**) with continuous domains

4 Conclusion

By using a sharp interface model of compatible ferroelectric microstructures, the set of distinct rank-1 and rank-2 periodic laminates that satisfy exact compatibility conditions in the tetragonal crystal system has been identified. These topologies represent low energy periodic microstructures; similar (though not perfectly periodic) structures are likely to form in tetragonal ferroelectrics such as barium titanate. Other potential unit cells of periodic, low energy microstructure were identified by using a phase-field model. It has been shown that some of the resulting periodic assemblies are special cases of multi-rank laminates in which the domain wall spacing produces highly symmetric structures. Several of the topologies identified in this work have been described in the literature, where they were found by a variety of methods. However, the present work reports a systematic method for generating low-energy periodic microstructures. Various laminate structures have been found to occur naturally in ferroelectric crystals. This raises the question: could assemblies of vortices form naturally or be engineered?

Acknowledgements J.E.H. Acknowledges support of EPSRC project No. EP/E026095/1. I.M. gratefully acknowledges the Karlsruhe House of Young Scientists for awarding a research fellowship to support his stay at the University of Oxford.

References

1. Ahluwalia R, Cao W (2001) Size dependence of domain patterns in constrained ferroelectric system. J Appl Phys 89:8105
2. Arlt G, Sasko P (1980) Domain configuration and equilibrium size of domains in $BaTiO_3$ ceramics. J Appl Phys 51:4956

3. Ball JM, James RD (1987) Fine phase mixtures as minimizers of energy. Arch Rat Mech Anal 100:13
4. Bhattacharya K (1993) Comparison of the geometrically nonlinear and linear theories of martensitic transformation. Cont Mech Thermo 5:205
5. Chen L-Q (2002) Phase-field models for microstructure evolution. Annu Rev Mater Res 32:113
6. Gruverman A, Wu D, Fan HJ, Vrejoiu I, Alexe M (2008) Vortex ferroelectric domains. J Phys Condens Matter 20:342201
7. Hu H-L, Chen L-Q (1998) Three-dimensional computer simulation of ferroelectric domain formation. J Am Ceram Soc 81:492
8. Jona F, Shirane G (1962) Ferroelectric crystals. Pergamon, Oxford
9. Kay HF (1948) Preparation and properties of crystals of barium titanate $BaTiO_3$. Acta Cryst 1:229
10. Kontsos A, Landis CM (2009) Computational modeling of domain wall interactions with dislocations in ferroelectric crystals. Int J Solids Struct 46:1491
11. Li JY, Liu D (2004) On ferroelectric crystals with engineered domain configurations. J Mech Phys Solids 8:1719
12. Münch I, Huber JE (2009) A hexadomain vortex in tetragonal ferroelectrics. Appl Phys Lett 95:022913
13. Naumov II (2004) Unusual phase transitions in ferroelectric nanodisks and nanorods. Nature 432:737
14. Prosandeev S, Ponomareva I, Naumov I, Kornev I , Bellaiche L (2008) Original properties of dipole vortices in zero-dimensional ferroelectrics. J Phys Condens Matter 20:193201
15. Shu YC, Bhattacharya K Domain patterns and macroscopic behaviour of ferroelectric materials. Philos Mag B 81:2021
16. Shu YC, Yen JH (2007) Pattern formation in martensitic thin films. Appl Phys Lett 91:021908
17. Su Y, Landis CM (2007) Continuum thermodynamics of ferroelectric domain evolution: Theory, finite element implementation, and application to domain wall pinning. J Mech Phys Solids 55:280
18. Tsou NT, Huber JE (2009) Construction of compatible microstructures for tetragonal ferroelectric single crystals. Proc SPIE 7289:72890B
19. Wang J, Shi S-Q, Chen L-Q, Li Y, Zhang T-Y (2004) Phase field simulations of ferroelectric/ferroelastic polarization switching. Acta Mat 52:749
20. Wang J, Kamlah M, Zhang T, Li Y, Chen L (2008) Size-dependent polarization distribution in ferroelectric nanostructures: Phase field simulations. Appl Phys Lett 92:162905